SOLAR MODULATION OF PROTONS AND HELIUM IN COSMIC RAYS WITH THE ALPHA MAGNETIC SPECTROMETER

A DISSERTATION SUBMITTED TO THE GRADUATE DIVISION OF THE UNIVERSITY OF HAWAIʻI AT MĀNOA IN PARTIAL FULFILLMENT OF THE REQUIREMENTS FOR THE DEGREE OF

DOCTOR OF PHILOSOPHY

IN

PHYSICS

JULY 2017

By

Claudio Corti

Dissertation Committee:

Veronica Bindi, Chairperson
Peter Gorham
Jason Kumar
John G. Learned
Sven Vahsen
R. Brent Tully

Keywords: AMS-02, cosmic rays, solar modulation, numerical model

To my wife,

Silvia,

who supported me throughout this long adventure.

ACKNOWLEDGMENTS

The first, huge, thanks is obviously for Veronica, my advisor, who was crazy enough to bring me to Hawaii as her first student. She always pushed me to go forward, even when I was critical with myself (basically always...). I really envy her strong will and her being so full of ideas: once she sets on a goal, she can not be stopped, no matter how many times I say "*No, we can't do this*". I am grateful to have worked in these years with her and with the AMS group at University of Hawaii at Manoa: I could not have hoped for better colleagues!

A special thanks to my thesis buddy, Katie: I already told you, you're a wonderful person. Seeing how you managed to work so hard and at the same time raise a baby motivated me in these last weeks of this thesis. Oh, by the way, thanks also for Nico: such a cute baby, he brought a lot of joy in the offices, providing a nice distraction from work!

A big thanks goes, of course, to Cristina, for all the amazing work she has done on the AMS data analysis in our group.

I am forever indebted to Prof. Potgieter, who invited me for three months in Potchefstroom, South Africa, to teach me the theory of the solar modulation of cosmic rays. A good part of this thesis would not have been written if it was not for him.

I would also like to thank: the members of my committee, for reviewing this work; Karen, Margie and Kevin, your help in navigating and surviving the UH system and rules has been invaluable; Alexis, for the english review of some of the chapters; Alberto, Nicola, Matteo, Stefano, David, Xi and Du Toit, for the interesting physics discussions; the AMS people at CERN for all the nice evenings and weekends spent *not* working; Pardis, because life (and dinners!) in Honolulu would have been boring without you; David and Ryan, my first year's flatmates, it was fun living with you; Nadia, for the opportunity to participate at the *tavola di conversazione italiana* (somebody had to teach the correct Italian pronunciation, *i.e. toscana*, to your students!); Andrea and Laura, I really miss you!; the hookii community, without which I would have probably finished earlier, but thanks to which I spent more time in this wonderful place; and, of course, all my family and friends back in Italy, for their support from far far away.

Last, but not least, the most important thanks goes to Silvia, my wife: I could not have done it without you, and I'm not only referring to the last insane weeks. Thanks for all the patience you showed me, for you never ending support, for sharing your life with me.

This work has been partially funded by Wyle Laboratories, Inc. under grant (NAS 9-02078).

All the analysis in this thesis has been performed with the `ROOT` framework developed at CERN.

ABSTRACT

The search for the local interstellar spectrum (LIS) of galactic cosmic rays (GCRs) and a full understanding of their propagation in the heliosphere are long-standing issues in the field of cosmic rays (CRs) and heliophysics. In recent years, the increasing precision of direct CR measurements lead to many advancements in different fields, such as acceleration and propagation processes of CRs in the galaxy and high-sensitivity indirect searches of dark matter. The study of how GCR fluxes change in time is also fundamental from the technological point of view: future human missions in deep space will require better predictions of radiation doses received by astronauts and electronics due to the long-term exposure to GCRs. The Alpha Magnetic Spectrometer (AMS) experiment, on board the International Space Station (ISS) since May 2011, is measuring with unprecedented accuracy the fluxes of GCRs from 0.5 GeV/n up to a few TeV/n. The large acceptance of AMS allows to perform a detailed study of the time variation of GCRs during an entire solar cycle, improving the understanding of the interplay between the different solar modulation processes.

In this work, AMS data have been analyzed to produce a very precise measurement of the monthly proton and helium fluxes. A new parametrization of the proton and helium LIS has been derived, based on the latest data from *Voyager 1* and AMS. Using the framework of the force-field approximation, the solar modulation parameter is extracted from the time-dependent fluxes measured by PAMELA, BESS and AMS. A modified version of the force-field approximation with a rigidity-dependent modulation parameter is introduced, yielding better fits than the force-field approximation. A comprehensive 3D steady-state numerical model is used to solve the Parker transport equation of GCRs in the heliosphere and to reproduce the proton monthly fluxes observed by AMS. The limitations of this approach in describing the modulation processes during the maximum of solar activity are discussed.

CONTENTS

LIST OF TABLES

LIST OF FIGURES

LIST OF ABBREVIATIONS AND SYMBOLS

ACC	Anti-coincidence counter
ACE	Advanced Composition Explorer
ACR	Anomalous cosmic ray
ADI	Alternating direction implicit
AMS	Alpha Magnetic Spectrometer
BESS	Balloon-borne Experiment with Superconducting Spectrometer
BMA	Backward moving average
BR	Bartels rotation
CERN	European Organization for Nuclear Research
CIR	Co-rotating interaction region
CME	Coronal mass ejection
CR	Cosmic ray
CRIS	Cosmic Ray Isotope Spectrometer
DAQ	Data acquisition
DC	Diffusion coefficient
DM	Dark matter
DSA	Diffusive shock acceleration
DSP	Digital signal processor
ECAL	Electromagnetic calorimeter
ENA	Energetic neutral atom
EPHIN	Electron, Proton and Helium INstrument
FD	Forbush decrease
FOV	Field of view
GCR	Galactic cosmic ray
GMIR	Global merging interaction region
HCS	Heliospheric current sheet
HMF	Heliospheric magnetic field

IBEX Interstellar Boundary EXplorer
IGRF International Geomagnetic Reference Field
ISM Interstellar medium
ISS International Space Station

LIS Local interstellar spectrum
LTOF Lower TOF

MC Monte Carlo
MDR Maximum detectable rigidity
MIP Minimum ionizing particle
MIR Merging interaction region
MLI Multi-layer insulation

NASA National Aeronautics and Space Administration
NM Neutron monitor

PAMELA Payload for Antimatter Matter Exploration and Light-nuclei Astrophysics
PFSS Potential Field Source Surface
PMT Photomultiplier tube
PWN Pulsar wind nebula

RICH Ring imaging Cherenkov

SAA South Atlantic Anomaly
SDE Stochastic differential equation
SEB Single event burnout
SEE Single event effect
SEL Single event latchup
SEP Solar energetic particle
SEU Single event upset
SILSO Sunspot Index and Long-term Solar Observations
SNR Supernova remnant
SOHO SOlar and Heliospheric Observatory
SPS Super Proton Synchrotron
SSN Sunspot number

TAS Tracker alignment system
TOF Time of flight
TR Transition radiation
TRD Transition radiation detector
TRK Tracker
TTCS Tracker thermal control system

UTOF Upper TOF

WIMP Weakly interacting massive particle
WSO Wilcox Solar Observatory

PREFACE

Galactic cosmic rays (GCRs) are charged particles produced by some of the most energetic phenomena in the Universe, which travel the endless voids of our galaxy before finally arriving at the edge of the solar system. Here they meet with the *heliosphere*, a huge cavity carved out of the interstellar space by a supersonic stream of magnetized plasma constantly blown out from the Sun, called *solar wind*. By the time GCRs reach Earth, they have interacted with the turbulent magnetic field embedded in the time-varying solar wind: the overall effect of the physical processes involved in this interaction is called *solar modulation*.

Cosmic rays (CRs) are, in a sense, cosmic messengers, because they allow us to probe the structure of the galaxy in a different way than by looking at the various frequencies of the electromagnetic spectrum. The history of CR exploration is a history of unexpected discoveries, both in astrophysics and in other areas of physics. Indeed, the field of particle physics is an offspring of the early experimental era of CR studies: starting from the positron, discovered by Anderson in 1932, the world of subnuclear particles was revealed to the physicists of the first half of the 20th century by staring at the trails that CRs left in photographic emulsions and bubble chambers, before the advent of powerful enough particle accelerators. In recent years, a new interest in CRs has spurred from the observations of an excess in their anti-matter components, positrons and anti-protons, suggesting an exotic origin, like dark matter annihilation or decay. Since the fluxes of the various species of GCRs are distorted by the influence of the Sun, a better understanding of the solar modulation and its time evolution is of paramount importance to correctly deduce their shape before they enter the heliosphere. This, in turn, will advance our knowledge of the acceleration and propagation mechanisms in the galaxy, so that, eventually, the study of CRs will lead to the solution of some of the currently open problems in cosmology and particle physics.

CRs are also an unavoidable challenge for any human space exploration program. Usually overlooked by the general public, CRs pose a real threat to the survival of humans in space or on planetary bodies without a magnetosphere: in fact, CRs are a highly ionizing form of radiation, which can penetrate the walls of a spacecraft, an astronaut spacesuit and the human body itself. Mitigating the radiation risks in space requires the expertise from fields as diverse as biophysics, material science, medicine and particle astrophysics. The solar modulation comes into play when deciding the timing of a mission: is it better to travel from Earth to Mars during periods of low or high solar activity? What is the maximum amount of time an astronaut can spend in deep space before the probability of developing a CR-induced cancer surpasses a certain threshold? The answers to these questions rely on the knowledge of the time variation of the CR flux, hence the study of the propagation of particles in the heliosphere will help reduce the uncertainties in the radiation dose predictions.

In May 2011, the Alpha Magnetic Spectrometer (AMS) experiment was installed on the Interna-

tional Space Station (ISS), with the purpose of measuring very accurately the various components of the GCR spectrum. Its large acceptance is a key factor for collecting the high statistics necessary for studying the rarest species of GCRs and how GCR fluxes change in time. The long-term duration of its mission will reveal the details of how GCRs are affected by the solar wind and the heliospheric magnetic field (HMF) in different phases of the solar activity. AMS started taking data during the rising phase of solar cycle 24, while now, in 2017, the Sun is going toward the minimum of its activity. The observation of the time variation of GCRs at different energies across the maximum of the solar cycle represents a milestone for heliophysics: until now, continuous measurements of GCR fluxes were available only at very low energies, below the range of interest for both particle astrophysics and radiation studies, while high energy measurements were sparse.

The work done in this thesis focuses on the analysis of the time variation of protons and helium in GCRs measured by AMS and the interpretation of this result by means of an analytical and a numerical model.

Chapter 1 is an introduction to the physics of CRs and heliophysics, covering the following topics: a brief review of CR history, origin and acceleration of GCRs, overview of CR experiments, different populations of CR in the heliosphere and the heliosphere structure, with a description of its main components. The propagation of GCRs inside the heliosphere will be also treated: the Parker transport equation is presented and an explanation of the various terms is provided. In the last section of the chapter, the force-field approximation, a widely used analytical solution of the Parker equation, is introduced, together with comments about its limitations. Chapter 2 describes in details the AMS experiment and its sub-detectors.

The next three chapters present the actual work done during these years. Chapter 3 contains the description of the analysis of the monthly proton and helium fluxes, as well as the experimental results and some model-independent analysis. Chapter 4 is a slightly revised and expanded version of the paper "*Solar modulation of the local interstellar spectrum with Voyager 1, AMS-02, PAMELA and BESS*", published on *The Astrophysical Journal* in 2016. A new parametrization for the proton and helium local interstellar spectrum (LIS) is presented and the force-field approximation is modified to better describe data from the various CR experiments. Two sections are added with respect to the content appeared in the paper: the application of the modified force-field approximation to the AMS proton and helium fluxes and a comparison with other LIS parametrizations published recently. In Chapter 5, a numerical model for solving the Parker equation is used to reproduce the AMS proton fluxes and to derive a prediction for the fluxes observed at Mars based on the measurements at Earth.

A summary of the work presented in this thesis is given in Chapter 7, together with general comments on the impact of the results found and future work.

CHAPTER 1
COSMIC RAYS IN THE HELIOSPHERE

1.1 The Sun and the solar activity

The Sun is the star at the center of our planetary system which provides enough light and heat to sustain the life on Earth. It is a giant ball of hot plasma, with a diameter approximately 110 times the Earth's diameter and a mass of $\approx 2 \times 10^{30}$ kg, corresponding to 333000 Earth's masses. The Sun is powered by nuclear fusion processes in its core, mostly from the conversion of hydrogen into helium. The core has a temperature of more than 15×10^6 K and extends up to 25 % of the solar radius. Beyond this distance, the temperature falls off, and nuclear fusion is not possible anymore. The heat produced by the nuclear fusion is transferred from the core to the visible surface of the Sun, called *photosphere*, through the radiative zone, where the heat is transported by gamma- and x-rays, and then through the convective zone, where the main heat transport process is the outward convective motion of plasma currents. The interface layer between the radiative and the convective zone is called *tachocline* and it's the region where the magnetic field of the Sun is supposed to be generated. The photosphere sits right on top of the convective zone and it is the source of the visible light from the Sun: below this surface, the Sun is opaque to visible light and its interior can only be observed indirectly, for example with the technique of helioseismology. The photosphere is relatively cold with respect to the rest of the Sun, having a temperature of only 5700 K, and it's 100 km thick. With increasing distance, the gas around the Sun rarefies and becomes its atmosphere, composed of different layers: the *chromosphere*, 2000 km thick, with a temperature around 20 000 K; the transition region, a thin layer where the temperature rises rapidly up to 10^6 K; and finally the *corona*, which can reach temperatures above 10×10^6 K and extends for few solar radii until it turns into *solar wind* [1]. The region of space surrounding the Sun in which the pressure of the extended corona is predominant with respect to the pressure of the interstellar medium (ISM) is called *heliosphere*: in a sense, we can say that all the planets of the solar system are embedded in the solar atmosphere.

Looking at the Sun in different wavelengths, it is possible to distinguish many features such as: *sunspots*, dark regions where the temperature drops to 3700 K; *granules*, bubbles of 1000 km in diameter representing the top of the convective cells which transport the hot plasma from the convective zone up to the surface; *prominences*, huge arches composed of denser and cooler plasma which can extend up to tens of thousands of kilometers above the solar surface. Figure 1.1 shows how the Sun appear in different wavelengths.

The sunspots have been noticed for the first time few centuries BC, both in China and in Greece, but it wasn't until the 17th century that a systematic observation of their time variation started. Figure 1.2 shows the yearly average of the sunspot number (SSN) since 1600. The periodic

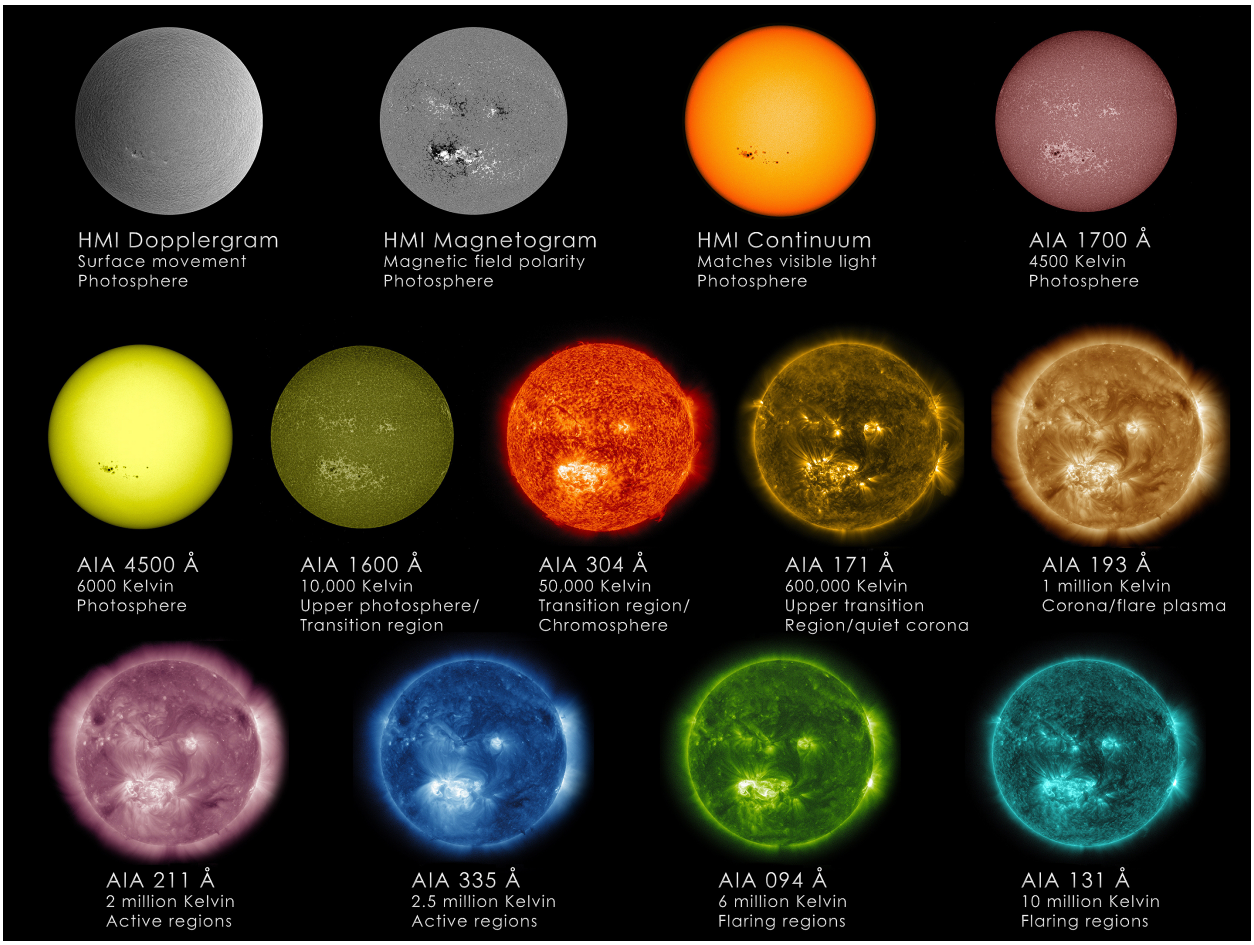

Figure 1.1: The Sun seen in different wavelengths by the Helioseismic and Magnetic Imager (HMI) and the Atmospheric Imaging Assembly (AIA) instruments on board the NASA's Solar Dynamic Observatory (SDO), a geosynchronous satellite. Each wavelength is emitted by different ions at different temperatures, thus the multi-wavelength observations allow to explore the various layers of the photosphere and solar atmosphere, revealing the dynamical and diverse features of the solar surface. Credits: NASA/SDO/Goddard Space Flight Center (`https://www.nasa.gov/mission_pages/sunearth/news/light-wavelengths.html`).

variation of the SSN is called *solar cycle* and it repeats approximately every 11 years. However, this periodicity is not stable in time: indeed, the most striking feature of the historical record of the SSN is the *Maunder minimum*, a period in which no sunspot was observed for 70 years. The amplitude of the solar cycle varies in time as well: for example, the last four solar cycles, including the current solar cycle 24, have been always weaker than the preceding one.

The SSN is strongly correlated with the magnetic activity of the Sun, as can be seen in Figure 1.3. The polar field varies with a similar period as the SSN, becoming zero in correspondence of the maximum of the solar cycle, while during the minimum its amplitude peaks. In addition to

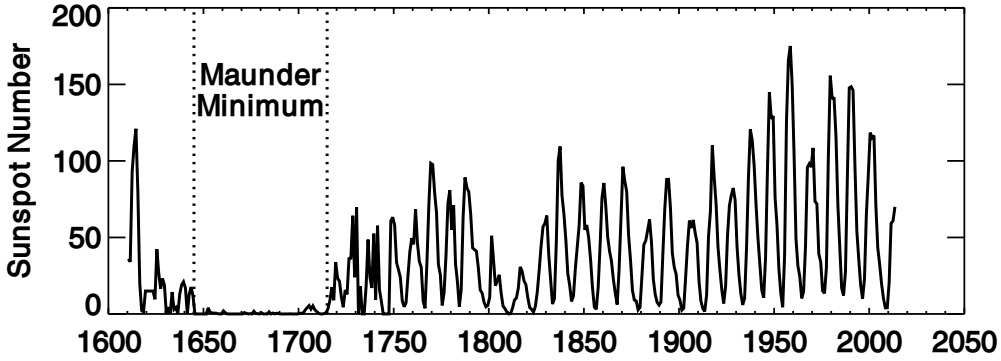

Figure 1.2: Time variation of the yearly average sunspot number since the 17th century [2].

the 11-year periodicity, a 22-year period is visible in the magnetic field, where the magnetic field polarity flips every 11 years.

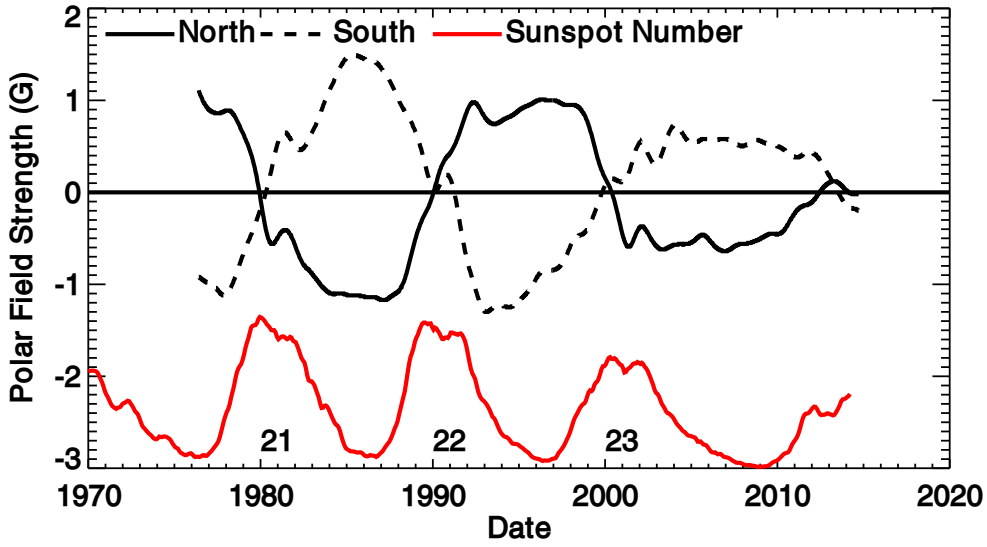

Figure 1.3: Time variation of solar polar field strength observed by the Wilcox Solar Observatory (WSO) in the northern (solid black) and southern (dashed black) hemisphere of the Sun. The scaled SSN (red) is included as reference [2].

The time variation of the solar activity has an impact on the propagation of galactic cosmic rays (GCRs) in the heliosphere. Indeed, this is what is being observed by neutron monitors (NMs), ground detectors that count the neutrons produced by the interactions of GCRs with the nuclei of the Earth's atmosphere. Figure 1.4 shows the time variation of the monthly counts of the Climax Neutron Monitor, together with the SSN. The first thing we notice is how the counts are anti-correlated with the SSN. In addition to this periodic variation in intensity, we also see a difference in the shape of the NM counts during the solar minimum. When the solar magnetic field in the northern hemisphere is directed outward from the Sun, the polarity of the magnetic field, indicated

with A, is defined positive ($A > 0$), while vice versa, when directed inward, is defined negative ($A < 0$). NM counts are flat during solar cycles with $A > 0$ and peaked when $A < 0$. This phenomenon is due to the drift motions of the GCRs in the heliosphere and it will be described in detail in Section 1.4.3.

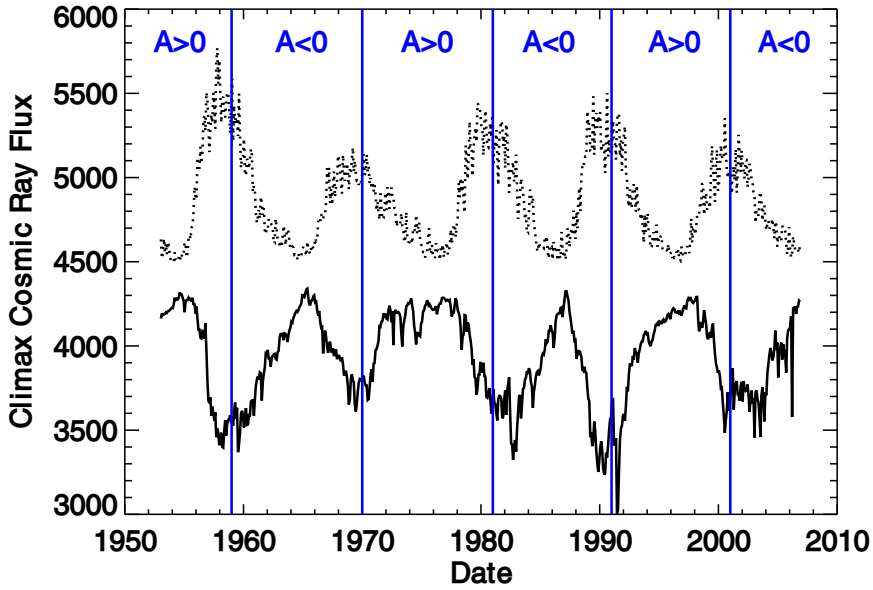

Figure 1.4: The solid black line represents the time variation of the neutron counts measured by the Climax Neutron Monitor, while the dotted line is the SSN, rescaled and shifted. The blue vertical lines identify the periods in which the polarity of the solar magnetic field flips. Figure adapted from [2].

1.2 Structure of the heliosphere

The heliosphere is a huge bubble created by the push of the solar wind against the ISM. The solar wind accelerates to supersonic speed very close to the Sun, then expands steadily until it undergoes a shock transition to subsonic velocities at the *termination shock* (see Section 1.2.1). Eventually, the solar wind pressure balances the pressure of the ISM, stopping: this interface is called *heliopause*. The region between the termination shock and the heliopause is called *inner heliosheath*. The ISM in front of the heliopause results compressed by the overall motion of the heliosphere with respect to the surrounding environment, forming a bow wave or a bow shock ahead the heliopause. The region between the heliopause and the bow wave/shock is called *outer heliosheath*. Recent observations by *Voyager 1* and by the Interstellar Boundary EXplorer (IBEX) represent a milestone in the exploration of the heliosphere, providing for the first time direct measurements of the heliopause properties.

Fast ions coming from the ISM can experience charge-exchange collisions with the ambient slow

neutral atoms, whereby the ions become neutral by stealing the electrons of the cold atoms. These collisions produce energetic neutral atoms (ENAs), which keep moving in a straight line in the same direction of the original ions. IBEX observes the influx of the ENAs created at the boundary of the heliosphere: by measuring the incoming direction of the ENAs, IBEX can image the heliopause. In 2009, IBEX produced the first ever image of the heliospheric boundary, revealing a hot spot for the ENAs emission, called *ribbon* because of its shape (see Figure 1.5 left) [3]. IBEX measured also the speed and direction of the interstellar flow with respect to the heliosphere: the found velocity, $(23.2 \pm 0.3)\,\mathrm{km/\,sec}$, is too low to form a shock, so the outer heliosheath is bounded by a bow wave (see Figure 1.5 right) [4].

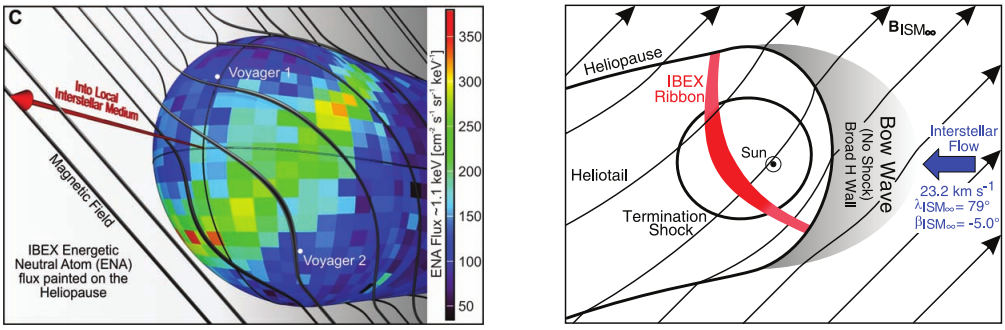

Figure 1.5: **Left**: IBEX map of ENAs emission, draped around the heliopause, together with a configuration of the interstellar magnetic field lines that could explain the ribbon. **Right**: Direction of motion of the heliosphere with respect to the interstellar flow. Figures adapted from [3] and [4].

In August 2012, *Voyager 1*, at a distance of 122 AU, entered a region in which the low energy particles were depleted, while the high energy GCR intensity increased and remained steady since then [5, 6], as shown in Figure 1.6. This phenomenon has been interpreted as the crossing of the heliopause, *i.e. Voyager 1* is now supposed to be in interstellar space. However, the plasma and magnetic field measurements of *Voyager 1* seems to be inconclusive regarding this point, suggesting that maybe the heliopause is yet to be crossed [7].

Figure 1.7 shows a simulation of the three-dimensional structure of the heliosphere, taken from [8]. The color maps to the magnetic field intensity in the meridional plane, both inside and outside the heliosphere. The bow wave is identified by the dashed black line, the heliopause by the dashed yellow line and the termination shock by the dashed magenta line. The yellow/orange circles correspond to the position of the *Voyager 1* and *Voyager 2* spacecraft in 2014. Three magnetic field lines extends from the Sun, to illustrate the shape of the heliospheric magnetic field (HMF) and of the heliospheric current sheet (HCS): Sections 1.2.2 and 1.2.3 will describe the HMF and the HCS in more details.

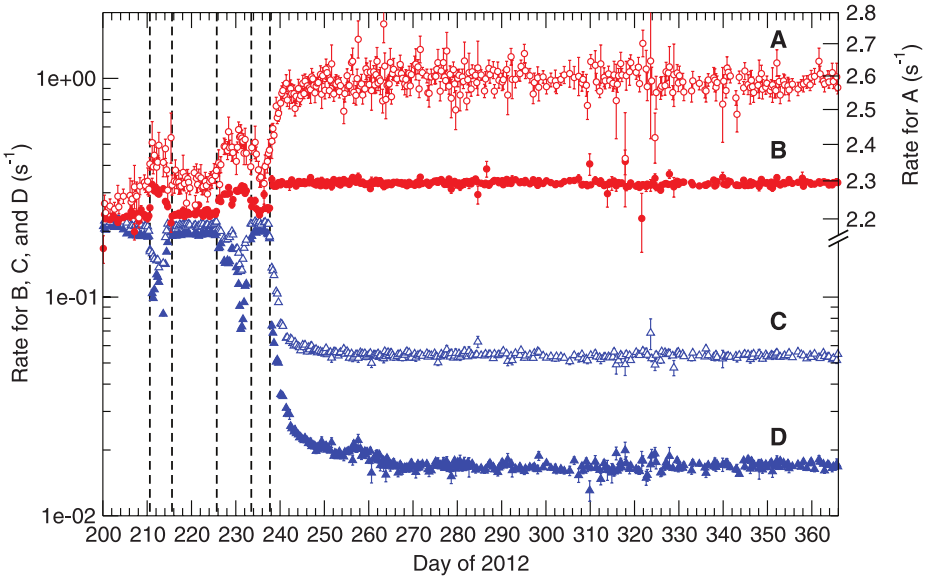

Figure 1.6: Time variation of the counting rate of low- and high-energy particles observed by *Voyager 1* in 2012. Protons above 70 MeV (A) and electrons between 6 and 100 MeV (B) abruptly increase, while simultaneously protons between 7 and 60 MeV (C) and protons between 0.5 and 30 MeV (D) decrease [5].

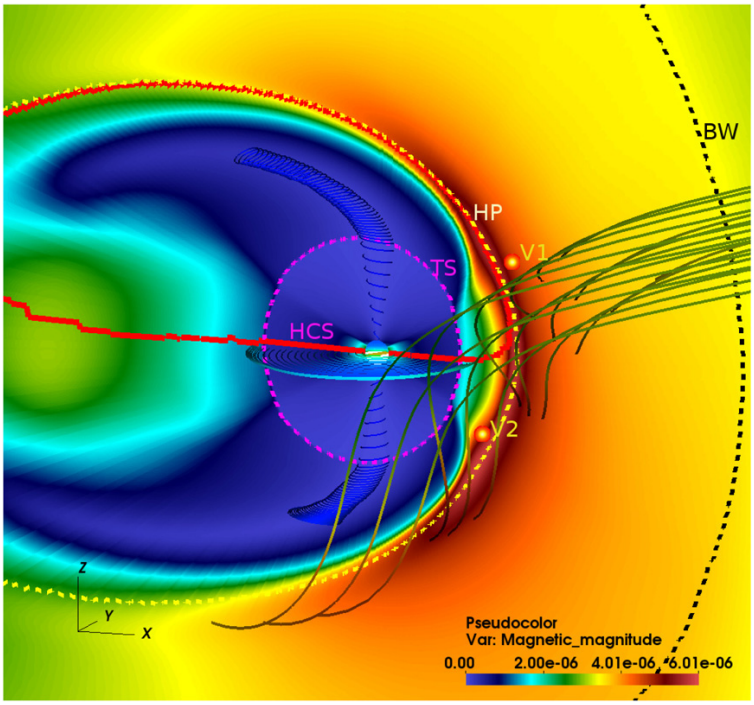

Figure 1.7: Three-dimensional structure of the heliosphere from a simulation of the magnetic field intensity in the heliosphere and in the ISM [8].

1.2.1 The solar wind

During the 1950s, the observations of the motion of the comet tails lead Biermann [9, 10] to suggest that a stream of ionized gas was continually emitted from the Sun, with velocities ranging between 500 km/ sec and 1500 km/ sec. Parker [11, 12] showed that the solar corona could not be in static equilibrium and would be expanding outward with velocities consistent with what Biermann estimated. This continuous outflow of plasma was named *solar wind* by Parker.

Parker's argument is the following: due to the high temperature, the gas in the corona is fully ionized, thus both electrons and protons contribute to the total pressure P, *i.e.* $P(r) = 2k_B n(r)T(r)$, where k_B is the Boltzmann constant and $n(r)$ and $T(r)$ are, respectively, the ion density and temperature as a function of the distance r from the Sun. If the corona was in static equilibrium, the outward force exerted by the thermal pressure of the plasma should be equal to the gravitational attraction of the Sun:

$$\frac{dP}{dr} = 2k_B \frac{d}{dr}(nT) = -G\frac{M_\odot mn}{r^2}, \tag{1.1}$$

where G is the gravitational constant, $M_\odot$ the mass of the Sun, m the mass of a proton[1] and we dropped the explicitly dependence on r. Since far from the Sun there are no heat sources, it is reasonable to assume that the temperature falls off with the distance as $T(r) = T_0(r/a)^\alpha$, where T_0 is the value of the temperature at $r = a$, the radius of the corona, and $\alpha < 0$. Plugging this expression in Equation 1.1, we can solve for the density and get:

$$n(r) = n_0 \left(\frac{r}{a}\right)^{-\alpha} \exp\left\{\frac{GM_\odot m}{2k_B T_0 a}\frac{1}{\alpha+1}\left[\left(\frac{a}{r}\right)^{\alpha+1} - 1\right]\right\}, \tag{1.2}$$

where n_0 is the density at the base of the corona. We can now find the pressure of the corona at an infinite distance from the Sun:

$$P(r \to \infty) = P_0 \exp\left(-\frac{GM_\odot m}{2k_B T_0 a}\frac{1}{\alpha+1}\right), \tag{1.3}$$

where $P_0 = 2k_B n_0 T_0$. Eventually, the corona will meet the ISM, with an average density of the order of $0.3\,\mathrm{atoms/cm^3}$ and a temperature around $7000\,\mathrm{K}$, corresponding to a pressure $P_{ISM} \approx 5.8 \times 10^{-14}\,\mathrm{N\,m^2}$. Replacing the numerical values of all the constants in Equation 1.3, and knowing that for ionized hydrogen $\alpha \approx -2/7$ [13], we find that the corona pushes against the ISM with a pressure $\approx 6.6 \times 10^{-7}\,\mathrm{N/m^2} \gg P_{ISM}$, *i.e.* the solar corona can not be in static equilibrium.

Having shown that the solar corona inevitably expands, Parker proceeds by writing the equations of motion for the velocity $v(r)$ of the escaping gas, which follow from the conservation of mass and

[1] The electron mass is $\approx 1/2000$th of the proton mass, thus their contribution to the gravitational force can be safely neglected.

momentum, assuming spherical symmetry and steady-state conditions:

$$\begin{cases} mnv\dfrac{dv}{dr} = -2k_B\dfrac{d}{dr}\left(nT\right) - G\dfrac{M_\odot mn}{r^2} \\ \dfrac{d}{dr}(r^2nv) = 0 \end{cases}, \tag{1.4}$$

where we dropped the explicit dependence on r. From the second equation, we can express the density as a function of the velocity:

$$n(r) = \frac{n_0 v_0}{v(r)}\left(\frac{a}{r}\right)^2, \tag{1.5}$$

where v_0 is the velocity of the gas at $r = a$. Replacing $n(r)$ in the first equation, and using $dv^2 = 2v\,dv$, we find:

$$\frac{m}{2}\frac{dv^2}{dr}\left(1 - \frac{2k_BT}{mv^2}\right) = -2k_Br^2\frac{d}{dr}\left(\frac{T}{r^2}\right) - \frac{mGM_\odot}{r^2}. \tag{1.6}$$

Parker demonstrated that the only physical solution which admit a finite pressure at very large distances requires v to become supersonic and remain constant. The dependence of v on the radial distance for different values of T_0 is sketched in Figure 1.8, where we can see that the steady outflow of gas from the solar corona attain velocities of the same order needed by Biermann to explain the motion of the comet tails.

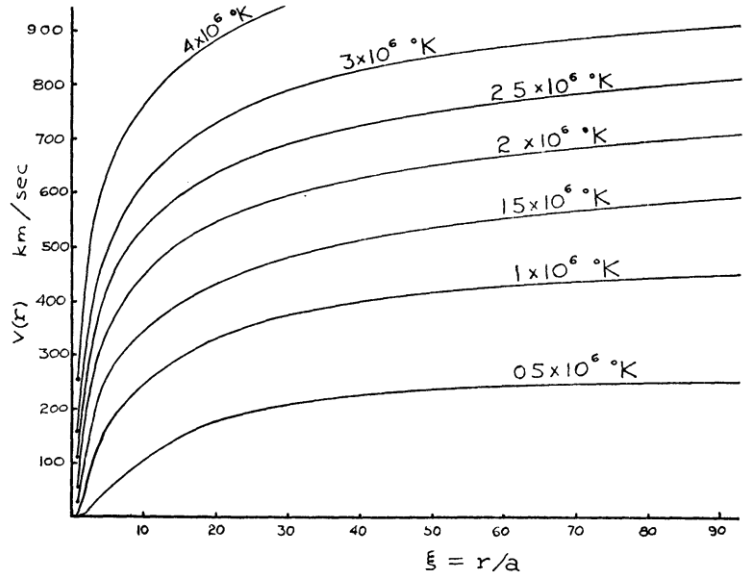

Figure 1.8: Expansion velocity of the solar corona as a function of the distance from the Sun, as computed by Parker [11]. The different curves corresponds to different values of T_0.

So far, the magnetic field of the Sun has been neglected in this discussion, but a realistic description of the solar wind can not avoid taking it into consideration. While far from the Sun the magnetic field is frozen inside the solar wind which expands radially (see Section 1.2.2), close to the Sun the interplay between the solar wind and the magnetic field is more complex. Observations of the solar corona paint a picture very different from the simple and uniform approximation assumed by Parker in its derivation of the solar wind expansion. The magnetic field lines, originating in the photosphere, form closed loops around the magnetic equator, where the inward magnetic pressure is higher than the outward heat pressure, thus inhibiting the escape of the gas. The field lines at the poles are instead open, allowing the solar wind to flow in the heliosphere. Figure 1.9 left shows a white light image of the solar corona taken during the eclipse of August 1, 2008, corresponding to a period of minimum solar activity. The white light, due to the free electrons in the corona scattering off the photospheric emission, traces the distribution of the coronal electron density and, as a consequence, the magnetic field lines. At mid latitudes, we can see the belt of bright *helmet streamers*, loop-like structures which connect regions of opposite magnetic polarity: the bulges at the base are stretched out by the push of the gas, which eventually reaches the height where the magnetic pressure is not strong enough to contain it, giving birth to the slow component of the solar wind, with velocities ranging from 300 to 400 km/ sec. Close to the poles, the darker *coronal holes* are visible, where the field lines are open and radially directed: these are the sources of the fast component of the solar wind, with an average speed of 750 km/ sec. During periods of high solar activity, the coronal holes almost disappear, while the streamers extend at higher latitudes, as can be seen in Figure 1.9 right. As a consequence of these changes in the corona, the slow component of the solar wind becomes predominant.

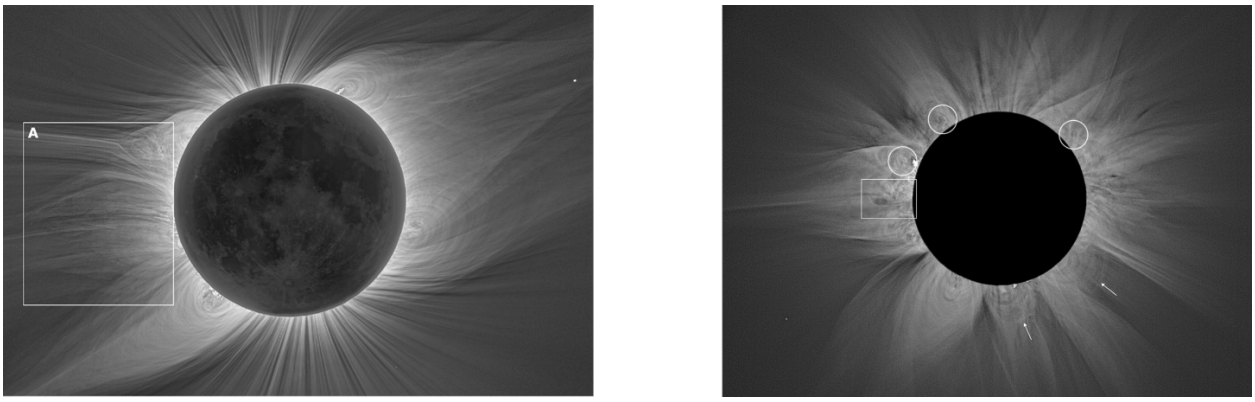

Figure 1.9: White light eclipse images of the solar corona. **Left**: August 1, 2008 (solar minimum). **Right**: June 21, 2001 (solar maximum). Figures adapted from [14].

The latitudinal dependence of the solar wind speed was directly observed for the first time by the *Ulysses* spacecraft, which orbited the Sun with an inclination of 80.2° from 1990 to 2009 [15]. Figure 1.10 top shows the solar wind speed and corona temperature as a function of the heliographic

latitude, measured by *Ulysses* in its first fast latitude scan, occurred during the minimum of 1995. The slow solar wind extends between $-30°$ and $30°$ and displays a high degree of variability, while the fast solar wind is more stable. In the right picture, the polarity of the magnetic field is also represented, showing that during the minimum the field is well organized in a dipolar structure. The second fast latitude scan, during the maximum of 2001, is shown in Figure 1.10 bottom: the solar wind speed is almost flat with latitude, although large variations are observed. Furthermore, the inward and outward magnetic field lines are not anymore well separated as during the minimum.

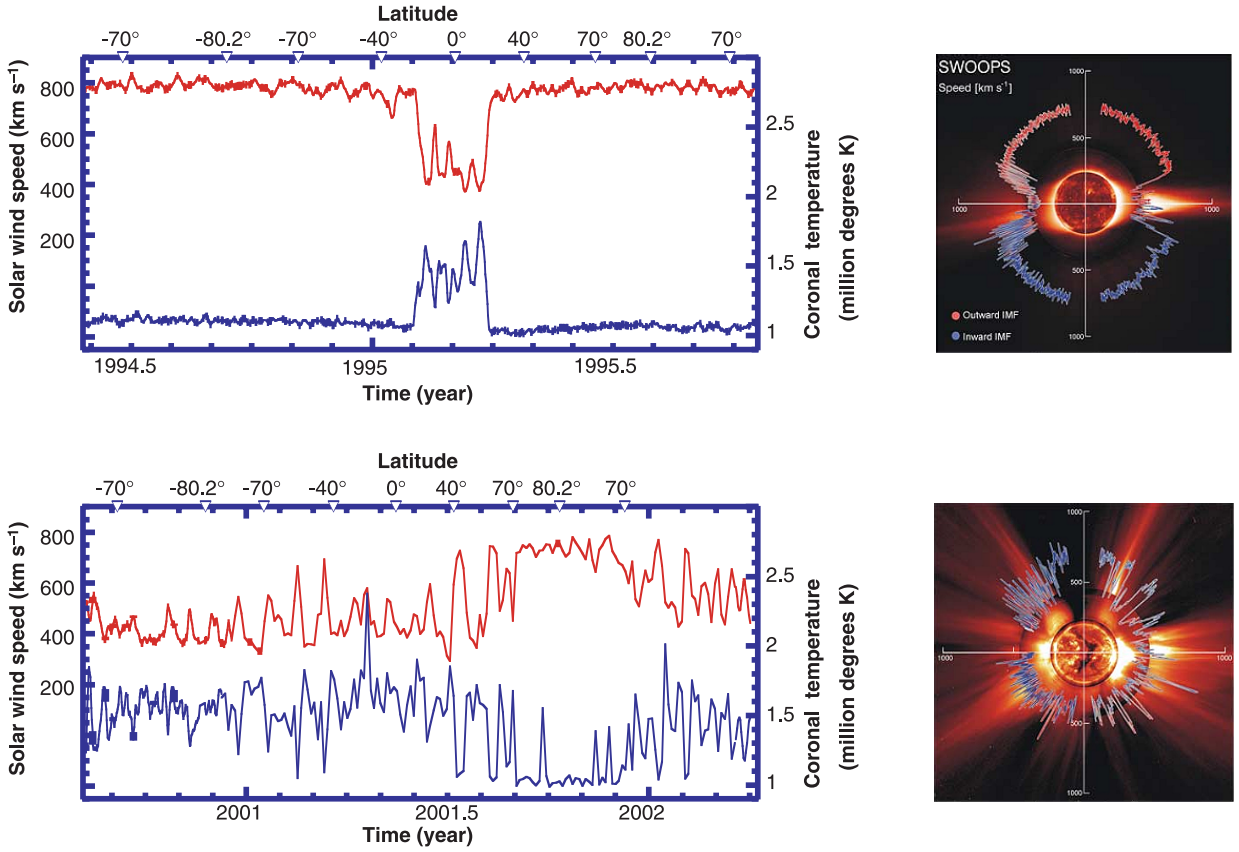

Figure 1.10: Latitude dependence of the solar wind speed observed by *Ulysses* during the fast latitudinal scans of 1995 (**top**) and 2001 (**bottom**), corresponding, respectively, to a period of minimum and maximum solar activity. Figures adapted from [16] and [17].

From Equation 1.5, we see that if v is constant, then the density of particles in the solar wind decreases as $1/r^2$, eventually becoming too sparse to withstand the inward push of the ISM. At this point, the solar wind speed becomes subsonic via a shock transition, called *termination shock*. More than 40 years after having been theorized, the termination shock was finally observed by the twins *Voyager* spacecraft: *Voyager 1* crossed the termination shock in 2004 at a distance of 94 AU [18, 19], while *Voyager 2* did it in 2007 at a distance of 84 AU [20, 21].

The solar wind displays transient phenomena, especially during the maximum, like coronal mass ejections (CMEs) and co-rotating interaction regions (CIRs). CMEs are huge clouds of plasma ejected from the Sun at velocities greater than the solar wind speed. The fastest CMEs can move at more than 2000 km/ sec, creating a shock in front of them in which particles can be accelerated. CIRs are shocks created at the interface between slow and fast solar wind streams, which corotates with the Sun, hence the name. In the outer heliosphere, these disturbances can coalesce, forming merging interaction regions (MIRs), huge structures with compressed magnetic field and plasma. An accumulation of MIRs can lead to the formation of global merging interaction regions (GMIRs), which have a wide latitudinal and longitudinal extent and affect the global structure of the HMF. The overall effect of all these solar wind structures is to create additional barriers for the inward propagation of GCRs.

1.2.2 The heliospheric magnetic field

Let's assume that, from a certain distance $r = b$ on, called *source surface*, the solar wind is perfectly radial and constant, as it is indeed observed, *i.e.* $\mathbf{V}'_{sw} = V_0\hat{\mathbf{r}}$. Then, in the reference frame corotating with the Sun, we have $\mathbf{V}_{sw} = \mathbf{V}'_{sw} - \boldsymbol{\Omega} \times \hat{\mathbf{r}} = V_0\hat{\mathbf{r}} - \Omega(r-b)\sin\theta\hat{\boldsymbol{\phi}} = V_r\hat{\mathbf{r}} + V_\phi\hat{\boldsymbol{\phi}}$, where Ω is the angular velocity of the Sun. The streamlines of the solar wind can be easily found by imposing $d\mathbf{r}/\,dt = \mathbf{V}_{sw}$, from which we can derive that:

$$\begin{cases} \dfrac{dr}{dt} = V_0 \\ r\dfrac{d\theta}{dt} = 0 \\ r\sin\theta\dfrac{d\phi}{dt} = -\Omega(r-b)\sin\theta \end{cases} \implies \begin{cases} \dfrac{d\phi}{dr} = -\dfrac{\Omega(r-b)}{V_0 r} \\ \dfrac{d\theta}{dt} = 0 \end{cases}. \tag{1.7}$$

Solving for ϕ, we find:

$$\phi - \phi_0 = -\frac{\Omega(r-b)}{V_0} + \frac{\Omega b}{V_0}\ln\frac{r}{b}, \tag{1.8}$$

where ϕ_0 is the azimuthal angle of the streamline at $r = b$. Equation 1.8 is the equation of an Archimedean spiral: the streamlines of the solar wind are spirals with a constant latitude.

The plasma in the solar wind is highly conductive, so that we can assume that the magnetic field lines are frozen inside it and forced to move along the solar wind streamlines [22]. We can therefore write $\mathbf{B} = \alpha\mathbf{V}_{sw}$, where α is a scalar function. One end of the field line is always fixed on the Sun, on a point called *footpoint*. In the reference frame in which the Sun rotates, the solar wind is directed radially, carrying with it the magnetic field line, Since the footpoint rotates with the Sun, the resulting field line is wound around the Sun, following the streamlines defined in Equation 1.8. This spiraling pattern is called *Parker spiral* and it is shown in Figure 1.11.

From the condition $\boldsymbol{\nabla} \cdot \mathbf{B} = 0$, expressed in spherical coordinates, we can derive the radial

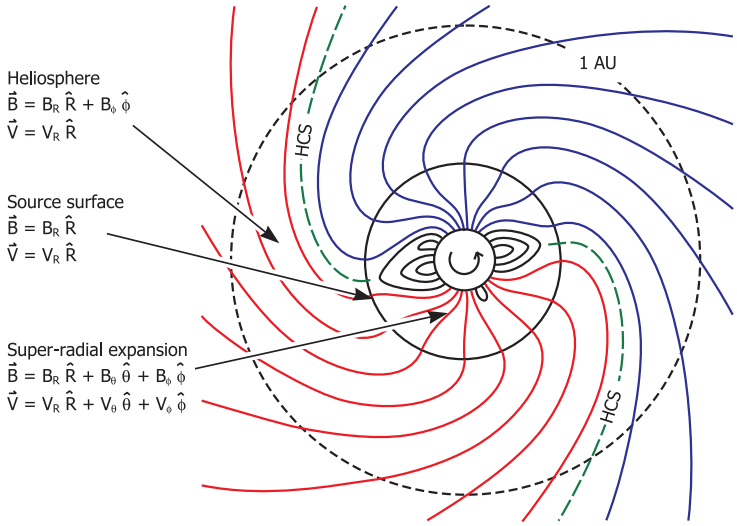

Figure 1.11: Steady-state magnetic field lines in the ecliptic plane [23]. The latitudinal and longitudinal components of the solar wind and magnetic field disappear at the source surface, leaving only a radial expansion for the solar wind, while the HMF follows the Parker spiral. Red and blue lines have opposite polarity and the green line that separates them is the HCS.

dependence of the HMF:

$$\begin{aligned} \boldsymbol{\nabla} \cdot (\alpha \mathbf{V}_{sw}) &= \frac{1}{r^2}\frac{\partial\left(r^2 \alpha V_r\right)}{\partial r} + \frac{1}{r\sin\theta}\frac{\partial\left(\alpha V_\phi\right)}{\partial \phi} = \\ &= \frac{V_0}{r^2}\frac{\partial\left(r^2\alpha\right)}{\partial r} - \frac{\Omega(r-b)}{r}\frac{\partial \alpha}{\partial \phi} = \\ &= V_0 \frac{\partial \alpha}{\partial r} - \frac{\Omega(r-b)}{r}\frac{\partial \alpha}{\partial \phi} + 2\frac{V_0}{r}\alpha = 0 \end{aligned} \tag{1.9}$$

Let's introduce the variable s, defined by the equations $dr/\,ds = V_0$ and $d\phi/\,ds = -\Omega(r-b)/r$; then, Equation 1.9 can be rewritten as:

$$\frac{dr}{ds}\frac{\partial \alpha}{\partial r} + \frac{d\phi}{ds}\frac{\partial \alpha}{\partial s} + 2\frac{V_0}{r}\alpha = 0 \quad \Longrightarrow \quad \frac{d\alpha}{ds} = -2\frac{V_0}{r}\alpha, \tag{1.10}$$

which can be easily solved, yielding $\alpha = \alpha_0 (b/r)^2$. Plugging the expression of α in the expression of the HMF, we finally find:

$$\begin{cases} B_r = B_0 \left(\dfrac{b}{r}\right)^2 \\ B_\theta = 0 \\ B_\phi = -B_0 \left(\dfrac{b}{r}\right)^2 \dfrac{\Omega(r-b)}{V_0}\sin\theta \end{cases}, \tag{1.11}$$

where $B_0 = \alpha_0 V_0$. This is the Parker HMF, which was derived by Parker together with the theory of the solar wind [11]. Various observations, like the white light eclipse image in Figure 1.9, show that the solar magnetic field has a dipolar structure at the minimum and a multipolar structure at the maximum, *i.e.* B_0 should be a function of the polar angle θ. However, *Ulysses* measured the quantity $r^2 B_r$ along its highly inclined orbit and did not find any latitudinal dependence [24]. This is due to the fact that at the polar caps, within a distance of few solar radii, the magnetic field pressure exceed the plasma pressure and so the solar wind is deflected at lower latitudes [25]. Beyond $r = b$, the two pressures balance and both the solar wind velocity and the magnetic field become radial. Since this is the assumption under which Equation 1.11 was obtained, B_0 can be considered a constant. The angle between the field lines and the radial direction is called *spiral angle* ψ and it's defined by the relation $\tan\psi = B_\phi/B_r = -\Omega(r-b)\sin\theta/V_0$. The HMF can then be written in a more compact form $\mathbf{B}(r,\theta,\phi) = B_0(b/r)^2\left(\hat{\mathbf{r}} - \tan\psi\hat{\boldsymbol{\phi}}\right)$, with the magnitude $B = B_0(b/r)^2\sqrt{1+\tan^2\psi}$.

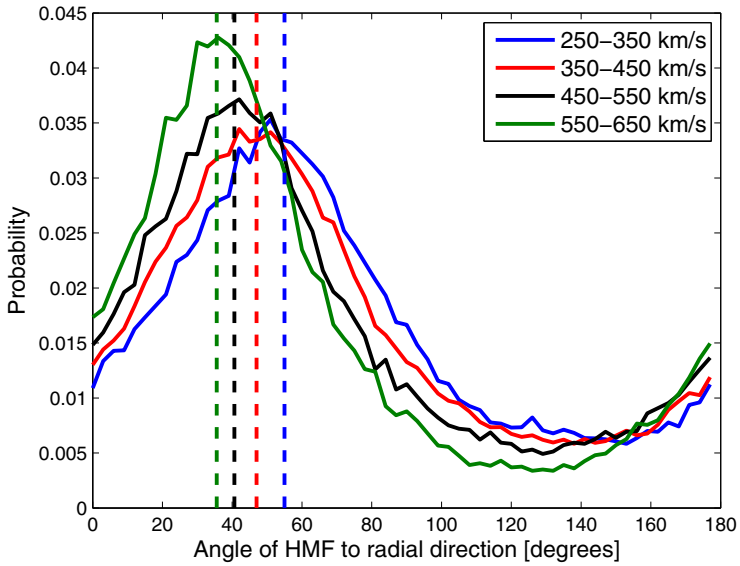

Figure 1.12: Distribution of the spiral angle for different solar wind velocities. The vertical lines represent the values predicted by the ideal Parker HMF. Figure adapted from [23].

Observations in different positions of the heliosphere and at different times confirmed that the HMF is very close to the Parker field, although the similarity only works in a probabilistic sense. At very short time scales, the HMF is highly turbulent, displaying a non-null polar component and a spiral angle different from the expected value, but by taking averages over longer period of times, like one hour, the distribution of B_0 and ψ are peaked at the values predicted by Parker. Figure 1.12 shows the distribution of the hourly averaged spiral angle measured by near-Earth spacecraft between 1965 and 2012, for different intervals of the solar wind speed. The most probable value is very close to the Parker spiral angle, but the distributions have large tails, indicating the high

variability of the HMF direction on short time intervals.

Over the course of the time, many modifications to the Parker HMF have been proposed, to account for the observed small discrepancies. We will discuss only two of them: the Smith-Bieber modification, because it will be used in the numerical description of the propagation of protons in the heliosphere (see Section 5.1), and the Fisk field, which represents the more general expression of the HMF.

The Smith-Bieber modification

Observations near-Earth and up to few AU show that the spiral angle is slightly larger than the Parker value, which means that an additional azimuthal component is needed. Smith and Bieber [26] attributed this difference to the differential rotation of the Sun. The angular velocity of the Sun is in fact dependent on the latitude: at the equator, the Sun completes a full rotation in 24.47 days, while the period at the poles is almost 38 days. This process results in the magnetic field lines being wound below the photosphere. If a small azimuthal component survive up to the corona, it will be convected in the solar wind at the source surface, adding a term to the Parker B_ϕ. The overall effect is to transform the spiral angle:

$$\tan\psi(r,\,\theta) = \frac{\Omega(r-b)\sin\theta}{V_{sw}(r,\,\theta)} - \frac{r}{b}\frac{V_{sw}(b,\,\theta)}{V_{sw}(r,\,\theta)}\frac{B_\phi(b)}{B_r(b)}. \tag{1.12}$$

Smith and Bieber found that with $b = 20\ r_\odot$ and $B_\phi(b)/B_r(b) \approx -0.02$, their modified HMF matched the data.

The general Fisk field

One of the unexpected observations by *Ulysses*, was the presence at high latitudes of energetic particles produced in shocks from mid latitudes. The propagation along the Parker field lines would forbid particles to jump from a latitude to another, so some other process was involved in their transport. One of the explanations was an increased particle diffusion along the polar direction [27], while another was a modification of the HMF taking into account the differential rotation of the Sun, the polar coronal holes and the non-radial expansion of the solar wind and magnetic field below the source surface [28]. Fisk observed that the polar coronal holes rotate rigidly with the same angular velocity of the equator, while at the same time the closed loops of the photosphere rotate at the polar frequency. The different rotation velocity of these two objects means that the closed photospheric fields will traverse the coronal holes, opening up during the crossing period and then reconnecting again after. Putting together the tilt of the dipole magnetic axis and the non-radial expansion below the source surface, Fisk showed that a field line originating at the border of the coronal hole, having a certain latitude, will be transported to a lower latitude on the source surface. The overall effect is the creation of a polar component of the HMF, which complicates the

expression of the magnetic field:

$$\begin{cases} B_r = B_0 \left(\frac{b}{r}\right)^2 \\ B_\theta = B_0 \left(\frac{b}{r}\right)^2 \frac{r-b}{V_{sw}} \sin\beta \sin\left(\phi + \frac{\Omega(r-b)}{V_{sw}}\right) \\ B_\phi = B_0 \left(\frac{b}{r}\right)^2 \frac{r-b}{V_{sw}} \left[\omega \sin\beta \cos\theta \cos\left(\phi + \frac{\Omega(r-b)}{V_{sw}}\right) + \sin\theta\,(\omega\cos\beta - \Omega)\right] \end{cases} , \tag{1.13}$$

where $\omega = \Omega - \Omega(\theta)$ is the difference between the angular velocity at the equator and at high latitudes and β is the angle between the magnetic dipole axis and the axis around which a field line originating in the photosphere rotate when arrives at the source surface.

Although the physical motivations behind the general Fisk field are sound (all the effects taken into account are actually observed), so far there has been no or weak evidence of its existence, due also to the fact that the correcting terms are anyway small.

1.2.3 The heliospheric neutral current sheet

As discussed before, the closed loops in the helmet streamers are stretched out by the slow solar wind, which eventually escapes carrying with itself the coronal magnetic field lines. When the field line of a closed loop separates, the two resulting lines have opposite polarity: one of them will have a magnetic field directed inward to the Sun, while the other will be directed outward[2]. The boundary which separates field lines with opposite polarity is called the *heliospheric current sheet* (HCS).

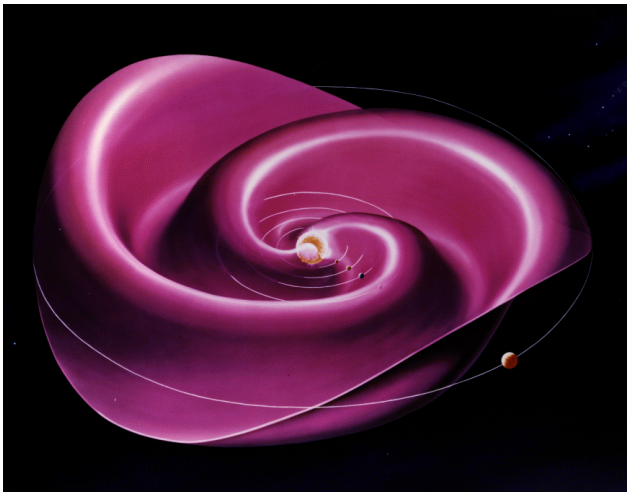

Figure 1.13: The wavy shape of the HCS while it expands and rotates around a tilted axis. Credits: NASA/Werner Heil.

[2]It is important to note that, since $\nabla \cdot \mathbf{B} = 0$ everywhere, no field line in the heliosphere is truly open: the separated field lines will eventually reconnect in the outer heliosphere.

The HCS acts as a magnetic equator and is carried throughout the whole heliosphere by the slow solar wind. Due to the tilted axis of the magnetic dipole and to the rotation of the Sun, the HCS warps while it expands, assuming a wavy shape, akin to a ballerina's skirt, as shown in Figure 1.13

While the Earth moves along its orbit, it traverses regions with different magnetic field polarity, called *magnetic sectors*; the crossing of the HCS is called *sector boundary crossing*. During the minimum, the magnetic field is well organized and only two sector boundary crossings are seen in the ecliptic, while during the maximum the large dipole axis inclination and the additional multipoles can lead to more than two boundary crossings. The angle between the magnetic dipole axis and the rotational axis of the Sun is called *tilt angle* and it is easy to see that it corresponds to the maximum latitudinal extent of the HCS. The tilt angle is not measured directly, but can be inferred by observations of the photospheric magnetic field. The WSO measures the magnetic field on the photosphere for every solar rotation and then computes the coronal field by using the Potential Field Source Surface (PFSS) model [29, 30, 31]. The results of this computation can be seen in Figure 1.14, for both the solar minimum and maximum.

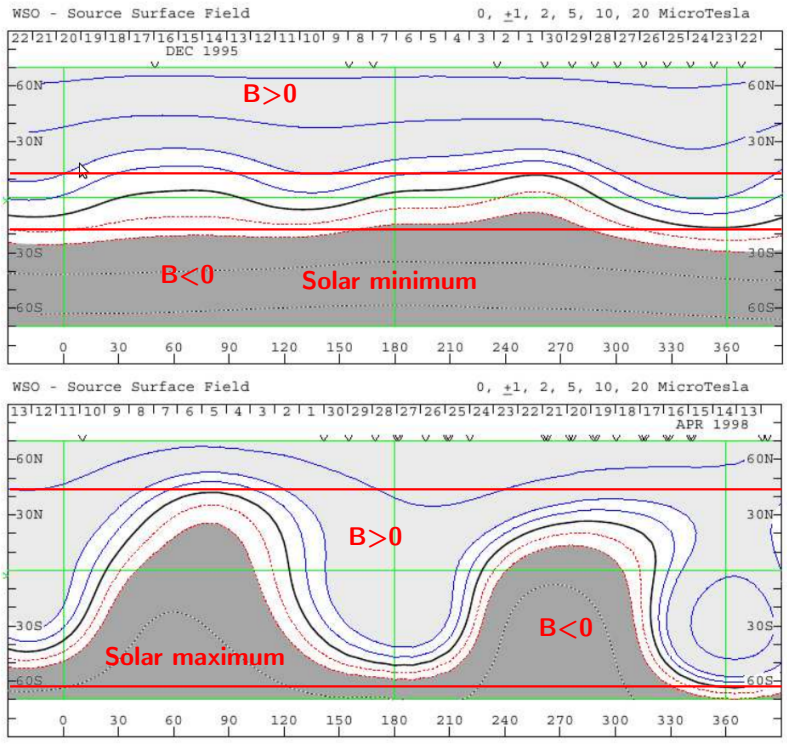

Figure 1.14: Coronal field maps obtained with the PFSS model during the minimum (**top**) and the maximum (**bottom**). Contour lines indicate the field strength, while the black solid line corresponds to the magnetic equator or HCS. Different shades of grey represent different polarities. The red horizontal lines mark the maximum latitudinal extent of the equator in both hemispheres. Figures adapted from the WSO (`http://wso.stanford.edu/synsourcel.html`).

The HCS (the black line) is almost flat during the minimum, while it's highly fluctuating during the maximum. The red lines indicate the maximum latitudinal extent of the magnetic equator, *i.e.* the tilt angle of the HCS. The photospheric field is observed from ground, so the polar regions are not completely visible and the model can be computed only up to 70° of latitude. Two different methods are used to compute the coronal field: the *classical* model adopts a line-of-sight boundary condition and includes a polar field correction, while the *radial* model assumes that the photospheric field is radial, with no polar correction. The time variation of the tilt angle derived from the two models during the last four solar cycle is shown in Figure 1.15, where a periodicity of approximately 11 years can be seen. Due to the limited observations of the polar photospheric field, both models have an upper limit around 75°. The cycle of the tilt angle is in phase with the cycle of the SSN, making it another proxy of the level of solar activity.

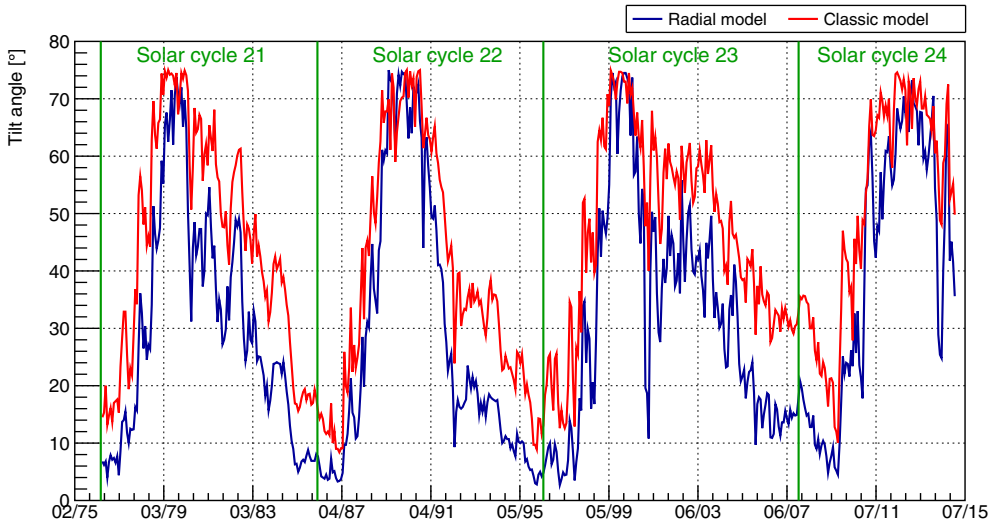

Figure 1.15: Time variation of the tilt angle computed by the WSO with the classic (red) and radial (blue) model. Data from the WSO (`http://wso.stanford.edu/Tilts.html`).

The HCS and the tilt angle play a fundamental role in the drift processes, as will be discussed in Section 1.4.3.

1.3 Energetic particles in the heliosphere

The heliosphere is pervaded by charged particles ranging from energies around keV up to 10^{11} GeV and above. The spectrum of the various particle populations is shown in Figure 1.16. At the lowest energies is the solar wind, with a long supra-thermal tail. Around 0.1 MeV/n we start to see energetic particles accelerated in interplanetary shocks, CIRs and solar flares. A detailed account of the acceleration of solar energetic particles (SEPs) and their study with the Alpha Magnetic Spectrometer (AMS) is given in the PhD thesis of Kathryn Whitman [32]. Between 1 MeV/n and

few hundreds of MeV/n we find the anomalous cosmic rays (ACRs). Interstellar neutral atoms get ionized via photo-ionization or change-exchange processes with the solar wind. These so-called *pickup ions* are advected away by the solar wind until they cross the termination shock, where they undergo diffusive shock acceleration (DSA), returning in the inner heliosphere with higher energy. The observations of *Voyager 1* and *Voyager 2* revealed unexpectedly that ACRs were not accelerated at the termination shock. Many alternative explanations have been hypothesized, but the origin of ACRs is still an open problem [33].

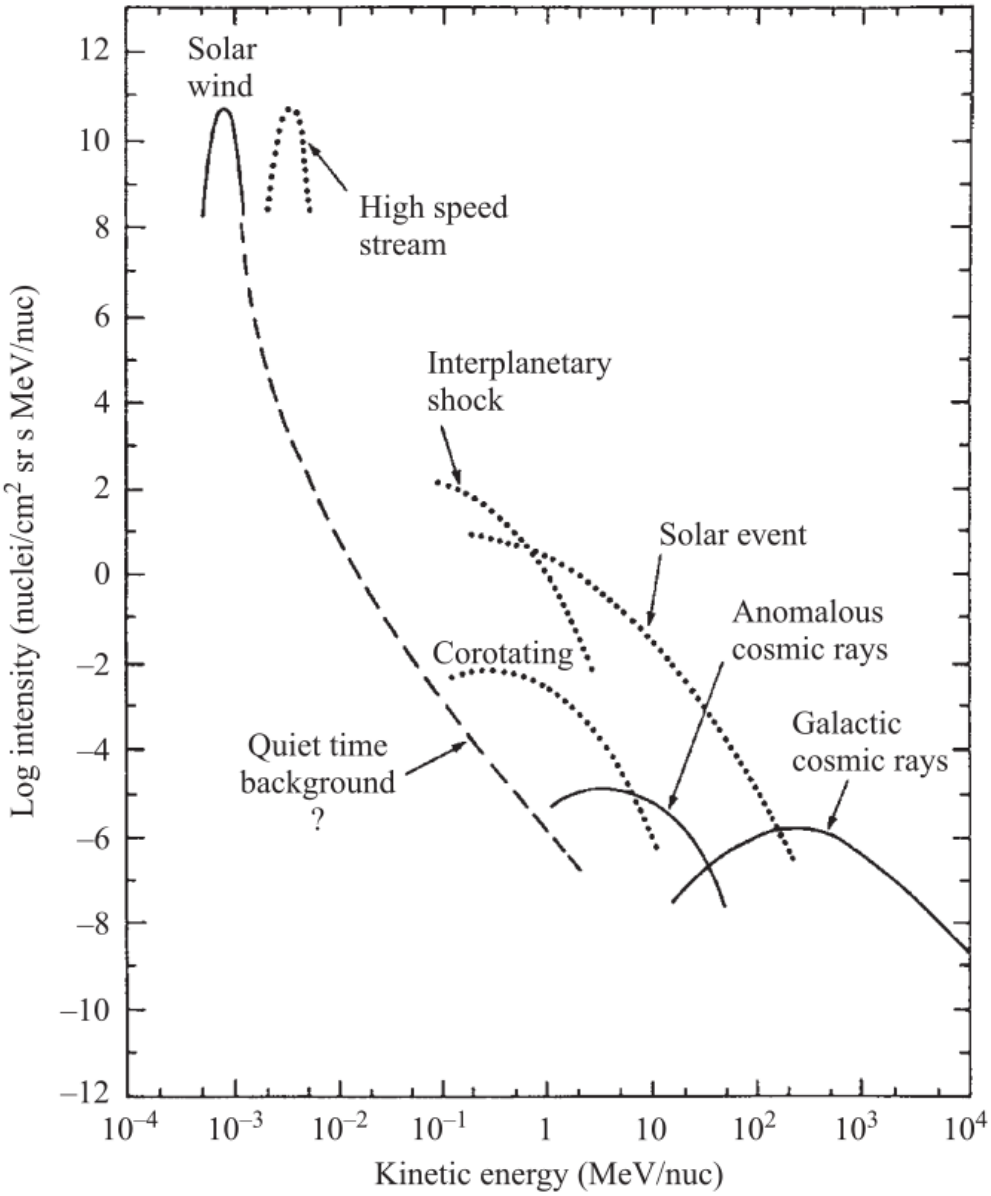

Figure 1.16: The various populations of charged particles found in the heliosphere. Figure adapted from [34].

In this work we will concentrate on the last population of energetic particles in the heliosphere: galactic cosmic rays.

1.3.1 Galactic cosmic rays

Cosmic rays, early known as cosmic radiation, were discovered at the beginning of the twentieth century, observing a discharge of electroscopes even when they were far away from radioactive sources. Subsequent studies by Pacini and Wulf showed that the ionization was decreasing under the water and increasing on the top of the Eiffel Tower. Finally, Victor Hess ascended up to 5 km with a balloon, clearly showing that the source of the ionization was coming outside the Earth: this remarkable feat won him the Nobel Prize in 1936 [35].

GCRs are charged particles, spanning a wide range of energies, from few tens of MeV/n up to 10^{11} GeV, and of intensity, from almost 10^4 particles/m^2/sr/s/GeV around 1 GeV to less than 1 particle/m^2/sr/year/GeV above 10^5 GeV. Roughly 99 % of GCRs is composed of nuclei, while the remaining 1 % is mostly electrons. Protons are the predominant component of the nuclei, around 90 %, followed by helium (9 %) and all the other nuclei. A very small fraction of GCRs is due to antimatter particles, namely positrons and anti-protons [36].

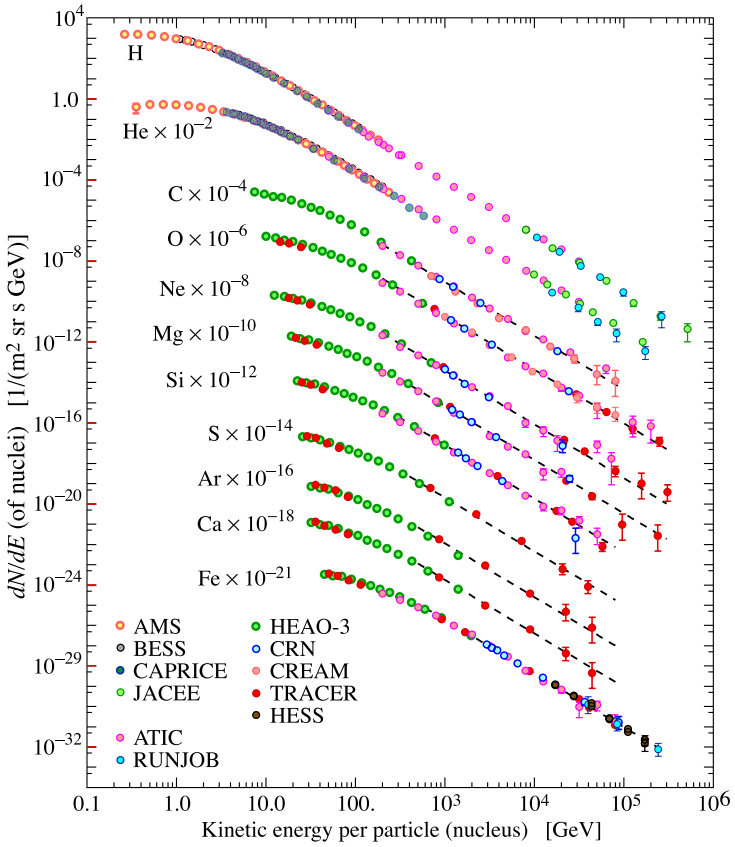

Figure 1.17: Spectrum of nuclei in cosmic rays, measured by different experiments [36].

According to the general consensus, GCRs below 10^6 GeV are accelerated in supernova remnants (SNRs) within our galaxy via DSA [37]. Evidence for this theory comes, for example, from the observations of gamma rays associated with the decay of neutral pions produced by the interaction of the accelerated particles with the surrounding environment of the SNR [38]. Once GCRs escape the accelerating region, they propagate through the galaxy before arriving at the heliopause: they are advected away by the galactic wind originating in the galaxy bulk and streaming out towards the galactic halo [39, 40]; they scatter on the irregularities of the galactic magnetic field, which isotropizes their arrival direction [41]; they undergo stochastic acceleration, also known as re-acceleration, by interacting with the turbulence of the galactic fields [42]; they can decay, if they are unstable nuclei, and can fragment on the ISM gas, producing additional particles not accelerated in SNRs; and, finally, they lose energy by ionization (for nuclei) and by synchrotron radiation and inverse Compton scattering (for electrons and positrons) [43]. The propagation through the galaxy modify the source spectrum of GCRs: when they arrive at the heliosphere, their spectrum is called *local interstellar spectrum* (LIS).

1.3.2 Solar modulation of galactic cosmic rays

This section is adapted from the paper "*Overview of galactic cosmic ray solar modulation in the AMS-02 era*", currently accepted for publication in *Advances in Space Research* [44].

In Figure 1.4 we saw how the intensity of GCRs varies with time, anti-correlating with the strength of the solar activity. Upon entering the heliosphere, GCRs diffuse by scattering on irregularities in the HMF, drift along magnetic field gradients and the HCS, are convected away by the solar wind and lose energy via adiabatic losses due to the solar wind expansion. The overall effect of these processes is called *solar modulation*.

Since the discovery of cosmic rays by Victor Hess in 1912, much has been learned about them [45]. In 1927 a significant latitude effect was discovered related to the Earth magnetosphere and the geomagnetic cutoff; in 1933 Rossi measured the East-West effect, an asymmetry in the arrival direction of low energy cosmic rays related to the presence of the Earth's magnetic field; in 1938 Forbush observed a sudden decrease in GCRs due to the presence of interplanetary coronal mass ejection emitted by the Sun [46].

Continuous monitoring of cosmic ray intensity began in 1937. Ground measurements from neutron monitors provided significant discoveries such as the presence of the solar modulation in 1954 by Forbush and, more recently, the evidence of its two main periodicities (11 and 22 years), and the effect of the change in the solar magnetic polarity [47]. While ground level experiments continuously monitor the GCR flux at Earth, the particles they measure are the result of the showers created by GCRs interacting with the atmosphere and, for this reason, they do not have information about the original primary particles. On the other hand, balloon experiments measure the original particle before entering in the atmosphere, but have a short duration that spans from 1 day up to

a month. Thus, they miss the detailed information of the flux variation over time with the solar cycle. Since 1950 multiple balloon missions have been launched into the stratosphere (from 18 km to 41 km), carrying increasingly bigger and heavier scientific payloads (up to 1400 kg) to collect different species of GCRs in different phases of the solar cycle over a period of time ranging from 1 day to 42 days. For example, the Balloon-borne Experiment with Superconducting Spectrometer (BESS) flew on balloons ten times between 1993 and 2008, sampling the solar modulation in different solar cycle conditions for protons and helium [48]. In addition, spacecraft such as *Pioneer 10 & 11* [49], *Ulysses* [15] and *Voyager 1 & 2* [50] have flown in space over long periods of time with the goal to provide a more coherent picture of the conditions of the heliosphere and give context to cosmic ray measurements at Earth. In August 2012, the *Voyager 1* spacecraft, launched in 1977, crossed the heliopause and entered interstellar space. A debate is still ongoing whether the heliopause can be considered the modulation boundary or not [51, 8, 52, 53], but so far the GCR flux measured by *Voyager 1* has remained steady[3], thereby suggesting that what is being observed is probably the LIS. A fleet of satellites near Earth is dedicated to the study of particles, the local magnetic environment, and space weather. For example, the Cosmic Ray Isotope Spectrometer (CRIS) instrument on board the Advanced Composition Explorer (ACE) spacecraft has been functioning well for a very long time, recording GCR spectra and intensities for the period of solar minimum and solar maximum [54]. The CRIS elemental data between 50 and 500 MeV/n are available for the full solar cycle and are released to the space physics community on a regular basis.

More recently, a new generation of space experiments were born. PAMELA[4] and AMS-02 are long duration space missions dedicated to the measurement of GCRs. The Payload for Antimatter Matter Exploration and Light-nuclei Astrophysics (PAMELA) [55] can provide precise measurement of particles at high energies (up to hundreds of GeV) and down to 70 MeV, due to its elliptical quasi orbital orbit (300 to 600 km of altitude) which approaches latitudes of 70.4 degrees. PAMELA, with its effective area of 21.5 cm^2 sr and mass of 470 kg, has been measuring GCRs in space since 2006 providing new insights in many fields including the origin of antimatter, the nature of dark matter, SEPs from the Sun, solar modulation, and the interaction between particles and the Earth's magnetic field. The PAMELA mission was extended beyond the original 3 year plan and in June 2016 it celebrated 10 years in space.

In Figure 1.18, an overview of space and balloon experiments measuring p, He and ions over different solar cycles is shown. The sunspot number is shown as reference at the top of the figure to indicate the phase of the solar activity during which the data were taken. The pink bands indicate the periods in which the solar magnetic field reversal occurred. All the GCR data shown in this paper have been downloaded from the cosmic-ray database[5] [56].

[3] See, for example, the proton rates between 2013 and 2017 at `https://voyager.gsfc.nasa.gov/flux.html`
[4] `http://pamela.roma2.infn.it/index.php`
[5] `https://lpsc.in2p3.fr/cosmic-rays-db`

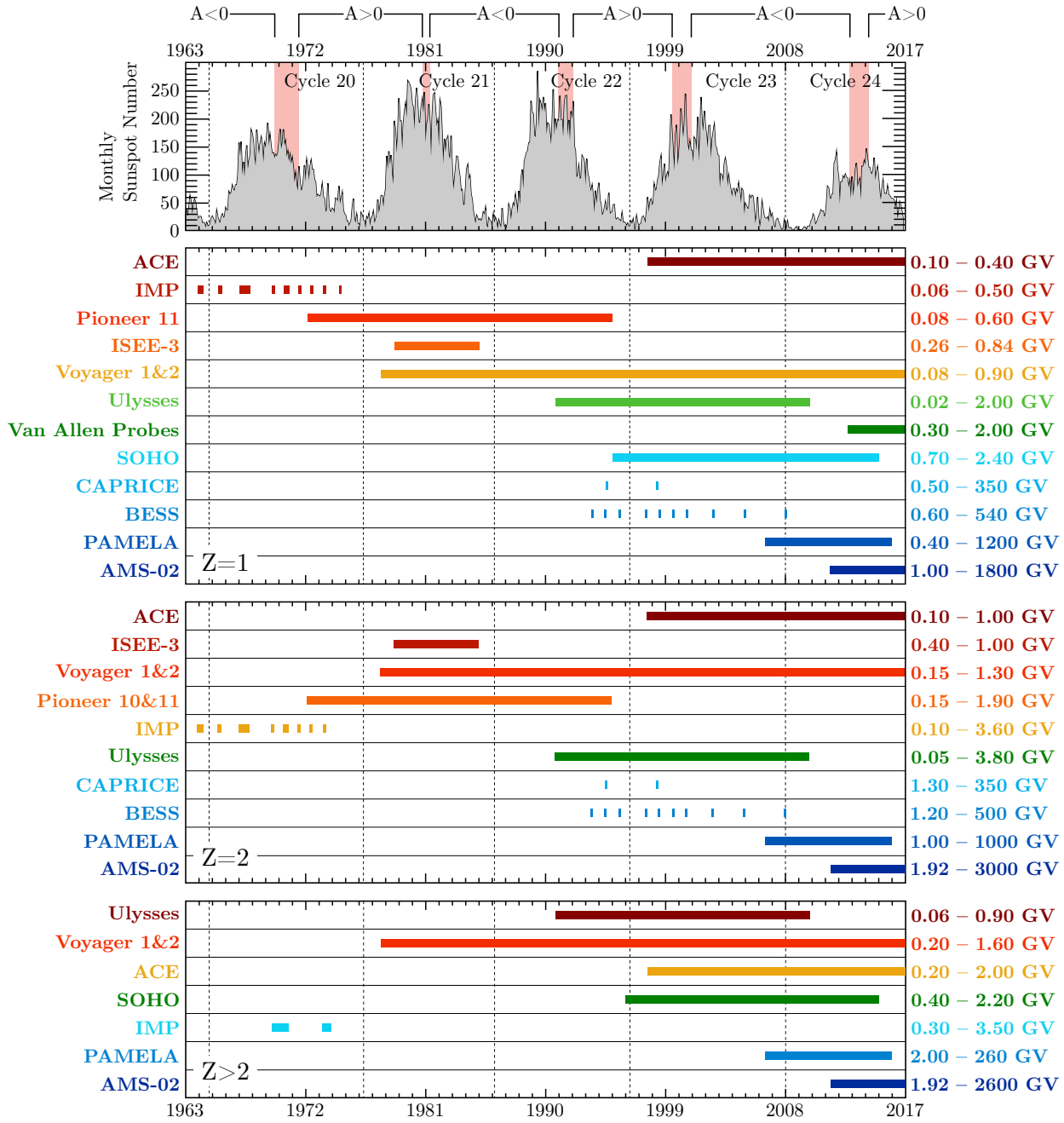

Figure 1.18: Overview of space and balloon experiments measuring p, He and ions over different solar cycles. The sunspot number is shown at the top of the figure as a proxy of the phase of the solar activity during which the data where taken. The pink bands mark the periods of the solar magnetic field reversal. Only experiments providing multiple measurements in the rigidity range where anomalous cosmic rays are negligible ($R \gtrsim 0.4$ GV) have been included.

1.4 The Parker transport equation

The transport equation of GCRs was first derived by Parker [57]. Let's consider the particle distribution function $f(\mathbf{r}, \mathbf{p})$, such that $dN = f(\mathbf{r}, \mathbf{p})\, d^3r\, d^3p$ is the number of particles in the volume element d^3r and with momentum between $\mathbf{p}$ and $\mathbf{p} + d\mathbf{p}$. The continuity equation in differential form,

$$\frac{\partial f}{\partial t} + \nabla \cdot \mathbf{S} = 0, \tag{1.14}$$

describes the fact that in a given volume, the rate of change of the number of particles, $\partial f/\partial t$, is given by the number of particles that flow across the surface enclosing the volume, assuming no sources of particle is present. $\mathbf{S}$ is the flux (or streaming current density) of particles across the surface, and its caused by the physical processes typical of the examined system. In the case of GCRs propagating in the heliosphere, the two processes contributing to the flow of particles are the radial outward convection of the solar wind, $\mathbf{V}_{sw} f$, and the scattering on the magnetic field irregularities, which generates a diffusive flux given by the Fick's law, $-\mathsf{K}\nabla f$.

According to the Lorentz force $\mathbf{F} = q(\mathbf{v} \times \mathbf{B})$, a charged particle in a magnetic field will spiral along the magnetic field lines. The details of this spiraling motion depends on the geometry of the field $\mathbf{B}$ and on the ratio of the gyroradius $r_L = p/(ZeB)$, where Ze is the charge of the particle, and the scale length λ of the magnetic field irregularities. Figure 1.19 illustrates the different possibilities.

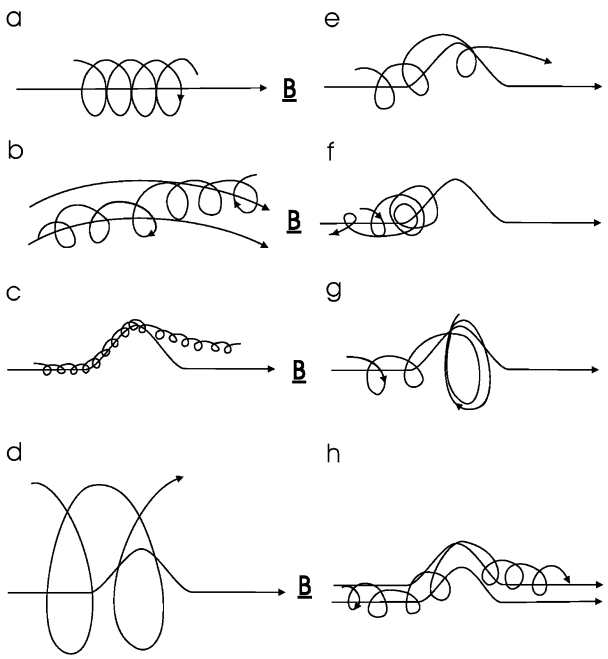

Figure 1.19: Motion of a charged particle in a magnetic field, depending on the ratio of the gyroradius to the magnetic field irregularities scale [58]. See the text for a description of the different cases.

If the field is uniform (panel a) or $r_L \gg \lambda$ (panel d), the particle will keep its direction of motion. If the field is not uniform (panel b), a drift motion will appear, displacing the particle from one field line to another. If $r_L \ll \lambda$ (panel c), the particle will follow the shape of the field line, eventually jumping to another field line due to the non-zero drift velocity induced by the curvature of the field. Finally, if $r_L \sim \lambda$ (panels e-h), the particle can be scattered with a pitch angle depending on the gyrophase of the trajectory when it meets the irregularity.

All these effects can be included in a quantity called *diffusion tensor*:

$$\mathsf{K} = \begin{pmatrix} k_{\parallel} & 0 & 0 \\ 0 & k_{\perp,\theta} & k_A \\ 0 & -k_A & k_{\perp,r} \end{pmatrix}, \tag{1.15}$$

where the three principal axes have been chosen to be aligned to the magnetic field. $k_{\parallel}$ is the diffusion coefficient (DC) parallel to the field line, $k_{\perp,r}$ and $k_{\perp,\theta}$ are the DCs perpendicular to the field line, respectively, in the radial and polar direction, and k_A is the drift coefficient.

While the particles are spiraling and drifting along the HMF, the solar wind expands, adiabatically cooling the GCRs. This has the same effect of a flow in momentum space [58], with the associated divergence of flux, which, in case of an isotropic particle distribution, is:

$$\nabla \cdot \mathbf{S}_p = \frac{1}{p^2} \frac{\partial}{\partial p} \left(p^2 \langle \dot{p} \rangle f \right). \tag{1.16}$$

It can be shown that the average change in momentum is $\langle \dot{p} \rangle = -p/3 \nabla \cdot \mathbf{V}_{sw}$ [59]. Let's note that if the solar wind compresses, for example at the termination shock, its divergence becomes negative and the momentum increases, *i.e.* we have adiabatic acceleration. Putting all together, we arrive at the Parker transport equation:

$$\frac{\partial f}{\partial t} + \nabla \cdot (\mathbf{V}_{sw} f - \mathsf{K} \nabla f) - \frac{\nabla \cdot \mathbf{V}_{sw}}{3p^2} \frac{\partial}{\partial p} \left(p^3 f \right) = 0. \tag{1.17}$$

Gleeson and Axford [60] derived the transport equation in a more rigorous way, starting from the Boltzmann equation and explicitly calculating collision term due to the scattering on the magnetic field irregularities and assuming a negligible directional anisotropy of the distribution function. By rearranging the convective flux and the energy losses terms, we can write the Parker equation in an equivalent form:

$$\frac{\partial f}{\partial t} + \nabla \cdot (C \mathbf{V}_{sw} f - \mathsf{K} \nabla f) - \frac{1}{3p^2} \frac{\partial}{\partial p} \left(p^3 \mathbf{V}_{sw} \cdot \nabla f \right) = 0, \tag{1.18}$$

where $C = -1/3 \; \partial \ln f / \partial \ln p$ is the Compton-Getting coefficient [61, 62], which arises when analyzing the equation in the reference frame stationary with the solar system.

The Parker equation can be casted in a third simpler form, which is the one mostly used in

numerical models:

$$\frac{\partial f}{\partial t} + \mathbf{V}_{sw} \cdot \nabla f - \nabla \cdot (\mathsf{K} \nabla f) - \frac{\nabla \cdot \mathbf{V}_{sw}}{3} \frac{\partial f}{\partial \ln p} = 0 \tag{1.19}$$

1.4.1 The steady-state Parker equation in spherical coordinates

In a steady-state approximation, $\partial f / \partial t = 0$. It is also convenient to use spherical coordinates, since the geometry of the heliosphere is more or less spherical[6]. Before doing so, we need to convert the diffusion tensor from a field-aligned coordinate system to a system corotating with the Sun, *i.e.* $\mathsf{K} \rightarrow \mathsf{T}\mathsf{K}\mathsf{T}^T$, where T is the coordinate transformation matrix, and $\mathbf{V}_{sw} \rightarrow \mathbf{V}_{sw} - \Omega \times \hat{\mathbf{r}}$. It is easy to show that the field-aligned system, for a Parker-like HMF, has the following basis:

$$\begin{aligned} \mathbf{e}_{\parallel} &= \cos\psi \hat{\mathbf{r}} - \sin\psi \hat{\boldsymbol{\phi}} \\ \mathbf{e}_{\perp,\theta} &= \hat{\boldsymbol{\theta}} \\ \mathbf{e}_{\perp,r} &= \sin\psi \hat{\mathbf{r}} + \cos\psi \hat{\boldsymbol{\phi}} \end{aligned} \quad , \tag{1.20}$$

where ψ is the HMF spiral angle. The rotation matrix T is then defined as:

$$\mathsf{T} = \begin{pmatrix} \cos\psi & 0 & \sin\psi \\ 0 & 1 & 0 \\ -\sin\psi & 0 & \cos\psi \end{pmatrix} \tag{1.21}$$

We can now write the diffusion tensor in spherical coordinates:

$$\begin{aligned} \begin{pmatrix} \mathsf{K}_{rr} & \mathsf{K}_{r\theta} & \mathsf{K}_{r\phi} \\ \mathsf{K}_{\theta r} & \mathsf{K}_{\theta\theta} & \mathsf{K}_{\theta\phi} \\ \mathsf{K}_{\phi r} & \mathsf{K}_{\phi\theta} & \mathsf{K}_{\phi\phi} \end{pmatrix} &= \\ &= \begin{pmatrix} \cos\psi & 0 & \sin\psi \\ 0 & 1 & 0 \\ -\sin\psi & 0 & \cos\psi \end{pmatrix} \begin{pmatrix} k_{\parallel} & 0 & 0 \\ 0 & k_{\perp,\theta} & k_A \\ 0 & -k_A & k_{\perp,r} \end{pmatrix} \begin{pmatrix} \cos\psi & 0 & -\sin\psi \\ 0 & 1 & 0 \\ \sin\psi & 0 & \cos\psi \end{pmatrix} = \\ &= \begin{pmatrix} k_{\parallel}\cos^2\psi + k_{\perp,r}\sin^2\psi & -k_A\sin\psi & (k_{\perp,r} - k_{\parallel})\cos\psi\sin\psi \\ k_A\sin\psi & k_{\perp,\theta} & k_A\cos\psi \\ (k_{\perp,r} - k_{\parallel})\cos\psi\sin\psi & -k_A\cos\psi & k_{\parallel}\sin^2\psi + k_{\perp,r}\cos^2\psi \end{pmatrix} \end{aligned} \tag{1.22}$$

Let's note that $\mathsf{K}_{r\theta} = -\mathsf{K}_{\theta r}$, $\mathsf{K}_{\phi\theta} = -\mathsf{K}_{\theta\phi}$ and $\mathsf{K}_{r\phi} = \mathsf{K}_{\phi r}$ and that the drift terms do not mix with the diffusion terms: if the HMF was a Fisk-type field, then we would have also a polar component, thus another angle around which rotate, and the diffusion tensor would be more complicated.
Plugging this expression in Equation 1.19, applying the steady state condition, changing sign and

[6] We neglect here any asymmetry in the termination shock and the heliotail.

writing all the derivatives in spherical coordinates, we get:

$$
\begin{aligned}
0 = & -V_{sw}\frac{\partial f}{\partial r} - \Omega\frac{\partial f}{\partial \phi} + \\
& + \frac{1}{r^2}\frac{\partial}{\partial r}\left[r^2\left(\mathsf{K}_{rr}\frac{\partial f}{\partial r} + \frac{\mathsf{K}_{r\theta}}{r}\frac{\partial f}{\partial \theta} + \frac{\mathsf{K}_{r\phi}}{r\sin\theta}\frac{\partial f}{\partial \phi}\right)\right] + \\
& + \frac{1}{r\sin\theta}\frac{\partial}{\partial \theta}\left[\sin\theta\left(\mathsf{K}_{\theta r}\frac{\partial f}{\partial r} + \frac{\mathsf{K}_{\theta\theta}}{r}\frac{\partial f}{\partial \theta} + \frac{\mathsf{K}_{\theta\phi}}{r\sin\theta}\frac{\partial f}{\partial \phi}\right)\right] + \\
& + \frac{1}{r\sin\theta}\frac{\partial}{\partial \phi}\left[\left(\mathsf{K}_{\phi r}\frac{\partial f}{\partial r} + \frac{\mathsf{K}_{\phi\theta}}{r}\frac{\partial f}{\partial \theta} + \frac{\mathsf{K}_{\phi\phi}}{r\sin\theta}\frac{\partial f}{\partial \phi}\right)\right] + \\
& + \frac{1}{3r^2}\frac{\partial}{\partial r}\left(r^2 V_{sw}\right)\frac{\partial f}{\partial \ln p} = \\
& = \left[\frac{1}{r^2}\frac{\partial}{\partial r}\left(r^2\mathsf{K}_{rr}\right) + \frac{1}{r\sin\theta}\frac{\partial}{\partial \theta}\left(\mathsf{K}_{\theta r}\sin\theta\right) + \frac{1}{r\sin\theta}\frac{\partial \mathsf{K}_{\phi r}}{\partial \phi} - V_{sw}\right]\frac{\partial f}{\partial r} + \\
& + \left[\frac{1}{r^2}\frac{\partial}{\partial r}\left(r\mathsf{K}_{r\theta}\right) + \frac{1}{r^2\sin\theta}\frac{\partial}{\partial \theta}\left(\mathsf{K}_{\theta\theta}\sin\theta\right) + \frac{1}{r^2\sin\theta}\frac{\partial \mathsf{K}_{\phi\theta}}{\partial \phi}\right]\frac{\partial f}{\partial \theta} + \\
& + \left[\frac{1}{r^2\sin\theta}\frac{\partial}{\partial r}\left(r\mathsf{K}_{r\phi}\right) + \frac{1}{r^2\sin\theta}\frac{\partial \mathsf{K}_{\theta\phi}}{\partial \theta} + \frac{1}{r^2\sin^2\theta}\frac{\partial \mathsf{K}_{\phi\phi}}{\partial \phi} - \Omega\right]\frac{\partial f}{\partial \phi} + \\
& + \frac{2\mathsf{K}_{r\phi}}{r\sin\theta}\frac{\partial f}{\partial r\,\partial \phi} + \mathsf{K}_{rr}\frac{\partial^2 f}{\partial r^2} + \frac{\mathsf{K}_{\theta\theta}}{r^2}\frac{\partial^2 f}{\partial \theta^2} + \frac{\mathsf{K}_{\phi\phi}}{r^2}\sin^2\theta\frac{\partial^2 f}{\partial \phi^2} + \\
& + \frac{1}{3r^2}\frac{\partial}{\partial r}\left(r^2 V_{sw}\right)\frac{\partial f}{\partial \ln p}.
\end{aligned}
\tag{1.23}
$$

This equation will be the starting point of the numerical model described in Chapter 5.

1.4.2 Particle diffusion

Diffusion plays a fundamental role in the solar modulation and a great deal of efforts was poured in trying to derive the diffusion tensor from first principles and from measurements of the magnetic field turbulence. Although the first theory of particle diffusion appeared more than 50 years ago (Jokipii, 1966 [63]), this field is still very active. In the last years, the focus has shifted from purely theoretical reasoning to the exploitation of the ever increasing computing resources in performing magnetohydrodynamics (MHD) and particle-in-cell (PIC) simulations. The first class of simulations aims at solving a system of coupled hydrodynamic and Maxwell equations, while the second class tries to reproduce the complexities of the magnetic field embedded in a plasma by following the

trajectories of pseudo-particles (or fluid elements) in the phase space, akin to a Monte Carlo method.

Parallel and perpendicular diffusion have different origins: indeed, while the theory of parallel diffusion it's simpler and better understood, a satisfying theory of perpendicular diffusion appeared only relatively recently (Matthaeus et al., 2003 [64]). The basis of diffusion theory is the pitch angle scattering, *i.e.* the distribution of the angle between the direction of motion of a particle and the direction of the magnetic field. Since the underlying physics process is scattering, it's useful to rewrite the DC in term of the mean free path λ between two successive scatterings:

$$k = \frac{v}{3}\lambda. \tag{1.24}$$

The theory that describes the parallel diffusion is called *quasi-linear theory* (QLT). The parallel DC can be expressed as a function of the cosine of the pitch angle, μ:

$$k_{\parallel} = \frac{v^2}{8}\int_{-1}^{1} \frac{(1-\mu^2)^2}{D_{\mu\mu}}\, d\mu, \tag{1.25}$$

where $D_{\mu\mu}$ is the pitch angle Fokker-Planck coefficient, *i.e.* the rate of particle scattering, derived from the power spectrum of the magnetic fluctuations [65]. The result of the integral depends on the turbulence model considered [66, 67, 68, 69], but a good approximation consists in considering a double power law for the rigidity dependence and the inverse of the HMF magnitude for the spatial dependence.

The field lines of the HMF follow a random walk too, so that a particle spiraling around them will result to have scattered perpendicularly with respect to the nominal background field. This effect was finally considered in the theory of the perpendicular diffusion in the *non-linear guiding center* (NLGC) theory. The result is an expression for the perpendicular DC depending on the parallel diffusion [64]. For this reason, typically, perpendicular DC is modeled with the same rigidity and spatial dependence of the parallel DC, simply rescaled by a factor around few percent.

1.4.3 Particle drifts

Although an asymmetric diffusion tensor was already present in the original derivation of the Parker equation [57], the importance of drift processes was neglected until Jokipii [70] showed that its effects on the solar modulation could be significant. Drift motions are caused by gradients and curvature in the global HMF and by the HCS. Figure 1.20 show the direction of the drift patterns depending on the HMF polarity: during $A < 0$ cycles, protons propagates in the heliosphere mostly through the HCS, while during $A > 0$ cycles they enter predominantly from the poles.

Looking at Equation 1.23, we can see that the drift terms can be grouped in a drift velocity term

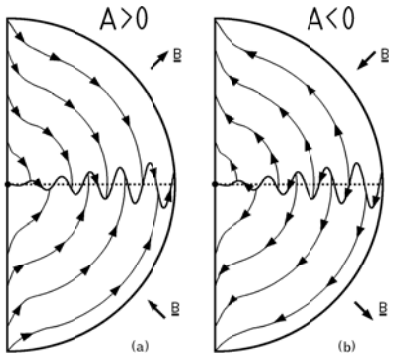

Figure 1.20: Drift patterns in the heliosphere, for positive (left) and negative (right) polarity. Figure adapted from [71].

similar to the solar wind convection term, $\langle \mathbf{v}_A \rangle \cdot \nabla f$, where the components of the drift velocity are:

$$\begin{aligned}
\langle \mathbf{v}_A \rangle_r &= -\frac{A}{r \sin\theta} \frac{\partial}{\partial \theta} \left(\mathsf{K}_{\theta r} \sin\theta \right) \\
\langle \mathbf{v}_A \rangle_\theta &= -\frac{A}{r} \frac{\partial}{\partial r} \left(r \mathsf{K}_{r\theta} \right) + \frac{A}{r \sin\theta} \frac{\partial \mathsf{K}_{\phi\theta}}{\partial \phi}, \\
\langle \mathbf{v}_A \rangle_\phi &= -\frac{A}{r} \frac{\partial \mathsf{K}_{\theta\phi}}{\partial \theta}
\end{aligned} \tag{1.26}$$

where we esplicitly added the dependence on the HMF polarity A, which changes sign every 11 years. The drift velocity is related to the drift coefficient k_A via the relation:

$$\langle \mathbf{v}_A \rangle = \nabla \times k_A \frac{\mathbf{B}'}{B}, \tag{1.27}$$

where $\mathbf{B}' = \mathbf{B}[1 - 2H(\theta - \theta_{HCS})]$. This multiplicative term contains the Heavyside step function, whose argument is the difference between the latitude θ and the latitudinal position of the HCS: if $\theta > \theta_{HCS}$ the term is -1, while if $\theta < \theta_{HCS}$ the term is 1. Essentially, this changes the direction (inward or outward) of the magnetic field above and below the HCS. The drift velocity is then composed of two components, the first related to gradient and curvature drifts, the second related to the HCS drifts:

$$\langle \mathbf{v}_A \rangle = \nabla \times \left(k_A \frac{\mathbf{B}}{B} \right) [1 - 2H(\theta - \theta_{HCS})] + 2\delta(\theta - \theta_{HCS}) k_A \frac{\mathbf{B}}{B} \times \nabla(\theta - \theta_{HCS}). \tag{1.28}$$

The drift coefficient is given by:

$$k_A = \frac{v}{3} r_L \frac{(\omega \tau_A^2)}{1 + (\omega \tau_A)^2}, \tag{1.29}$$

where r_L is the gyroradius, ω is the gyrofrequency and τ_A is a time scale related to the scattering due to turbulence, which suppresses the drift motions [72, 73, 74, 75]. If $\omega \tau_A \gg 1$, the scattering is

small, thus the particles experience a large number of gyrations around the field line, corresponding to a large drift velocity. This limit is called *weak scattering* limit.

1.5 The force-field solution

Gleeson and Axford [76] solved the Parker equation by assuming steady state conditions, spherical symmetry and a vanishing Compton-Getting corrected streaming current density. The last assumption is usually verified for protons and helium at Earth with kinetic energies above 400 MeV/n. The Parker equation then simplifies to:

$$CV_{sw}f - k\frac{\partial f}{\partial r} = 0 \quad \Longrightarrow \quad \frac{1}{3}pV_{sw}\frac{\partial f}{\partial p} + k\frac{\partial f}{\partial r} = 0, \tag{1.30}$$

where the diffusion tensor is now a single number k. Let's change variable, from the momentum p to the rigidity R, and rearrange the terms:

$$\frac{\partial f}{\partial r} + \frac{RV_{sw}}{3k}\frac{\partial f}{\partial R} = 0 \tag{1.31}$$

This equation, called *force-field* equation, is easily solvable with the method of the characteristics: $f(r, R)$ is constant along the trajectories in the phase space which satisfy the characteristic equation $dR/\,dr = RV_{sw}/(3k)$. In particular, we have that $f(r_E, R_E) = f(r_{HP}, R_{HP})$, *i.e.* the GCR distribution function at Earth is equal to the GCR distribution function at the heliopause. Assuming that the radial and rigidity dependence of the DC can be separated, $k(r, R) = \beta k_1(r)k_2(R)$, we can solve the characteristic equation:

$$\int_{R_E}^{R_{HP}} \frac{\beta k_2(R')}{R'}\, dR' = \int_{r_E}^{r_{HP}} \frac{V_{sw}(r')}{3k_1(r')} \equiv \phi(r_E) \tag{1.32}$$

$\phi(r)$ is called *force-field parameter* or *modulation parameter* or *modulation potential*. The name force-field comes from the fact that $RV_{sw}/(3k)$ has the units of an electric field, so Equation 1.31 can be interpreted as the equation of motion of a charged particle sitting in a central electric field generated by the potential $\phi(r)$. Of course, this is only an analogy, since no electric field originates from the Sun and pervades the heliosphere.

The particle distribution function $f(r, R)$ is related to $J_T = dJ/\,dT$, the *differential intensity* as a function of the kinetic energy measured by cosmic ray experiments, *i.e.* the number of particles between T and $T + dT$ per unit area, per unit time and per unit of solid angle. In fact, we can write:

$$f(r, R) = \frac{dN}{dV\,R^2\,d\Omega\,dR} = \frac{dN}{dAv\,dtR^2\,d\Omega\,dR} = \frac{Ze\,dN}{dA\,dtR^2\,d\Omega\,dT} = \frac{ZeJ_T(r, T)}{R^2}, \tag{1.33}$$

because $v\,dR = dT/(Ze)$. The solution of the force-field equation becomes

$$\frac{J_T(r_E, T_E)}{R_E^2} = \frac{J_T(r_{HP}, T_{HP})}{R_{HP}^2} \quad \Longrightarrow \quad \frac{J_T(r_E, T_E)}{T_E(T_E + 2M)} = \frac{J_T(r_{HP}, T_{HP})}{T_{HP}(T_{HP} + 2M)}, \tag{1.34}$$

which relates the differential intensity measured near Earth with the one at the entrance of the heliosphere.

If we posit that $k_2(R) \propto R$, which at the times of Gleeson and Axford was a reasonable assumption, the integral defining $\phi(r)$ is easily solved, yielding:

$$\phi(r_E) = \int_{R_E}^{R_{HP}} \frac{\beta k_2(R')}{R'}\, dR' = \int_{R_E}^{R_{HP}} \beta\, dR' = \int_{R_E}^{R_{HP}} \frac{1}{Ze}\frac{dT}{dR'}\, dR' = \frac{T_{HP} - T_E}{Ze}, \tag{1.35}$$

i.e. $T_{HP} = T_E + Ze\phi$, so that

$$\frac{dJ}{dT}(T) = \frac{T(T + 2M)}{(T + Ze\phi)(T + Ze\phi + 2M)} \frac{dJ_{LIS}}{dT}(T + Ze\phi) \tag{1.36}$$

This last equation is called *force-field approximation* and describes the overall effect of the solar modulation as the energy lost during the propagation inside the heliosphere, $Ze\phi$, whose value in principle depends only on the distance from the Sun and can be directly computed when knowing the radial dependence of the DC. Given its simplicity, the force-field approximation is widely used, especially in fields like high-energy astrophysics and radiation hazard, where the solar modulation is just a *nuisance* and not the main topic of study.

The force-field approximation works well at intermediate rigidities and close to Earth, while it fails to reproduce the solution of the full Parker equation below 100 MeV/n, where the convective and diffusive fluxes do not balance, and at large distance from the Sun, overestimating the adiabatic energy losses [77].

CHAPTER 2
THE AMS-02 EXPERIMENT

The Alpha Magnetic Spectrometer (AMS)[1] is a high-precision particle detector built to operate in space. It was installed on the International Space Station (ISS) in May 19th 2011 during the STS-134 NASA Endeavour Shuttle mission and it started taking data few days later. AMS-02 is the successor of AMS-01, a simpler detector that flew in June 1998 on the Shuttle Discovery (NASA mission STS-91). The experiment (from now on called AMS) will run up to the decommissioning of the ISS, scheduled for 2024.

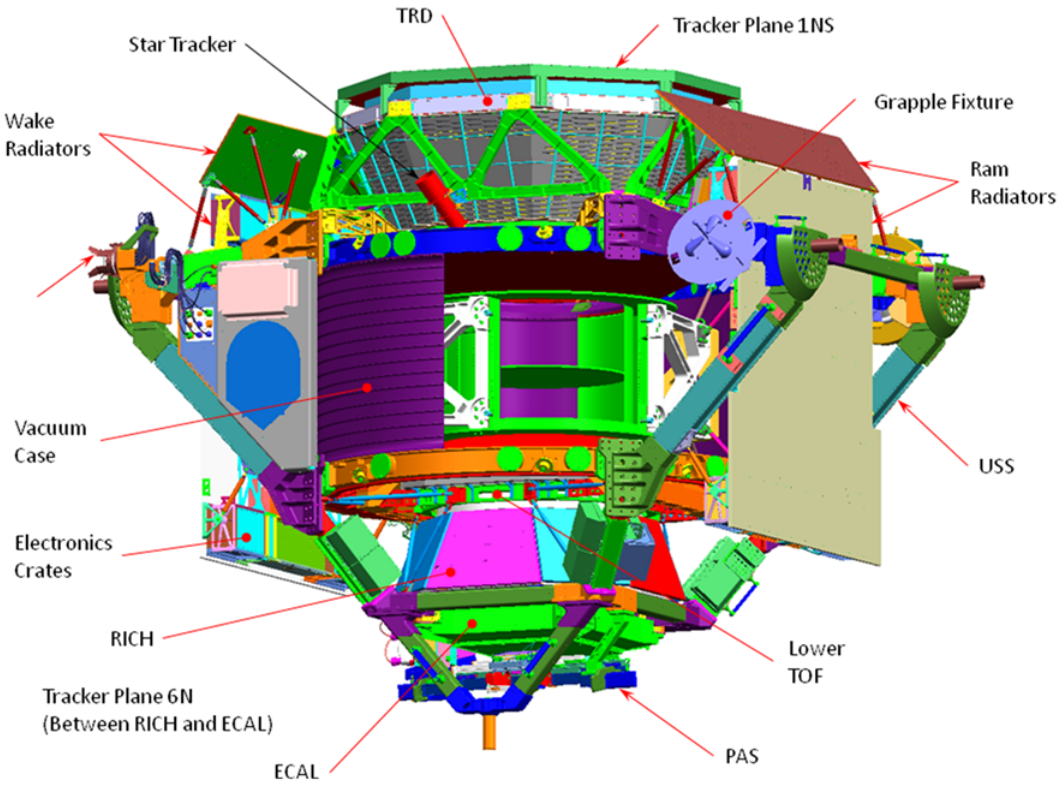

Figure 2.1: The AMS experiment, with its sub-detectors and other sub-systems labeled.

AMS has been designed as a scaled-down version of the detectors sitting inside particle accelerators. At its core, a cylindrically shaped permanent magnet generates a magnetic field of $\approx 0.15\,\mathrm{T}$ which bends the trajectory of charged particles traversing it. A multi-layer silicon tracker precisely measures the X and Y position and charge of the particles: seven layers are inside the magnet bore, constituting the inner tracker, while two are outside, increasing the lever arm from approximately 1 m to almost 3 m. Together with the magnet, the tracker acts as a spectrometer, measuring the

[1] www.ams02.org

particle rigidity in the range 1 GV to few TV. A time of flight (TOF) system composed of four layers of segmented scintillators (two above and two below the magnet) provides the main trigger to the experiment, measures the particle velocity and absolute charge and discriminates between up-going and down-going particles. The inner tracker is surrounded by an anti-coincidence counter (ACC), a series of scintillating paddles which veto in the trigger particles entering AMS from the sides. Three additional sub-detectors enrich the capabilities of AMS to identify particles: a transition radiation detector (TRD), on top of the experiment, separates $e^{\pm}$ from hadrons and measures the absolute charge of nuclei; a ring imaging Cherenkov (RICH), below the magnet, extends the velocity measurement range of the TOF and provides isotopic separation; finally, the electromagnetic calorimeter (ECAL), at the bottom of the experiment, precisely measures the energy of $e^{\pm}$ and photons in the range 0.5 GeV to 1 TeV and increase the lepton-hadron discrimination power of AMS.

The redundant measurement of the different properties of particles allows AMS to pursue many goals. The main one is the search for primordial anti-helium nuclei ($\overline{\text{He}}$): the Standard Model of Big Bang cosmology assumes that at the beginning of the Universe there was an equal amount of matter and antimatter, but no trace of antimatter domains has ever been found in the Universe. The Standard Model of particle physics predicts a small CP violation which implies a different behavior of matter and antimatter, but this violation is not enough to explain the asymmetry we see at the present. Since the probability of production of $\overline{\text{He}}$ by interaction of galactic cosmic rays (GCRs) with the interstellar medium is negligible, detecting it would be a proof of the existence of antimatter domains formed in the early period of the Universe [78]. AMS is expected to improve the current upper limit on $\overline{\text{He}}$ detection by at least two orders of magnitude (see Figure 2.2).

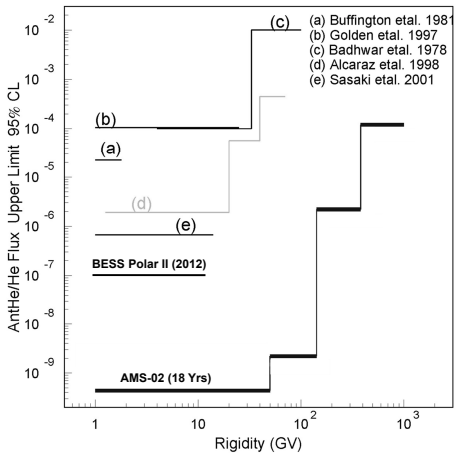

Figure 2.2: AMS predicted sensitivity in the search for $\overline{\text{He}}$ for 18 years of data taking, compared with the available upper limits by other experiments [79].

Another relevant goal is the indirect observation of dark matter (DM) [80, 81]: according to the prevalent explanation, DM is composed of weakly interacting massive particles (WIMPs), which

eventually decay and/or annihilate into Standard Model particles [82]. The signature of DM decay/annihilation should be visible in the spectra of the most rare GCR components – like anti-protons ($\overline{\mathrm{p}}$), positrons (e^+) and anti-deuterons ($\overline{\mathrm{d}}$) – as an excess over the astrophysical background [83, 84, 85] (see Figure 2.3). However, any excess could also be attributed to a point-like source in the proximity of the Solar System: in particular, pulsar wind nebulæ (PWNs) are expected to produce additional $\mathrm{e}^{\pm}$ couples, not accounted for in the current description of GCR production and acceleration [86]. The observation of an anisotropy in the e^+ channel compatible with the predicted anisotropy from the PWNs closest to us would certainly weaken the DM interpretation of a e^+ excess.

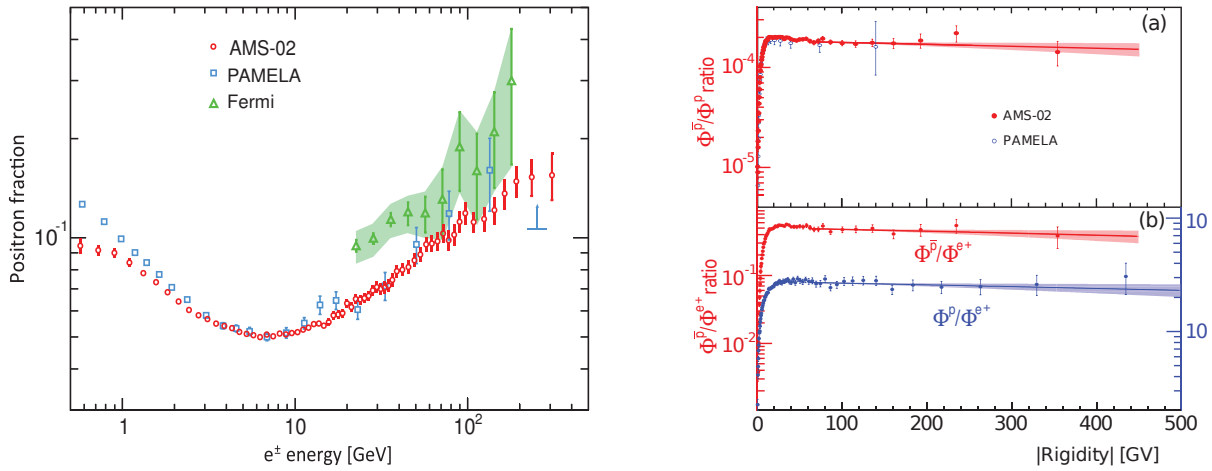

Figure 2.3: **Left**: Positron fraction, *i.e.*, $\mathrm{e}^+/(\mathrm{e}^+{+}\mathrm{e}^-)$, measured by AMS, compared to the most recent measurements [87]. The rise of the fraction above 10 GeV is most probably due to additional sources, namely DM or PWNs. **Right**: (a) $\overline{\mathrm{p}}/\mathrm{p}$ ratio measured by AMS, compared to the most recent measurements. (b) $\overline{\mathrm{p}}/\mathrm{e}^+$ and p/e^+ ratios measured by AMS [88]. Above 100 GV all ratios are flat in rigidity, suggesting a similar production mechanism for $\overline{\mathrm{p}}$ and e^+. However, it's still unclear whether the measured $\overline{\mathrm{p}}$ flux is consistent with the astrophysical background predictions.

The indirect search of DM requires a precise knowledge of the astrophysical background: the large acceptance and long duration mission of AMS are key ingredients in reducing the uncertainties related to the propagation of GCRs in the galaxy. AMS is able to measure the flux of all elements up to iron from few GV to few TV with an unprecedented accuracy (see Figure 2.4).

The continuous measurement of the low-energy range of GCR fluxes for an entire solar cycle will contribute to a better understanding of the solar modulation and transient phenomena related to the solar activity [92, 44].

AMS has been built to withstand the strong vibrations at the launch (up to 150 dB) and the wide range of temperatures expected during its operations in space, varying between −30 °C and 50 °C. A system of heaters and radiators allows to maintain all sub-detectors and their electronics in

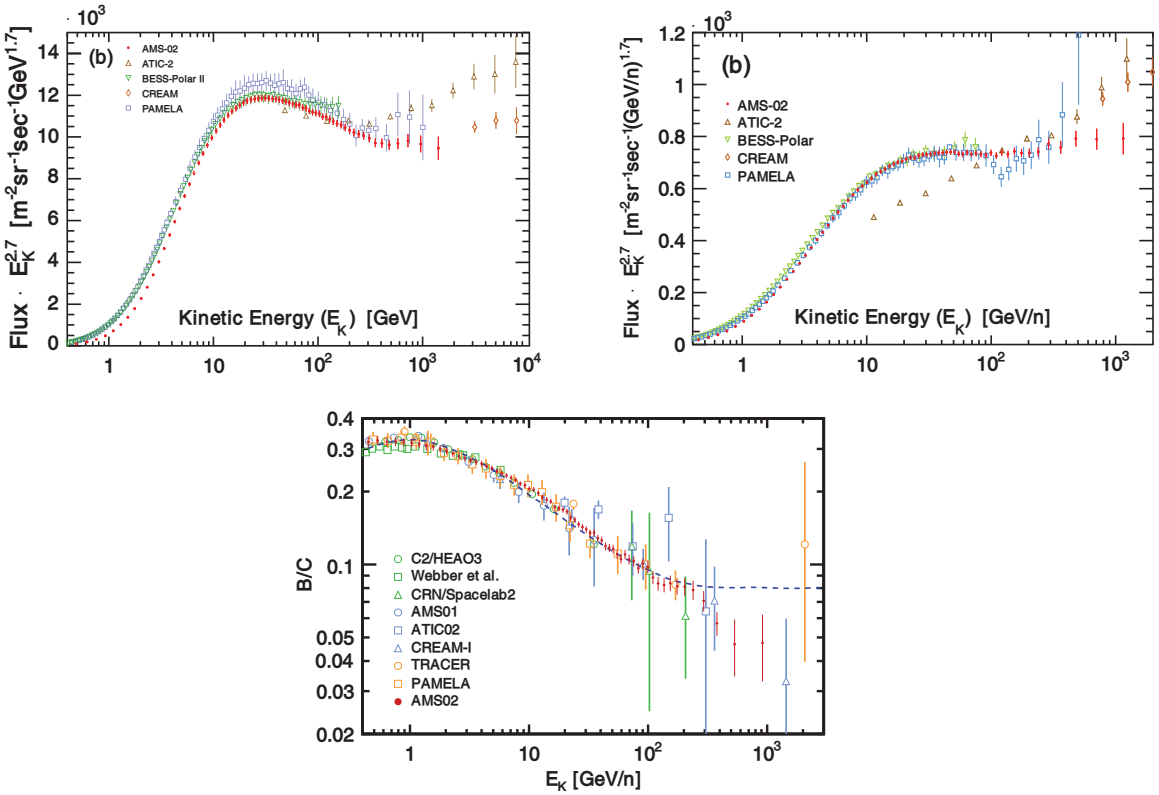

Figure 2.4: **Top left**: Proton flux measured by AMS, compared to the most recent measurements [89]. **Top right**: Helium flux measured by AMS, compared to the most recent measurements [90]. The p and He fluxes change slope around 300 GV: this feature can be ascribed both to GCR acceleration and propagation. **Bottom**: B/C ratio measured by AMS, compared with the most recent measurements [91]. The dashed blue line on top of the B/C ratio is a prediction from a model that explains the positron fraction and $\overline{\mathrm{p}}/\mathrm{p}$ ratio measured by AMS solely by secondary production in GCR propagation. The model is incompatible with the B/C data, strengthening the excess interpretation of the positron fraction.

their operational temperature ranges. To ensure the reliability of the electronics in the high ionizing environment of space, redundancy of each electronic sub-system was implemented. The challenges of operating a high-energy physics experiment in space include also the restriction on the weight imposed by the Space Shuttle (7 t maximum), the low-power consumption due to the ISS supply ($\leqslant 2$ kW) and the limited bandwidth available for transferring data to the ground.

2.1 Transition Radiation Detector

The transition radiation (TR) is a type of electromagnetic radiation emitted when charged particles cross the boundary between two media with different dielectric properties [93]. The probability for a particle to emit a TR X-ray at a single interface is proportional to the Lorentz gamma factor

$\gamma = E/m$ and it's very small ($\approx 1\,\%$), so usually a multi-layer structure is used to increase the X-ray yield, as shown in Figure 2.5.

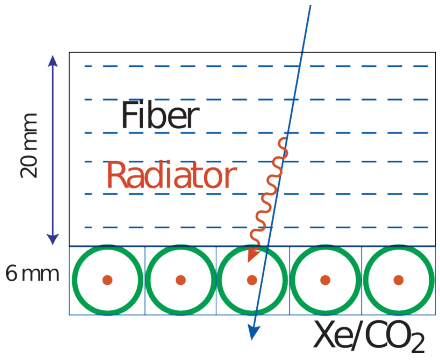

Figure 2.5: Principle of operation of the TRD.

The TRD [94] is located between the first silicon plane of the tracker and the two upper layers of the TOF. It is composed of 328 modules (see Figure 2.6) with lengths between 0.8 m and 2 m. Each module contains 22 mm of polypropylene/polyethylene fiber fleece radiators on top of 16 straw tubes. Each straw tube is a proportional chamber with a diameter of 6 mm, filled with 80 % Xe and 20 % CO_2, and it operates in full avalanche mode (≈ 1.5 kV). A 30 µm thick fine gold-plated wire in the center of the tube acts as anode, while the wall, a 72 µm thick double-layered kapton-aluminum foil, acts as cathode. The multi-layer structure enhances the TR emission up to 50 %.

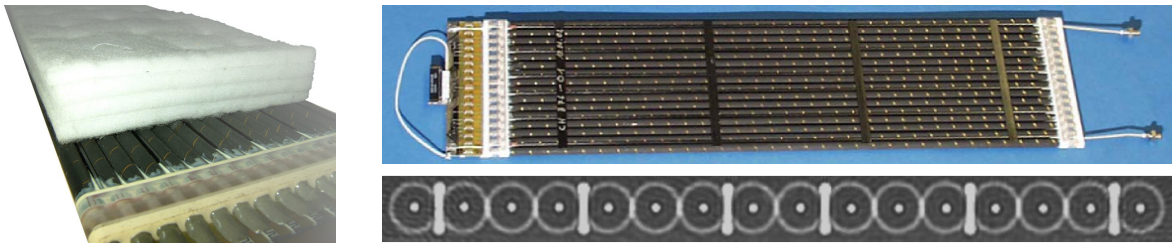

Figure 2.6: **Left**: Close up view of polypropylene/polyethylene fiber fleece radiator layers on top of the straw tubes. **Right**: Straw tubes, with carbon fiber stiffeners placed longitudinally and transversally to stabilize their position.

Modules are arranged in 20 layers inside an octagonal 80 cm height truncated pyramidal structure made of aluminum honeycomb walls and carbon fiber skins and bulkheads. Four layers at the top and at the bottom of the structure are oriented parallel to the AMS magnetic field, while the middle twelve ones are perpendicular to the field, thus providing 3D tracking capabilities.

The straw tubes measure the energy deposited by ionization in the gas mixture and the TR X-rays produced by highly relativistic particles are absorbed by the Xe. Combining the signal of all tubes into a single likelihood estimator, the TRD is able to discriminate between leptons and hadrons up to 1 TeV, attaining a proton rejection factor well above 10^3 below 200 GeV at 90 % $e^{\pm}$ efficiency

(see Figure 2.7). Above 400 GeV, protons start to produce TR and the TRD discrimination power notably decreases.

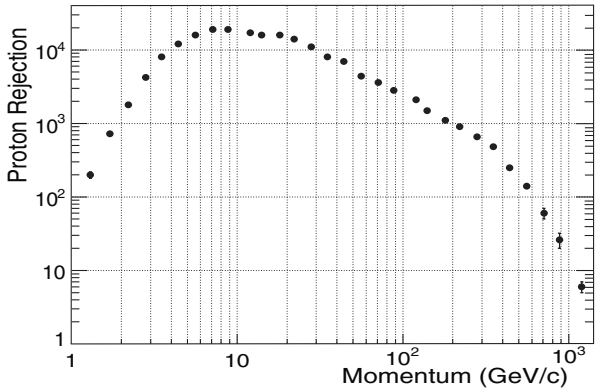

Figure 2.7: TRD proton rejection at 90 % $e^{\pm}$ efficiency, directly measured from data [87].

The CO_2 inside the straw tubes leaks with a rate of 4.5 mbar/day, so a gas supplier system keeps the gas inside the modules at a stable pressure.

2.2 Time of Flight

The TOF system [95, 96] is composed of four roughly circular planes of polyvinyl-toluene scintillating material (see Figure 2.8): two planes are positioned above the permanent magnet (upper TOF) and two below (lower TOF).

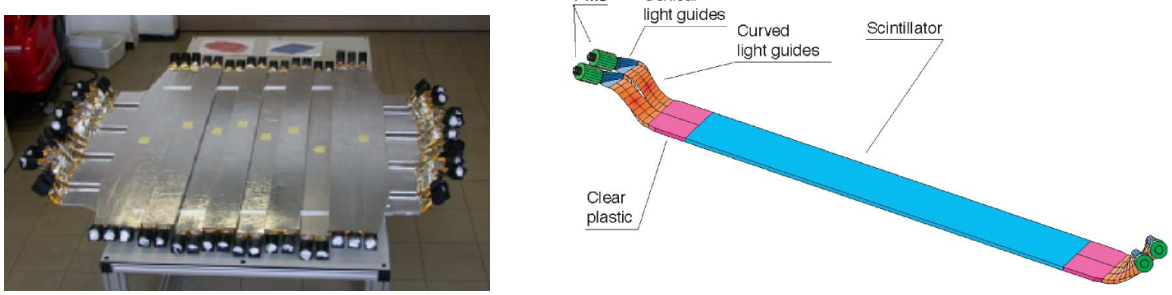

Figure 2.8: TOF sub-detector. **Left**: The upper TOF, with the paddles in the first plane running perpendicular to the paddles in the second plane. **Right**: Structure of a paddle, with the scintillating area, the curved and conical light guides and the photomultiplier tubes (PMTs).

Each plane has a sensitive area of 1.2 m^2 and it's divided into a variable number of 1 cm thick paddles (from top to bottom: 8, 8, 10 and 8). The paddles have a rectangular or trapezoidal shape, depending on whether they are in the middle or at the sides of a plane, and are 110 cm to 134 cm long. They overlap between each other by 0.5 cm to avoid geometrical inefficiencies. For

efficient background rejection and for a rough estimation of the tracks incoming point, paddles in two adjacent planes are perpendicular, providing a $12 \times 12\,\mathrm{cm}^2$ 2D position resolution. Each paddle is read at both ends by two or three fine-mesh PMTs, able to operate in the residual field of the permanent magnet (up to 3 kG). The angle between the PMTs and the light guides with respect to the external magnetic field has been optimized to further reduce the effects of the fringe magnetic field on the light collection efficiency.

The TOF provides the fast trigger for charged particles (see Section 2.8) and, thanks to its excellent time resolution (48 ps for carbon nuclei, see Figure 2.9 left), is able to distinguish down-going particles from up-going ones at a level of 10^{-9}. The TOF measures the particle velocity $\beta c = \Delta s/\Delta t$ using the time of flight Δt between the upper and lower planes and the trajectory length Δs. The velocity resolution has been measured directly from data to be around 4 % for $Z = 1$ nuclei and 1 % for $Z \geqslant 4$. The energy deposited by a particle inside a paddle is used to derive the absolute charge ($dE/\,dx \propto Z^2$). The anode measures up to $Z = 4$, then it saturates and the dynode is used to extend the charge measurement up to $Z = 30$. Figure 2.9 right shows the good charge separation between different nuclei, up to Zn.

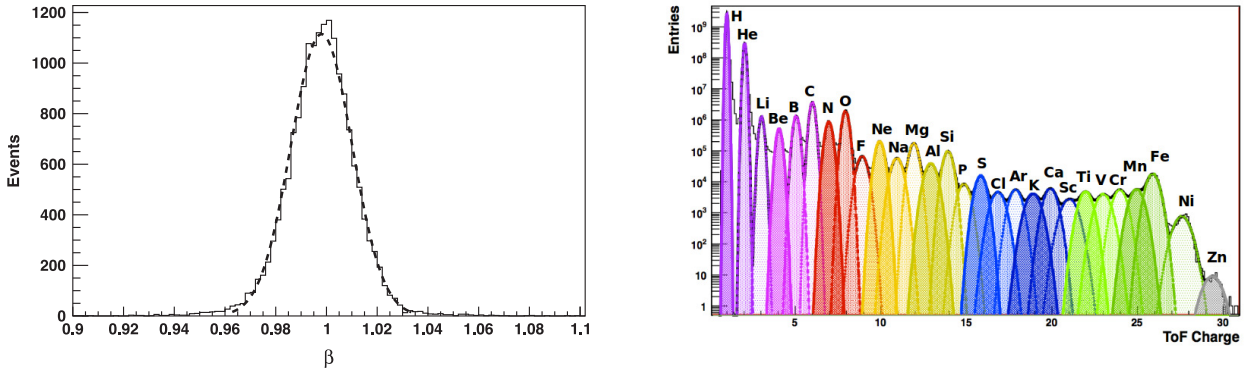

Figure 2.9: **Left**: Measured TOF velocity distribution for carbon nuclei with $R > 20\,\mathrm{GV}$ (solid line). The standard deviation of the gaussian fit (dashed line) is 1.2 %, corresponding to a time resolution of 48 ps. **Right**: Charge distribution of GCRs as measured by the TOF (black line). The colored lines and areas are charge templates from Monte Carlo simulations [97].

2.3 Anti-Coincidence Counter

The ACC [98, 99] is formed by 16 scintillation paddles ($220 \times 830 \times 8\,\mathrm{mm}^3$) arranged on a cylinder surrounding the inner tracker. Wavelength shifter fibers of 1 mm diameter collect the light produced by the scintillators and transport it to 16 PMTs (8 on the top side and 8 on the bottom side) similar to the TOF ones. The ACC has a very high efficiency (99.999 %) in vetoing particles passing through AMS, but not crossing all sub-detectors. This veto is included in the AMS trigger, in order to reject particles outside the tracker acceptance.

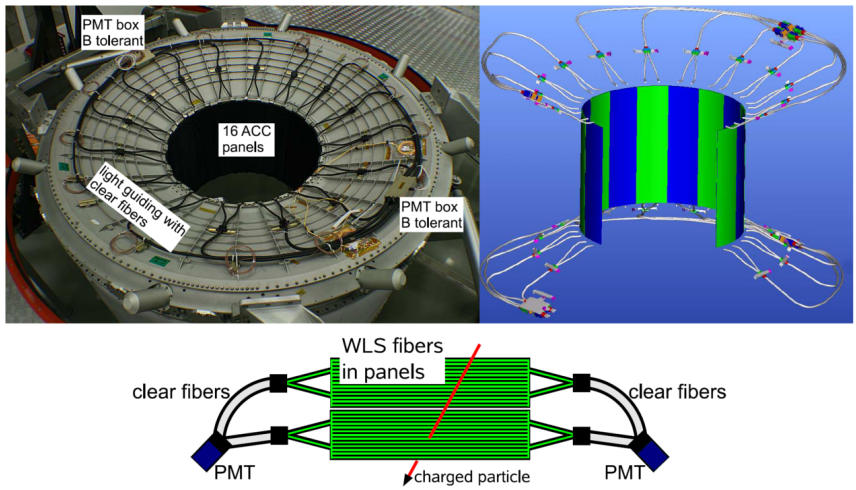

Figure 2.10: The ACC system. **Top**: Scintillating paddles and other components arrangement. **Bottom**: Principle of operation of the ACC [99].

2.4 Permanent magnet

The core of AMS is the permanent magnet. Originally, the experiment was supposed to have a superconducting magnet with a lifetime of 3 years, but the extension of the ISS mission up to 2024 forced the collaboration to re-design the experiment and revert to the permanent magnet already used for AMS-01 [100] (see Figure 2.11). The magnetic field was mapped before the launch and its intensity was found to be unchanged with respect to flight on the Space Shuttle Discovery in 1998.

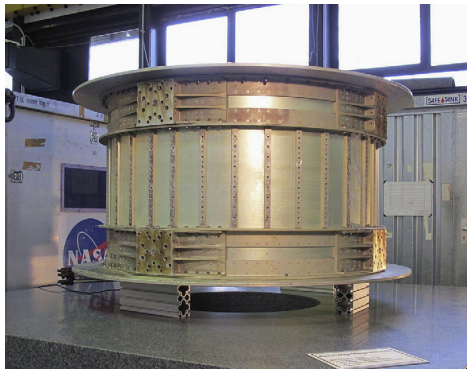

Figure 2.11: The AMS permanent magnet [100].

The magnet is made of 6400 high-grade Nd-Fe-B blocks with dimensions $5 \times 5 \times 2.5\,\mathrm{cm}^3$. The blocks are arranged in a toroidal structure 1 m high with inner and external radius respectively 111.5 cm 129.9 cm. The generated magnetic field has a dipole of 0.149 T inside the magnet and a negligible external field (less than 3 G at a distance of 2 m from the center), to avoid interference with the life support system of the astronauts and mechanical torques on the ISS, in accordance

with NASA requirements. The center of the magnet is the origin of the AMS coordinate system: the Z axis is parallel to the cylindrical symmetry axis of the magnet, pointing to the top of the detector, the X axis is parallel to the magnetic lines and the Y axis completes the right-handed system (see Figure 2.12).

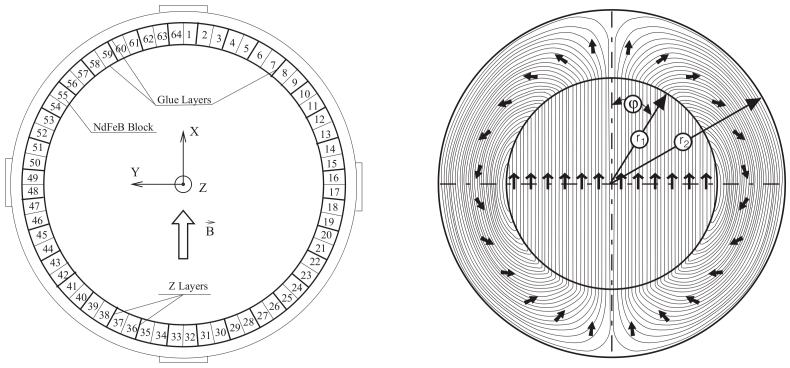

Figure 2.12: **Left**: The AMS magnet blocks configuration and coordinate reference frame. **Right**: Magnetization vector. The magnetic flux is confined within the magnet volume [101].

2.5 Silicon tracker

The AMS silicon tracker (TRK) [102] is the largest spectrometer built for a space-borne experiment; the major challenges were to maintain the required mechanical precision (despite the strong vibrations during the launch) and low-noise performance in this large scale application. The tracker is composed of $72 \times 41 \times 0.3\,\mathrm{mm}^3$ double-sided silicon micro-strip sensors, for a total detection area of $\approx 6.4\,\mathrm{m}^2$. The strips on each face of the sensors run in perpendicular directions, providing a 2D measurement for each sampling. The p-side measures the y coordinate, while the k-side measures the x coordinate. For readout and biasing, the silicon sensors are grouped together in ladders designed to match the cylindrical geometry of the magnet, for a total of 192 units, corresponding to $\approx 200,000$ readout channels. The ladders are installed in 9 layers. 7 layers are placed inside the magnetic field (inner tracker). One external layer is placed on top of the TRD, and the other one is placed between the RICH and the ECAL (see Figure 2.13).

The carbon fiber support structure of the tracker can have excursions up to 30 µm, mostly due to change in thermal conditions, so it is necessary to realign the ladders and the planes. A tracker alignment system (TAS) [104] monitors the movement of the inner tracker layers by using 5 laser beams installed on the layer 2 support structures. The alignment of all the sensors is performed offline using cosmic protons to correct for each sensor shift. With this procedure, the external layers alignment is known with a precision of 3 µm. Each particle trajectory point is determined with an accuracy better than 10 µm in the bending direction (Y), and 30 µm in the non bending one (X) for

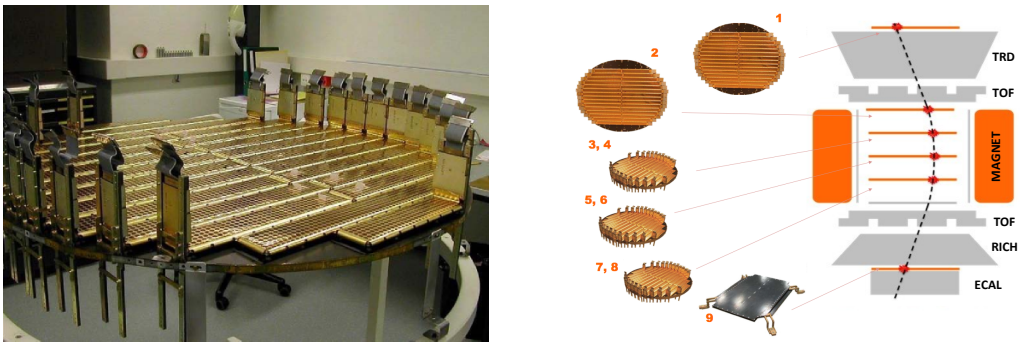

Figure 2.13: **Left**: Layer 2 with ladders and readout channels. **Right**: Arrangement of the silicon tracker layers [103].

$Z = 1$ particles (see Figure 2.14 left). The tracker, like the TOF, provides also charge information up to $Z = 25$ (see Figure 2.14 right).

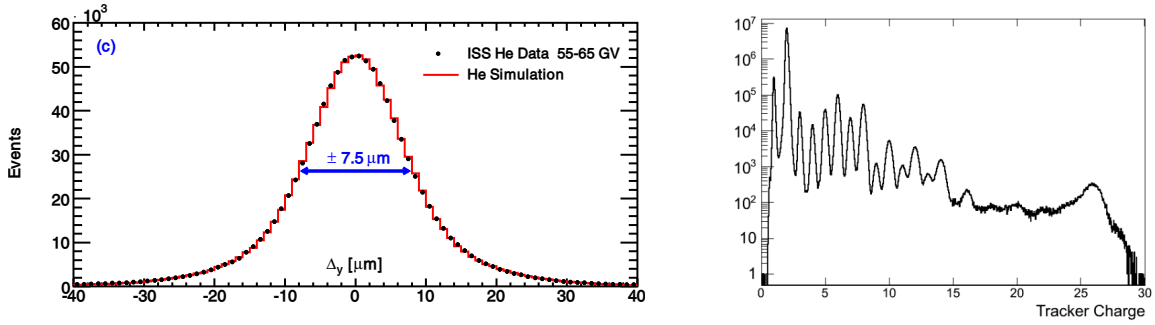

Figure 2.14: **Left**: Difference in the bending coordinate y between the measured position in one layer and the extrapolated position from the track fit using the other layers for He nuclei. The picture shows a very good agreement between real data and simulation [90]. **Right**: Tracker charge estimator measured from data. The misidentification probability from neighbor species is lower than 10^{-6} for carbon, at 99 % selection efficiency [105].

A particle with charge $q = Ze$ and rigidity $R = pc/q$ which moves in a uniform magnetic field B follows an helical trajectory with radius of curvature:

$$\rho = \frac{R}{Bc\sin\theta}$$

where θ is the angle between the particle momentum and B. AMS magnetic field is not uniform, so the trajectory is more complicated, but since B is known, the reconstruction of the full trajectory can be used to obtain R. If σ_{pos} is the spatial resolution of the tracker in the bending direction, l the lever arm inside the magnet (from layer 2 to layer 8) and L the full lever arm (from layer 1 to

layer 9), the relative uncertainty on R can be written as

$$\frac{\Delta R}{R} \propto \frac{R\sigma_{pos}}{BlL}$$

When $\Delta R/R = 1$, the corresponding value of R is called the maximum detectable rigidity (MDR). For the inner tracker, the MDR is around 200 GV for protons and 300 GV for helium, while for the full span the MDR is around 2 TV for protons and 3.2 TV for helium (see Figure 2.15).

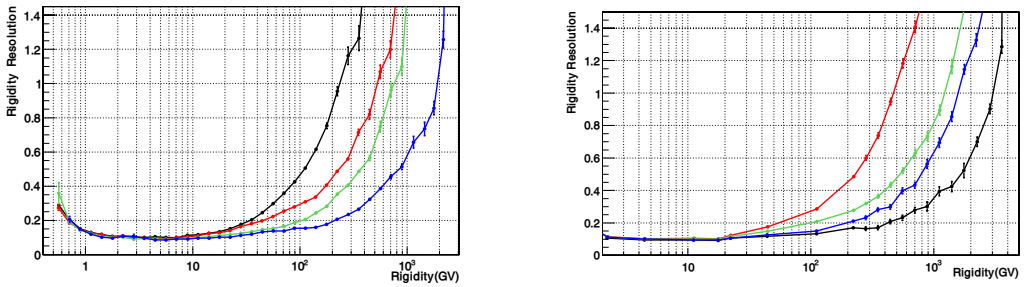

Figure 2.15: Resolution of the rigidity measured by the silicon tracker for protons (**left**) and helium (**right**) estimated from simulations. Different colors refer to different tracker spans. The use of both external layers improves the MDR of the inner tracker by a factor 10 [103].

The tracker is the sub-detector with the highest number of readout channels and thus it produces a lot of heat ($\approx$ 200 W), which must be dissipated before the temperature reaches the maximum working limit of 30 °C. The tracker thermal control system (TTCS) [106] takes care of keeping the tracker ladders and electronics stable within 1 °C. It is a two-phase loop thermal cooling system which pumps liquid CO_2 through thermal bars connected directly to the electronics: the CO_2 absorbs the heat and transports it to dedicated radiators where the now boiling CO_2 cools down.

2.6 Ring Imaging Cherenkov Counter

When a charged particle passes through a material at a velocity greater than the speed of light in that material, Cherenkov radiation is emitted in a cone of aperture angle:

$$\cos(\theta_C) = \frac{1}{\beta n(\omega)}$$

where n is the refractive index of the material. The number of photon N_γ emitted in a range of frequency $d\omega$ and for a traversed length dx is:

$$\frac{d^2N_\gamma}{d\omega dx} = \alpha_{em} Z^2 \sin^2(\theta_C)$$

where Z is the charge of the particle. The RICH [107, 108] can measure both the velocity (with a resolution $\sigma_\beta/\beta \sim 0.1\,\%/Z$) and the absolute charge of the particle (up to $Z = 26$ with a charge confusion less than 10 %), independently from TOF and tracker. Figure 2.16 shows the good agreement in charge measurement between RICH, TOF and tracker.

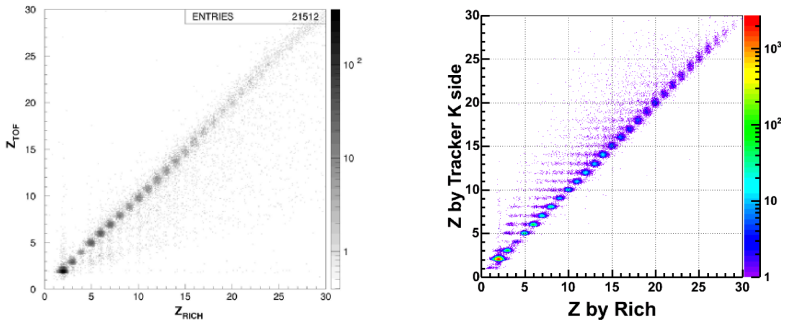

(a) TOF - RICH (b) Tracker - RICH.

Figure 2.16: Correlations between charge measurements from RICH and TOF/tracker.

The RICH has a truncated conical shape. The top plane contains 2.5 cm thick silica aerogel tiles ($SiO_2 : 2H_2O$) with refractive index $n \approx 1.05$ and 5 mm thick NaF blocks with refractive index $n \approx 1.33$. The lower plane hosts 680 4×4 multi-anode PMTs which provide a granularity of $8.5 \times 8.5\,\mathrm{cm}^2$. The lateral surface is covered by a 47 cm high mirror, in order to maximize the acceptance of the emitted photons. Given this structure, up-going particles cannot be detected; as a consequence, the RICH improves the discrimination power of the TOF in the identification of up-going and down-going particles. In the center of the lower plane there is a $64 \times 64\,\mathrm{cm}^2$ hole to let unaffected particles reach the ECAL (see Figure 2.17).

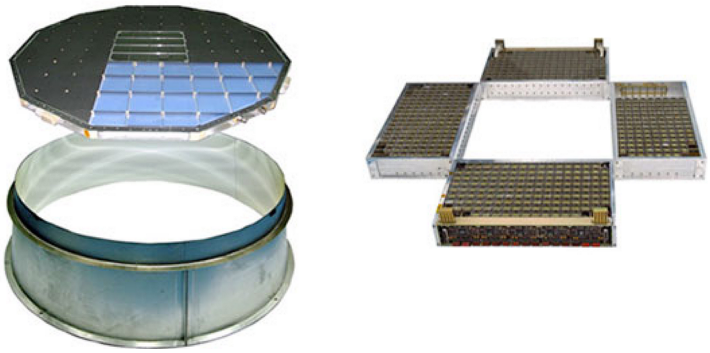

Figure 2.17: RICH exploded view. **Left**: The radiator plane and the conical mirror. **Right**: The detection plane.

2.7 Electromagnetic Calorimeter

The ECAL [109, 110, 111] is a lead-scintillating fiber sampling calorimeter with high granularity, that allows a precise 3D imaging of the longitudinal and lateral profile of the electromagnetic showers, providing a good energy resolution and a hadron rejection.

The ECAL is made of lead, fiber and glue in a volume ratio of 1:0.57:0.15 cm^3; it has an average density of $\sim 6.8\,g/cm^3$ and a radiation length X_0 of about 1 cm. The active volume is built up by 9 superlayers (SLs), each consisting of 11 grooved lead foils (1 mm thick) interleaved by 1 mm plastic scintillating fibers (see Figure 2.18a). Fibers are glued by means of optical cement and are stacked alternatively parallel to the Y-axis (5 SL) and X-axis (4 SL). Each superlayer is designed as a square parallelepiped with 68.5 cm side and 61.5 cm height, for a total active dimension of $68.5 \times 68.5 \times 16.7\,cm^3$, corresponding to $\approx 17X_0$ for perpendicular incident particles. The ratio between the nuclear interaction length and the radiation length is ≈ 26: this ensures that almost 50 % of the hadrons do not interact in the calorimeter.

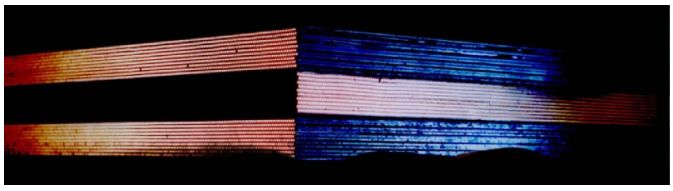

(a) Three superlayers.

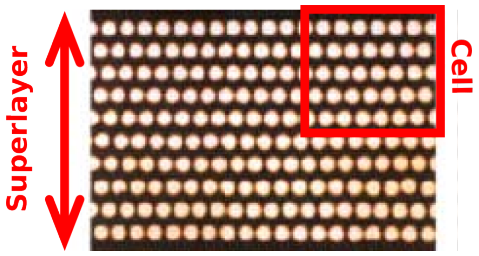

(b) Cross section of the lead-fiber-glue composite structure.

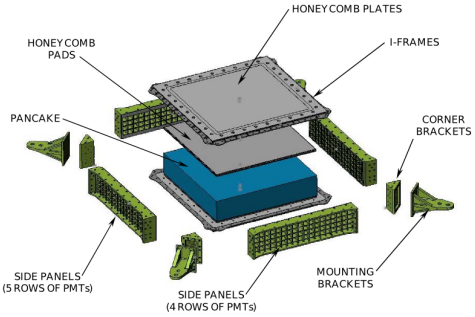

(c) Exploded view of the mechanical support structure.

Figure 2.18: The ECAL structure.

Each superlayer is read out by 36 multi-anode PMTs which have been chosen to fit the ECAL granularity and to work in the magnet fringe field, arranged alternatively on the two opposite ends to avoid mechanical interference. The coupling to the fibers is realized by means of Plexiglas light guides, that maximize light collection and reduce the cross-talk between different channels. Optical contact is enhanced by silicone joints positioned in front of the light guides. Finally, the PMTs are shielded from the magnetic field by a 1 mm thick soft iron square parallelepiped tube, which also acts as a mechanical support for the light collection system. Each anode covers an active area of

$8.9 \times 8.9\,\mathrm{mm}^2$, corresponding to around 36 fibers, defined as a cell, the minimum detection unit (see Figure 2.18b). In total the ECAL is subdivided into 1296 cells (324 PMTs) arranged in a 18×72 grid and this allows for an accurate 3D imaging-sampling of the longitudinal and transversal shower profile.

The PMT high voltage is provided by a custom programmable power supply, which sets the average value around 700 V, corresponding to a gain factor $\sim 2 \cdot 10^5$. Only 240 high voltage channels out of 324 are independent. The front-end electronics and digitization cards are directly located behind the PMT base. In order to obtain the necessary energy resolution on minimum ionizing particles (MIPs) (used for detector performance monitoring and equalization) and to measure energies up to 1 TeV using standard 12 bit ADC, the digitization is performed at two different gains: a high gain mode (HG) for low energy measurements (up to $\sim 2\,\mathrm{GeV}$ per cell) and a low gain mode (LG), when the HG saturates, for the highest ones (up to $\sim 66\,\mathrm{GeV}$ per cell), with a conversion factor $HG/LG \approx 33$. Each PMT last dynode signal is also a readout signal and its information is used to have a redundant signal in case of anode breakdowns.

The energy resolution of ECAL has been measured to be [112]:

$$\frac{\sigma(E)}{E} = \frac{(10.40 \pm 0.02)\,\%}{\sqrt{E(\mathrm{GeV})}} \oplus (1.4 \pm 0.1)\,\%$$

Exploiting the different shape of the showers between leptons and hadrons, the ECAL is able to discriminate $e^{\pm}$ from p. A Boosted Decision Tree algorithm takes into account many properties of the shower (starting point, position of the maximum, lateral width, etc) to define a lepton classifier [113, 114]. The BDT classifier and E/R, the ratio between the energy deposited inside the ECAL and the rigidity measured by the tracker, are used to reject hadrons. Figure 2.19 shows the ECAL proton rejection power, which is independent from the rejection attained by the TRD.

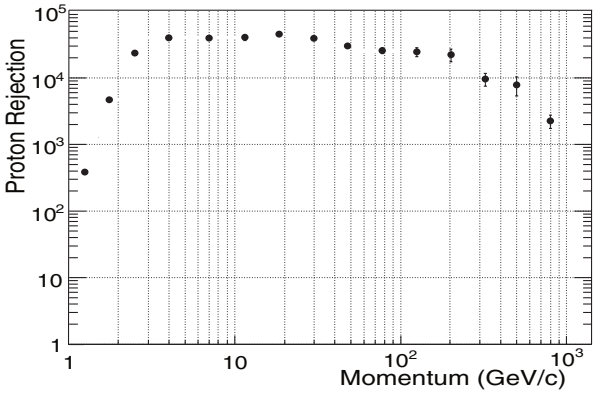

Figure 2.19: Electron/proton rejection measured directly from data using the signals from the ECAL. The rejection factor is well above 10^4 across most of the energy range, remaining above 10^3 at 1 TeV [87].

2.8 Electronics and Data Acquisition

The AMS data acquisition (DAQ) system [115] collect signals from $\approx 300,000$ analog channels, which are then processed by 300 digital signal processors (DSPs), producing 7 Gibit/s. Immediately after the front-end electronics, 264 data reduction boards (xDR, where x stands for a specific sub-detector) apply a fast online algorithm, called zero-suppression, to reduce the amount of data transferred to the ground. The compressed data are then collected by fourteen JINF nodes, which pack all the signals belonging to the same event and send them to the master interface JINJ. The main computer JMDC receives the data from the JINJ and coordinates all the other sub-systems (diagnostics, TRD gas system, power distribution, TTCS). The TOF, ACC and ECAL signals are partly duplicated and sent to the trigger board JLV1, which instructs the JINJ to build the different parts of the event related to each sub-detector. Every computer and connection is at least doubly redundant, except for the JINJ and the JMDC, which are four times redundant. The electronic boards are located in separate radiators, so they can easily exchange the heat produced with the external environment.

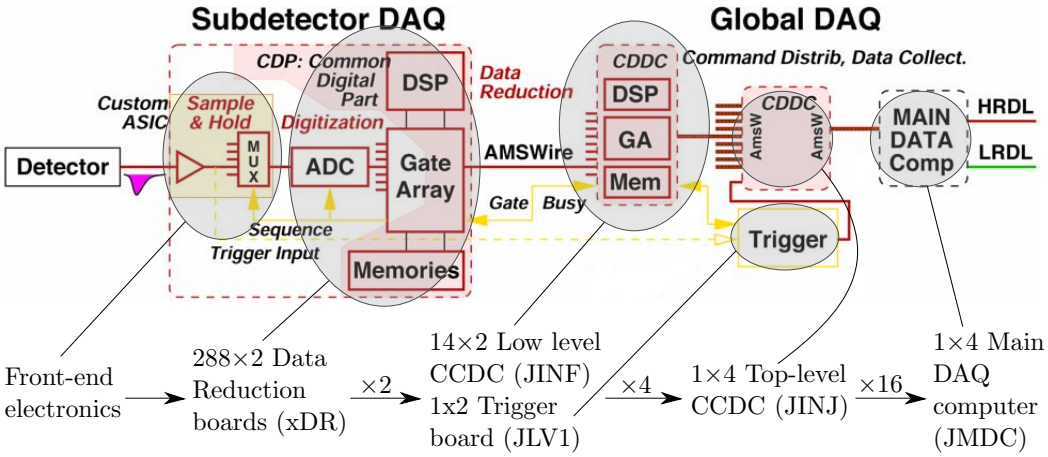

Figure 2.20: The AMS DAQ system. Signals travel from left to right and are processed by the different computers as discussed in the text. The redundancy factor for each electronic board and connection is also shown. Figure adapted from [115].

The AMS trigger recognizes charged particles by a logical combination of TOF, ACC and ECAL responses, producing a fast trigger and a level 1 trigger (LVL1). The trigger system is very flexible, using pre-programmed masks that can be changed from the ground. The LVL1 is divided in seven sub-trigger signals: a single charge (all TOF layers above a high threshold, corresponding to 50 % of a proton MIP, with zero ACC fired), normal ions (all TOF layers above a super-high threshold, corresponding to 400 % of a proton MIP, with no requirements on the ACC), slow ions (same as normal ions, but in a longer time window), electrons (same as single charge, plus energy deposited in the ECAL above threshold in both X and Y projections), photons (same as electrons, but no

requirements on the TOF and the electromagnetic shower axis must point inside the AMS field of view) and finally two unbiased triggers (3/4 TOF layers above high threshold; energy deposited in the ECAL above threshold in any projection) prescaled respectively by a factor 100 and 1000. The JMDC samples the status of the DAQ every 20 ns, thus counting the fraction of time in a second (called the live-time) in which the detector is not busy, *i.e.*, is ready to collect a new event. Figure 2.21 shows how the AMS trigger rate and live-time vary along the orbits of the ISS, because of the Earth's magnetic field. The rate varies between 200 Hz at the Equator to almost 2000 Hz at the magnetic poles and in the South Atlantic Anomaly (SAA). The poles and the SAA are regions with a lower geomagnetic field, thus with a much higher flux of low-energy particles. The live-time is always greater than 90 % except at the magnetic poles and in the SAA. In the SAA, the rate is so high that the AMS DAQ saturates and the live-time goes to zero.

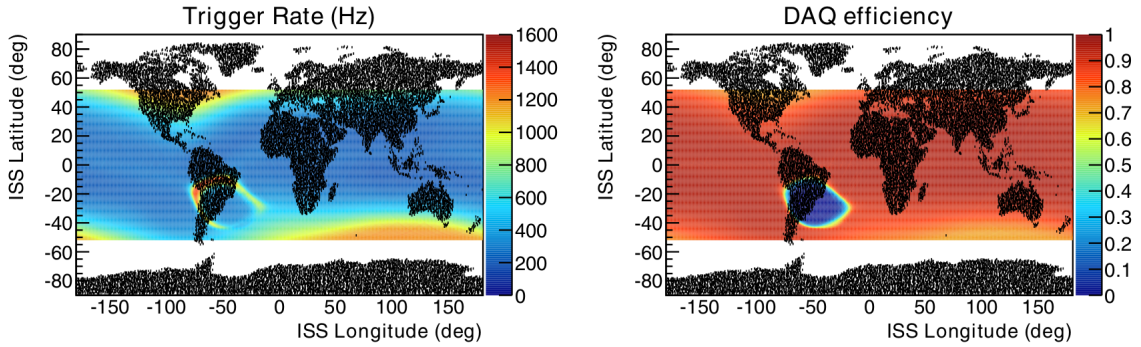

Figure 2.21: **Left**: AMS trigger rate map in geographical coordinates. The increase of particle rate due to the lower geomagnetic field is visible in the SAA (over South America) and at the South and North magnetic poles, respectively below Australia and above Canada. **Right**: AMS live-time map. The decrease due to a higher trigger rate is visible at the magnetic poles. In the SAA, the detector is flooded with so many low-rigidity particles that the live-time falls to zero.

CHAPTER 3
MEASUREMENT OF THE TIME VARIATION OF THE PROTON AND HELIUM FLUX WITH AMS-02

The physical quantity of interest in cosmic ray (CR) physics is the *flux* (sometimes also called *differential intensity*), defined as the number of particles of a given species per unit of time, area, solid angle and energy. Since AMS is a magnetic spectrometer and most of the acceleration and transport processes of CRs involve interactions between charged particles and magnetic fields, it is natural to use rigidity instead of energy, therefore the units of the CR flux measured by AMS are $1/(\mathrm{m}^2\,\mathrm{sr}\,\mathrm{s}\,\mathrm{GV})$. For an ideal detector, measuring a flux simply consists in counting how many particles with a given rigidity cross the detector volume in a chosen time interval. In reality, a detector is never perfect and the measurement of the various particle properties needed for the identification capabilities (energy and/or momentum, velocity, mass and charge) is always affected by many factors that can be intrinsic to the instrument (*e.g.* the quantum efficiency of a PMT or the efficiency of a selection rejecting uninteresting events) or extrinsic (*e.g.* the time-varying magnetic field of the Earth). These effects must be corrected in order to derive the so-called *top-of-the-instrument* flux, which can be directly compared with theoretical predictions. In particular, a continuous measurement of the rigidity is not possible, due to the measurement uncertainties, so usually events are grouped together in rigidity bins, whose width depends on the rigidity resolution of the detector. The ensemble of factors needed to correct the observed counts of particles is usually called *effective acceptance*, with the units of $\mathrm{m}^2\,\mathrm{sr}$. Using dimensional analysis, the formula for the flux Φ in the i-th rigidity bin of width ΔR can be written as:

$$\Phi_i = \frac{dJ_i}{dR} = \frac{N_i}{\Delta R_i\ \Delta T_i\ A_i}, \tag{3.1}$$

where $dJ/\,dR$ is the differential intensity, N is the number of observed particles in the rigidity range $[R,\ R+\Delta R]$, corrected for bin-to-bin migration effects with an unfolding procedure, ΔT is the time interval, more properly called *exposure time*, and A is the effective acceptance.

In the rest of this chapter, the ingredients necessary for measuring the time dependence of the proton flux will be described. The analysis program has been developed mostly by Cristina Consolandi. The main contributions of this work to the analysis were the study of the impact of the digital signal processor (DSP) errors on the exposure time (Section 3.2.1), the study of the energy losses inside AMS (Section 3.6), the flux unfolding (Section 3.7), the estimation of the systematic errors stemming from the rigidity measurement (Section 3.8.1), a model-independent analysis of the time variation of the proton-to-helium ratio (Section 3.10.3) and of the rigidity dependence of the solar modulation (Sections 3.10.1 and 3.10.2).

3.1 The AMS Monte Carlo simulation

The estimation of the absolute normalization of the flux at the top of AMS requires the knowledge of the detection efficiencies of each sub-detector and the overall instrument geometrical factor. An extensive test beam campaign was conducted in 2010 at the CERN SPS[1], using electrons, positrons, protons and pions for different combinations of energy, position and inclination. This allowed the calibration and verification of the performances of the various components. Nevertheless, the number of combinations tested was not enough to directly measure the effective acceptance as needed for the flux computation. Furthermore, the launch and the constantly varying thermal environment of the low Earth orbit introduced changes in the whole detector configuration (*e.g.* the alignment of the tracker layers or the voltage requirements for the PMTs of the TOF, RICH and ECAL). For these reasons, the AMS collaboration developed a Monte Carlo (MC) description of the entire apparatus, based on the GEANT-4.9.6 package [116, 117, 118]. The software simulates the electromagnetic and nuclear interactions of particles with the passive and active material of the detector. The simulated analog signals are then digitized with the same algorithms of the electronic boards, so that the output of the program can be treated as real data. These digital raw data then undergo the same reconstruction process used for the events collected on the International Space Station (ISS).

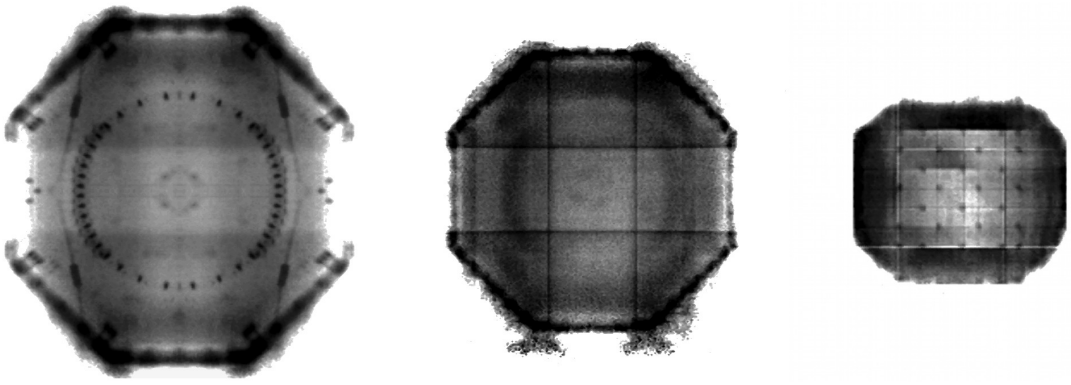

Figure 3.1: AMS hadronic tomography from CR data [119]. The He/p track density ratio at a given position depends on the amount of material traversed up to that point, revealing the distribution of the different materials. **Left**: Slice at $z = 165\,\text{cm}$, corresponding to the first layer of the tracker, just above the TRD. The black dots arranged in circle are the screws of the layer support plane. **Center**: Slice at $z = 132\,\text{cm}$, corresponding to the upper part of the TRD. The vertical and horizontal lines are the bulkheads of the honeycomb support structure. **Right**: Slice at $z = 65.5\,\text{cm}$, corresponding to the area between the first and second plane of the TOF. The black spots are the small mechanical elements that connect the TOF paddles.

A lot of care has been taken in reproducing the instrument materials as close as possible to reality: CAD drawings, blueprints, photos and actual measurements performed during the detector

[1]The Super Proton Synchrotron (SPS) is a circular accelerator situated at CERN (European Organization for Nuclear Research), capable of accelerating protons up to 400 GeV/c.

integration have been used to simulate a copy of all the mechanical and electronics components of AMS. In addition to that, different procedures have been developed by the collaboration to fine-tune the amount of material present in the MC program using galactic cosmic ray (GCR) data. Figures 3.1 and 3.2 show the material distribution inside AMS at different positions, obtained with the techniques of hadronic tomography [119] and TRD vertex reconstruction [120].

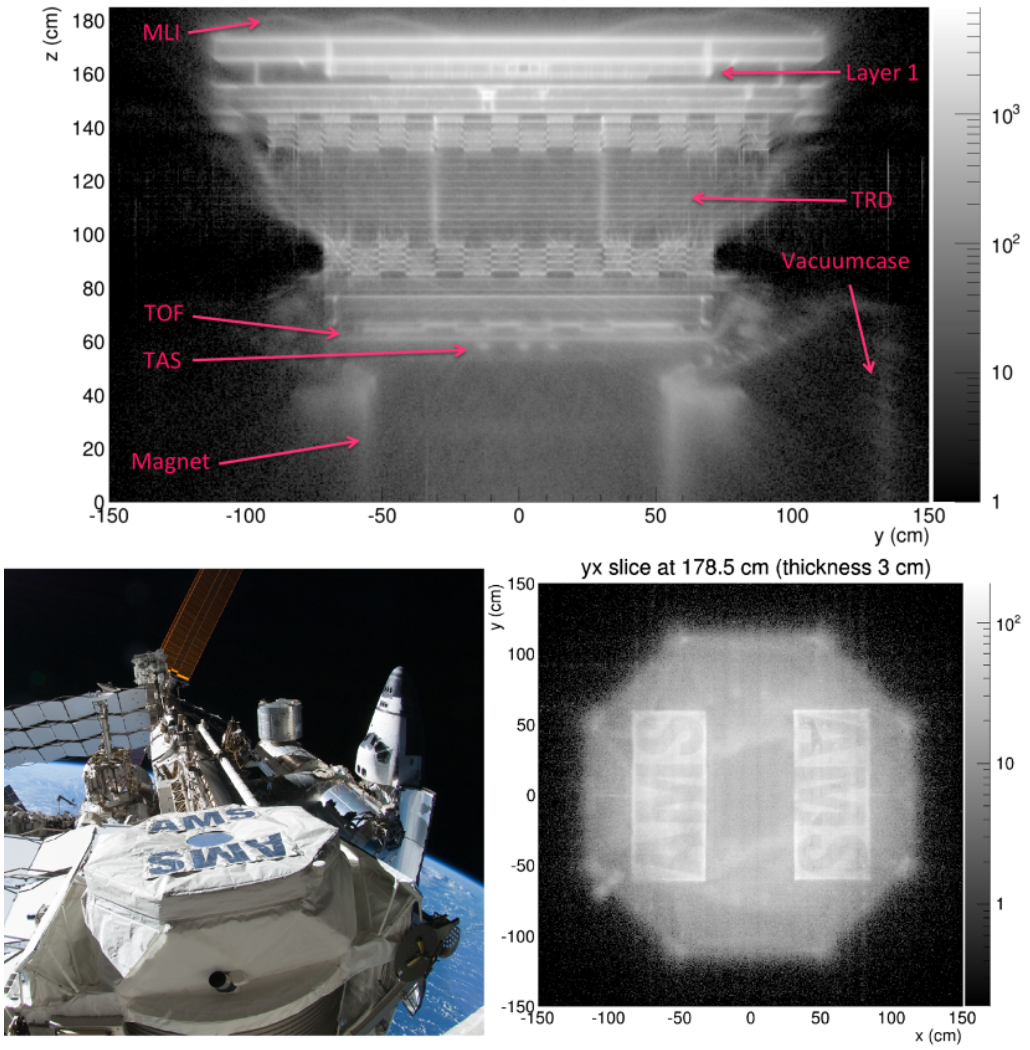

Figure 3.2: Distribution of interaction vertices reconstructed with the TRD from multi-track events. **Top**: Vertical slice showing the material distribution in the upper part of AMS. The main structures are identified by arrows. Fine structures, like the plastic tubes of the TRD, are also visible [120]. **Bottom**: AMS letters on the multi-layer insulation (MLI) cover on top of the detector. The letters appear darker in the right picture because they are cut out of the MLI cover. Credits: A. Bachlechner, RWTH Aachen University.

3.1.1 MC events reweighting

The simulated events have been generated isotropically from a cube concentric to AMS with a side length of 3.9 m. The rigidity interval from 0.5 GV to 4 TV has been divided in three ranges: (0.5–10) GV, (10–200) GV, (200–4000) GV. In each range, the events are generated with a probability proportional to $1/R$, *i.e.* they are uniformly distributed in log space. This choice is a trade-off between the need for a high statistics and a longer computing time at high rigidities, due to the many secondaries produced in inelastic interactions. Ideally, simulating a realistic flux falling as $R^{-2.7}$ would be better to study the detector response, but this would mean having the bulk of the events concentrating at lower rigidities. In order to have enough data at the TV scale, the total MC statistics would need to be so high that the dataset size would quickly become unmanageable. To overcome this problem, the MC generated spectrum can be reweighted with a more natural shape, thus reproducing the correct detector response, while keeping a more or less uniform statistics at all the rigidities and a reasonable dataset size.

Before reweighting the MC, the three ranges must be equalized, so that their different statistics does not introduce discontinuities in the generated spectrum. The probability distribution for the events generated in the range i is $dP/\,dR = k^{(i)}/R$, where $k^{(i)}$ is a normalization constant depending on the statistics of the range. In fact, we have:

$$N^{(i)}_{gen} = \int_{R^{(i)}_{min}}^{R^{(i)}_{max}} \frac{k^{(i)}}{R}\, dR = k^{(i)} \log \frac{R^{(i)}_{max}}{R^{(i)}_{min}} \quad \Longrightarrow \quad k^{(i)} = \frac{N^{(i)}_{gen}}{\log\left(R^{(i)}_{max}/R^{(i)}_{min}\right)}, \tag{3.2}$$

where $N^{(i)}_{gen}$ is the total number of generated events in the range, and $R^{(i)}_{min}$ and $R^{(i)}_{max}$ are, respectively, the minimum and maximum rigidity of the range. We can now choose a reference normalization k_{ref} to which equalize all the ranges: each event will be assigned a weight $w^{(i)}_{eq} = k_{ref}/k^{(i)}$. It's important to retain the original information about the number of events generated in each rigidity bin, otherwise we could simply get a statistical error equal to zero by simply choosing a huge value for k_{ref}: this, of course, would be wrong, since the statistical fluctuations present in the MC depends on $k^{(i)}$ and not on k_{ref}. Once all the ranges have been equalized, we can finally reweight the generated spectrum with a given shape. Let $\Phi(R)$ be the flux we want to simulate in the MC; then each event will have a weight $w^{(i)}_{flux}(R) = w^{(i)}_{eq}\Phi(R)R$, where the R multiplying Φ is there to remove the original $1/R$ probability distribution. Finally, the histogram of the generated events can be obtained by setting the content of each rigidity bin j to:

$$N^{(i)}_{gen,flux}(R_j,\, R_{j+1}) = w^{(i)}_{eq} \int_{R_j}^{R_{j+1}} \Phi(R)\, dR \;= \sum_{R_j \leqslant R < R_{j+1}} w^{(i)}_{flux}(R), \tag{3.3}$$

where R_j and $R_{j+1} = R_j + \Delta R_j$ are, respectively, the edges of the bin and $N_{gen,flux}$ is the number of generated events distributed as the chosen flux Φ. Figure 3.3 shows an example of MC reweighted

spectrum. The different statistics of the three ranges is clearly visible. The histogram of generated events is not exactly uniform in each range, because the chosen binning is based on the tracker resolution, which yields a rigidity dependent bin width different than for a uniform logarithmic binning. The overall normalization k_{ref} has been chosen in such a way that the total statistics of the three ranges is the same for both histograms, *i.e.* $k_{ref} = \sum_i N_{gen}^{(i)} / \log(4\,\mathrm{TV}/0.5\,\mathrm{GV})$.

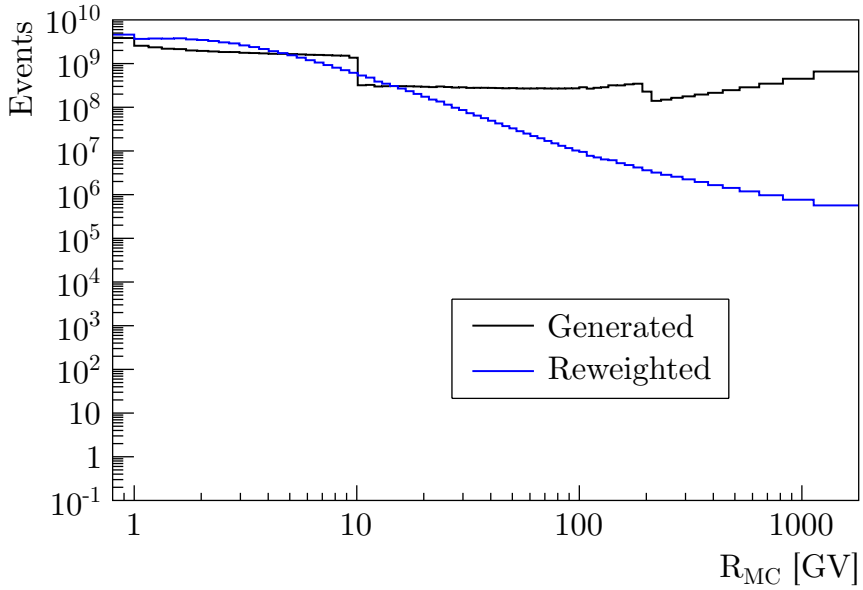

Figure 3.3: Comparison between generated (black) and reweighted (blue) spectrum of the MC. The discontinuities in the generated spectrum are due to the different statistics of the three MC ranges, which are instead equalized in the reweighted spectrum.

The reweighting will play also a fundamental role in the unfolding procedure, as described in Section 3.7.

3.2 Exposure time

The periods in which the data acquisition (DAQ) was busy reading the signals from the front-end electronics following a triggered event must be excluded from the time interval used to normalize the number of observed particles. AMS measures directly its live-time on a second basis, so the exposure time is simply the sum of the live-time of all the seconds considered in the analysis. A number of cuts are applied, to remove seconds in which the flux measurement could be unreliable:

1. **Only "vertical" runs**. The ISS attitude (*i.e.* its orientation with respect to the direction of motion) varies in time, depending on many factors, like: the docking of a Soyuz spacecraft or other vehicles launched from Earth; a reboost, to maintain the station at a safe altitude[2]; a

[2]The residual atmosphere at an altitude of 400 km is usually considered negligible, but the drag is enough to affect

debris avoidance maneuver, to avoid collision with other objects (usually space junk) crossing the path of the station. During these changes of attitude, the AMS pointing direction can shift from outer space to the Earth limb or even to Earth itself. To discard these uninteresting periods, the AMS vertical is required to be within 25° from the zenith.

2. **Live-time $>$ 0.5**. A low live-time is characteristic of a high particle rate, which can affect negatively the trigger efficiency and lead to more complicated multi-particle events. Usually this happens at the geomagnetic poles following the arrival of solar energetic particles (SEPs) or during a geomagnetic storm.

3. **South Atlantic Anomaly (SAA) exclusion**. For the same reason, the SAA is geometrically excluded. In this region, the rate of low-rigidity particles can be so high that the live-time sometimes falls to zero.

4. **Good alignment of the external layers**. The constantly changing temperature of the surrounding space induces thermal contractions and expansions of the detector support structure, in particular for L1 and L9. Since the tracker alignment system (TAS) is only available for the inner tracker, GCRs are used to keep the external layers aligned to the inner layers. Two different algorithms exist in the collaboration: when the difference between the two alignments is larger than 35 µm for L1 and 45 µm for L9, the second is rejected, to avoid badly reconstructed tracks.

5. **No bad runs**. Especially at the beginning of the mission, some runs were devoted to trigger efficiency studies, so they are not usable for a physics analysis.

AMS is immersed in the Earth's magnetosphere, which alter the trajectories of the CRs (see Figure 3.4). In order to be sure to collect only primary GCRs, *i.e.* coming from outside the geomagnetosphere, the rigidity of a particle must be above the local geomagnetic cutoff. The rigidity cutoff is defined as the minimum rigidity that a particle must have to reach a given position from a given direction. Since the AMS angular aperture is wide, a particle is considered primary if its rigidity is above the maximum cutoff inside the field of view (FOV). The geomagnetic cutoff depends on the position of the ISS. A map of the rigidity cutoff has been computed by the collaboration by backtracing particles in the Earth's magnetic field, described with the IGRF model. Short time scale variations of the geomagnetosphere, for example induced by the arrival of a coronal mass ejection (CME), are not included in the magnetic field model, but for the purpose of the monthly flux measurement they are not important. A safety factor of 1.2 is applied to the maximum cutoff, to take into account small changes of the real cutoff with respect to the computed map and the uncertainty in the measured rigidity and to completely exclude the penumbra region, where both primary and secondary particles are allowed to enter the FOV. The geomagnetic cutoff effectively forbids

the ISS orbit over a period of one month.

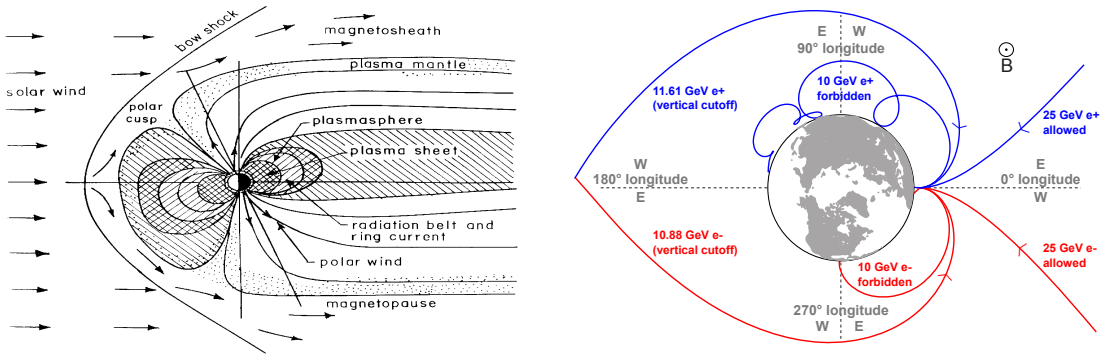

Figure 3.4: **Left**: The Earth magnetosphere [121]. Different regions arise from the interactions of the geomagnetic field with the solar wind and the surrounding particle environment. The day side is flattened by the constant push of the solar wind, while the night side extends in a long magnetotail. **Right**: Trajectories of charged particles (positrons in blue, electrons in red) inside the magnetosphere. Low-energy particles remain trapped or are swooped out before reaching Earth, while high-energy particles are able to penetrate at lower altitudes. Figure adapted from [122].

primary GCRs below a certain rigidity to reach AMS, depending on its position around the Earth. To correct for this effect, the exposure time is computed separately for each rigidity bin: only the seconds in which the lower bin edge is above the maximum cutoff are counted for that bin. Figure 3.5 shows the exposure time as a function of rigidity: the exposure time monotonically increases with rigidity, until it reaches a constant value around 30 GV, corresponding to the maximum cutoff along the ISS orbits.

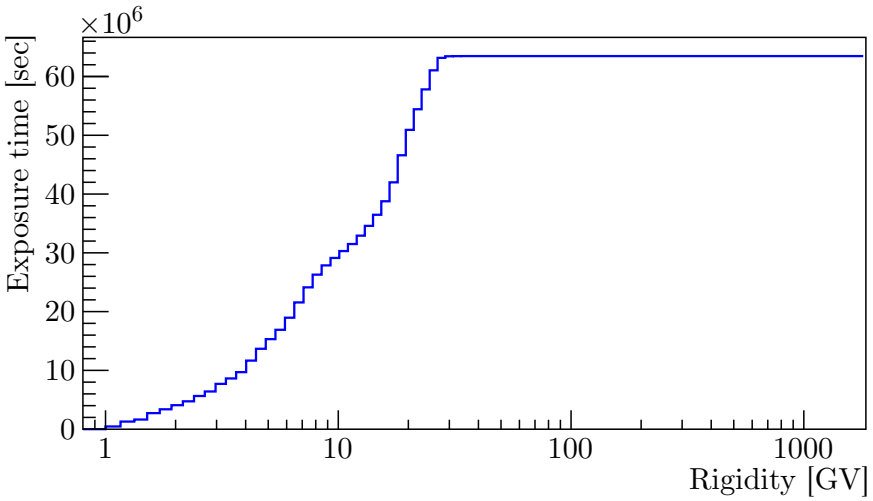

Figure 3.5: AMS exposure time for the period from May 20, 2011 to November 26, 2013. The rigidity dependence is due to the geomagnetic cutoff, which forbids low-rigidity particles to reach AMS position.

3.2.1 DSP errors

Charged particles passing through a microelectronic circuit can cause errors called single event effects (SEEs). A short-circuit between the p and n substrate of a semiconductor can be created by the ionization track induced by a heavy ion or by the recoil of a proton interacting with the nuclei of the circuit. SEEs can be classified in three categories: single event upsets (SEUs), transient soft errors, like a bit flip, which can be recovered by resetting or rewriting the affected device; single event latchups (SELs), hard errors, in which the generated current is above the device working limit, requiring an immediate power reset to avoid permanent damage; single event burnouts (SEBs), in which the induced high current destroys immediately the device.

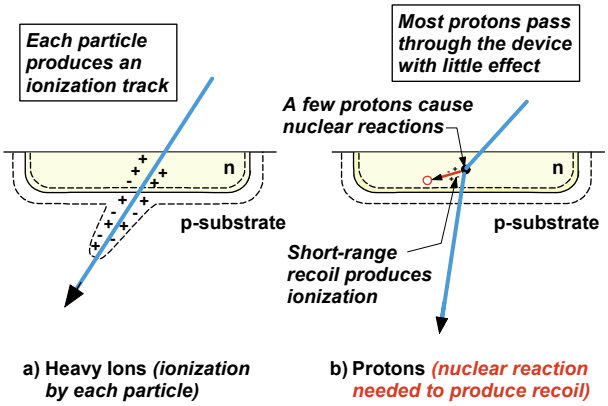

Figure 3.6: SEEs in microelectronic circuits caused by heavy ions (**left**) and interacting protons (**right**) [123].

All AMS electronics have been qualified in multiple heavy ion beam campaigns, which lead to the choice of the most radiation-resistant devices: only components with an expected SEU and SEL rate less than one per day were accepted for integration. The xDRs, JINJs, JINFs and JMDCs contain DSPs which digitize and compress the data from the different sub-systems. At the end of each run (roughly every 23 minutes), a CRC test (CRC-16-CCITT) is performed on the program memory of all DSP nodes. If an error is detected, the failed node is rebooted as soon as possible, but only if the ISS is in an equatorial zone, where the particle rate is lower due to the higher geomagnetic cutoff. For this reason, the exact time of the error is not known: it could have happened anytime between the last successful test and the failed one. Depending on the affected node, a DSP error could influence the result of the analysis during the period when the program memory was modified: it's clear that an error in the JMDC could be potentially more dangerous that an error in a sub-detector data reduction board. It is therefore necessary to study how the DSP errors are distributed in time and geographical position and which nodes are most sensitive to SEEs.

Figure 3.7 shows the daily distribution of DSP errors: on average, there are 1.5 errors per day, with a constant trend in time. The difference in 2011 with respect to the rest of period is due to

the fact that at the beginning of the mission the DSP test procedure was not yet automatic.

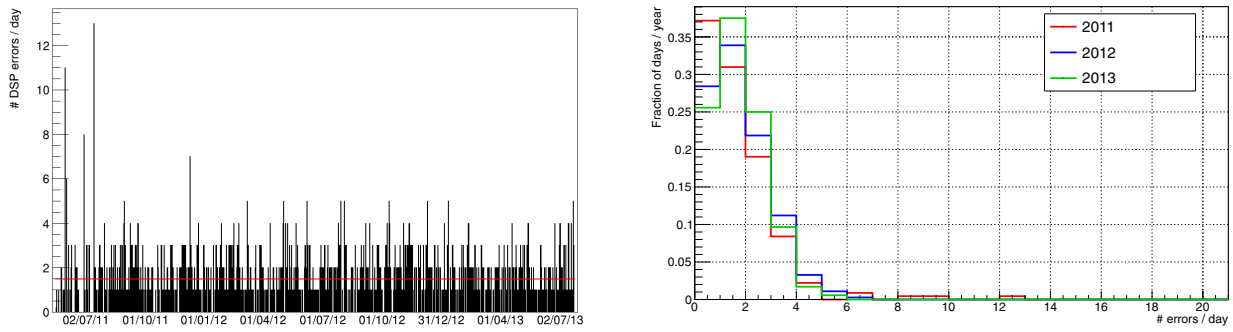

Figure 3.7: Distribution of number of DSP errors per day. **Left**: Time dependence of the daily distribution. **Right**: Daily distribution for different years.

Figure 3.8 shows how the errors are distributed among different categories of electronic boards: detectors, trigger (JLV1) and main computers (JINJ). 80 % of the errors are related to the tracker, since it has the largest number of xDRs (208). Normalizing the number of errors to the number of DSP per category, the error rate is more or less similar for all categories, except for the tracker and the RICH which display a higher sensitivity to radiation effects.

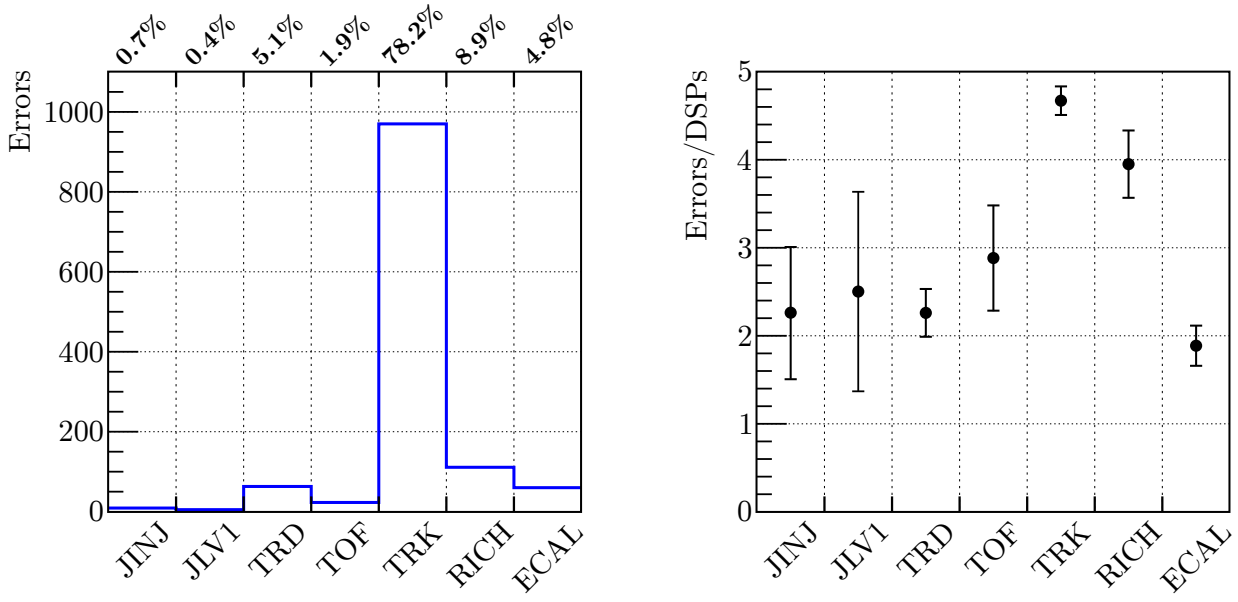

Figure 3.8: Distribution of DSP errors for different electronic board categories. **Left**: Absolute number of errors in each category. **Right**: Number of errors per DSPs in each category.

Since the time of the error is not known, we can assign a uniform probability for the error to have happened in any second of the period between a successful and a failed test. This usually corresponds to a quarter of an orbit. Figure 3.9 shows the position of the ISS during this period,

normalized by the total time spent by the ISS in each position. The map indicates a clear excess of errors in a region overlapping with the SAA, which is understandable, since it's where the highest particle rate is recorded. Overall, 50 % of the errors happen during orbits passing through the SAA. The remaining 50 % is distributed in the geomagnetic poles (35 %) and in the equatorial region (15 %), which is consistent with the expectation that the DSP error rate is proportional to the particle rate.

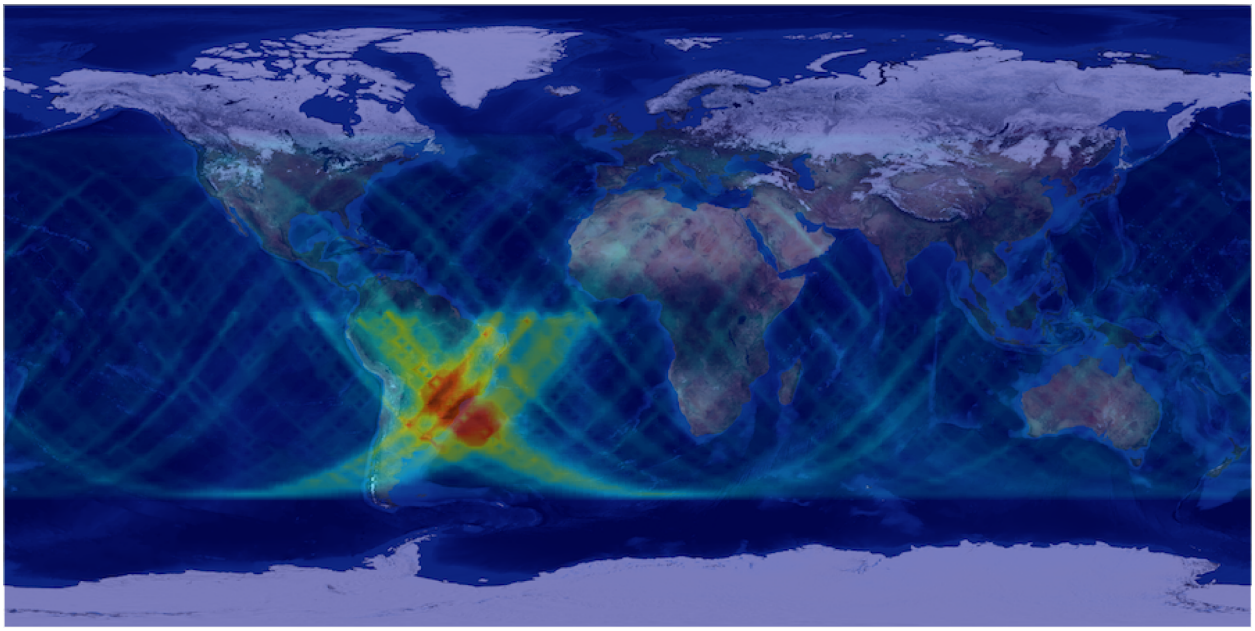

Figure 3.9: Heat map of the DSP error rate: red shades represent a high probability of having an error, while blue shades represent a low error rate.

Since the SAA is excluded from the flux analysis, the DSP error rate drops to 0.75 per day. Also, the amount of time spent in the polar regions is only 20 % of all the time, so the error rate becomes much smaller than 1 per day. Most of the errors come from a tracker reduction board, but no performances difference was seen for events with hits from ladder managed by failed nodes with respect to events with no error, so we can conclude that there's no need for cutting seconds with DSP errors, *i.e.* the exposure time is not affected by SEEs.

3.3 Trigger efficiency

AMS has two triggers dedicated for the measurement of the trigger efficiency directly from data: the unbiased TOF and ECAL triggers. The unbiased triggers are designed to have an efficiency much higher than 99 %, by requiring only 3 out of 4 TOF planes with a signal, contrary to the physical (or biased) triggers which must have a signal in all four planes. Since the preselection requires the charged trigger bits set, the unbiased ECAL trigger has not been used in the analysis. To evaluate

the trigger efficiency, the physical trigger request has been released from the selection, so that after the last cut both biased and unbiased events are in the data sample. The trigger efficiency can then be computed with the following formula:

$$\varepsilon_{trg}(R,\, R+\Delta R) = \frac{N_b(R,\, R+\Delta R)}{N_b(R,\, R+\Delta R) + f_s N_u(R,\, R+\Delta R)}, \tag{3.4}$$

where N_b and N_u are the number of selected protons in the rigidity range $[R,\, R+\Delta R]$ with, respectively, physical and unbiased trigger bits. These two triggers are exclusive, so the two samples are disjoint. Since the unbiased TOF triggers are prescaled with a factor $f_s = 100$, we have $N_u \ll N_b$, so that the error on the trigger efficiency is driven by the low statistics of the unbiased triggers, especially at high rigidities. For each rigidity bin, the error on ε_{trg} has been computed in the following way. First, let's define $\varepsilon^*_{trg} = N_b/(N_b + N_u)$. The uncertainty on ε^*_{trg} is obtained by the usual error propagation formula:

$$\Delta\varepsilon^*_{trg} = \sqrt{\left(\frac{\partial\varepsilon^*_{trg}}{\partial N_b}\Delta N_b\right)^2 + \left(\frac{\partial\varepsilon^*_{trg}}{\partial N_u}\Delta N_u\right)^2} = \sqrt{\frac{N_u^2 N_b + N_b^2 N_u}{(N_b+N_u)^4}}, \tag{3.5}$$

where N_b and N_u are treated as Poisson variables. From Equation 3.4, we can find N_b as a function of f_s:

$$N_b = \varepsilon_{trg}(N_b + f_s N_u) \quad \Longrightarrow \quad N_b = f_s N_u \frac{\varepsilon_{trg}}{1-\varepsilon_{trg}}. \tag{3.6}$$

Plugging this expression in the definition of ε^*_{trg}, we have:

$$\varepsilon^*_{trg} = \frac{N_b}{N_b+N_u} = \frac{\varepsilon_{trg} f_s}{1+\varepsilon_{trg}(f_s-1)} \quad \Longrightarrow \quad \varepsilon_{trg} = \frac{\varepsilon^*_{trg}}{f_s - (f_s-1)\varepsilon^*_{trg}}. \tag{3.7}$$

We can now propagate the error from ε^*_{trg} to ε_{trg}:

$$\Delta\varepsilon_{trg} = \left|\frac{\partial\varepsilon_{trg}}{\partial\varepsilon^*_{trg}}\Delta\varepsilon^*_{trg}\right| = \frac{f_s}{\left[f_s - (f_s-1)\varepsilon^*_{trg}\right]^2}\Delta\varepsilon^*_{trg}. \tag{3.8}$$

Figure 3.10 shows the trigger efficiency measured directly on data, together with the spline fit used to smooth out the statistical fluctuations. The efficiency starts at 95 % at low rigidities and decreases at 92 % around 6 GV. In this rigidity range, the charged trigger from the ECAL kicks in, because protons have enough energy to create a hadronic shower with signals above the trigger thresholds. The efficiency remains stable around 94 % up to 300 GV, where it starts decreasing down to 90 % at 1 TV. This decrease is due to the secondaries, produced by inelastic interactions, crossing the anti-coincidence counter (ACC) paddles, which impose a veto on the trigger in order to have clean proton events.

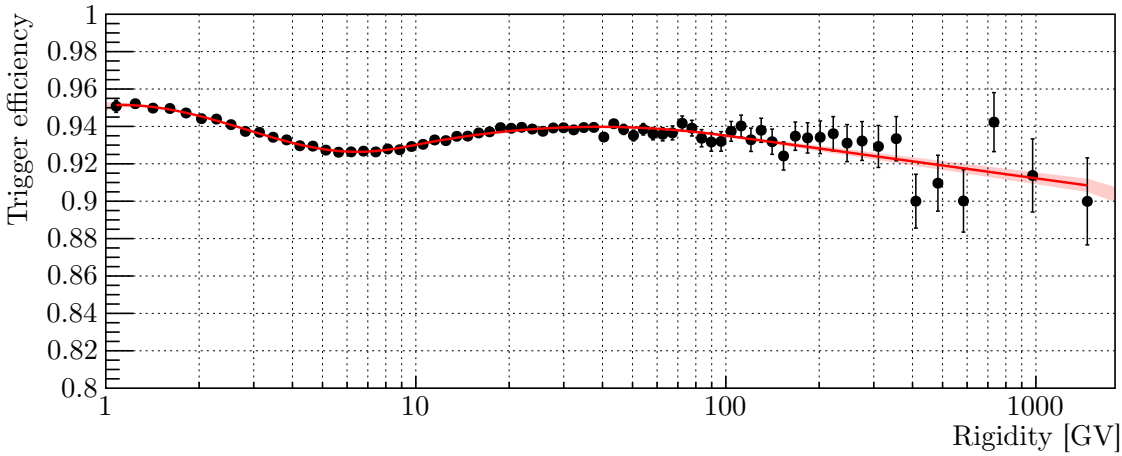

Figure 3.10: Trigger efficiency measured on data (black dots) and its spline parametrization (red). The pink band is the confidence interval around the fit.

3.4 Data selection

The key step in the flux calculation is the selection of good proton events among all the particles collected by the detector. Protons are the most abundant species of GCR, so their selection is not overly complicated. First, a loose set of cuts, called *preselection*, is used to get rid of spurious, misreconstructed or uninteresting events. Every selected event is required to have:

1. **Charged trigger**. The bits associated with trigger coming from TOF signals must be set. This cut rejects events in which the trigger originates only from the ECAL, like photons or out-of-acceptance charged particles.

2. **Reconstructed particle**. During the event reconstruction phase, common to all the collaboration, every sub-detector identifies clusters of signals, following different algorithms (*e.g.* adjacent cells from ECAL with signal above a certain threshold or aligned straw tubes in different layers of the TRD), building low-level objects like `TRDTrack`, `TOFTrack`, `TRKTrack`, `EcalShower`[3], etc. These objects are then grouped into particles, trying to associate the various clusters in many combinations: for example, a `TOFTrack` and a `TRDTrack` are assumed to come from the same particle if their trajectories matches within certain limits, both in position and direction. Basically, all of the events have at least one particle, so this cut rejects only badly reconstructed events. The majority of the events ($\gtrsim 90\,\%$, depending on the rigidity) have only one particle; in case more than one particle is reconstructed, the particles are sorted according to their quality (*e.g.* particles with a `TRKTrack` are better than particles without

[3] A `TRDTrack` is a track built from aligned tubes in different TRD layers. A `TOFTrack` is a track built from aligned clusters in different TOF planes, matching also in time. A `TRKTrack` is a track built from hits in different tracker layers, arranged along a fitted trajectory. An `EcalShower` is a collection of cells from different ECAL layers, with deposited energy above a given threshold and with an angular matching.

it) and the first one is selected. The probability of having multiple particles triggering AMS at the same time is negligible, except when the ISS is close to the geomagnetic poles or in the SAA, so most of the time an event with more than one reconstructed particle is due to clusters misassociation or particle fragmentation on the instrument material.

3. **Good `TOFTrack`**. A downgoing `TOFTrack` built with clusters from at least 3 out of 4 TOF planes, with measured $\beta > 0.3$ (corresponding to $R \gtrsim 300\,\mathrm{MV}$). The `TOFTrack` must point within the geometrical acceptance of the external layers of the tracker (from now on called L1 and L9) and must be associated with the particle `TRKTrack`, *i.e.* the `TRKTrack` extrapolated in the TOF planes must match with the position of the clusters used by the `TOFTrack`. In addition, the number of TOF clusters associated to the `TOFTrack` matching in time must be at most 4: this cut ensures that around the selected `TOFTrack` there are no other clusters that could confuse the velocity measurement.

4. **`TOFTrack` charge consistent with 1**. The charge measured by the selected `TOFTrack` in the two bottom TOF planes – from now on called lower TOF (LTOF) – must be between 0.5 and 3. The lower cut is needed to reject events with misreconstructed charge. The upper cut allows to select also helium events, since their preselection is the same as for protons.

After the preselection, another set of cuts, called *selection*, is applied, to ensure the presence of a well-reconstructed `TRKTrack`, with a good rigidity measurement, and a high purity proton sample.

1. **Physical trigger**. The trigger must be biased, *i.e.* 4 out of 4 TOF planes have been used to build the trigger (see Section 2.8).

2. **Inner tracker `TRKTrack`, consistent with charge = 1**. The selected `TRKTrack` must have at least 3 hits on different layers of the inner tracker (layers 2 to 8) compatible with the fitted trajectory. The charge measured by the combined signals of all the associated inner tracker hits must be between 0.7 and 1.5.

3. **Good full-span `TRKTrack`, consistent with charge = 1**. The selected `TRKTrack` must have one hit in L1 and one in L9, with measured charge between 0.6 and 1.9 in both the external layers. The fitted trajectory (called full-span track) must have $\chi^2/\mathrm{dof} < 10$.

4. **Mass cut**. A cut in the $\beta - R$ plane which suppresses the contamination of pions below 2 GV produced by the interactions of GCRs with the upper part of AMS above L1.

3.5 Acceptance

The effective acceptance is computed repeating the analysis on the MC generated proton datasets and counting how many events passed the preselection and selection cuts:

$$A_{eff}(R,\ R+\Delta R) = A_{geom}\frac{N_{sel}(R,\ R+\Delta R)}{N_{gen}(R,\ R+\Delta R)}, \tag{3.9}$$

where A_{geom} is a geometrical factor, in units of $\mathrm{m}^2\,\mathrm{sr}$, and N_{gen} and N_{sel} are, respectively, the number of generated and selected events in the rigidity range between R and $R+\Delta R$. The geometrical factor depends on the geometry and angular distribution chosen for simulating the events: for downgoing events generated isotropically from a single face of a cube with a side length l, we have:

$$A_{geom} = \int_S \int_\Omega \hat{r}\cdot d\vec{S}\, d\Omega = l^2 \int_\Omega \cos\theta \sin\theta\, d\theta\, d\phi = l^2 \int_0^{2\pi} d\phi \int_0^1 \cos\theta\, d\cos\theta = \pi l^2, \tag{3.10}$$

so that, with $l = 3.9\,\mathrm{m}$, the generating geometrical factor is $\approx 47.78\,\mathrm{m}^2\,\mathrm{sr}$. In the first and second MC range, the events were generated from all the faces of the cube, so A_{geom} was six times larger than in the third range. Figure 3.11 shows the MC acceptance obtained with Equation 3.9.

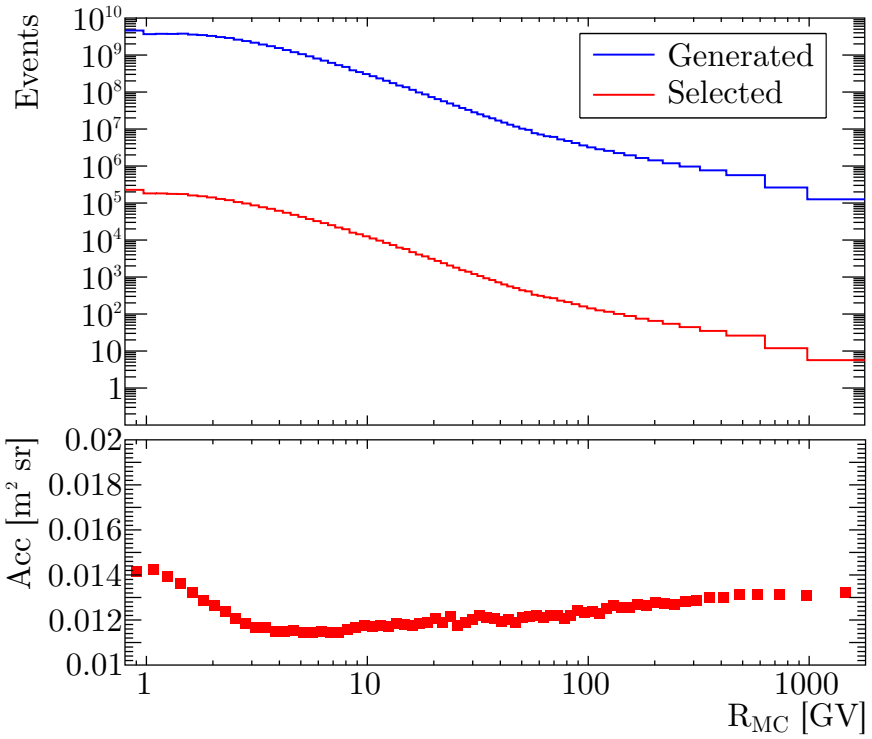

Figure 3.11: **Top**: Comparison between generated and selected events in the MC. **Bottom**: Acceptance computed according to Equation 3.9. The reduction factor between the generated and selected events is mostly due to the restricted FOV of the full-span geometry.

The reduction factor with respect to the generated events is more than four orders of magnitude. N_{sel} includes contributions from the preselection and selection efficiencies, as well as from the intrinsic geometrical acceptance of the detector. Indeed, the FOV of the inner tracker is 40°, while for the full-span is 25°.

Although the material description of the AMS MC is pretty accurate, there could still be some minor differences in the efficiencies measured on data and on MC, due to various factors, like uncertainties in elastic and inelastic cross-sections and simulation of a static and non realistic environment around the detector. For this reason, the effective acceptance computed from the MC is multiplied by a correction factor $\delta_{corr}(R) = \varepsilon_{data}(R)/\varepsilon_{MC}(R)$. The efficiencies that were found to be different between data and MC are the inner tracker efficiency and the full-span efficiency, shown in Figure 3.12.

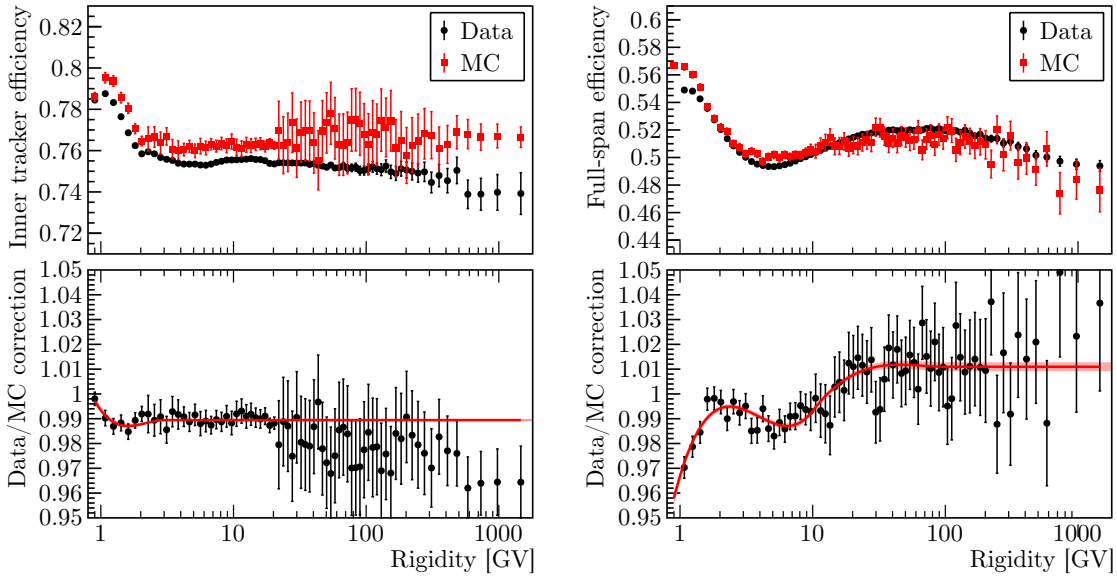

Figure 3.12: Comparison of the efficiencies measured on data (black circles) and on MC (red squares). The bottom panels show the ratio $\delta_{corr}(R) = \varepsilon_{data}(R)/\varepsilon_{MC}(R)$, used to correct the effective acceptance computed from the MC, together with a spline fit (red line) and its confidence interval (pink band). **Left**: Inner tracker efficiency. **Right**: Full-span efficiency.

The inner tracker efficiency is defined as the efficiency of reconstructing an inner tracker `TRKTrack`, given a sample of preselected events. This efficiency is measured with a dedicated sample in which the tracker is not used in the preselection. In particular, the matching between the `TOFTrack` and the `TRKTrack`, required in the "good `TOFTrack`" cut, is replaced with a match between the `TOFTrack` and the `TRDTrack`. The 20 layers of the TRD act as a tracking device, although not as precise as the silicon tracker. Nevertheless, its pointing accuracy is good enough, as demonstrated by the vertex reconstruction technique shown in Figure 3.2. Since the `TRKTrack` is not available in this sample, the rigidity is estimated with different techniques, depending on the rigidity range: below

2 GV, the velocity measured by the TOF is used; between 2 GV and 20 GV, the rigidity is derived from the geomagnetic cutoff; above 20 GV, the rigidity is inferred by the energy deposited in the ECAL. Figure 3.12 left shows the comparison of the inner tracker efficiency between data and MC: $\delta_{corr,TRK}$ is around 0.98, with an almost flat behavior in rigidity.

The full-span efficiency is defined as the efficiency of reconstructing a good full-span `TRKTrack`, consistent with charge = 1, given a sample of good inner tracker `TRKTrack`s, identified as protons by the charge and mass cuts. In this case, the same sample used for the analysis can be used, but the rigidity is the one measured with the inner tracker. Figure 3.12 right shows the comparison of the full-span efficiency between data and MC: $\delta_{corr,FS}$ varies between 0.97 at 1 GV and 1.01 above 30 GV. The differences between data and MC are due to the elastic interactions on L1 and L9, which worsen the match between the inner tracker `TRKTrack` extrapolated in the external layers and the real position of the hits.

The effective acceptance and the data/MC corrections have been fitted with a spline to smooth out statistical fluctuations. The value of the fit in the center of the bin has been used in Equation 3.1 to compute the flux.

3.6 Energy losses in the detector

Although AMS has been designed to minimize the amount of material in the inner tracker, the grammage above it is not negligible, especially inside the LTOF and the TRD. Particles traversing the instrument will deposit their energy via ionization both in the active and the passive material, resulting in a measured rigidity lower with respect to the rigidity they had at the top of the instrument. The effect of the energy losses is to move events from higher to lower rigidity bins, distorting the spectral shape. Furthermore, for some analysis, for example the study of CR trapped in the magnetosphere or the anisotropy in the incoming directions of SEPs, the particles collected by AMS must be backtraced to derive their entry point and direction at the border of the magnetosphere. If the rigidity is underestimated due to energy losses, the backtracing result will be biased. For all these reasons, a study of the effect of the energy losses on the particle rate has been performed and a recovery procedure has been implemented.

The first step has been the development of a dedicated software tool inside the AMS MC to study in detail the energy deposited in all the materials by a particle and its secondary products. This tool has also been used by the collaboration to improve the description of the elastic and inelastic cross-sections for the measurement of the light nuclei fluxes ($2 \leqslant Z \leqslant 8$). A custom MC data sample of protons from 0.1 GV to 10 GV has been generated, saving much more informations with respect to the official MC samples, namely the position and energy of all the steps propagated by GEANT along the particle trajectory. A loose selection based on the inner tracker only has been applied to select proton events. Figure 3.13 top shows the relative difference between the generated and reconstructed curvature, as a function of the generated rigidity. Below 1 GV a shift of the mean

of the distribution towards positive values is visible, *i.e.* the reconstructed rigidity on average is underestimated due to the energy lost in the detector. The tail above 0.5 for $R > 1\,\text{GV}$ is due to events with inelastic interactions in which the selected track is one of the secondaries, thus having a smaller rigidity than the original particle. The tail disappears after discarding these events, as shown in Figure 3.13 bottom.

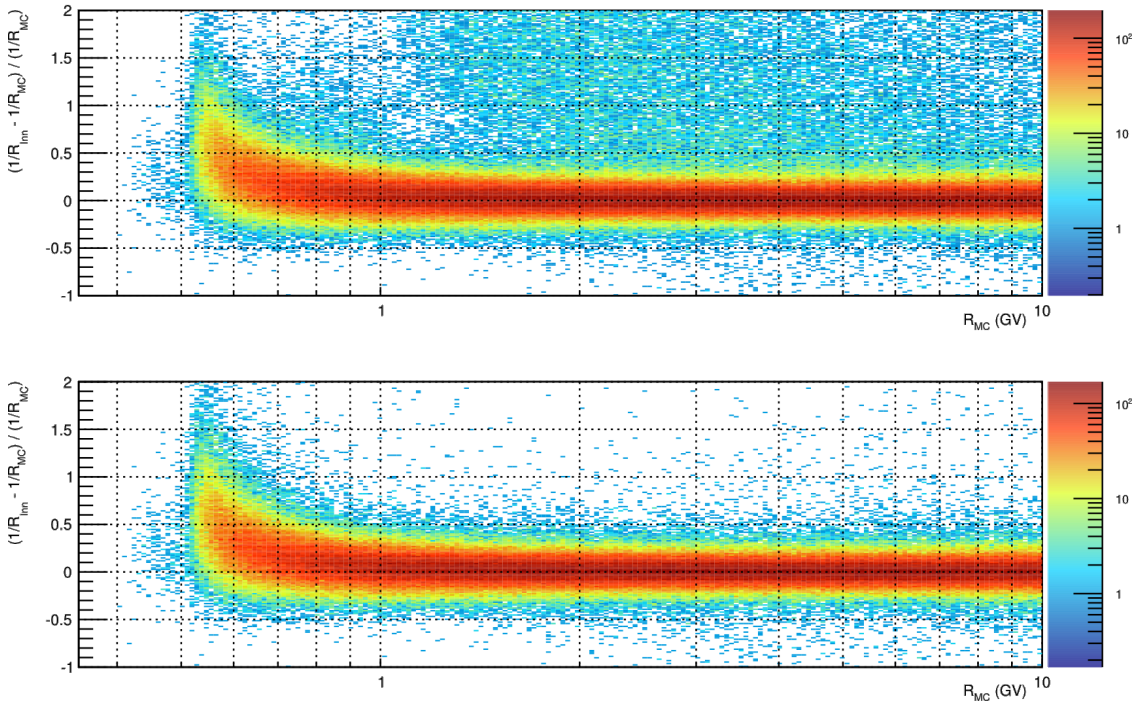

Figure 3.13: Comparison between generated and reconstructed curvature, as a function of the generated rigidity. **Top**: All selected events. **Bottom**: After removing the interactions.

The energy deposited in the active material of the TRD, TOF and tracker is presented in Figure 3.14. The left side shows the energy deposited read directly from the GEANT steps, while the right side shows the energy deposited in the reconstructed hits. The generated and reconstructed distributions agree very well, except for a tail in the TRD around 1 keV (thus completely negligible) and a small population in the tracker, due to a bug in the reconstruction software, now corrected. It is evident that the majority of the energy is lost while traversing the TOF paddles (between 10 MeV and 60 MeV below 1 GV). The tracker contributes only few MeV, while the active material of the TRD is two orders of magnitude less important than the TOF.

However, the energy deposited in the TOF and the tracker it's only 30 % of the total energy lost in the total material of AMS up to the LTOF, as shown in Figure 3.15.

This result implies that it's not possible to fully recover the energy lost on an event-by-event basis. Nevertheless, the energy lost in the active material it's not negligible and can be taken into account separately for each event. The recovery procedure is thus divided in two steps:

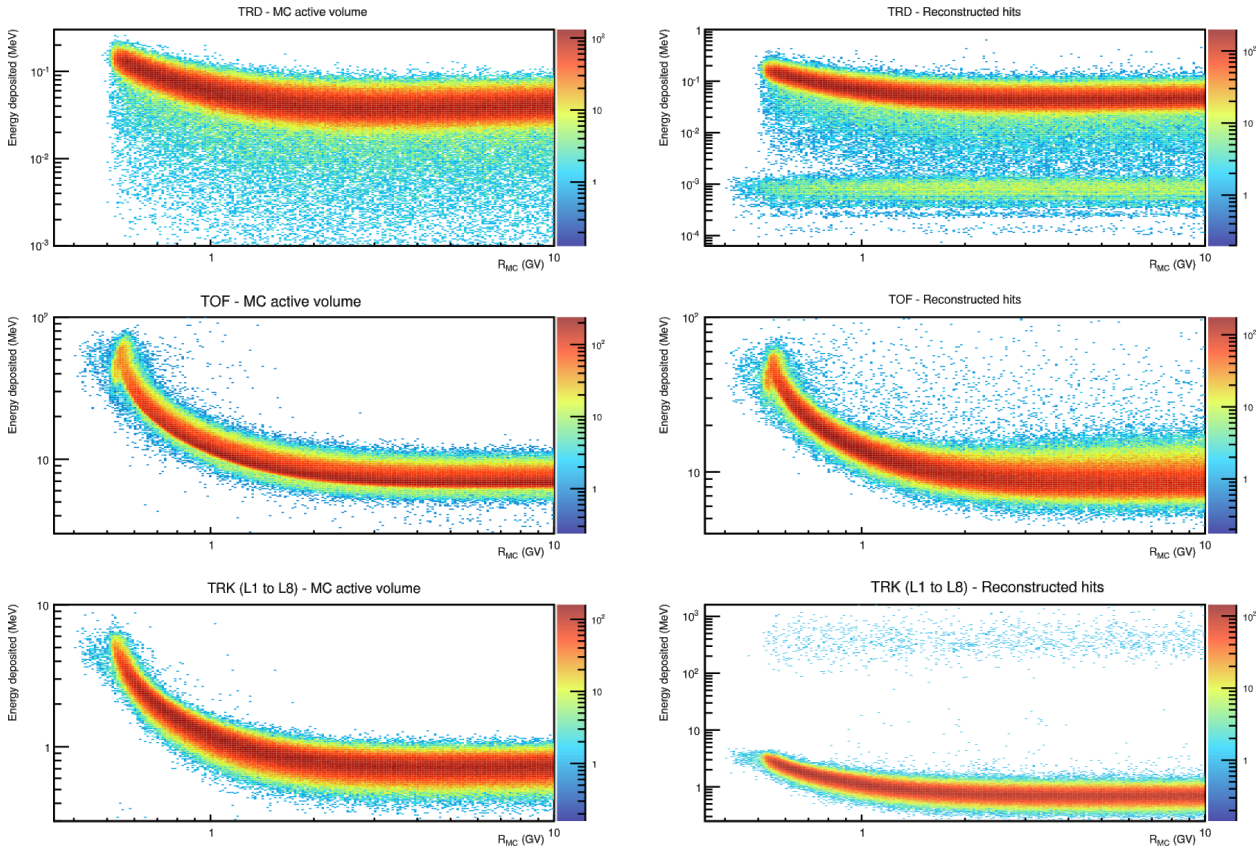

Figure 3.14: Energy deposited in the active material of the TRD (**top**), TOF (**center**) and tracker (**bottom**), according to the MC truth (**left**) and to the reconstructed hits (**right**).

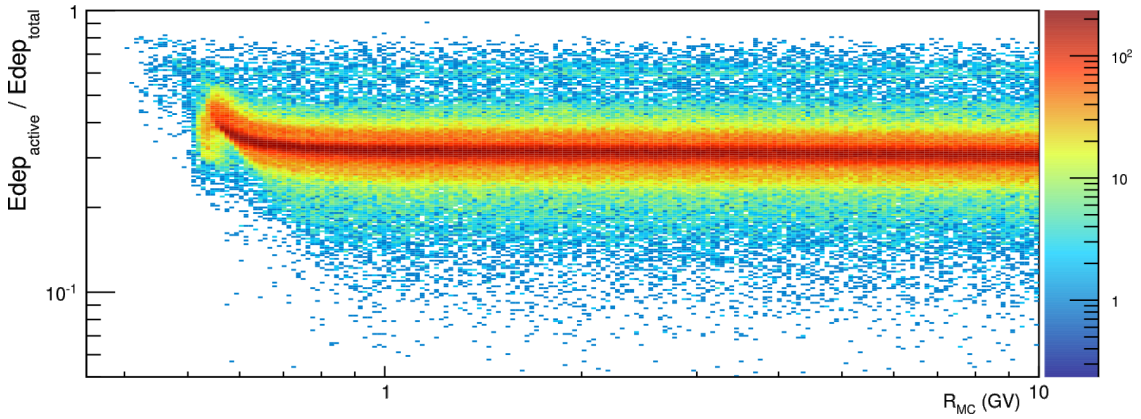

Figure 3.15: Ratio of the energy deposited in the active material with respect to the total material up to the TOF.

1. **Event-by-event correction**. The energy lost in the upper TOF (UTOF), in the inner tracker and in L1 is added to the rigidity measured by the inner tracker, according to the following

formulas:

$$E_{Inn} = \sqrt{R_{Inn}^2 + M_p^2} \implies E_{Inn,EvCorr} = E_{Inn} + E_{dep,UTOF} + E_{dep,L1} + E_{dep,Inn} \implies$$
$$\implies R_{Inn,EvCorr} = \sqrt{E_{Inn,EvCorr}^2 - M_p^2}, \tag{3.11}$$

where M_p is the proton mass, R_{Inn} the rigidity measured by the inner tracker and $E_{dep,X}$ is the energy deposited in the sub-detector X.

2. **Average correction**. The difference between the rigidity corrected in the previous step, $R_{Inn,EvCorr}$, and the generated one is parametrized with a spline as a function of the velocity measured by the TOF (see Figure 3.16), obtaining $R_{Inn,AvgCorr} = (1 + f(\beta))R_{Inn,EvCorr}$.

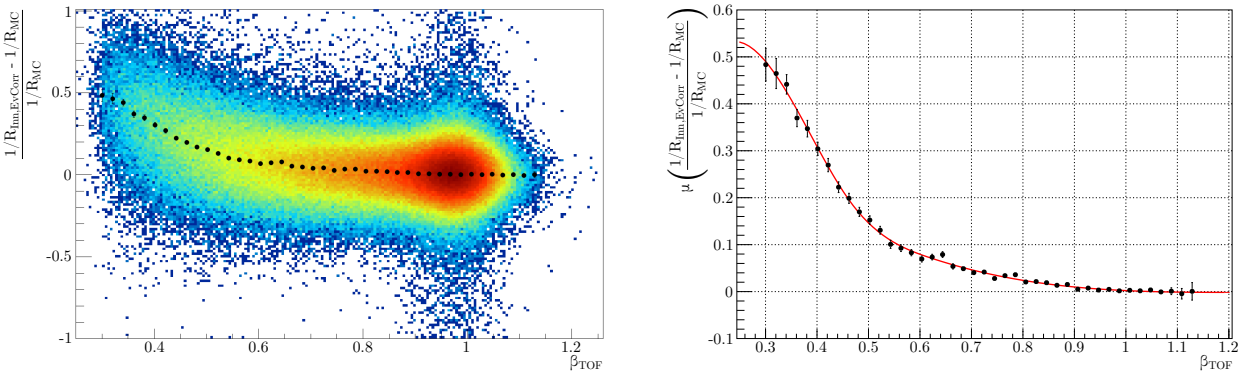

Figure 3.16: Parametrization of the difference between the event-by-event corrected rigidity, $R_{Inn,EvCorr}$, and the generated rigidity, R_{MC}, as a function of the β measured by the TOF. **Left**: Distribution of the difference. The black dots represent the mean of the distribution in each slice of β. **Right**: Spline fit of the mean of the distribution.

Figure 3.17 left shows the relative difference between the generated and corrected curvature, $1/R_{Inn,AvgCorr}$, as a function of the generated rigidity: the distribution is now flat with generated rigidity. Indeed, a linear fit of the mean of the distribution yields an average value consistent with zero (see Figure 3.17 right).

In order to study the performances of the two corrections, the distribution of the relative difference of the generated to reconstructed curvature has been parametrized with a sum of two asymmetric gaussians:

$$N \times \begin{cases} \rho \exp\left[-\frac{1}{2}\left(\frac{x-\mu}{\sigma_{l1}}\right)^2\right] + (1-\rho)\exp\left[-\frac{1}{2}\left(\frac{x-\mu}{\sigma_{l2}}\right)^2\right] & x \leqslant \mu \\ \rho \exp\left[-\frac{1}{2}\left(\frac{x-\mu}{\sigma_{r1}}\right)^2\right] + (1-\rho)\exp\left[-\frac{1}{2}\left(\frac{x-\mu}{\sigma_{r2}}\right)^2\right] & x > \mu \end{cases} \tag{3.12}$$

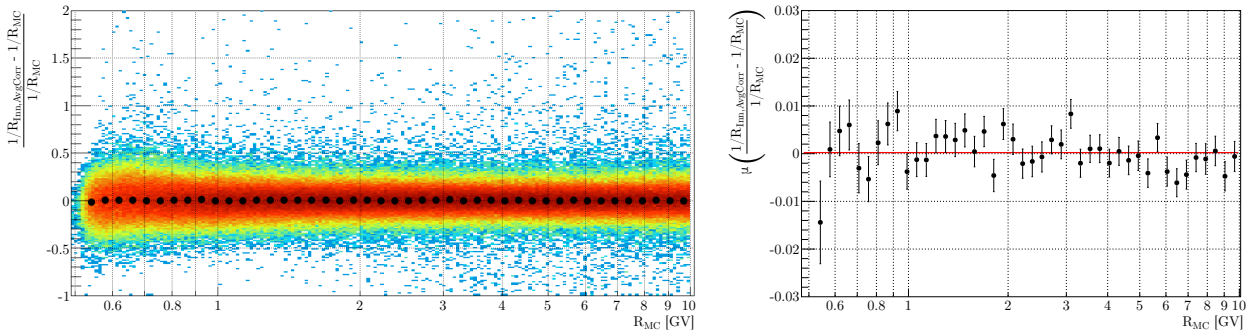

Figure 3.17: Comparison between generated and corrected curvature, $1/R_{Inn,AvgCorr}$, as a function of the generated rigidity. **Left**: Distribution of the difference. The black dots represent the mean of the distribution in each slice of R_{MC}. **Right**: Linear fit to the mean of the distribution.

where ρ is the relative weight between the two gaussians and σ_l and σ_r are the width, respectively, to the left and the right of the mean μ. In first approximation, the measured curvature follows a normal probability distribution, but the multiple scattering and residual interactions increase the height of the tails, requiring additional parameters with respect to the mean and the width of a simple gaussian. Figure 3.18 shows an example of such a fit, in the generated rigidity range (0.64–0.68) GV. Different parametrizations have been tested: a gaussian, a sum of two gaussians, an asymmetric gaussian and the sum of two asymmetric gaussians, which was chosen because yielded the minimum normalized χ^2 in all bins.

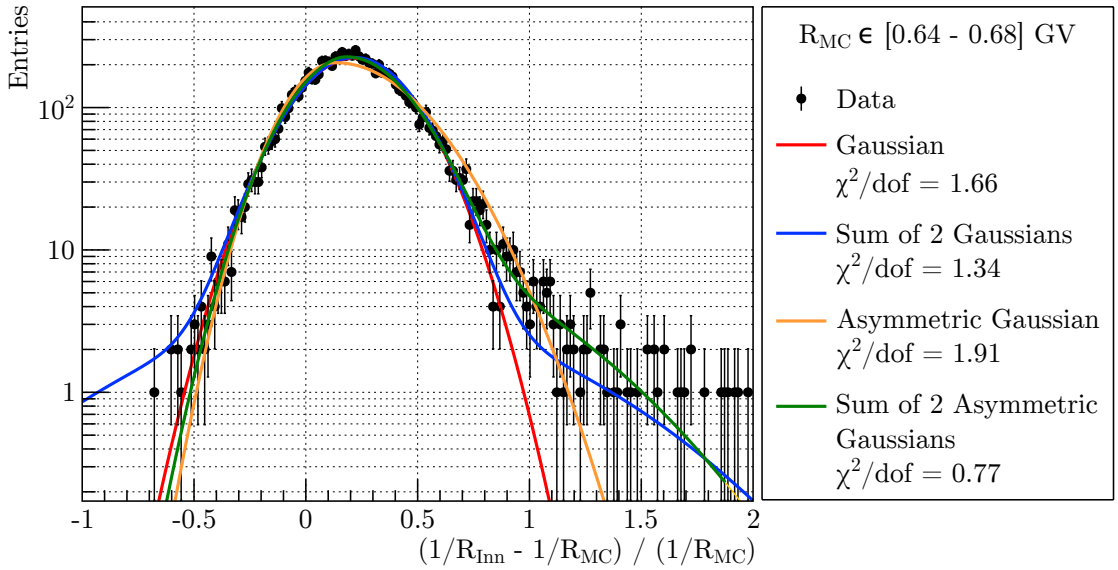

Figure 3.18: Binned likelihood fit of the curvature difference, with different parametrizations: gaussian (red), sum of two gaussians (blue), asymmetric gaussian (orange), sum of two asymmetric gaussians (green).

The fitted parameters μ, σ_{l1} and σ_{r1} are shown in Figure 3.19, as a function of the generated rigidity, before and after the event-by-event correction. The relative weight ρ is always around 0.98, while σ_{l2} and σ_{r2} lie between 0.3 and 0.4. The event-by-event correction reduces the average difference between the generated and reconstructed curvature by $\approx 30\,\%$ around 0.5 GV. The right width σ_{r1} is reduced by almost 50 % at the lowest rigidity and the distribution becomes more symmetric: σ_{l1} and σ_{r1} are nearly the same after the correction.

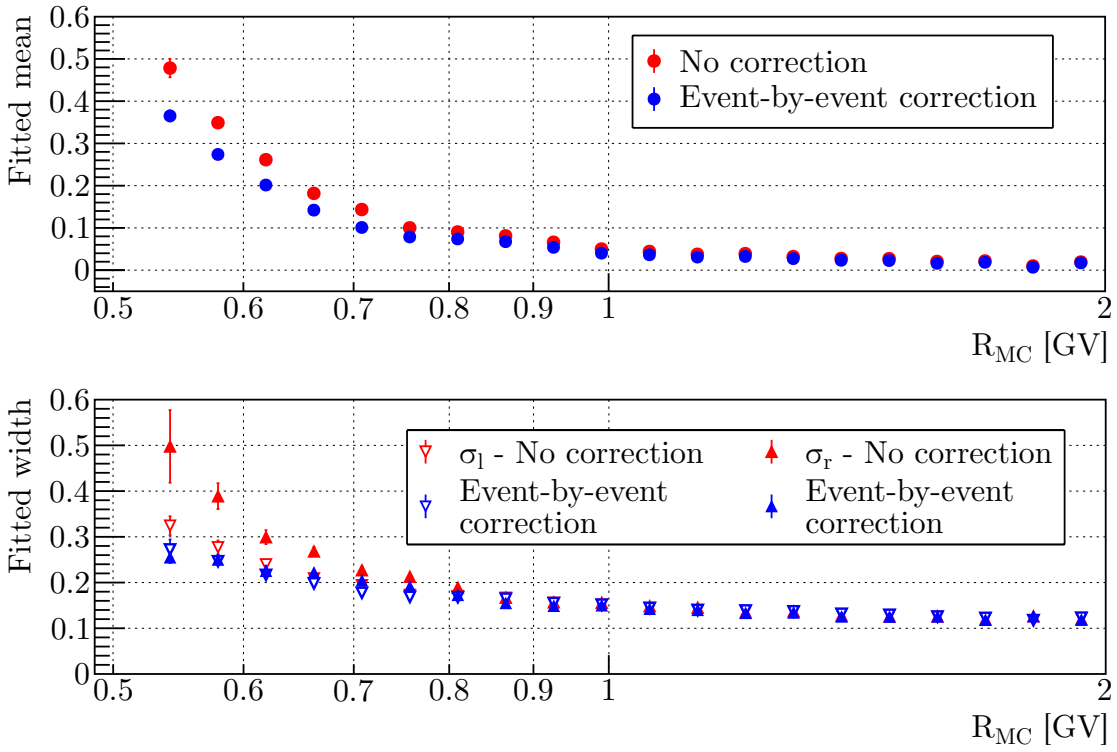

Figure 3.19: Fitted parameters of the curvature difference distribution, as a function of the generated rigidity. **Top**: Comparison of the mean μ before (red) and after (blue) the event-by-event correction. **Bottom**: Comparison of the left width σ_{l1} (empty downward triangles) and right width σ_{r1} (full upward triangles) before and after the event-by-event correction.

A side-effect of the energy losses recovery is the improvement of the inner tracker resolution. If we consider only the multiple scattering and the finite measurement resolution, the uncertainty on the curvature k is $\delta k = \sqrt{\delta^2 k_{res} + \delta^2 k_{MS}}$. In first approximation, δk_{res} is a constant value independent from the curvature[4], while δ_{MS} can be approximated as $a/(\beta R)$, with a containing detector-related factors influencing the amount of multiple scattering [124]. Rewriting δk_{MS} as a

[4] According to [124], the second order correction in $(kL)^2$ is negligible for $p_t[\mathrm{GeV}] > 0.46 B[\mathrm{T}] L[\mathrm{m}]$, where p_t is the transverse momentum, L the track length and B the magnetic field. For the inner tracker, $B \approx 0.15$ T and $L \gtrsim 1$ m, so that the first approximation is valid for $p_t \gtrsim 100$ MeV, which is satisfied for protons with rigidities above 0.5 GV and a maximum inclination of 40°, corresponding to the inner tracker FOV.

function of the curvature, remembering that $R \propto 1/k$, we find:

$$\delta k_{MS} = \frac{ak}{\alpha}\sqrt{1+\frac{M_p^2 k^2}{\alpha^2}} \quad \Longrightarrow \quad \frac{\delta k}{k} = \sqrt{\frac{\delta^2 k_{res}}{k^2} + \frac{a}{\alpha} + \frac{M_p^2 a^2}{\alpha^4}k^2}, \tag{3.13}$$

where α is the proportionality factor between R and k and M_p is the proton mass. This formula does not hold anymore when considering the energy losses: an additional term $1/k^4$ must be added under the square root. Figure 3.20 shows the comparison of the fitted widths σ_{l1} and σ_{r1}, as a function of the generated rigidity, without and with the final correction. The dashed lines represent the best fits of Equation 3.13 to the widths. It is evident that with no correction Equation 3.13 does not describe the resolution of the inner tracker, while after the final correction, $R_{Inn,AvgCorr}$ attains the minimum possible resolution.

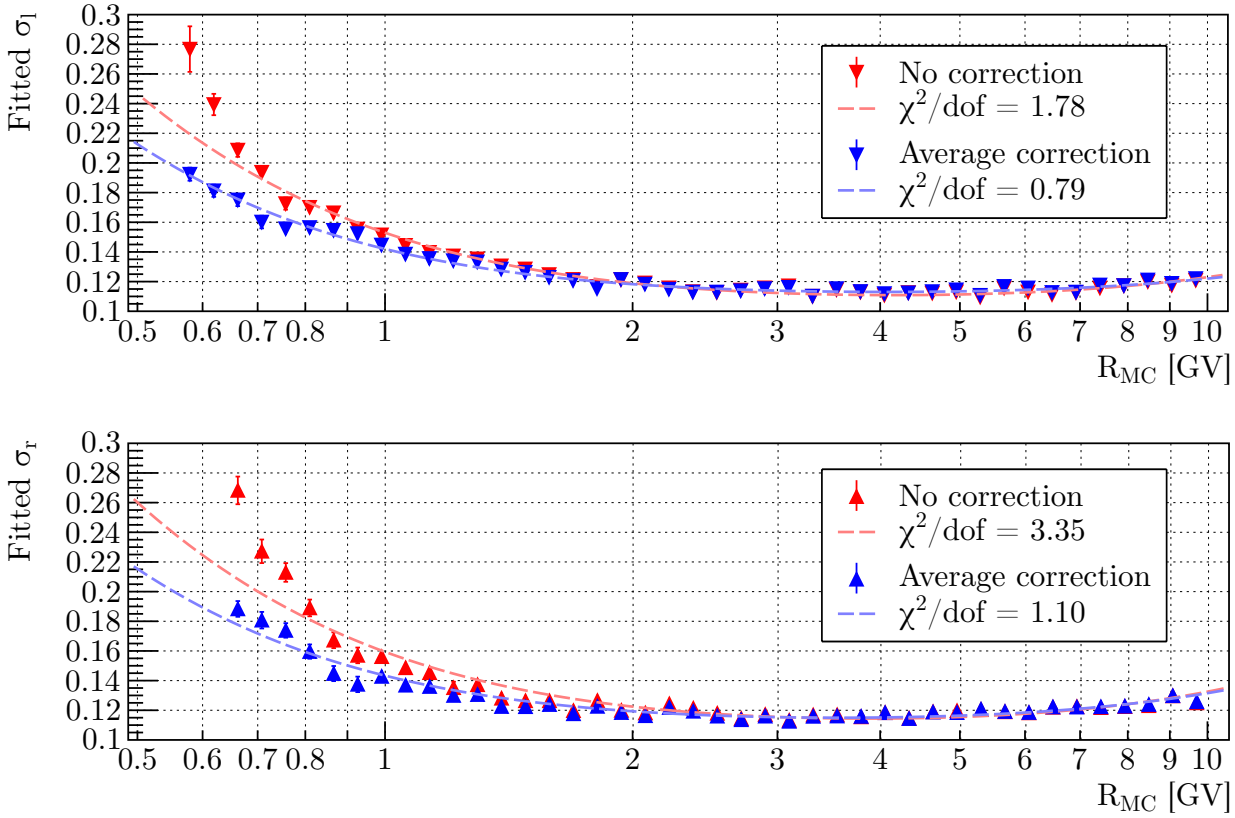

Figure 3.20: Comparison of inner tracker resolution before (red) and after (blue) the energy losses recovery procedure. The dashed lines are the best fits of Equation 3.13 to the measured σ_{l1} (**top**) and σ_{r1} (**bottom**).

Figure 3.21 illustrates the effect of the energy losses in the detector on the rate measured by AMS. On the left panel, the MC acceptance is plotted: the blue curve is the acceptance as a function of the generated rigidity, while the red and green curves are the acceptance as a function

of, respectively, the uncorrected and corrected reconstructed rigidity. The acceptance is much higher than the one shown in Figure 3.11 because the selection is looser and the inner tracker has a larger FOV than the full-span. Looking at the differences between the red and green curve, we see that the acceptance computed after the recovery procedure is higher than the one with no rigidity correction above 0.6 GV: this is because the particles have now a higher reconstructed rigidity and so they are moved from the left to right. Furthermore, we see that the acceptance sharply drops below 0.6 GV, meaning that without considering the effect of the energy losses, we would have thought to be able to measure particle with a much lower rigidity than in reality. The right panel shows the ratio of the rate measured using the corrected reconstructed rigidity to the rate measured with the uncorrected reconstructed rigidity. Above 3 GV the ratio is below 1 %, it becomes 5 % around 1.3 GV and remains positive down to 0.8 GV. At very low rigidities, below 0.6 GV, the rate measured without corrections is overestimated by more than 20 %.

In conclusion, this study shows that the energy losses must be taken into account when measuring the flux below 2 GV.

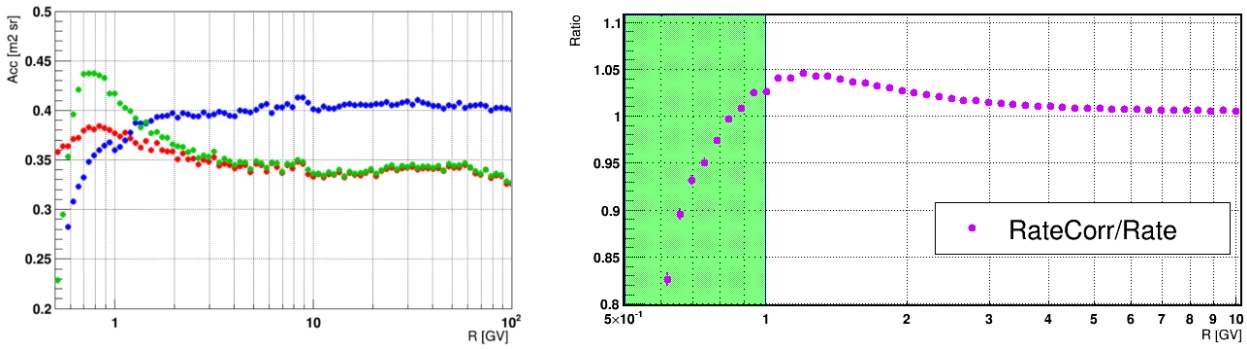

Figure 3.21: Effect of the energy losses on the measured rate. **Left**: Comparison of the MC acceptance as a function of the generated rigidity (blue) and as a function of the reconstructed rigidity, without (red) and with (green) the energy losses correction. **Right**: Ratio of the measured rate without and with the energy losses correction.

3.7 Rigidity unfolding

In the previous Section we saw how the energy losses distort the distribution of the measured rigidities. However, we also need to take into account the effect of the rigidity resolution on the flux, in particular at high rigidities, where the resolution degrades, becoming proportional to the measured rigidity, until the error on the measurement reaches 100 %. The non-zero width of the curvature difference distribution means that protons in a given bin of true rigidity may end up in a different bin of reconstructed rigidity, a process called *bin-to-bin migration*. For an ideal detector, capable of measuring the rigidity with no uncertainty, given a flux $\Phi(R)$, the number of events in a

bin would be:

$$\widetilde{N}(R,\, R+\Delta R) \;=\; \Delta T(R,\, R+\Delta R) \int_{R}^{R+\Delta R} \Phi(R_0) A(R_0)\, dR_0, \tag{3.14}$$

where the exposure time ΔT is assumed to vary slowly in the rigidity bin, so that it can be brought outside of the integral. For a real instrument, though, the number of events in the same bin becomes:

$$N(R,\, R+\Delta R) \;=\; \Delta T(R,\, R+\Delta R) \int_{R}^{R+\Delta R} dR' \int_{0}^{+\infty} \Phi(R_0) A(R_0) P(R'|R_0)\, dR_0, \tag{3.15}$$

where $P(R'|R_0)$ is the probability of measuring a proton with true rigidity R_0 with reconstructed rigidity R', also called *migration probability*. Let's note that the ideal case can be obtained simply by putting $P(R'|R_0) = \delta(R' - R_0)$, where δ is the Dirac delta function. This formula tells us that all the rigidities R_0 contribute to the events of a given bin, each rigidity weighted by its probability of being reconstructed with the desired rigidity R'. The quantity measured by the detector is N, but we are actually interested in $\widetilde{N}$: this is the *unfolding* problem, *i.e.* how to reverse the distortion introduced by a probability $P \neq \delta$. Incidentally, solving this problem also takes care of the energy losses at low rigidities, since P contains all the detector effects.

Let's define the *migration matrix* (also known as *unfolding matrix*) M:

$$M(R,\, R+\Delta R,\, R_0,\, R_0+\Delta R_0) \;=\; \frac{\displaystyle\int_{R}^{R+\Delta R} dR' \int_{R_0}^{R_0+\Delta R_0} \Phi(R_0) A(R_0) P(R'|R_0)\, dR_0}{\displaystyle\int_{R_0}^{R_0+\Delta R_0} \Phi(R_0) A(R_0)\, dR_0}, \tag{3.16}$$

which represents the average migration probability in a 2D bin of reconstructed and true rigidity, weighted by the flux multiplied by the acceptance. An example of the migration matrix of AMS for protons is shown in Figure 3.22. The effect of the energy losses can be seen below 1 GV, while at high rigidities the tracker resolution increases, reaching $\Delta R/R = 1$ around 2 TV. The horizontal population around 0.5 GV in reconstructed rigidity is due to residual interactions not rejected by the selection: most of these events disappear from data collected on the ISS, because they are usually below the geomagnetic cutoff.

The unfolding problem can then be casted in a very simple way. Indicating with i the bins of reconstructed rigidity and with j the bins of true rigidity, we have:

$$N_i = \sum_j M_{ij} \widetilde{N}_j. \tag{3.17}$$

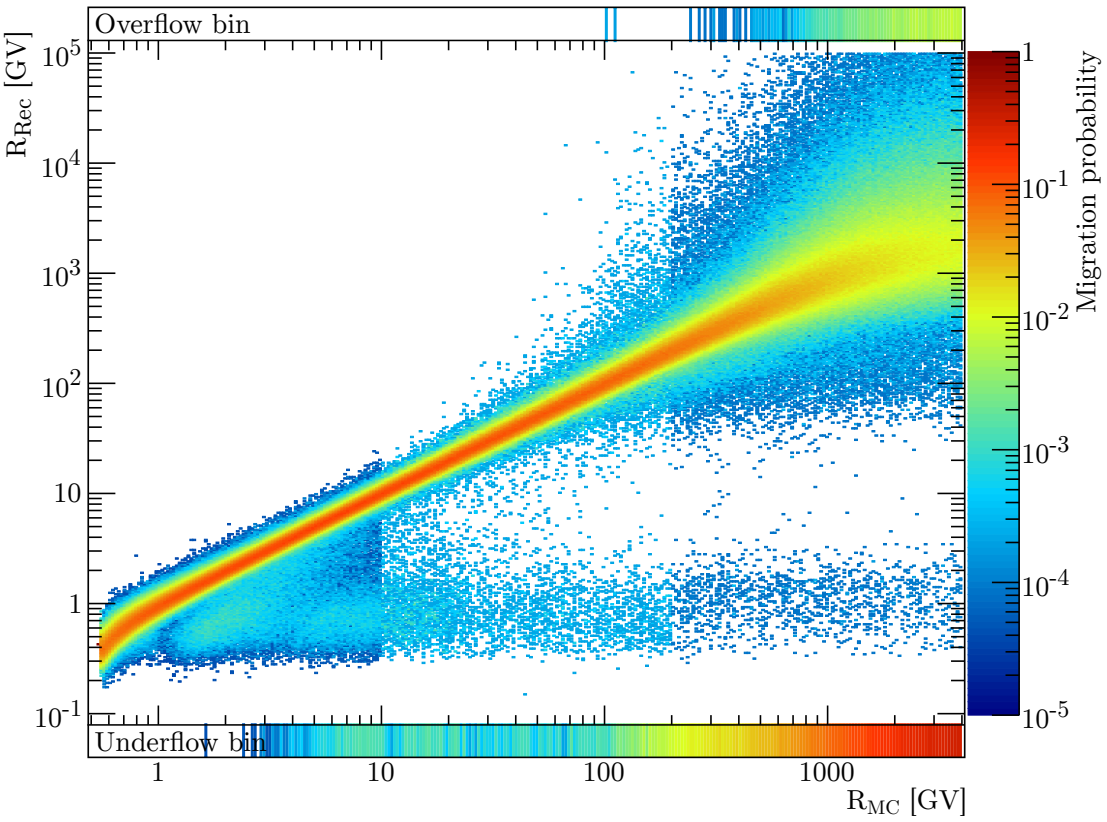

Figure 3.22: Migration matrix, as defined in Equation 3.16, for protons measured by AMS. Each column, corresponding to a bin j in generated rigidity, is normalized such that $\sum_i M_{ij} = 1$, *i.e.* an event coming from a bin j will migrate for sure in any of the bins i in reconstructed rigidity. Underflow and overflow events are taken into account in the normalization, so that events lost because outside the binning used in the analysis do not bias the migration probability. The lower and upper rows represent the migration probability towards, respectively, underflow and overflow bins. Events in the underflow bin are mostly coming from negatively reconstructed rigidities: in the last bin used for this analysis (1800 GV) the migration probability to underflow bin is $\approx 16\,\%$.

Solving the unfolding problem is just a matter of inverting the unfolding matrix, so that $\widetilde{N}_j = \sum_i M_{ij}^{-1} N_i$. Unfortunately, M is rarely analytically invertible and a numerical inversion is not guaranteed to give a stable solution, since M can be rectangular.

The procedure adopted in this work is called *folded acceptance unfolding* and it's an iterative method. The measured flux Φ_i in a bin i is:

$$\Phi_i = \frac{1}{\Delta R_i} \int_{R_i}^{R_i + \Delta R_i} \Phi(R_0)\, dR_0. \tag{3.18}$$

We want to find the correction factor a_i that converts the flux Φ_i in the observed number of particles

$N_i = \Delta T_i \Delta R_i a_i \Phi_i$. A comparison with Equation 3.15 yields:

$$a_i = a(R_i,\, R_i + \Delta R_i) = \frac{\displaystyle\int_{R_i}^{R_i+\Delta R_i} dR' \int_0^{+\infty} \Phi(R_0) A(R_0) P(R'|R_0)\, dR_0}{\displaystyle\int_{R_i}^{R_i+\Delta R_i} \Phi(R_0)\, dR_0}. \tag{3.19}$$

a is called *folded acceptance*, hence the name of the method: it has the same units of an acceptance and it is the average value in the bin i of the acceptance multiplied by the migration probability, weighted by the flux Φ. We can now compute the flux using Equation 3.1, replacing A_i with a_i. This method only works if the flux used to derive a is the true flux, which is albeit unknown. For this reason, we procede in an iterative way:

1. We assume an initial guess for the flux, $\Phi^{(0)}$: for example, the flux computed without unfolding, *i.e.* A_i in Equation 3.1 is the acceptance as a function of generated rigidity.

2. We reweight the MC with $\Phi^{(n)}$.

3. We compute the folded acceptance $a^{(n)}$, by filling the histogram of the selected events as a function of reconstructed rigidity and dividing it by the histogram of generated events, filled as a function of generated rigidity. This is equivalent to computing the integrals in Equation 3.19, without the need to know the expression of $P(R'|R_0)$. Figure 3.23 shows the difference between the generated and folded acceptance.

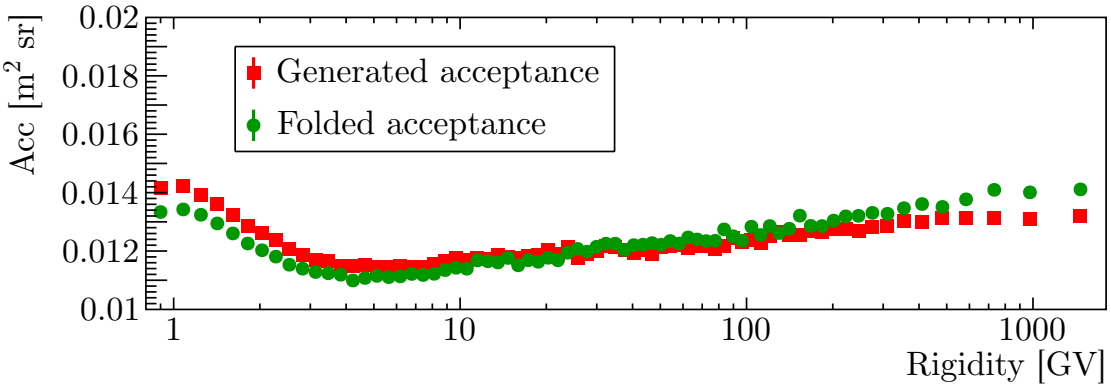

Figure 3.23: Comparison between generated acceptance (red) and the folded acceptance (green). The major differences are, as expected, around 1 GV, because of the energy losses, and at 1 TV, close to the MDR, where the bin-to-bin migration is very large.

4. The folded acceptance is fitted with a spline, to smooth out statistical fluctuations and then

multiplied by $\delta^{(n)}_{corr} = \varepsilon_{data}/\varepsilon^{(n)}_{MC}$, where both efficiencies are now functions of the reconstructed rigidity.

5. The flux $\Phi^{(n+1)}$ is computed using Equation 3.1, with $A_i = a_i^{(n)}$ and then parametrized with a spline. An example of such parametrization is shown in Figure 3.24.

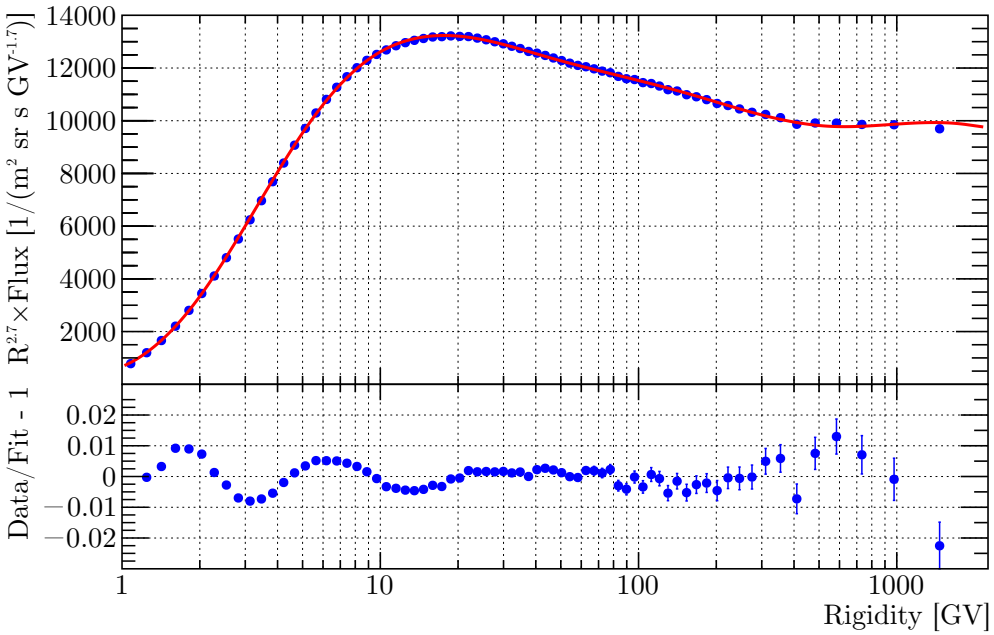

Figure 3.24: **Top**: The flux $\Phi^{(n)}$ (blue dots), rescaled by $R^{2.7}$ to highlight the high-rigidity range, together with the spline parametrization (red line). **Bottom**: Relative difference between the flux and the spline. The parametrization describes the flux within 1 % accuracy.

6. Repeat from 1), reweighting the MC with the spline parametrization of $\Phi^{(n+1)}$.

The method stops when the unfolded flux converges, *i.e.* when $\Phi^{(n)}/\Phi^{(n-1)} \lesssim 0.1\,\%$. As can be seen from Figure 3.25, the convergence is fast: only 6 iterations are necessary before reaching a stable solutions. The fitted folded acceptance at different iterations is shown on the left: at low rigidities, after the first iteration the folded acceptance remains stable, while at high rigidities we can see the acceptance decreasing until it does not change anymore after the third iteration. On the right, instead, the relative difference between the flux at the iteration n and the flux at the previous iteration is plotted. After the first iteration, almost all rigidities remain stable, except at high rigidities, where the difference decreases until it becomes smaller than 0.1 %.

The proton flux obtained with the analysis described in this work is consistent with the one published by the AMS collaboration [89], as shown in Figure 3.26: the ratio of the two fluxes is well within the total uncertainty on the published result.

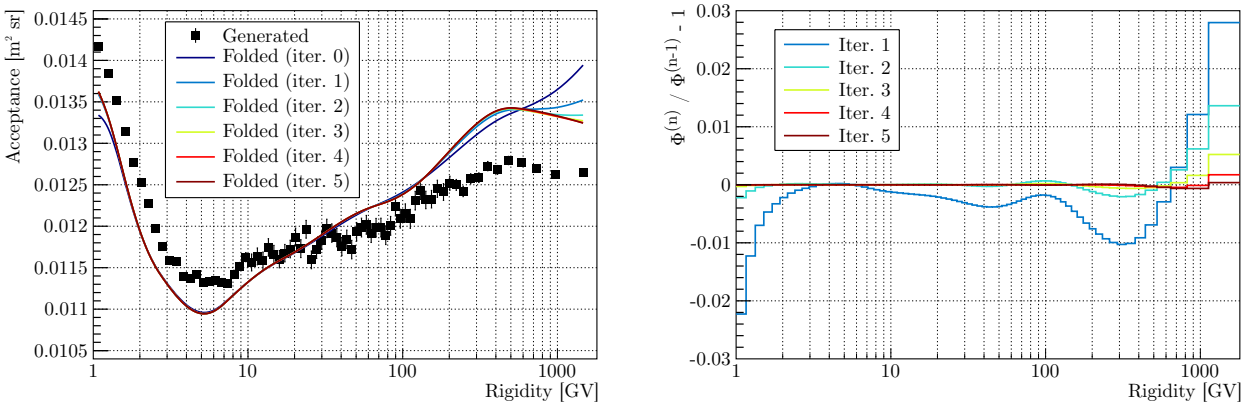

Figure 3.25: Comparison of the folded acceptance (**left**) and the ratio $\Phi^{(n)}/\Phi^{(n-1)}$ (**right**) for different iterations.

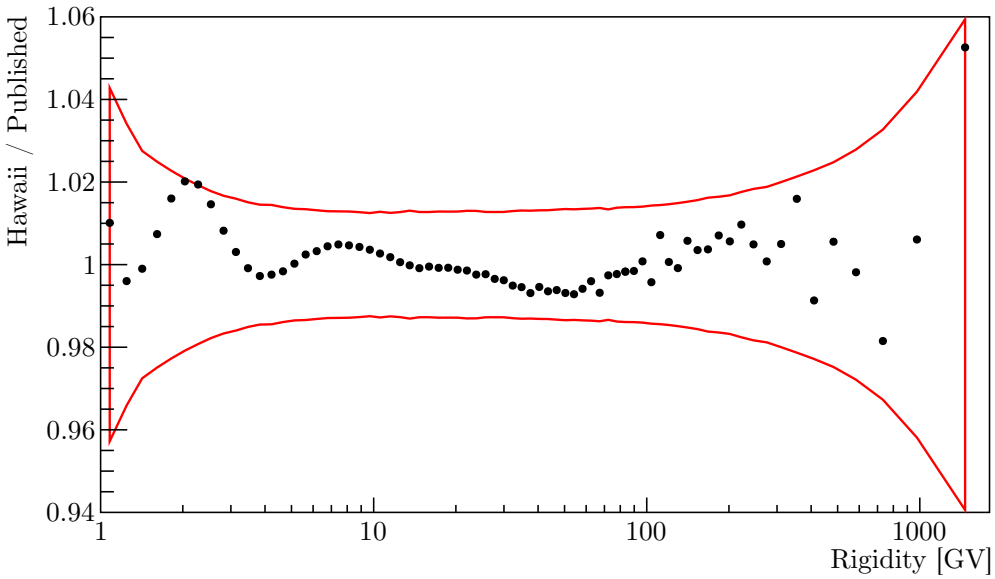

Figure 3.26: Ratio of the proton flux (measured between May 15, 2011 and November 26, 2013) obtained with this analysis to the result published by AMS. The red line is the total uncertainty (statistical plus systematic, added in quadrature) on the official flux.

3.8 Systematic uncertainties

In the course of the analysis, many details could have been slightly different, potentially leading to a diverse final result. The systematic uncertainties on the proton flux due to the choices made at various stages of the analysis have been extensively studied:

1. **Selection cuts**. The number of selected events depends on the cuts imposed on the various charge estimators (UTOF, LTOF, L1, L9 and inner tracker), the cut on the normalized chi-squared of the fitted track and the safety factor multiplying the geomagnetic cutoff. The

analysis has been repeated 1000 times, each time randomly varying all the cut values within a reasonable range. The distribution of the fluxes obtained from all the analysis is roughly gaussian in every bin and the flux of the reference analysis is always very close to the mean of the distribution, meaning that the chosen working point was the optimal one. The width of the distribution gives an estimate of the systematic uncertainty due to the selection cuts: at 1 GV the error is 2.5 %, due to the dependence of the flux on the cutoff safety factor, while from 1.5 GV to 40 GV the error remains constant around 0.7 %, rising up to 1.5 % at 1 TV.

2. **Smoothing parametrizations.** The trigger efficiency, the acceptance and the data/MC corrections are fitted with splines, to smooth out statistical fluctuations coming from the limited statistics of the unbiased triggers and of the MC. The systematic error due to this smoothing procedure is computed as $\Delta y = |y_{data} - y_{fit}|/y_{data}$, where y_{data} is the value of any of the measured efficiencies, corrections or acceptance and y_{fit} is the value of the fitted spline. For the acceptance and the inner tracker efficiency correction, Δy does not depend on the rigidity and it is around 0.5 % for the acceptance and 0.2 % for the inner tracker efficiency correction. For the full-span efficiency correction, Δy is 0.4 % at low rigidities and grows linearly up to 4 % at 2 TV. For the trigger efficiency, Δy is around 0.1 % at 1 GV and rises linearly up to 3 % at 2 TV.

3. **Cross-sections**. Most of the detector material is composed of carbon and aluminum, so it's important to precisely know the inelastic cross-sections p + C and p + Al. The uncertainty on the cross-sections measured at accelerators are 10 % at 1 GV, 4 % at 300 GV and 7 % at 1.8 TV [125, 126, 127, 128, 129, 130]. Dedicated MC samples with inelastic cross-sections varied by ±10 % have been produced by the collaboration. They were analyzed in the same way of the reference MC and the difference between them has been used to derive the systematic error, defined as $\Delta A_{\pm 10\,\%}/2 \times \Delta_{XS}/0.1$, where $\Delta A_{\pm 10\,\%}$ is the relative difference in the folded acceptance between the MC with a +10 % bias in the cross-section and the MC with a −10 % bias, while Δ_{XS} is the relative uncertainty in the cross-sections measured at the accelerators. The difference in the folded acceptance is 5 %, constant at all rigidities, but reduces to 4 % after including the data/MC corrections. The systematic error induced on the flux is 1.9 % at 1 GV, 0.8 % between 10 and 300 GV and 1.3 % at 1.8 TV.

4. **Rigidity scale and resolution**. The systematic error associated to the measurement of the rigidity is described in details below.

3.8.1 Rigidity scale and resolution

Three different rigidity-related effects contribute to the systematic error:

1. **Uncertainty in the magnetic field map**. The magnetic field inside AMS is known with an

accuracy of 0.2 %. In order to assess the effect of this uncertainty on the flux, the reconstructed rigidity was modified as $R \to R \times (1 \pm 0.002)$: since the rigidity is proportional to the magnetic field, a 0.2 % variation in B translates in a 0.2 % variation in R. The systematic error associated to the magnetic field is half the difference between the fluxes computed with a ± 0.2 % bias in the rigidity, and it is below 0.5 % at all rigidities.

2. **Absolute rigidity scale**. A residual misalignment in the tracker induces a shift in the measured curvature, thus affecting the absolute rigidity scale. This misalignment was measured in the test beam with 400 GV protons and resulted in a curvature shift of $1/300\,\mathrm{TV}^{-1}$. On the ISS, the misalignment was inferred by the difference in the peak position of the E/R distribution between electrons and positrons, where E is the energy measured by the ECAL. It was found to be $1/26\,\mathrm{TV}^{-1}$, due to the limited statistics of high-energy positrons. This uncertainty has been taken into account by repeating the analysis with a shifted reconstructed rigidity, *i.e.* $1/R \to 1/R \pm 1/26\,\mathrm{TV}^{-1}$, and by taking half the difference between the resulting fluxes. The systematic error is negligible at low rigidities, as expected, and rises linearly up to 3.5 % at 1.8 TV.

3. **Resolution**. The uncertainty on the maximum detectable rigidity (MDR) and the normalization of the non-gaussian tails was studied using ISS data and the test beam and it was found to be, respectively, 5 % and 20 %. The parametrization of the curvature difference used in the study of the energy losses is not valid at high rigidities, so a new function was used to describe the migration matrix in the whole MC rigidity range:

$$P\left(\delta_k = \frac{1}{R_{Rec}} - \frac{1}{R_{MC}} \,\middle|\, R_{MC}\right) = \begin{cases} e^{-\frac{\alpha_L^2}{2}} \left(\dfrac{n_L}{n_L - \alpha_L^2 - \alpha_L \frac{\delta_k - \mu}{\sigma}} \right)^{n_L} & \frac{\delta_k - \mu}{\sigma} < -\alpha_L \\ \exp\left[-\dfrac{1}{2} \left(\dfrac{\delta_k - \mu}{\sigma} \right)^2 \right] & -\alpha_L \leqslant \frac{\delta_k - \mu}{\sigma} \leqslant \alpha_R \\ e^{-\frac{\alpha_R^2}{2}} \left(\dfrac{n_R}{n_R - \alpha_R^2 + \alpha_R \frac{\delta_k - \mu}{\sigma}} \right)^{n_R} & \frac{\delta_k - \mu}{\sigma} > \alpha_R, \end{cases} \tag{3.20}$$

which is a generalization of the Crystal Ball distribution [131], *i.e.* a gaussian core with asymmetric power-law tails. Figure 3.27 shows the curvature difference in different bins of generated rigidity fitted with the asymmetric Crystal Ball distribution.

The new parametrization works well at all rigidities: below 1 GV, the peak is shifted at lower reconstructed rigidities because of the energy losses, while the right tail is coming from residual interactions; at intermediate rigidities, around 100 GV, the peak is centered at zero and the distribution becomes more and more symmetric, the tail of the residual interactions vanishing, while the tails due to the intrinsic resolution appear; at high rigidities, the distribution is

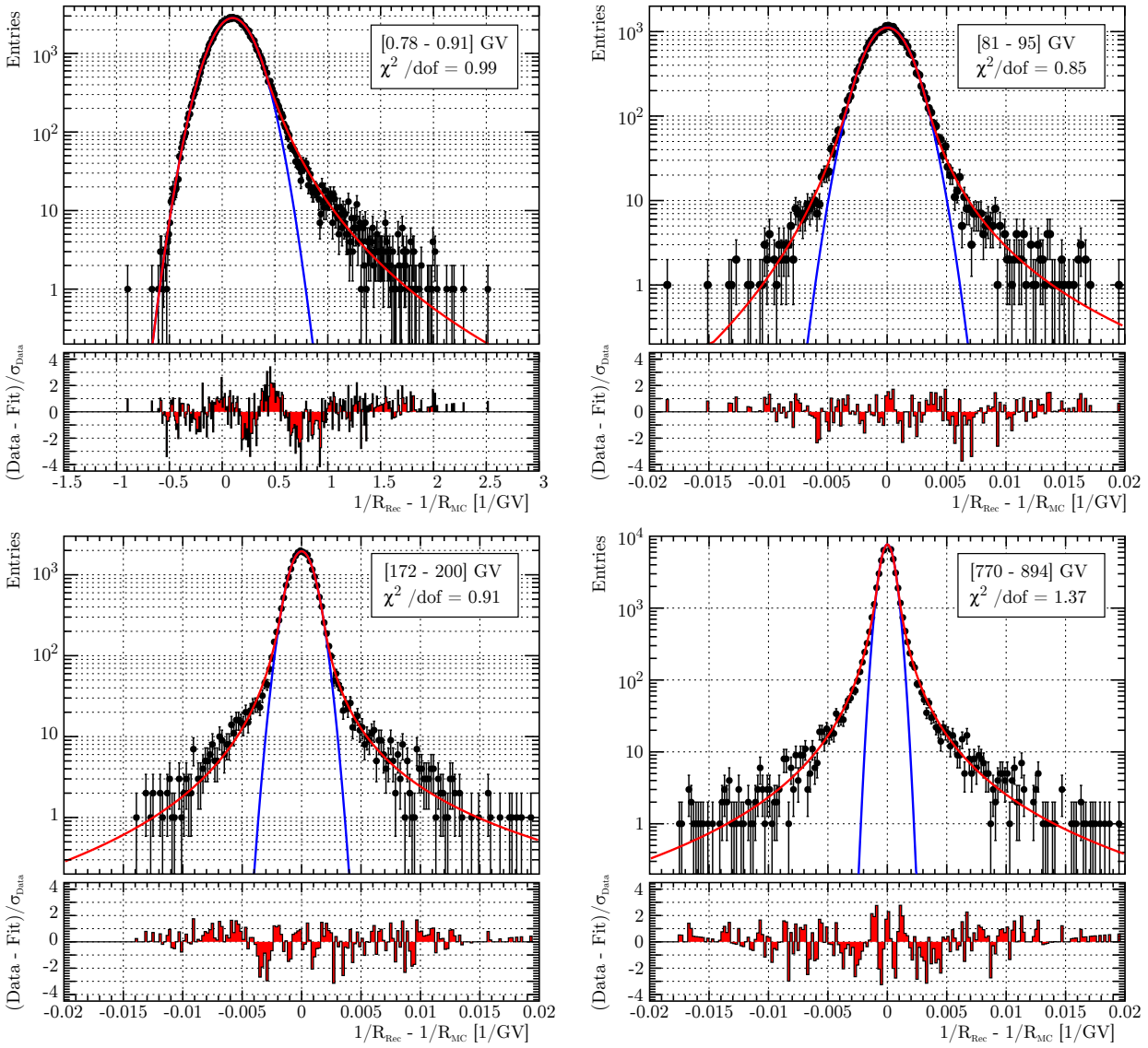

Figure 3.27: Examples of migration matrix slices fitted with the asymmetric Crystal Ball distribution (red). The gaussian core is highlighted in blue.

symmetric. The rigidity dependence of the fitted parameters is shown in Figure 3.28.

The parametrization of the migration matrix is used in the folded acceptance unfolding to estimate the systematic error related to the uncertainties in the resolution. The flux is unfolded with the folded acceptance computed from the parametrization, varying separately σ by $\pm 5\,\%$ and the height of the tails by $\pm 20\,\%$, and the half difference between the obtained fluxes in the two cases is used as systematic error.

The four systematic uncertainties associated with the measurement of the rigidity are shown in Figure 3.29. The total error is obtained by adding the separate contributions in quadrature, and

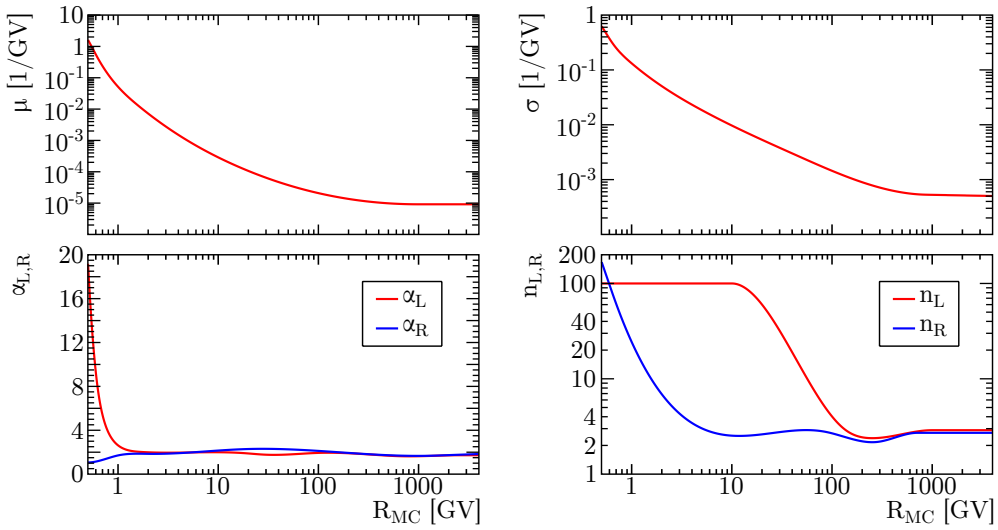

Figure 3.28: Rigidity dependence of the asymmetric Crystal Ball parameters: μ (**top left**), σ (**top right**), α_L and α_R (**bottom left**), n_L and n_R (**bottom right**). At high rigidities, $\alpha_L \simeq \alpha_R$ and $n_L \simeq n_R$, *i.e.* the matrix is symmetric.

it's consistent with the one from the proton flux publication, although slightly larger below 2 GV and above 100 GV.

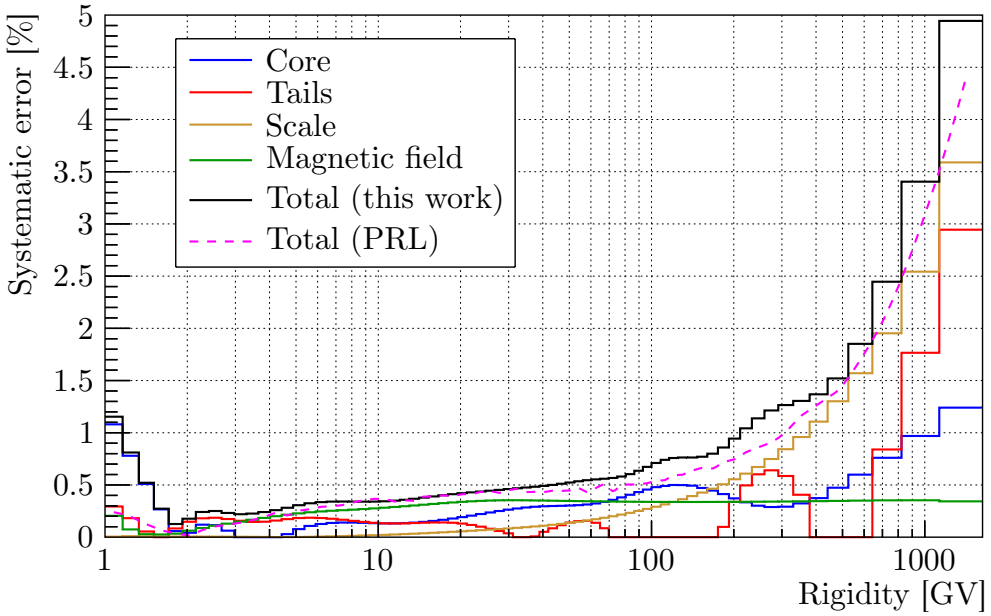

Figure 3.29: The different systematic uncertainties related to the rigidity measurement (colored solid lines), together with the total systematic error obtained in this work (black) and the published one (magenta).

3.9 Time-dependent analysis

The period from May 20, 2011 to November 26, 2016 has been divided in 75 intervals of 27 days each, called Bartels rotations (BRs). The length of a BR is very close to the synodic rotation period of the Sun (26.64 days), *i.e.* the time it takes for a fixed point on the surface of the Sun at 26° latitude to rotate until it returns to the same position as seen from Earth. The BR number was introduced by Julius Bartels in 1934, who arbitrarily fixed the start date of BR 1 on February 8, 1832 [132]. In the rest of this work, the BR fluxes measured by AMS will be sometimes referred to also as monthly fluxes.

The analysis of the time dependence of the proton flux is the same as described before, except that the trigger efficiency, the folded acceptance and the data/MC corrections are evaluated for each time interval. The trigger efficiency was fitted with a shape fixed to the entire period above 20 GV, with only a free scale factor, to avoid spurious variations at high rigidity due to the limited number of unbiased triggers. Below 20 GV the fit was left free to vary. The folded acceptance, inner tracker and full-span efficiency corrections were fitted with splines, with all the parameters left free. The initial flux guess for the unfolding is the measured flux on the entire period: in most of the cases, the unfolding converges after three iterations, while some BR require four iterations.

Figure 3.30 shows the time dependence of the trigger, inner tracker and full-span efficiencies around 1.4 GV and 50 GV.

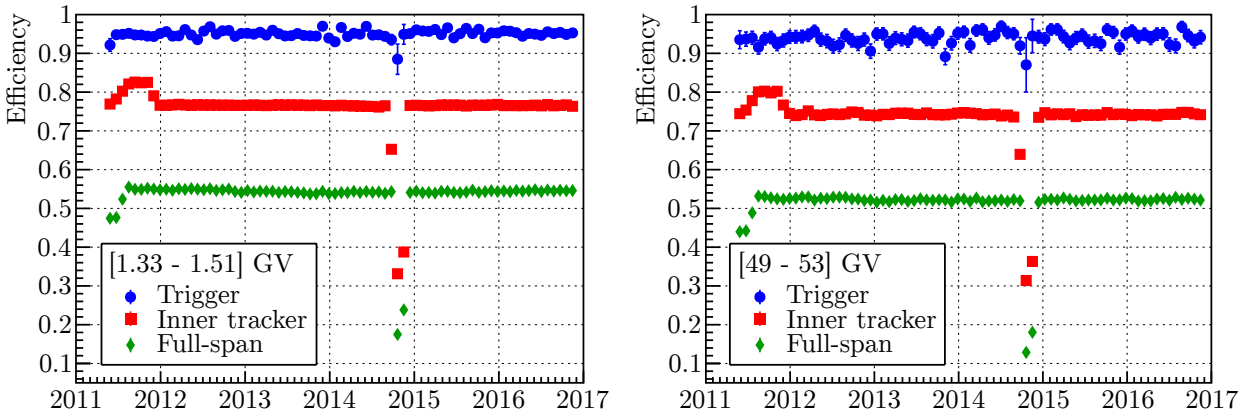

Figure 3.30: Time dependence of the AMS proton efficiencies, for two different rigidity bins: trigger (blue), inner tracker (red) and full-span (green).

For the trigger efficiency no long-term trend is visible, only statistical fluctuations, especially at high rigidity. The inner tracker and full-span efficiencies display some steps, in correspondence to know events related to the tracker: for example, the increase in both efficiencies in the first months is due to the new reconstruction algorithm of the tracker, while the drop in the inner tracker efficiency at the end of 2011 is due to 6 broken ladders scattered across multiple planes of the inner tracker. The drop in all efficiencies in October and November 2014 is due to the failure of one of the four

cooling pumps: to avoid damages to the remaining pumps, the collaboration decided to switch off the tracker thermal control system (TTCS) and, alternatively, one side of the tracker for two months, to study the behavior of the cooling system, before turning it on again in December 2014.

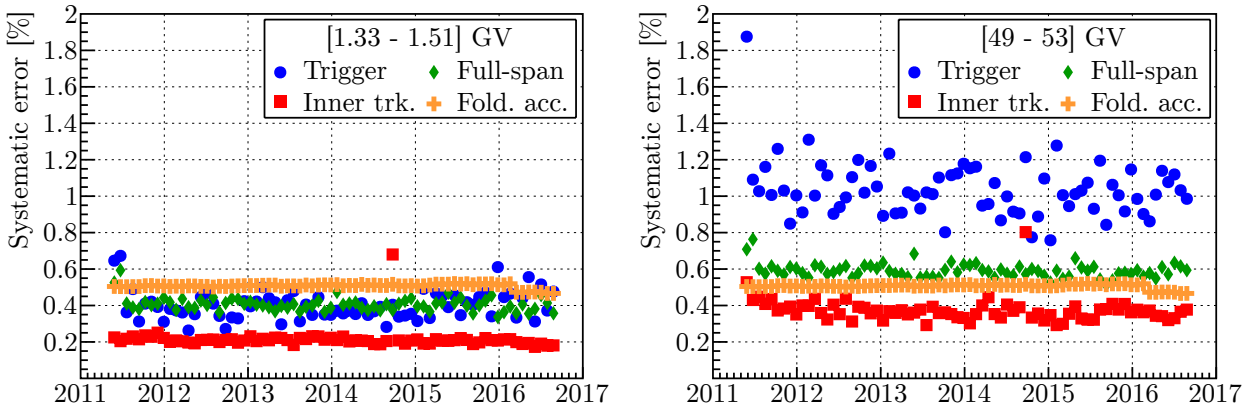

Figure 3.31: Time dependence of the systematic error associated with the efficiencies, for two different rigidity bins: trigger (blue), inner tracker (red), full-span (green) and folded acceptance (orange).

The systematic errors were estimated separately for each BR and they resulted to be pretty stable in time and consistent with the published ones, as shown in Figure 3.31, where the systematic errors due to the parametrizations of the efficiencies and the folded acceptance are reported. As expected, the error on the trigger efficiency is the one which fluctuates most, especially above few tens of GV, because of the low statistics of the unbiased trigger sample.

3.10 The proton and helium monthly fluxes

The description of the helium flux analysis is beyond the scope of this work, but the procedure is very similar to the one used for the proton flux, with an additional correction due to the fragmentation of helium nuclei in the upper part of the detector. The fluxes presented in this section are the results of the work of Cristina Consolandi, to be published in future by the AMS collaboration.

Figure 3.32 left shows all the proton and helium monthly fluxes measured by AMS as colored lines. The colors go from blue shades to red shades, where dark blue is the first time interval (BR 2426, May 20 – June 10, 2011) and dark red is the last time interval (BR 2500, November 2 – 26, 2016). The red lines are higher than the others because they correspond to the descending phase of the solar cycle 24, when the solar modulation strength is declining, while the green lines correspond to the months of the solar maximum, when the solar modulation strength was at its peak, and so they are the lowest ones. The fluxes measured at the beginning of the mission, the blue lines, are hidden behind the fluxes collected at later dates with a similar level of modulation strength. For comparison, the published proton and helium flux measured by AMS are plotted in black squares.

They nicely sits in the middle of the variation band encompassed by the monthly fluxes: the publication period was from May 20, 2011 to November 26, 2013, which corresponds to the rising phase of the solar cycle 24 and the beginning of the maximum. The total time period analyzed in this work is roughly two times longer than the published one and, by chance, it's symmetric around the solar maximum, thus the published flux represents the average flux measured by AMS from May 2011 until the end of 2016. Figure 3.32 right focuses on the proton flux: the time runs from right to left on the X axis, while the rigidity is on the Y axis and the flux value on the vertical axis. Red shades represent high intensities of the flux, while blue shades low intensities. This 3D view allows to better appreciate the time variation of the flux. The effect of the solar modulation is clearly visible: the flux in 2011 is at moderate intensities, it starts decreasing, reaching a minimum value around 2014, and then recovers, until in 2016 it surpasses the intensity observed at the beginning of the mission. In addition to this long-term trend, there are many variations due to short-term solar activity and transient phenomena, like CMEs and co-rotating interaction regions (CIRs), which causes temporary decreases in the flux. These variations are analyzed in detail in the PhD thesis by Kathryn Whitman [32].

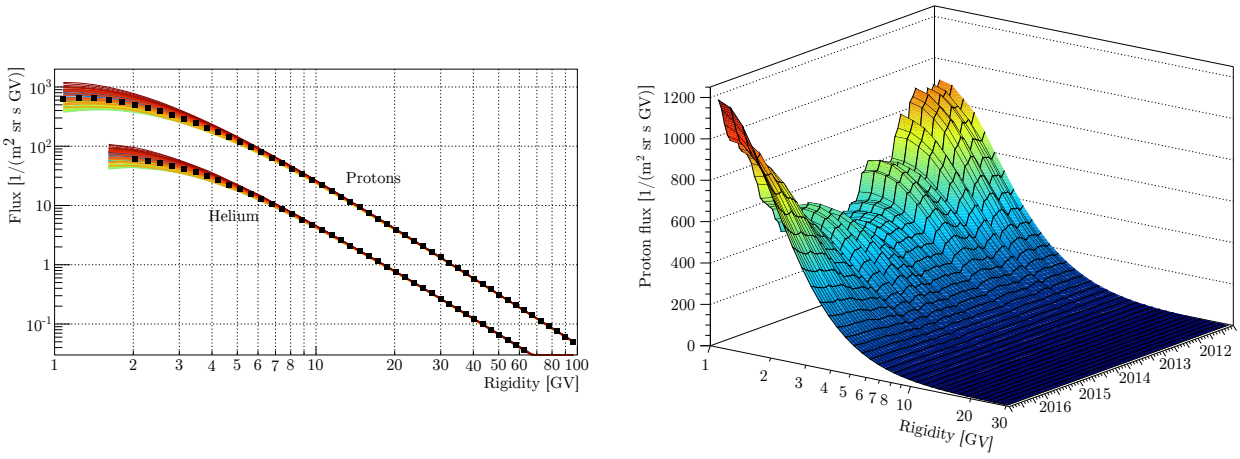

Figure 3.32: **Left**: Proton and helium monthly fluxes measured by AMS (colored lines). In black, for reference, the published proton and helium flux. **Right**: 3D visualization of the monthly proton fluxes, with time on the X axis, rigidity on the Y axis and the flux on the Z axis. Blue shades correspond to low intensity, red to high intensity.

The time dependence of selected rigidity bins is displayed in Figure 3.33. The top panel shows the daily SSN [133], smoothed with a 27-day long moving average, and the line-of-sight average tilt angle of the heliospheric current sheet (HCS)[5] [134]; the two vertical dashed lines mark the beginning and the end of the period during which the magnetic field of the Sun reversed [135]. The middle and bottom panel show, respectively, the variation of the proton and helium flux. The monthly fluxes are normalized to the value observed in the first BR, separately for each rigidity

[5]Tilt angle data have been downloaded from the WSO: `http://wso.stanford.edu/Tilts.html`

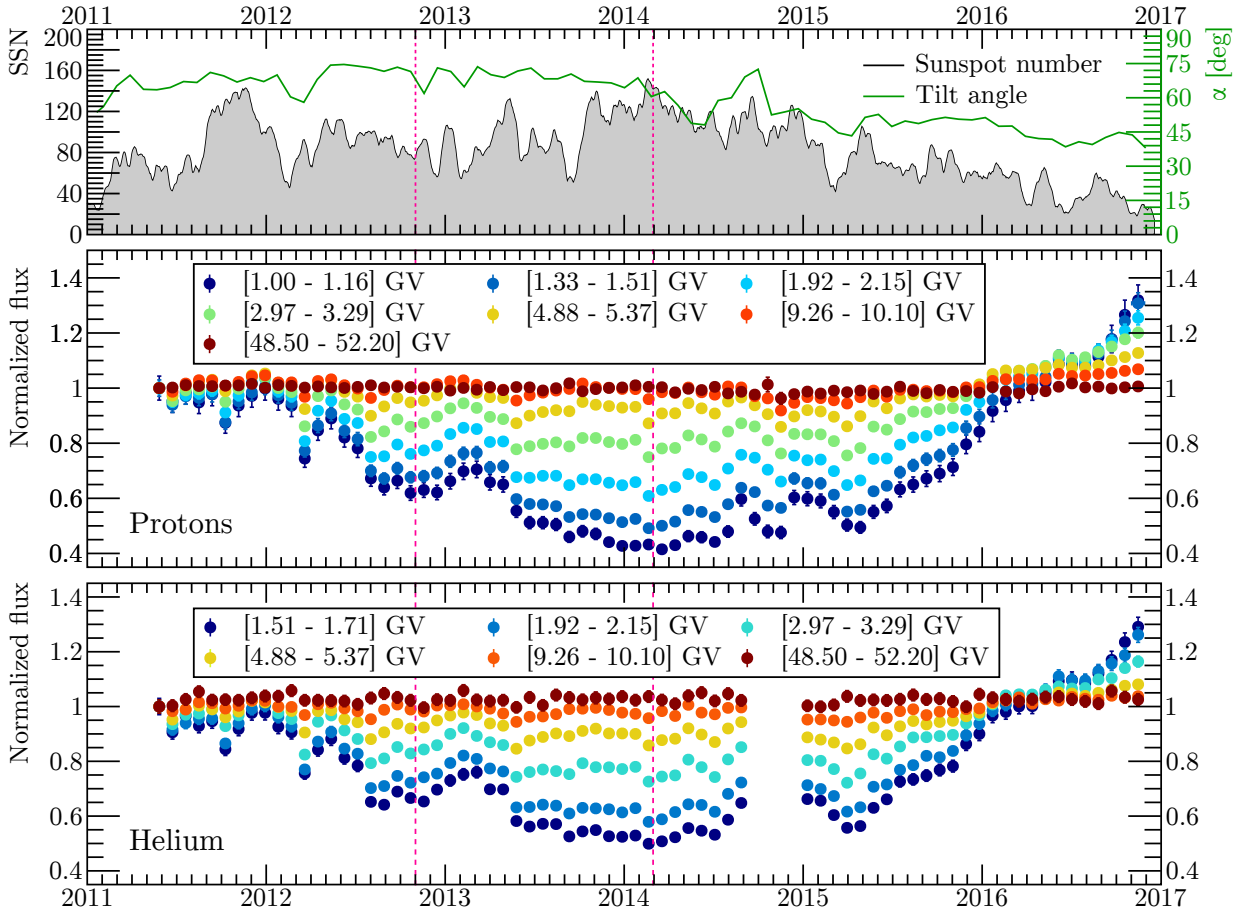

Figure 3.33: **Top**: Daily sunspot number (SSN) (black) and tilt angle (green). The vertical dashed magenta lines mark the period of magnetic polarity reversal. **Middle** and **Bottom**: Time dependence of selected bins of, respectively, proton and helium fluxes. The fluxes are normalized to the value measured in the first BR (May 15 – June 10, 2011).

bin. The dark blue circles are the lowest rigidity bin, respectively (1–1.16) GV for protons and (1.51–1.71) GV for helium. The dark red circles are an intermediate rigidity bin (around 50 GV) where the solar modulation effects are not anymore distinguishable from statistical fluctuations. The long-term trend due to the different phases of the solar cycle is clearly visible, especially for the lowest rigidity bins, as well as all the short-term variations. The BRs during which the TTCS was off were not analyzed for the helium. Of notable interest is the drop in March 2012, where the second strongest solar event of this cycle occurred, followed by the most intense Forbush decrease (FD), which lasted for 20 days and affected rigidities up to 30 GV. After this event, the spread in the fluxes at different rigidities increases a lot, while before the fluxes were less modulated. The minimum of the flux happened around February 2014 at all rigidities, except for the lowest proton bin, which attained the minimum between March and April 2014. At the peak of the solar activity,

protons at 1 GV were reduced by 60 % with respect to May 2011. In May 2015, the flux starts rising, displaying also less short-term variations, until it reaches and exceed the value observed in May 2011 in the first months of 2016, depending on the rigidity. For the lowest rigidities, the flux at the end of 2016 was 30 % higher than in the first month or 90 % higher than the observed minimum flux.

The GCR intensity will keep increasing at all rigidities, going towards the minimum of the solar activity, predicted for 2020 (see, for example, `https://solarscience.msfc.nasa.gov/predict.shtml`). If the next minimum will be even weaker than the previous one in 2009, as it is believed by the general decreasing trend in solar activity in the last two decades, then the flux of all GCRs will be the highest ever observed since the start of the space age, posing problems for any deep-space human exploration program. In July 2012 there was a decrease caused by a passing CME which, contrary to the others FDs, did not recover in the next days. The flux remained low for several months, until in May 2013 there was another sharp drop at all rigidities, this time not associated to any local disturbances in the solar wind. After that, the flux persisted at a very low level of intensity until August 2014. Furthermore, while before the drop all rigidities seemed to be modulated in the same way, after May 2013 the flux in the lowest rigidity bin kept decreasing, while above 2 GV stayed flat. The drop happened roughly 6 months after the beginning of the magnetic field reversal, so this strange behavior could be related to the different way in which charged particles propagate in the heliosphere with no well-defined polarity.

3.10.1 Solar modulation effects at different rigidities

In this section, a method to determine if different rigidities are affected in the same way by the solar modulation is presented. As discussed before, there is at least a period, during the polarity reversal, in which this does not seem to be the case, so we would like to statistically quantify if this is true or not. The method does not rely on any particular theory of solar modulation, but only on the assumption that the solar modulation is a phenomenon whose strength depends monotonically on the rigidity: if the solar activity increases, GCRs at all rigidities will decrease, with the intensity of the decrease inversely proportional to the rigidity; vice versa, if the solar activity decreases, GCRs at all rigidities will increase. Eventually, high rigidity particles will be unaffected by solar modulation, thus invalidating the assumption, but here we concentrate only on the low-rigidity range, below 20 GV, where the effects are still visible.

Given the assumption, we expect the flux at different rigidities to be positively correlated, *i.e.* $\rho(R_1, R_2) > 0$, where ρ is the Pearson's correlation coefficient between the flux at different rigidities. The strategy is to compute the correlation coefficient between a given rigidity bin and the lowest bin (where the modulation effects are larger), look for the highest rigidity for which the correlation is not consistent with zero at the 95 % confidence level and then see if it depends on time or not. For this study, we will use only the proton fluxes, since they have smaller errors and thus a higher

significance. Figure 3.34 shows few examples of correlation plots between different bins and the bin at (1–1.16) GV, considering all the monthly fluxes. We can see that the correlation worsen at high rigidities, because statistical fluctuations increase while the modulation effects fade away.

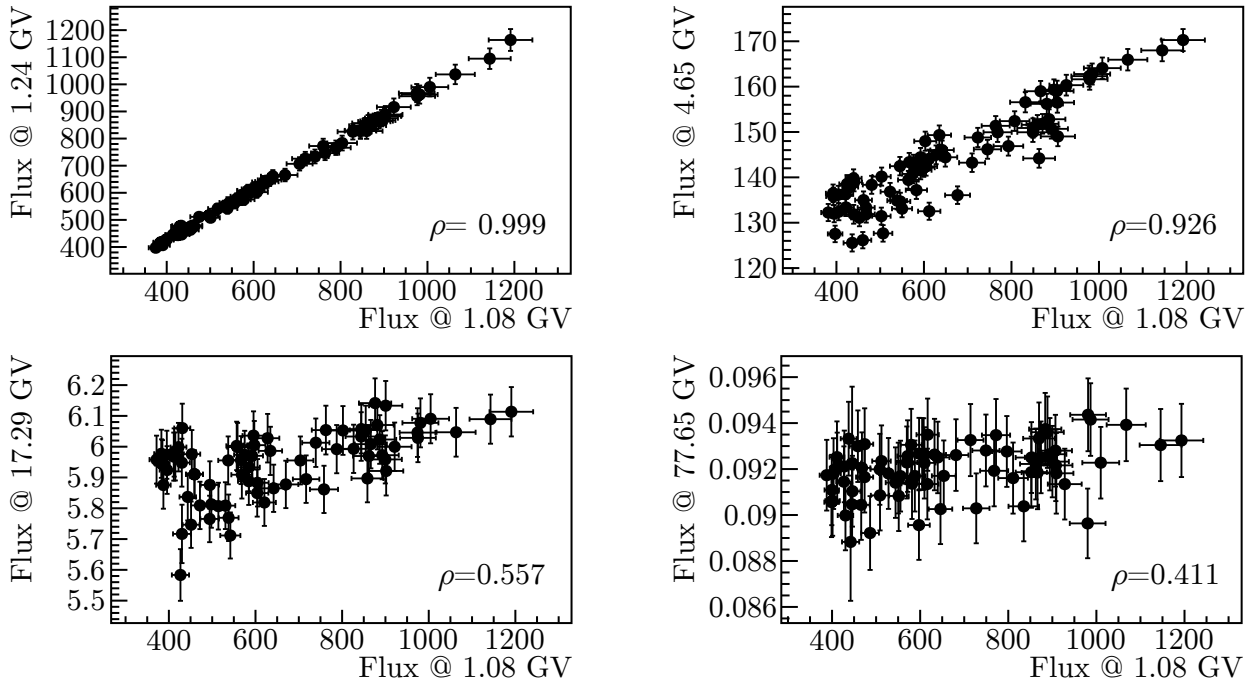

Figure 3.34: Correlation plots between different rigidities and the lowest bin, for all the monthly fluxes.

Given an observed correlation coefficient r, we can use the Fisher transformation $F(r) = \operatorname{arctanh} r$. It can be shown that $F(r)$ is normally distributed with $\mu = F(\rho)$ and $\sigma = 1/\sqrt{n-3}$, where ρ is the true correlation and n is the number of data points. We can then perform a two-tailed *Z-test* to reject the null hypothesis $\rho = 0$. Let's define $z = (F(r) - \mu)/\sigma = F(r)\sqrt{n-3}$: this variable will be distributed as a standard gaussian, so that the p-value is $P(Z < |z| \mid H_0 : \rho = 0) = 2\int_{|z|}^{\infty} N(0,1)\, dZ$. The Pearson correlation is computed assuming a perfect knowledge of the data, but this is not true. To take into account the errors on the measured fluxes, a toy MC is used: 10^4 samples are generated in which each data point is randomly picked according to a normal distribution with the mean equal to the measured flux and the sigma equal to the flux uncertainty, *i.e.* $\Phi_{MC}(R,t) \sim N(\Phi_{AMS}(R,t), \sigma_{AMS}(R,t))$. For each sample, the correlation coefficient and the corresponding p-value are computed and their distribution in every bin is used to derive the median value and the confidence intervals. An example of the results of the toy MC is displayed in Figure 3.35 for two bins: the central panels show the distribution of the correlation coefficient, together with the median value (dashed line) and the 68 % central confidence interval (gray area); the right panels show the distribution of the p-value, together with the median value and the confidence

interval. In the first row, the correlation for the bin (12–13) GV is clearly not consistent with zero: the distribution of ρ is far from zero, while the maximum p-value is less than 10^{-4}, *i.e.* $\rho \neq 0$ with a significance of more than 4σ. In the second row, the correlation for the bin (80.5–86.5) GV is consistent with zero: the lower edge of the confidence interval of the ρ distribution is in fact negative, and the median p-value is greater than 0.1, thus we cannot reject the null hypothesis with a 95 % confidence level.

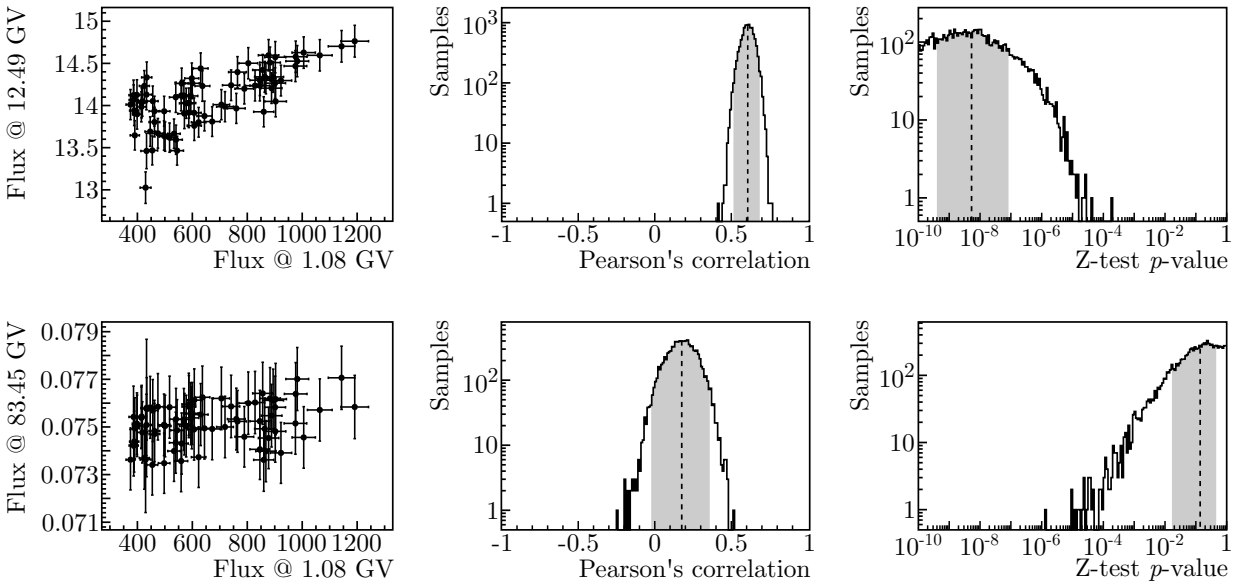

Figure 3.35: Toy MC distributions of the correlation coefficient and *p-value for two selected bins.*

Figure 3.36 shows the rigidity dependence of the median values of the correlation coefficient and the p-value, together with the confidence intervals. Choosing a conservative approach, we can use the upper limit of the p-value to find the maximum rigidity R_M with a correlation not consistent with zero at the 95 % confidence level, by looking for the crossing point of the upper edge of the pink band with the 2σ line. Considering all the monthly fluxes together, this rigidity is 22 GV.

Incidentally, this method can be used to get an estimate of the maximum rigidity below which solar modulation effects are statistically significant, given the error on the measured fluxes. In Section 3.10.2 additional statistical tests to find the maximum rigidity at which rigidity AMS is sensitive to the solar modulation are presented.

In order to study the time dependence of the rigidity R_M for which $\rho(R_M, R_1)$ is consistent with zero, we repeat the study on sliding windows of variable length[6]. The formula for the p-value requires at least 4 data points to be defined, but we found that a minimum of 6 data points are needed to have $R_M > R_1$. The reason is that, with few data points, the variation due to the errors is too big and all the correlations are consistent with zero. We chose a window length of 12 BRs as

[6]We acknowledge the use of `GNU Parallel` [136] for the parallelization of this analysis pipeline.

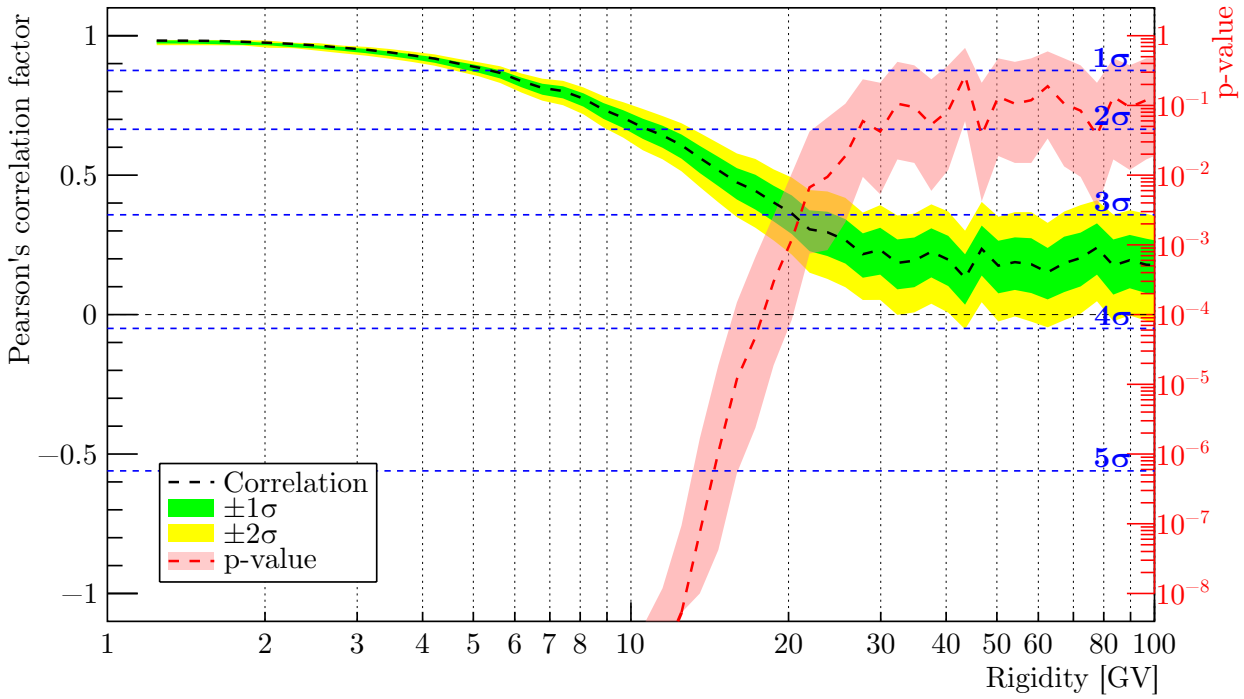

Figure 3.36: Rigidity dependence of the correlation coefficient (black dashed line) and p-value (red solid line), for all the monthly fluxes. The green and yellow bands represent, respectively, the 1σ and 2σ confidence intervals for the correlation, while the pink band is the 1σ confidence interval for the p-value. The horizontal dashed blue lines indicate the $n\sigma$ levels of significance.

a good trade-off between statistical significance and time resolution. The time dependence of R_M is shown in Figure 3.37 bottom, while, for comparison, the normalized flux for three rigidity bins is displayed in the top panel.

The solid black line is the 2σ contour for R_M, *i.e.* at a given BR, the rigidities below are not consistent with $\rho = 0$ at the 95 % confidence level for the next 12 BRs. The horizontal dashed black line indicates the minimum rigidity that can be tested, which corresponds to the second rigidity bin of AMS, (1.16–1.33) GV. A heat map represents the significance level in σ, with dark blue being 0σ and dark red being 5σ. The red circle highlights the period between August and November 2014 in which $R_M \lesssim 1.16$ GV, *i.e.* no rigidity bin is correlated with the lowest bin. The red ellipse in the top panel covers the corresponding BRs contained in the three windows starting in the period identified before. Our observation that during the period of maximum solar activity and polarity reversal the flux behaves differently at different rigidity is hereby confirmed by this study. Furthermore, there is another period in which R_M falls below 2 GV, around June/July 2012, when the decrease with the very slow or no recovery happened.

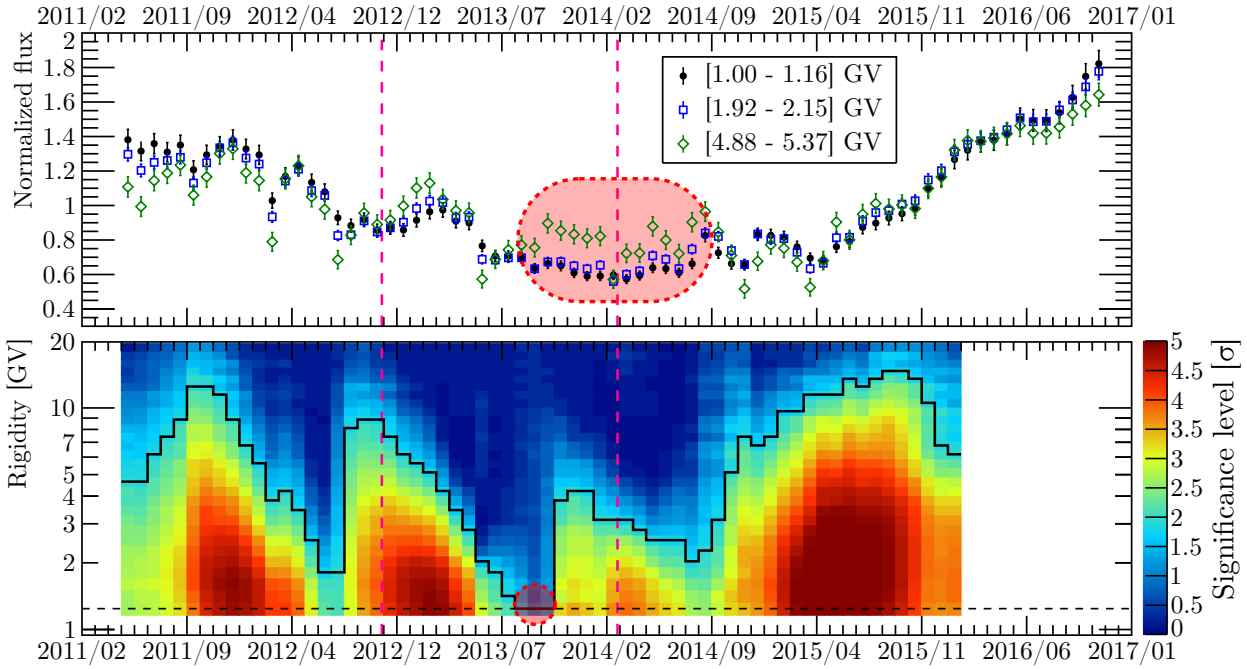

Figure 3.37: Time dependence of the maximum rigidity not consistent with zero correlation, using a sliding window of length 12 BRs. **Top**: Proton flux for the bins (1–1.16) GV (black), (1.92–2.15) GV (red) and (4.88–5.37) GV (green), normalized to the respective average values. The two vertical lines mark the magnetic field reversal period. The red ellipse highlights the fluxes measured in the period corresponding to the red circle in the bottom plot. **Bottom**: Heat map of the statistical significance for the test $\rho(R, R_1) \neq 0$: time on the X axis, rigidity on the Y axis. Dark blue is 0σ, while dark red is 5σ. The solid black line represents the 2σ contour, while the horizontal dashed black line indicates the minimum rigidity for which the test can be performed. The red circle highlights the period in which R_M is less or equal to this minimum rigidity.

3.10.2 Maximum rigidity affected by the solar modulation

What is the maximum rigidity at which AMS is still sensitive to solar modulation effects? The answer to this question depends on two factors: how much the solar modulation strength decreases at higher rigidities and the value of the errors on the measured fluxes. If a quantity is constant in time, it means that every data point y is distributed according to a gaussian with a mean equal to the true value of the constant, estimated as the average $\bar{y}$, and a sigma equal to the data uncertainty σ_y. We expect the residuals $r = (y - \bar{y})/\sigma_y$ to be randomly distributed around zero, *i.e.* r should follow a standard normal distribution: this is the null hypothesis, against which the data will be tested. Many statistical tests exist in literature to quantify the agreement between a set of measured values and a given distribution: for this study, we chose four of them.

1. **Wald-Wolfowitz runs test**. This test counts how many times the residuals change from

positive to negative and vice versa, assuming that the negative and positive residuals are independent and identically distributed. If there is a trend in time, there will be more positive (or negative) residuals and/or the number of sign changes will be too few.

2. **Pearson chi-squared test**. This is the same test used in the least-square fit: the sum of the squares of the residuals should be distributed as a χ^2 with $n-1$ degrees of freedom, where n is the number of data points. This test checks how big is any discrepancy from zero. The chi-squared test and the runs test are non-parametric and complementary: the first one tests the distance, but not the sign; the second one tests the sign, but not the distance.

3. **Anderson-Darling test**. This test is based on the empirical cumulative distribution function and explicitly checks if the residuals are coming from a gaussian distribution with $\mu = 0$ and $\sigma = 1$. It's particularly sensitive to residuals in the tails of the gaussian.

4. **Kolmogorov-Smirnov test**. It is similar to the Anderson-Darling test, checking explicitly for a gaussian with $\mu = 0$ and $\sigma = 1$, but it's less powerful.

For each rigidity bin, the residuals and the p-value of the four tests are computed, then we look for the maximum rigidity R_M for which the p-value becomes greater than 5 %. The results of the tests will be slightly different, since each of them is sensitive to a different property of the residuals. When computing the residuals, it's important to use the right uncertainty as σ_y: in principle, any error which does not depend on the time should not be taken into account, because it's effect on the time variation of the flux would be a rigid shift in the same direction for all the months. As we saw in Section 3.9, the systematic errors related to the smoothing parametrization of the efficiencies and acceptance seem to be stable in time, fluctuating around a constant value. A similar time behavior is seen in the systematic uncertainties due to the selection cuts, the cross-sections and the rigidity measurement. If we consider all the systematic errors to be constant, then σ_y would be equal to the statistical error only. However, such assumption could be too much optimistic, so all the tests were performed twice, once with $\sigma_y = \sigma_{stat}$ and once with $\sigma_y = \sigma_{stat} \oplus \sigma_{syst}$. These are two extremal cases, so the correct result will be somewhere in between.

Figure 3.38 show the rigidity dependence of the p-values of the tests. For protons, considering only the statistical error, R_M is around 55 GV for all the tests, except for the Pearson test, which yields $R_M = 70$ GV. When the total error is used, R_M decreases to 18 GV for the Pearson test, 16 GV for the Anderson-Darling test and 12 GV for the Kolmogorov-Smirnov. The Wald-Walfowitz test p-value does not change, because it's independent from the value of the errors. As we can see, the choice of the error has a profound effect on the maximum rigidity. In the previous Section, from the correlation study we found that $R_M = 22$ GV, when using all the monthly fluxes. Since the correlation method compares two different bins with their total errors, we expect 22 GV to be a lower limit to the real maximum rigidity, meaning that the values found from the tests using the

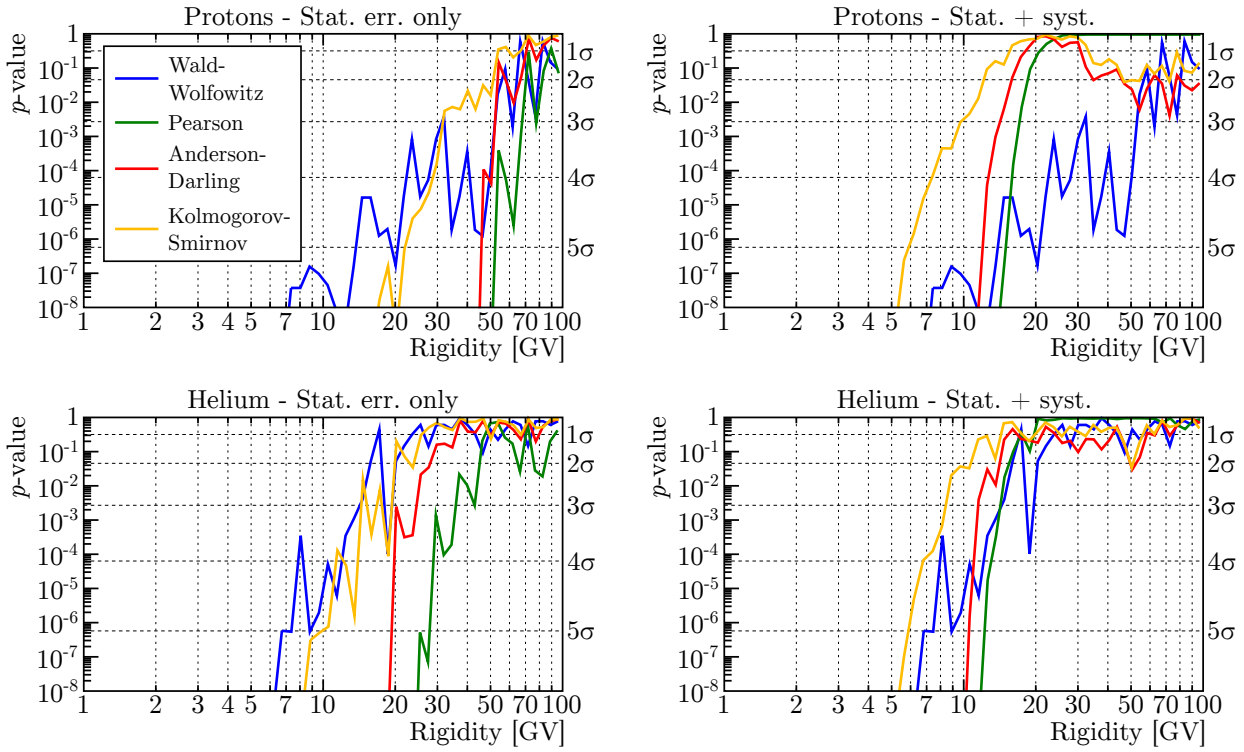

Figure 3.38: Rigidity dependence of the p-value of different statistical tests (colored lines) for finding the maximum rigidity affected by solar modulation in AMS for protons (**top**) and helium (**right**), considering only statistical errors (**top**) and the sum in quadrature of statistical and systematic errors (**bottom**).

total error are too conservative. At the same time, $R_M = 70\,\text{GV}$ from the Pearson test with the statistical error only is probably too high. We can conclude that the solar modulation effects in the protons measured by AMS are still visible above 22 GV and disappear for sure above 50 GV. Looking at the helium results, we find that, considering only the statistical error, R_M is 16 GV for the Wald-Wolfowitz test, 20 GV for the Kolmogorov-Smirnov, 28 GV for the Anderson-Darling test and 46 GV for the Pearson test. Using the total error, all the tests give a similar R_M around 15 GV. Making the same considerations as for protons, AMS is able to distinguish solar modulation effects in the helium flux up to at least 15 GV. Overall, the Kolmogorov-Smirnov seems the most conservative test, while the Pearson test is probably too sensitive to large fluctuations.

3.10.3 Time dependence of the proton-to-helium ratio

Figure 3.39 shows the time dependence of the proton-to-helium ratio for selected rigidity bins. The daily SSN and the tilt angle are displayed on the top panel as reference. If the solar modulation was only a rigidity-scaling phenomenon, we would expect protons and helium with the same rigidity to modulate in the same way and thus the proton-to-helium should remain constant in time. With

respect to the separate proton and helium fluxes, p/He is indeed stable in time at all rigidities, except maybe in the first few bins. To quantify if and up to which rigidities the time variation is not consistent with a flat behavior, the same statistical tests described in the previous section were performed on the proton-to-helium ratio and the results are shown in Figure 3.40. Considering only statistical errors, R_M is equal to 3 GV for the Kolmogorov-Smirnov test, 3.5 GV for the Anderson-Darling test, 4 GV for the Wald-Wolfowitz test and 5.5 GV for the Pearson test. A strange structure is present in the Pearson p-value between 10 and 20 GV. As noted before, the Pearson test is very sensitive to large fluctuations: indeed, inspecting the time dependence of the residuals for the corresponding rigidity bins, there are few isolated clusters of three to four data points with $|r| > 3$. We do not think this structure is indicative of a time dependence of p/He at these rigidities: most probably, it is a combination of statistical fluctuations and some residual systematic effect due to the analysis.

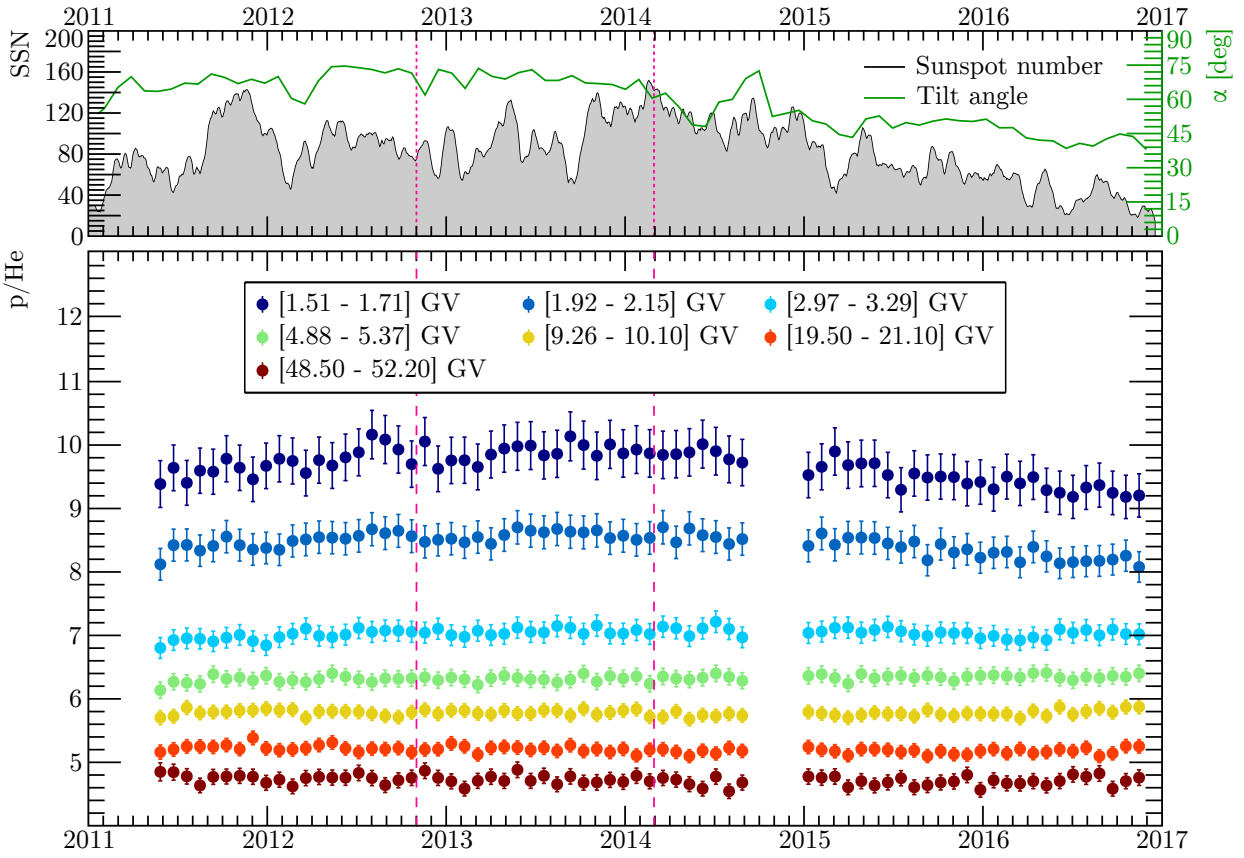

Figure 3.39: **Top**: Daily SSN (black) and tilt angle (green). The vertical dashed magenta lines mark the period of magnetic polarity reversal. **Bottom**: Time dependence of selected bins of the proton-to-helium ratio.

Taking into account the total error, all tests, except the Wald-Wolfowitz, which is independent

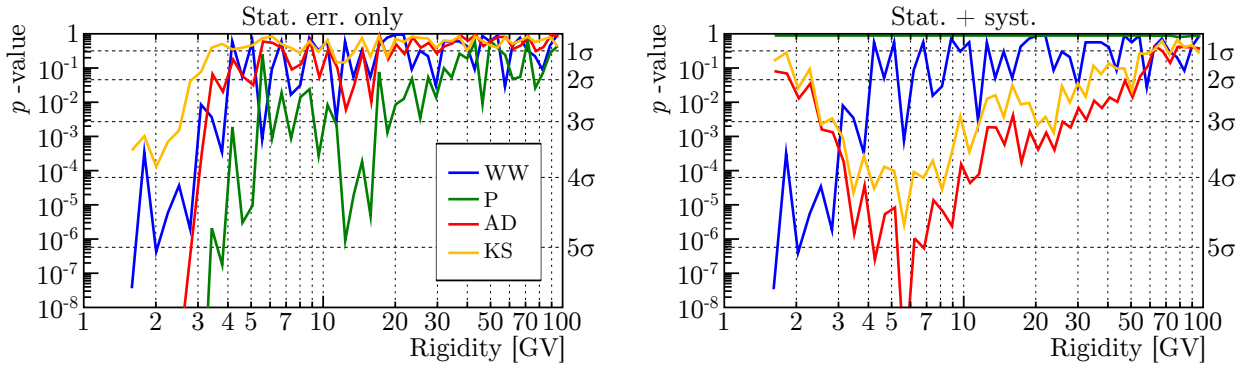

Figure 3.40: Rigidity dependence of the p-value of different statistical tests (colored lines) for finding the maximum rigidity affected by solar modulation in AMS for the proton-t-o-helium, considering only statistical errors (**left**) and the sum in quadrature of statistical and systematic errors (**right**).

from the errors, are consistent with a constant value of the proton-to-helium ratio. The Pearson p-value is always very close to 1, because the errors are too big for any time variation to be statistically significant. The Anderson-Darling and Kolmogorov-Smirnov p-values drop below 2σ between 2.5 GV and few tens of GV. However, this does not mean that p/He is changing in this rigidity range: in fact, the ratio is very flat, but the errors are so big that the width of the distribution of the residual is smaller than 1. Since these two tests are designed to verify if the parent distribution of the residual is a gaussian with $\mu = 0$ and $\sigma = 1$, their p-value indicates a significant departure from the null hypothesis, since $\sigma \ll 1$. If anything, this may suggest that the total error on the proton-to-helium ratio is overestimated in this rigidity range: indeed, we simply propagated the total errors from protons and helium, while a more accurate study of the systematic errors could reveal some correlation between the uncertainties of the two analysis, for example in the unfolding procedure.

In conclusion, there is evidence that the proton-to-helium ratio is time dependent below 3 GV. At these low rigidities, protons and helium are in different relativistic regimes, so they could be affected by any velocity- or mass-dependent process. Indeed, the diffusion coefficient is proportional to β, so a different behavior of protons and helium is not completely unexpected . Furthermore, the spectral index of their local interstellar spectrum (LIS) is not the same, so even if the solar modulation was only depending on rigidity, the diverse starting spectrum would induce differences in their propagation: for example, the term describing the adiabatic energy losses or gains contains $1/3(\partial f/\partial \log R)$, which is proportional to the spectral index. Complicating this matter is also the fact that helium in GCRs is actually a mixture of two different isotopes, ^{4}He and ^{3}He, whose ratio in the interstellar medium (ISM) is not known. The convolution of all these effects is likely to produce the observed difference in modulation between protons and helium, but their relative contribution is yet to be thoroughly understood.

CHAPTER 4

THE LOCAL INTERSTELLAR SPECTRUM OF PROTONS AND HELIUM AND THE MODIFIED FORCE-FIELD APPROXIMATION

Until few years ago, the majority of the local interstellar spectrum (LIS) parametrizations found in literature were based on spacecraft and balloon measurements of galactic cosmic rays (GCRs) before *Voyager 1* entered the interstellar space and did not take into account the change of spectral index at high rigidities ($R \gtrsim 300\,\mathrm{GV}$), which has been observed by PAMELA [137] and AMS [89]. The availability of the high-accuracy high energy proton flux from AMS and the low energy proton flux from *Voyager 1* represents an important progress towards the reduction of the uncertainty on the LIS shape, enabling a more accurate determination of the solar modulation parameter and improving the understanding of GCR propagation in the heliosphere. Figure 4.1 shows the ratio of *Voyager 1* [5] and AMS [89] proton fluxes and of various proton LIS parametrizations to the one used in [138] to extract the solar modulation parameter from neutron monitors (NMs) (from now on called BPH00). It is clear that the new data from *Voyager 1* and AMS are not well described by these LIS estimates. These discrepancies compel us to find a new parametrization based on the new results from *Voyager 1* and AMS.

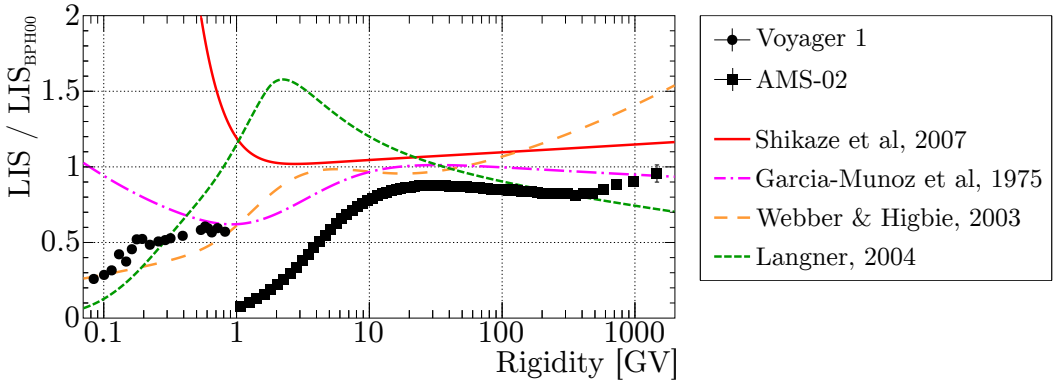

Figure 4.1: Ratio of various proton LIS estimates (lines) [139, 140, 141, 142] and *Voyager 1* (dots) and AMS (squares) proton fluxes to the BPH00 parametrization.

4.1 A new parametrization for the proton LIS

For the high-rigidity end of the proton LIS we use the parametrization adopted by the AMS collaboration [89] to describe a double power-law:

$$R^{\gamma}\left[1+\left(\frac{R}{R_b}\right)^{\Delta\gamma/s}\right]^{s}, \tag{4.1}$$

where $\Delta\gamma$ is the change in spectral index, R_b is the rigidity where the two power-laws cross each other and s determines the smoothness of the change ($s=0$ means a broken power-law). Recently, the analysis of γ-ray emissions from giant molecular clouds pointed to a low-energy break around 9 GeV, with the spectral index changing from ≈ -2 to ≈ -3 [143]. We generalize Equation 4.1 to describe two power-law breaks:

$$R^{\gamma_1}\left\{1+\left[\frac{R}{R_{b1}}\left(1+\left(\frac{R}{R_{b2}}\right)^{\Delta\gamma_2/s_2}\right)^{s_2}\right]^{\Delta\gamma_1/s_1}\right\}^{s_1}, \tag{4.2}$$

where the indices 1 and 2 stand for the low- and high-rigidity break respectively: if $R \ll R_{b1}$, Equation 4.2 reduces to $\approx R^{\gamma_1}$; if $R_{b1} \ll R \ll R_{b2}$, Equation 4.2 becomes $\approx R^{\gamma_1+\Delta\gamma_1} = R^{\gamma_2}$; and if $R \gg R_{b2}$, Equation 4.2 goes as $\approx R^{\gamma_1+(1+\Delta\gamma_2)\Delta\gamma_1} = R^{\gamma_3}$.

To describe the rigidity range spanned by the *Voyager 1* data, we note that if we divide the *Voyager 1* proton flux by a generic power law, as shown in Figure 4.2, the resulting ratio looks like a sigmoid function in $\ln R$; we assume the following parametrization to describe this ratio:

$$\left[1+\exp\left(-\frac{\ln R-\mu}{\sigma}\right)\right]^{-1/\nu}, \tag{4.3}$$

where μ is related to the rigidity where the ratio is 1/2, σ determines the steepness of the rise and ν describes a possible asymmetry.

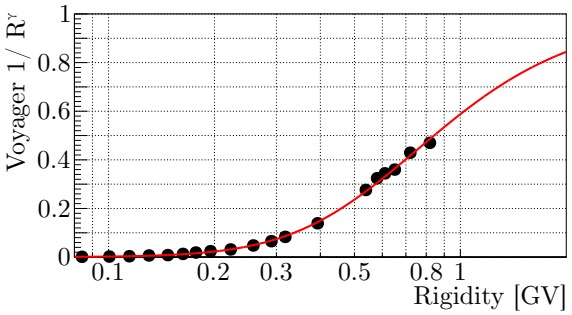

Figure 4.2: Ratio of the proton flux measured by *Voyager 1* to R^{γ} ($\gamma = -2$). The solid line is the formula in Equation 4.3.

The new parametrization for the LIS is therefore:

$$\frac{dJ_{LIS}}{dR}(R) = N\left[1+\exp\left(-\frac{\ln R-\mu}{\sigma}\right)\right]^{-1/\nu} R^{\gamma_1}\left\{1+\left[\frac{R}{R_{b1}}\left(1+\left(\frac{R}{R_{b2}}\right)^{\Delta\gamma_2/s_2}\right)^{s_2}\right]^{\Delta\gamma_1/s_1}\right\}^{s_1}, \tag{4.4}$$

where N is a normalization factor.

The available data in the rigidity range up to a few tens of GV are all affected by the solar modulation, hence a simple fit of Equation 4.4 to *Voyager 1* data and AMS data above 100 GV (to remove any residual modulation) is not able to correctly constrain all the parameters, especially γ_1, R_{b1}, $\Delta\gamma_1$ and s_1. To resolve this issue, we proceed by simultaneously fitting *Voyager 1* data with Equation 4.4 and AMS data with Equation 4.4 modulated with the force-field approximation; this way, we obtain at the same time the parameters for the LIS and the average solar modulation parameter throughout the AMS data time period. The least-squares fit is done with `MINUIT` [144], minimizing the following quantity:

$$\begin{aligned}\chi^2_{glob} &= \chi^2_{V1} + \chi^2_{AMS} = \\ &= \sum_i \frac{1}{\sigma^2_{V1}(i)}\left(y_{V1}(i) - \frac{1}{\Delta R_i}\int_{R_i}^{R_{i+1}} \frac{dJ_{LIS}}{dR}(R)\,dR\right)^2 + \\ &+ \sum_i \frac{1}{\sigma^2_{AMS}(i)}\left(y_{AMS}(i) - \frac{1}{\Delta R_i}\int_{R_i}^{R_{i+1}} \frac{dJ}{dR}(R)\,dR\right)^2\end{aligned} \tag{4.5}$$

where i is the binning index, R_i and R_{i+1} are the bin edges and $\Delta R_i = R_{i+1} - R_i$, $y(i)$ and $\sigma(i)$ are respectively the data and its associated error in the i-th bin and dJ/dR is defined as in Equation 1.36 after converting from kinetic energy to rigidity. *Voyager 1* errors are only statistical, so they over-constrain the LIS parameters. The result of the fit ($\chi^2_{glob}/\mathrm{dof} = 56/79$) is shown in Figure 4.3 and the fitted parameters are presented in Table 4.1:

The PAMELA experiment published the proton flux between 0.4 and 50 GV, integrated in Carrington rotation periods, from July 2006 to January 2010[1] [146]. This dataset provides valuable information for understanding the impact of the solar modulation on the differential flux. Using the force-field approximation from Equation 1.36, we fit the PAMELA data with the LIS in Equation 4.4. In order to take into account the uncertainty on the LIS in the error on the fitted ϕ, we also fit the PAMELA data with the LIS plus or minus the 1σ confidence interval, thus getting $\phi_{\pm1}$, and we take the difference $|\phi - \phi_{\pm1}|$ as an estimate of the error due to the LIS. Figure 4.4 illustrates examples of the fit results for the proton flux measured by PAMELA between July 2006 and March 2008 (from now on called integral flux) and during Carrington rotations 2045, 2060 and 2066 (2006 Jul 7 - 26; 2007 Aug 13 - Sep 6; 2008 Jan 24 - Feb 19); Table A.1, columns 3 to 5, presents the

[1]Tables for all the Carrington rotation periods are available online in the cosmic ray database of the Italian Space Agency: `http://tools.asdc.asi.it/cosmicRays.jsp`

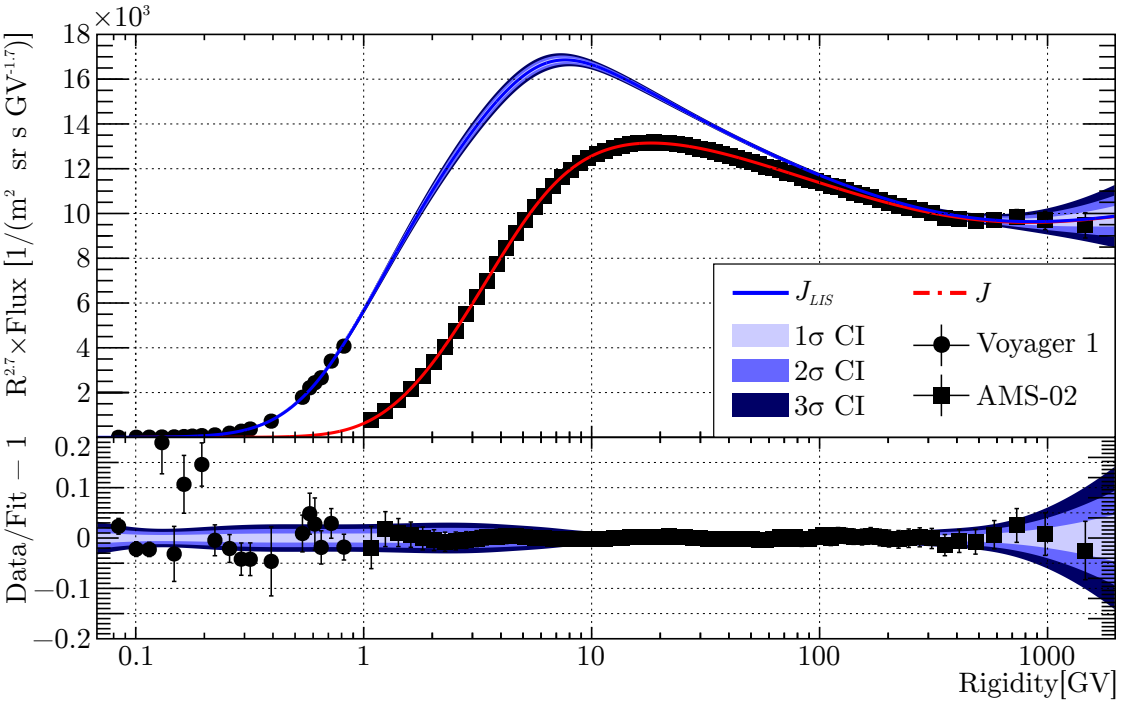

Figure 4.3: **Top**: Combined least-squares fit of *Voyager 1* proton data (dots) with J_{LIS} (solid line) and AMS proton data (squares) with J (dashed-dotted line). The shaded bands represent the 1, 2 and 3 σ confidence intervals around the best fit. Data and fit are rescaled by $\widetilde{R}^{2.7}$: see [145] for the definition of $\widetilde{R}$. **Bottom**: Fit residuals along with the confidence intervals.

Table 4.1: Fitted parameters of the combined fit of *Voyager 1* and AMS proton data with the force-field approximation.

Parameter	Units	Value	Error
N	$10^4/(\mathrm{m}^2\,\mathrm{sr\,s\,GV})$	1.174	0.018
μ	–	−0.559	0.011
σ	–	0.563	0.005
ν	–	0.431	0.005
γ_1	–	−2.4482	0.0054
R_{b1}	GV	6.2	0.2
$\Delta\gamma_1$	–	−0.4227	0.0081
s_1	–	−0.108	0.015
R_{b2}	GV	545	210
$\Delta\gamma_2$	–	−0.6	0.2
s_2	–	−0.4	0.2
ϕ	MV	600	8

fitted values of $\phi(t)$.

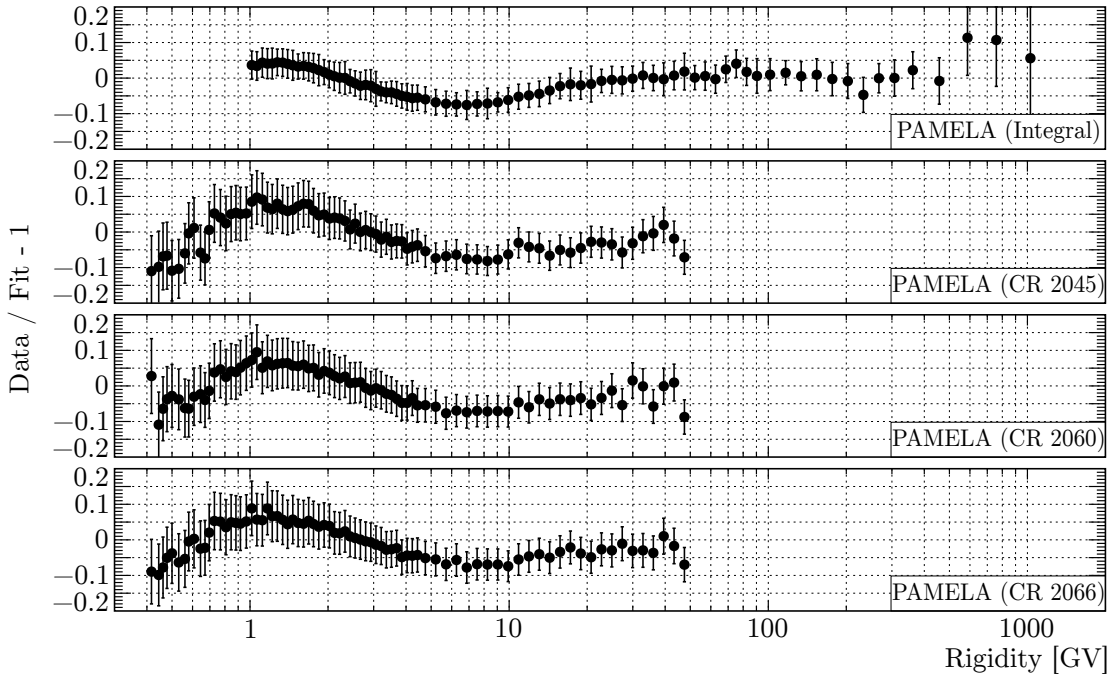

Figure 4.4: Residuals of the fit of the LIS modulated with the force-field approximation to the PAMELA integral proton flux and to the PAMELA proton flux measured during Carrington rotations 2045, 2060 and 2066.

Although the normalized chi-squared is good for all fits (respectively, 79/79 for the integral flux and between 40/77 and 80/77 for the monthly fluxes), the residuals have a structure with a bump around 1 GV and a dip around 7 GV, meaning that the modulated LIS does not completely describe the data. The same behavior is observed in the residuals of the fits to all PAMELA monthly fluxes, with the bump and the dip occurring around the same rigidities. In order to make sure that this effect is not due to our LIS parametrization, we fitted PAMELA data also with the LIS estimates shown in Figure 4.1, each separately tuned to reproduce *Voyager 1* and AMS results: the shape of the residuals is very similar to those presented in Figure 4.4. We believe that these structures are due to the fact that the force-field approximation does not correctly reproduce the solar modulation during the minimum of solar cycle 23/24 because some modulation processes are not considered: indeed, the assumption of a spherically symmetric diffusion tensor neglects the effects of gradient and curvature drifts, which have been shown to account for roughly half of the total modulation occurred during the solar minimum of 2006 to 2009 [147].

4.2 Beyond the force-field approximation

These results suggest that the solar modulation may affect GCRs below and above a few GV in different ways; a similar conclusion is found also in [148] by using a numerical model applied to

the PAMELA monthly proton fluxes and in [149] by comparing data from NMs, PAMELA and the Electron, Proton and Helium INstrument (EPHIN) instrument on board the SOlar and Heliospheric Observatory (SOHO) spacecraft.

The force-field approximation assumes that the diffusion coefficient is proportional to the rigidity, $k_2 \propto R$, but this is a simplification: both experimental data (as shown here) and turbulence theory [69, 67, 64] suggest a different power-law index below and above a certain rigidity, *i.e.*, $k_2 \propto R^{\delta_1}$ for $R \leqslant R_b$ and $k_2 \propto R^{\delta_2}$ for $R > R_b$. Plugging this expression in the integral defining ϕ, we find:

$$\begin{aligned}\phi &= \int_{R_E}^{R_b} \beta \frac{R^{\delta_1}}{R}\, dR + \int_{R_b}^{R_{HP}} \beta \frac{R^{\delta_2}}{R}\, dR = \\ &= \frac{1}{ZM(\delta_1+1)} \left[R_b^{\delta_1+1} {}_2F_1\left(\frac{1}{2}, \frac{\delta_1+1}{2}; \frac{\delta_1+3}{2}; -\frac{R_b^2}{M^2}\right) - R_E^{\delta_1+1} {}_2F_1\left(\frac{1}{2}, \frac{\delta_1+1}{2}; \frac{\delta_1+3}{2}; -\frac{R_E^2}{M^2}\right)\right] + \\ &+ \frac{1}{ZM(\delta_2+1)} \left[R_{HP}^{\delta_2+1} {}_2F_1\left(\frac{1}{2}, \frac{\delta_2+1}{2}; \frac{\delta_2+3}{2}; -\frac{R_{HP}^2}{M^2}\right) - R_b^{\delta_2+1} {}_2F_1\left(\frac{1}{2}, \frac{\delta_2+1}{2}; \frac{\delta_2+3}{2}; -\frac{R_b^2}{M^2}\right)\right],\end{aligned} \tag{4.6}$$

where ${}_2F_1(a, b; c; z)$ is the Gauss hypergeometric function. Unfortunately, this expression can not be analytically inverted to obtain R_{HP} as a function of R and ϕ. In order to maintain the simplicity of the force-field approximation approach, we consider a rigidity-dependent solar modulation parameter:

$$\phi(R) = \begin{cases} \phi_L & R < R_L \\ f(R, \phi_L, \phi_H) & R_L \leqslant R \leqslant R_H \\ \phi_H & R > R_H, \end{cases} \tag{4.7}$$

where the indices L and H stand for "low" and "high" rigidity and f is a transition function between ϕ_L and ϕ_H. We want f to have a zero derivative at R_L and R_H to avoid discontinuities in the spectral index: the simplest function that has this property is a third degree polynomial, which is completely constrained by the given boundary conditions. Defining $r = (R - R_L)/(R_H - R_L)$, the transition function is $f(R, \phi_L, \phi_H) = \phi_L + (\phi_H - \phi_L) r^2 (3 - 2r)$.

We then proceed as previously done: simultaneously fitting *Voyager 1* and AMS data, minimizing the global chi-squared defined in Equation 4.5 and replacing the solar modulation parameter in Equation 1.36 with the one defined in Equation 4.7. The result of the fit ($\chi^2_{glob}/\mathrm{dof} = 55/78$) is shown in Figure 4.5. The values of R_L and R_H have been fixed at 0.5 and 5 GV, while the fitted parameters are presented in Table 4.2. The asymptotic spectral indices at intermediate and high rigidities are, respectively, $\gamma_2 = -2.853 \pm 0.015$ and $\gamma_3 = -2.674 \pm 0.073$.

Figure 4.6 shows the residuals of the proton flux measured by PAMELA during the same time periods shown in Figure 4.4 fitted with the rigidity-dependent solar modulation parameter: the normalized chi-squared are, respectively, 13/78 for the integral flux and between 20/76 and 60/76 for the monthly fluxes and the structures of the residuals are now smaller with respect to the ones

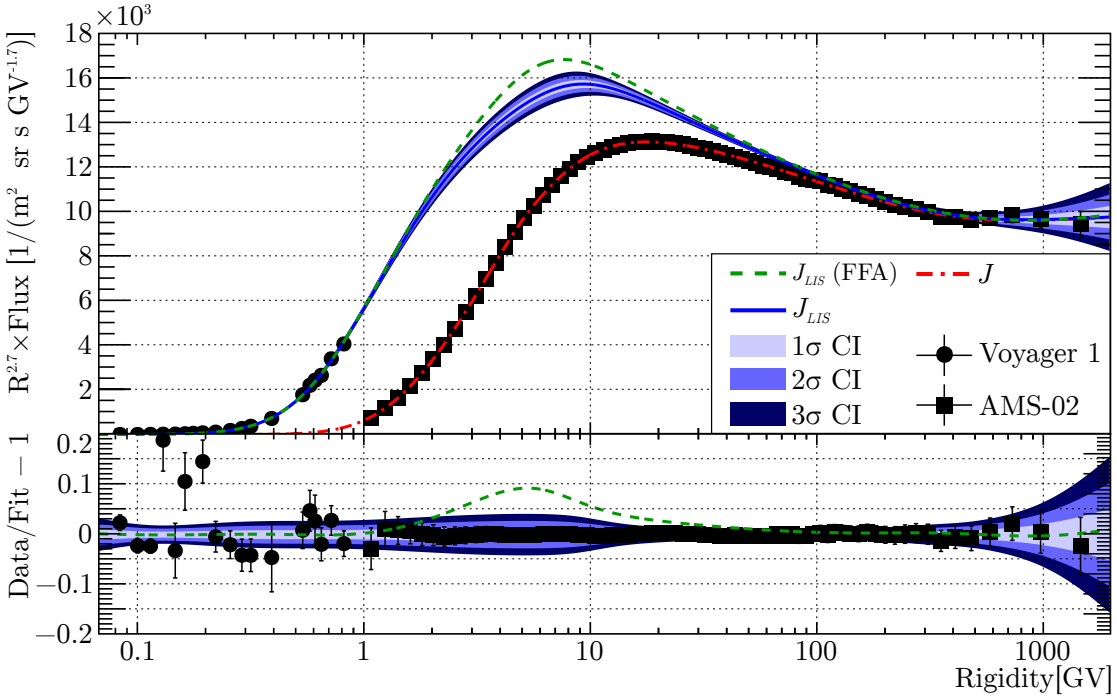

Figure 4.5: Same as Figure 4.3, but using the rigidity-dependent solar modulation parameter of Equation 4.7. For comparison, the LIS derived in Section 4.1 with the force-field approximation, J_{LIS} (FFA), is shown as a dashed line.

Table 4.2: Fitted parameters of the combined fit of *Voyager 1* and AMS proton data with the modified force-field approximation.

Parameter	Units	Value	Error
N	$10^4/(\mathrm{m}^2\,\mathrm{sr\,s\,GV})$	1.219	0.022
μ	–	−0.534	0.011
σ	–	0.5630	0.0048
ν	–	0.4221	0.0049
γ_1	–	−2.5462	0.0059
R_{b1}	GV	8.44	0.43
$\Delta\gamma_1$	–	−0.3051	0.0087
s_1	–	−0.078	0.016
R_{b2}	GV	400	180
$\Delta\gamma_2$	–	−0.56	0.26
s_2	–	−0.22	0.20
ϕ_L	MV	587.4	7.9
ϕ_H	MV	481	22

obtained with the force-field approximation, especially above few GV. Below 1 GV the residuals still show a decreasing trend: this is due to the fact that the streaming current is not negligible

anymore for energies below 400 MeV/n, thereby invalidating one of the assumptions used in the force-field approximation [76].

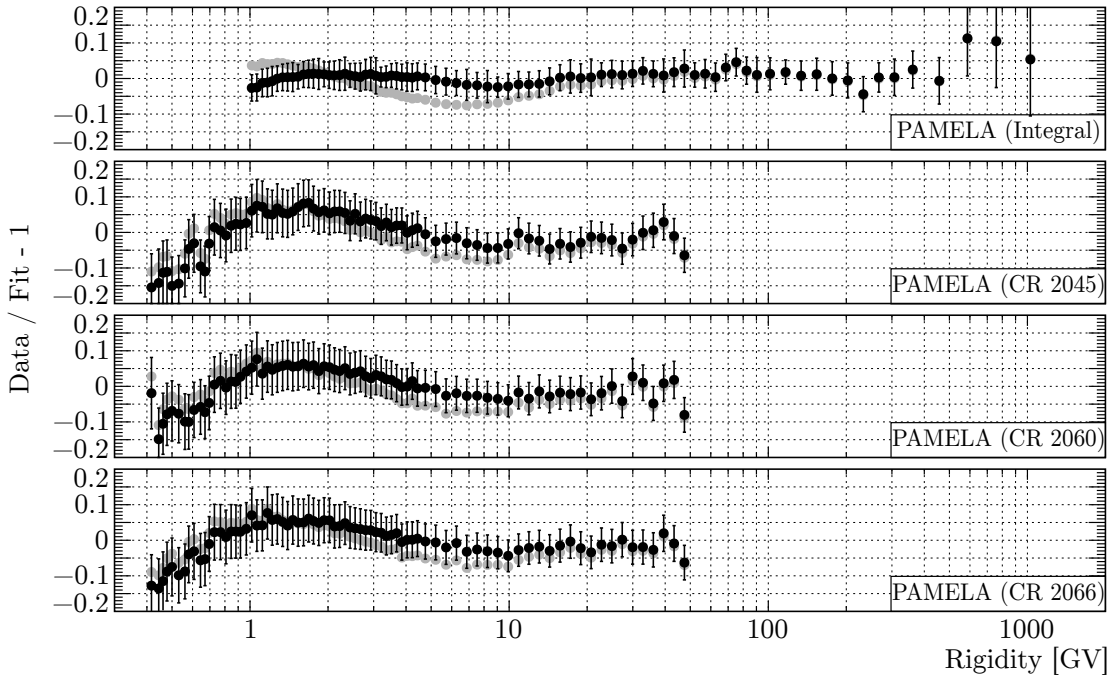

Figure 4.6: Same as Figure 4.4, but using the rigidity-dependent solar modulation parameter of Equation 4.7. For comparison, the residuals obtained with the force-field approximation are shown in light-gray.

The fit has been repeated on all monthly proton fluxes measured by PAMELA and the time dependence of the fitted solar modulation parameters ϕ_L and ϕ_H is plotted in Figure 4.7.

Interpreting the solar modulation parameters as the average energy losses experienced by the particles traveling from the edge of the heliosphere up to the Earth, these results show that, during the minimum of solar cycle 23/24, the energy losses are slightly higher at lower rigidities, while the force-field approximation predicts the same energy loss at all rigidities.

We applied our model also to the proton fluxes measured by BESS[2] [150, 151, 152, 139, 153]. The matching between data and fit when using the rigidity-dependent modulation parameter is improved with respect to the force-field approximation, especially for BESS93 (the normalized chi-squared changes from 71/13 to 4/12), BESS-TeV (χ^2/dof from 134/46 to 57/45) and BESS-Polar II (χ^2/dof from 341/88 to 30/87). The fitted values of $\phi_L(t)$ and $\phi_H(t)$ are presented in Table A.1, columns 6 to 11.

[2]BESS data have been downloaded from the cosmic-ray database [56]: `https://lpsc.in2p3.fr/cosmic-rays-db`.

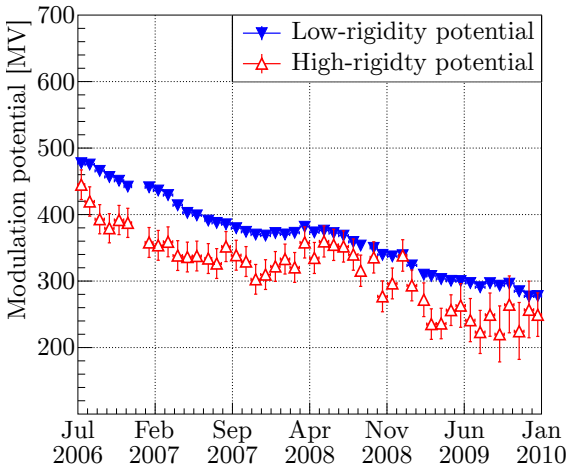

Figure 4.7: Time dependence of the solar modulation parameters ϕ_L (blue down triangles) and ϕ_H (red up triangles) derived from the monthly proton fluxes measured by PAMELA.

4.3 The helium LIS and the charge dependence of the solar modulation

Helium is a primary component of GCRs, so we expect it to have a similar behavior as protons: indeed, the measurement of the helium flux performed by AMS [90] shows at high rigidity a smooth change of slope at about the same rigidity break of the protons, although with a different spectral index. At low energy, the ratio of the helium flux measured by *Voyager 1* outside the heliopause [5] to a power law looks like the one for protons (see Figure 4.2). We assume, therefore, for the helium LIS the same parametrization used for protons in Equation 4.4.

The *Voyager 1* and AMS helium fluxes have been fitted both with the force-field approximation and with the rigidity-dependent solar modulation parameter, as described in section 4.1. The results of the fit (respectively, $\chi^2_{glob}/dof = 28/78$ and $\chi^2_{glob}/dof = 28/77$) are shown in Figure 4.8.

Contrary to protons, the difference between the helium LIS derived using the force-field approximation and the rigidity-dependent modulation parameter is negligible. The fitted parameters are presented in Table 4.3 (force-field approximation) and Table 4.4 (modified force-field approximation). The asymptotic spectral indices at intermediate and high rigidities are, respectively, $\gamma_2 = -2.7869 \pm 0.0006$ and $\gamma_3 = -2.64 \pm 0.20$. We note that the details of the rigidity breaks are not compatible between protons and helium.

The helium fluxes measured by BESS [150, 151, 152, 139, 153] have been fitted with the new LIS modulated first with the force-field approximation and then with the rigidity-dependent modulation parameter. The conversion from kinetic energy to rigidity has been done by assuming that the helium is composed by ^{4}He only. The modified force-field yields a better fit, especially for BESS93 (the normalized chi-squared changes from 42/13 to 7/12) and BESS-Polar I (χ^2/dof from 112/88

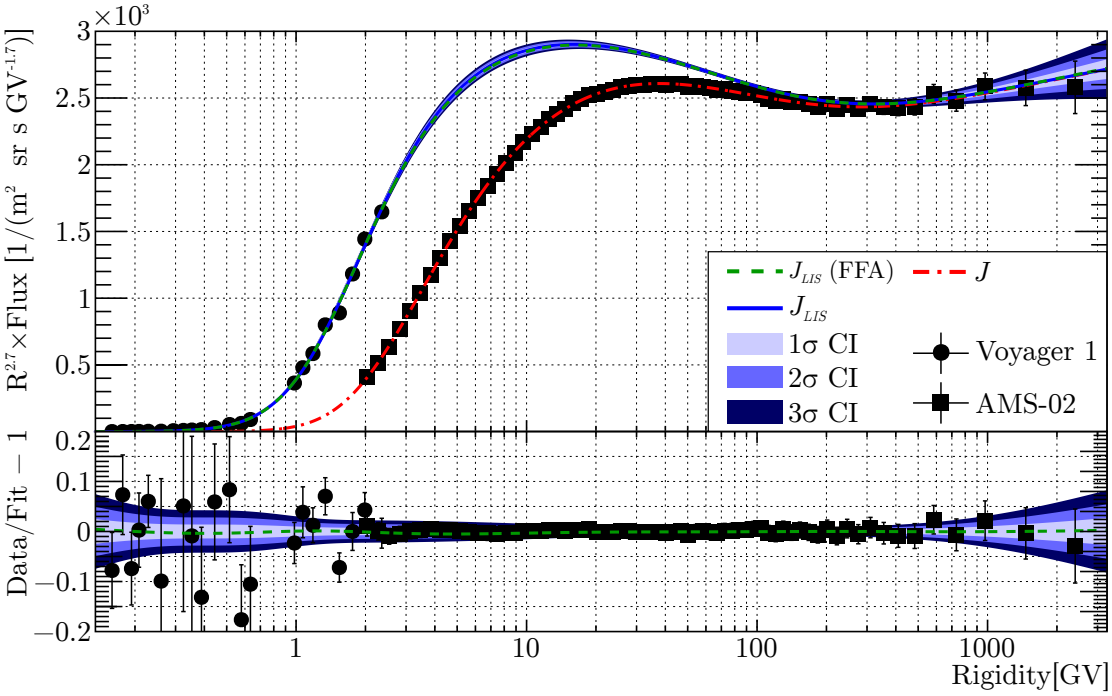

Figure 4.8: **Top**: Combined least-squares fit of *Voyager 1* helium data (dots) with J_{LIS} (solid line) and AMS helium data (squares) with J (dashed-dotted line), using the rigidity-dependent solar modulation parameter of Equation 4.7. The shaded bands represent the 1, 2 and 3 σ confidence intervals around the best fit. For comparison, the LIS derived with the force-field approximation, J_{LIS} (FFA), is shown as a dashed line. **Bottom**: Fit residuals along with the confidence intervals.

Table 4.3: Fitted parameters of the combined fit of *Voyager 1* and AMS helium data with the force-field approximation.

Parameter	Units	Value	Error
N	$10^4/(\mathrm{m}^2\,\mathrm{sr}\,\mathrm{s}\,\mathrm{GV})$	1.122	0.022
μ	–	0.197	0.023
σ	–	0.477	0.011
ν	–	0.559	0.019
γ_1	–	−1.9017	0.0056
R_{b1}	GV	2.14	0.05
$\Delta\gamma_1$	–	−1.1958	0.0083
s_1	–	−3.08	0.03
R_{b2}	GV	189	27
$\Delta\gamma_2$	–	−0.332	0.029
s_2	–	−0.232	0.044
ϕ	MV	568	8

Table 4.4: Fitted parameters of the combined fit of *Voyager 1* and AMS helium data with the modified force-field approximation.

Parameter	Units	Value	Error
N	$10^4/(\mathrm{m}^2\,\mathrm{sr}\,\mathrm{s}\,\mathrm{GV})$	1.160	0.023
μ	–	0.197	0.025
σ	–	0.479	0.011
ν	–	0.556	0.018
γ_1	–	−1.9032	0.0056
R_{b1}	GV	2.109	0.049
$\Delta\gamma_1$	–	−1.128	0.008
s_1	–	−3.102	0.031
R_{b2}	GV	189	27
$\Delta\gamma_2$	–	−0.334	0.029
s_2	–	−0.235	0.043
ϕ_L	MV	568	10
ϕ_H	MV	570	15

to 84/87). The fitted values of $\phi(t), \phi_L(t)$ and $\phi_H(t)$ are presented in Table A.2, columns 3 to 11.

The bump-and-dip structure in the residuals is evident in BESS93 and BESS-PolarII (for both p and He), which correspond to periods of low solar activity. This suggests that the force-field approximation is not as good at the solar minimum as it is at the solar maximum. Indeed, during the maximum the interplanetary magnetic field is more chaotic and so the diffusion processes play a more important role than the drift processes, which are not described in the force-field approximation. The rigidity-dependent modulation parameter partially recovers the drift effects, albeit only phenomenologically.

The force-field approximation and our modified force-field predict the same modulation parameter independently of the particle charge via $\Phi = Ze\phi$, but our results clearly indicate that this is not the case. Figure 4.9 shows the comparison of the modulation parameter between protons and helium for BESS and AMS, plotted along with the monthly average sunspot number (SSN)[3].

Both in the force-field approximation and in the modified force-field the ratio ϕ^p/ϕ^{He} is different from 1 and varies with time. It is known that the fitted modulation parameter depends on the chosen LIS [154] and since the proton and helium LIS are different, we do not expect ϕ^p and ϕ^{He} to be the same. Regarding the time dependence, we highlight the fact that the behavior of the ratio changes approximately at the same time during which the solar magnetic field reversed its polarity [155]. In the Parker equation, the polarity term appears only in the drift coefficient, which is responsible for the charge-sign dependent modulation of electrons and positrons and the alternating peaks and flat tops in NM counts. Interestingly, our results suggest that drift processes may have a different effect

[3]Data have been downloaded from the SILSO World Data Center [133]: `http://www.sidc.be/silso/datafiles`.

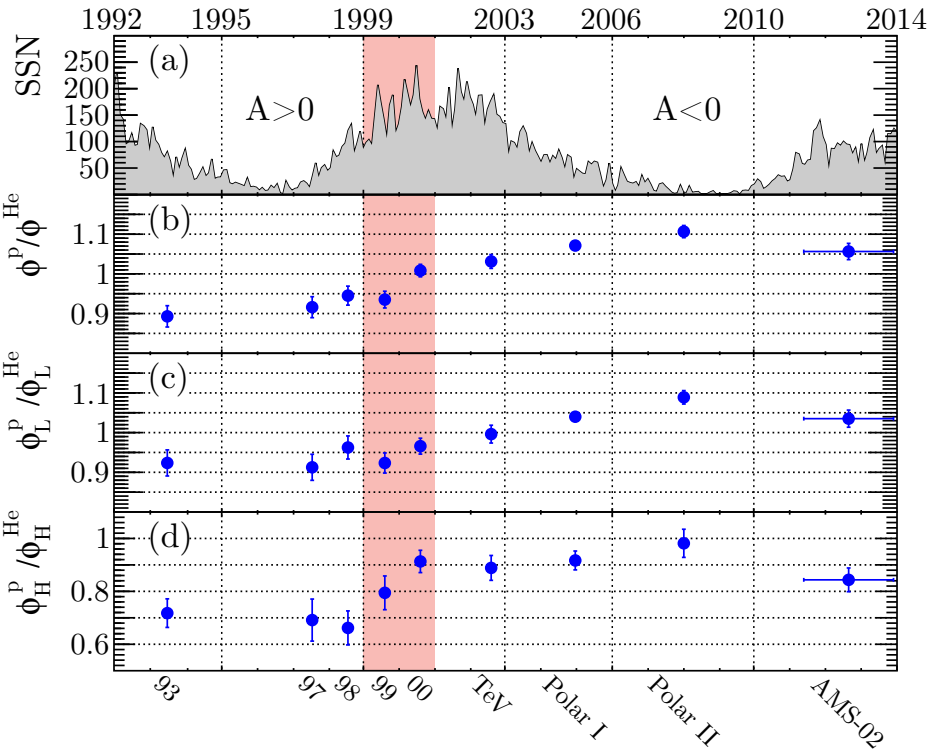

Figure 4.9: Comparison of the modulation parameters derived from BESS and AMS average proton and helium fluxes. **(a)** Monthly averaged sunspot number. **(b)** Ratio of the proton ϕ to helium ϕ, using the force-field approximation. **(c)** and **(d)** Respectively, ratio of the proton ϕ_L to helium ϕ_L and of the proton ϕ_H to helium ϕ_H, using the modified force-field. The red band between 1999 and 2001 indicates the period during which the polarity reversal of the solar magnetic field occurred.

on nuclei with differing charge, but same sign. The assumption that the measured helium is all ^{4}He introduces a bias in the fitted ϕ, but it is not enough to explain this effect: in fact, BESS93 and BESS98 measured the ^{4}He component of the helium spectrum, so we can use these data to estimate how this approximation changes our results. Fitting the He flux yields $\phi^p/\phi^{He} = 0.89 \pm 0.03$ in 1993 and $\phi^p/\phi^{He} = 0.95 \pm 0.03$ in 1998, while fitting the ^{4}He flux yields $\phi^p/\phi^{He} = 0.74 \pm 0.03$ in 1993 and $\phi^p/\phi^{He} = 0.82 \pm 0.03$ in 1998: the qualitative result does not change. It is worth noting that the time variation of ϕ_L and ϕ_H ratio is not the same, implying that this polarity-dependent effect is also rigidity-dependent.

4.4 Modulation parameters of AMS proton and helium fluxes

The data collected by AMS continuously cover the rising phase, the maximum, with the polarity reversal, and the descending phase of solar cycle 24, thus complementing the PAMELA fluxes from the past solar minimum. With these datasets it is possible to study in detail how different rigidities

are affected by the solar modulation in different phases of solar activity.

Each proton and helium flux measured by AMS has been fitted with the respective LIS, first with the force-field approximation and then with the modified force-field. The fitted values of $\phi(t)$, $\phi_L(t)$ and $\phi_H(t)$ are presented in Tables A.1 and A.2, columns 3 to 11. Figure 4.10 illustrates the goodness of fit for both solar modulation models. The first panel shows the daily SSN [133], separately for the northern and southern hemisphere, smoothed with a moving average of 27-days period, along with the line-of-sight average tilt angle of the heliospheric current sheet (HCS). The double-peak structure of the solar cycle maximum is clearly visible, while in the beginning of 2015 the SSN starts to decrease, faster in the North than in the South, meaning that the solar maximum is finally passed and the solar cycle is proceeding toward the minimum. The two vertical dashed magenta lines indicate the period during which the Sun reversed its magnetic field [135], transitioning from negative to positive polarity.

In the second panel, the normalized chi-squared from the fits with the force-field approximation is shown, along with the one obtained with the rigidity-dependent modulation parameter. The modified force-field yields a better fit in all BRs, both for protons (left side) and helium (right side), especially at the beginning of the mission and between middle 2013 and middle 2014, where the goodness of fit is improved by a factor between 2 and 6. The big increase of the normalized chi-squared of the force-field approximation around 2014 coincides both with the peak of the SSN in the northern hemisphere and with the magnetic polarity reversal: the force-field approach, whether modified or not, is unable to disentangle between these two effects, because of the spherical symmetry approximation. Unfortunately, a realistic modeling of a multipolar magnetic field and of an asymmetry of the solar activity in the two hemispheres goes also beyond the scope of the numerical model presented in Section 5.1. Nevertheless, this result provides a strong indication that, when analyzed with very precise data such as the new AMS fluxes, the force-field approximation fails to accurately describe the solar modulation even during the solar maximum, when in theory its assumptions should be more valid than during the solar minimum. The rise of the normalized chi-squared of the modified force-field from 2015 on, when the solar activity starts decreasing, suggests that also the rigidity-dependent modulation parameter has some problems in correctly reproducing the solar modulation at lower activity levels.

This is confirmed by looking at the third and fourth panels, which display the rigidity and time dependence of the residuals in units of data error, *i.e.*, the quantity $z = (\text{data} - \text{fit})/\sigma_{\text{data}}$, respectively for the fits with the force-field approximation and with the modified force-field. If the model was a good description of the data, z would be distributed around zero according to a gaussian with $\sigma = 1$. Azure and blue correspond to $z < -1$, which means the model is overestimating the data; green and yellow correspond to $|z| \leqslant 1$; orange and red correspond to $z > 1$, which means the model is underestimating the data. The black lines represent contours in which z is greater than the given $n\sigma$ level. Contours containing only one or two residuals with $z > n\sigma$ have been discarded,

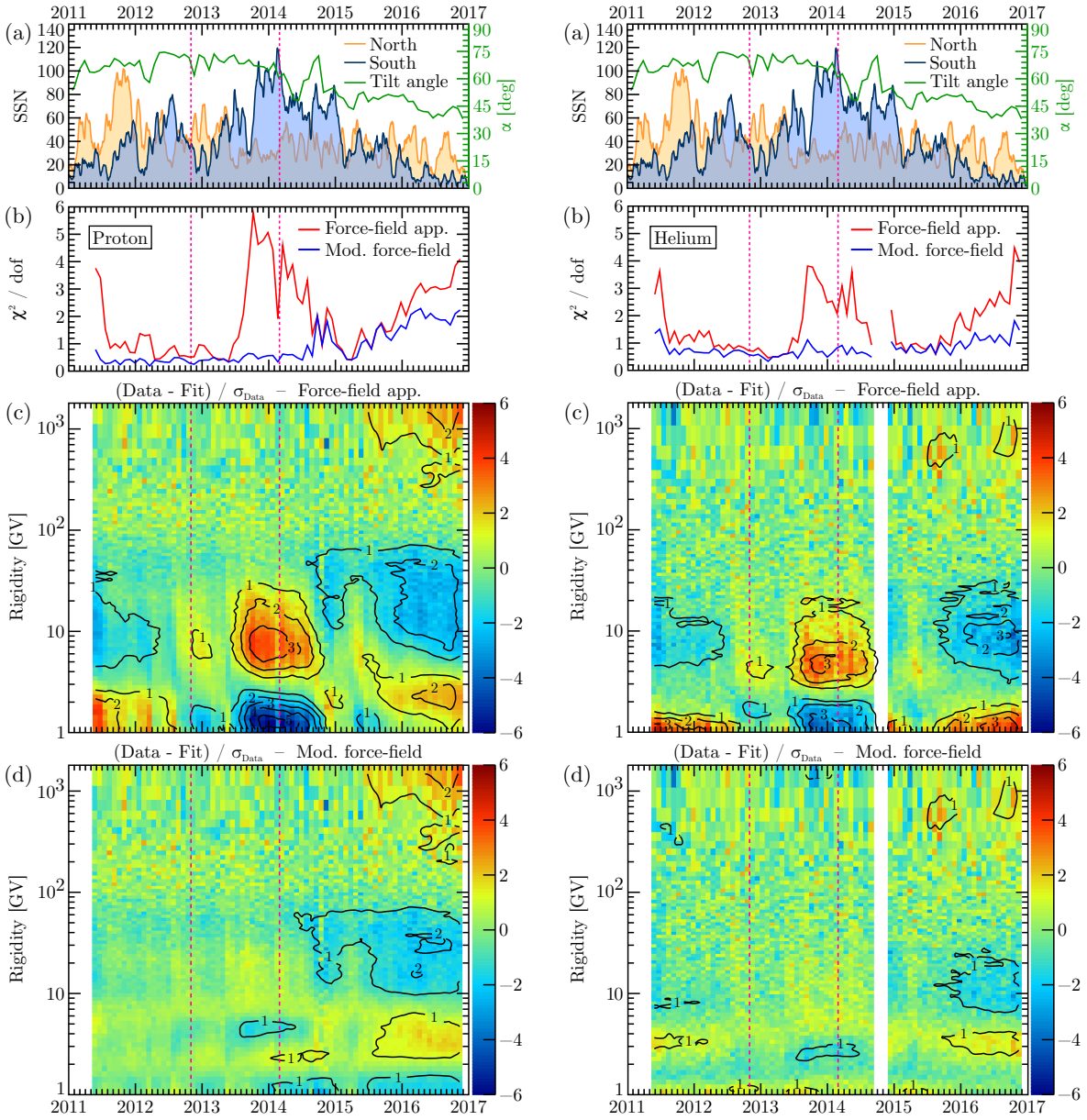

Figure 4.10: Rigidity and time dependence of the residuals of the fit of AMS protons (**left**) and helium (**right**) fluxes. **(a)** Daily hemispheric sunspot number in orange (North) and dark blue (South); tilt angle in dark green. The vertical dashed magenta lines mark the period of magnetic polarity reversal. **(b)** For each Bartels rotation (BR), normalized chi-squared of the fit with the force-field approximation (red) and the modified force-field (blue). **(c)** Residuals of the fit with the force-field approximation: green and yellow areas correspond to residuals between -1 and 1; orange and red areas correspond to positive residuals greater than 1; azure and blue areas correspond to negative residuals smaller than -1. Contours are shown with black lines: each contour encompass regions where the absolute value of the residuals is above the given $n\sigma$ level. **(d)** Same as (c), but for the modified force-field approximation.

since they are expected to occur simply by statistical fluctuations. In this representation, the bump-and-dip structure seen in PAMELA residuals translates to a patch of orange/red close to 1 GV and a patch of azure/blue at around 10 GV. A striking feature of AMS data taken during the maximum is the reversal of this structure during the period of the magnetic polarity reversal: around 2014, the model overestimates the proton flux at 1 GV by more than 5σ and the helium flux by more than 3σ, while underestimating both protons and helium at 5 GV by more than 3σ. The modified force-field fares much better during the polarity reversal and at the beginning of the mission, having only few scattered contours slightly above 1σ. From the beginning of 2015, though, a systematic underestimation of the flux around 3 GV and overestimation above 10 GV appears, although with a low statistical significance ($z \lesssim 2$). PAMELA residuals show a similar behavior, but at lower rigidities (underestimation around 1.5 GV and overestimation around 7 GV). Future data during the minimum of solar cycle 24 will show if the rigidities affected by this additional modulation effect not accounted for in the modified force-field will move toward the range observed by PAMELA or not. The worst match of the modified force-field approximation after 2015 may also be due to the different polarity of the solar magnetic field: indeed, the LIS parameters have been derived from AMS data taken during a negative polarity cycle, while in 2015 the polarity was positive. This fact suggests that the values of R_L and R_H may be different for different polarity periods.

Figure 4.11 illustrates the time dependence of the modulation parameters derived from the proton and helium fluxes measured by AMS. The first panel is the same as the top panel in Figure 4.10. The modulation potentials (ϕ_L in blue and ϕ_H in red) for protons and helium is shown, respectively, in the second and the third panel. The low-rigidity potential rises with time until February 2014, when it reaches its maximum at around 800 MV, for both protons and helium, and starts to smoothly decrease in June 2015. The upward jumps correspond to Forbush decrease (FD) events. The high-rigidity potential follows a similar behavior, but its rise and descent are less pronounced: this is due to the fact that the effects of solar modulation become smaller at higher rigidities. It is worthwhile to note that in February 2014 ϕ_H goes noticeably up, as a consequence of multiple FDs happening during that BR, while ϕ_L has only a small increase. The same thing also happens in June 2015. This is an additional indication of how low and high rigidities are affected differently, a phenomena which the force-field approximation is not able to describe. However, the bigger difference between ϕ_L and ϕ_H is their behavior during the period of the magnetic polarity reversal: while ϕ_L keeps increasing, ϕ_H remains almost flat, reflecting the flux behavior described in Section 3.10. The time dependence of the modulation parameters for helium is similar to the one for protons, but in the first and last period ϕ_H is greater than ϕ_L, suggesting that for helium sometimes the energy losses are bigger at high rigidities than at low rigidities. We can study the relative modulation of protons and helium by looking at the last panel, in which the ratio of the proton modulation potential to the helium modulation potential is shown. Short-term structures are visible for both ϕ_L and ϕ_H, but the ratio is basically constant in time until June 2015, when

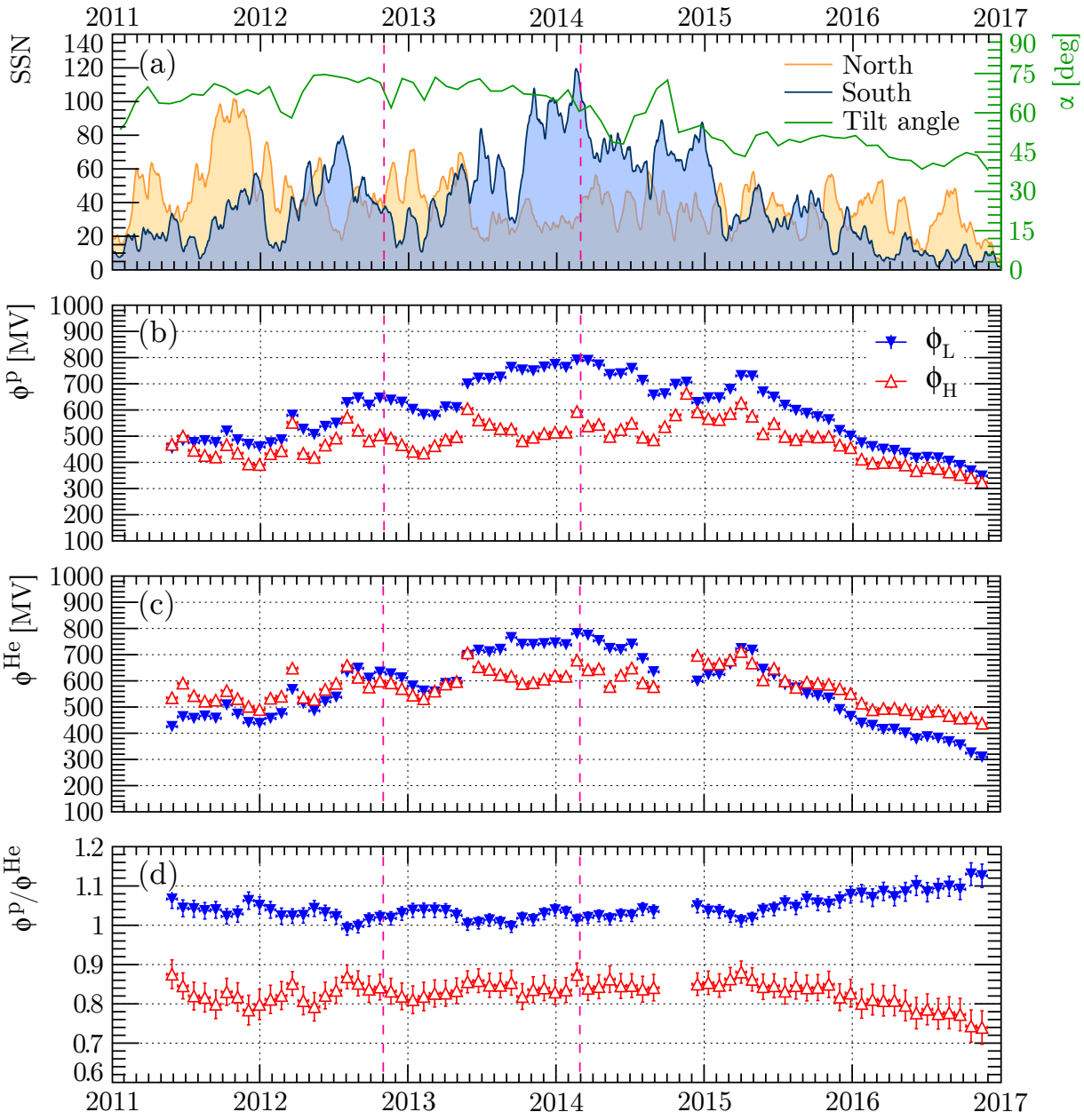

Figure 4.11: Time dependence of the solar modulation parameters ϕ_L (blue down triangles) and ϕ_H (red up triangles) derived from the monthly proton and helium fluxes measured by AMS. **(a)** Daily hemispheric sunspot number in orange (North) and dark blue (South); tilt angle in dark green. The vertical dashed magenta lines mark the period of magnetic polarity reversal. **(b)** Modulation potential for protons. **(c)** Modulation potential for helium. **(d)** Ratio of the proton ϕ to helium ϕ.

ϕ_L^p/ϕ_L^{He} starts to rise and ϕ_H^p/ϕ_H^{He} starts to descend. It is also interesting to note that the low-rigidity potential is very similar for protons and helium, albeit slightly larger for protons, while the high-rigidity potential is not, being between 10 % and 20 % larger for helium.

These results cleary show the need for a more sophisticated model for solar modulation, in order to better understand the time and rigidity dependence of its effects on different particle species.

4.5 Comparison with recent LIS parametrizations

In the last years, new parametrizations for the proton and helium LIS have been published, based on the latest *Voyager 1*, PAMELA and AMS data. In the following, the LIS derived in this Chapter will be compared with some of the newest LIS used by the heliophysics community. Bisschoff & Potgieter (2016) [156] (BP16 from now on) used the numerical code GALPROP [40] to solve the transport equation of GCRs in the galaxy and obtain the flux outside the heliosphere. They found that, in order to reproduce the low-energy data from *Voyager 1*, a plain diffusion model is not enough and reacceleration needs to be included. However, for helium it seems hard to describe both the low- and high-energy data: the plain diffusion model matches the PAMELA data above 50 GeV, but not *Voyager 1* data, while with the reacceleration a match with *Voyager 1* data is obtained, but now the model underestimates PAMELA data above 10 GeV. Nevertheless, the model with reacceleration fares better with protons and carbon, and thus is preferred over the plain diffusion model in this comparison. Ghelfi et al. (2016) [157] (G16 from now on) decided to use a different approach, similar to the one adopted in this work: the proton and helium fluxes are described non-parametrically with spline functions, determined by fitting various datasets (including BESS, PAMELA and AMS) to the LIS modulated with the force-field approximation. They found two sets of parametrizations, one that does not take into account the constraints imposed by the *Voyager 1* data, and one that does. We will use this last parametrization in this comparison[4]. Herbst et al. (2017) [158] (H17 from now on) took the LIS from [147], which is an analytical parametrization of an old GALPROP flux [159, 160] tuned to the PAMELA data, and modified it to match *Voyager 1* data; this parametrization is available only for protons.

Figure 4.12 compares the proton and helium LIS derived in this work with the ones presented above. The top panel shows the fluxes measured by *Voyager 1* and AMS, rescaled by R^2, along with the LIS parametrizations. All parametrizations have also been modulated with the modified force-field in order to fit the integral flux measured by AMS. The middle panel shows the ratio of the recent parametrizations to ours, together with the confidence intervals obtained by our fit (see Figures 4.5 and 4.8). For protons, BP16 and H16 are more than 50 % different from our model between 0.8 GV and 5 GV, while G16 has a 20 % discrepancy in the same rigidity range. This is the same rigidity range in which our spectrum has a 10 % difference between the one derived with the force-field approximation and the one derived with the modified force-field. It is not unreasonable to expect that, if these parametrizations were obtained by using the rigidity-dependent modulation potential, their difference with our model would be smaller. For helium, G16 is in very good agree-

[4]Table 3 in [157] contains some errors. A revised set of parameters was provided by the authors in a private communication, with the caveat that the helium parametrization is valid only up to 300 GV.

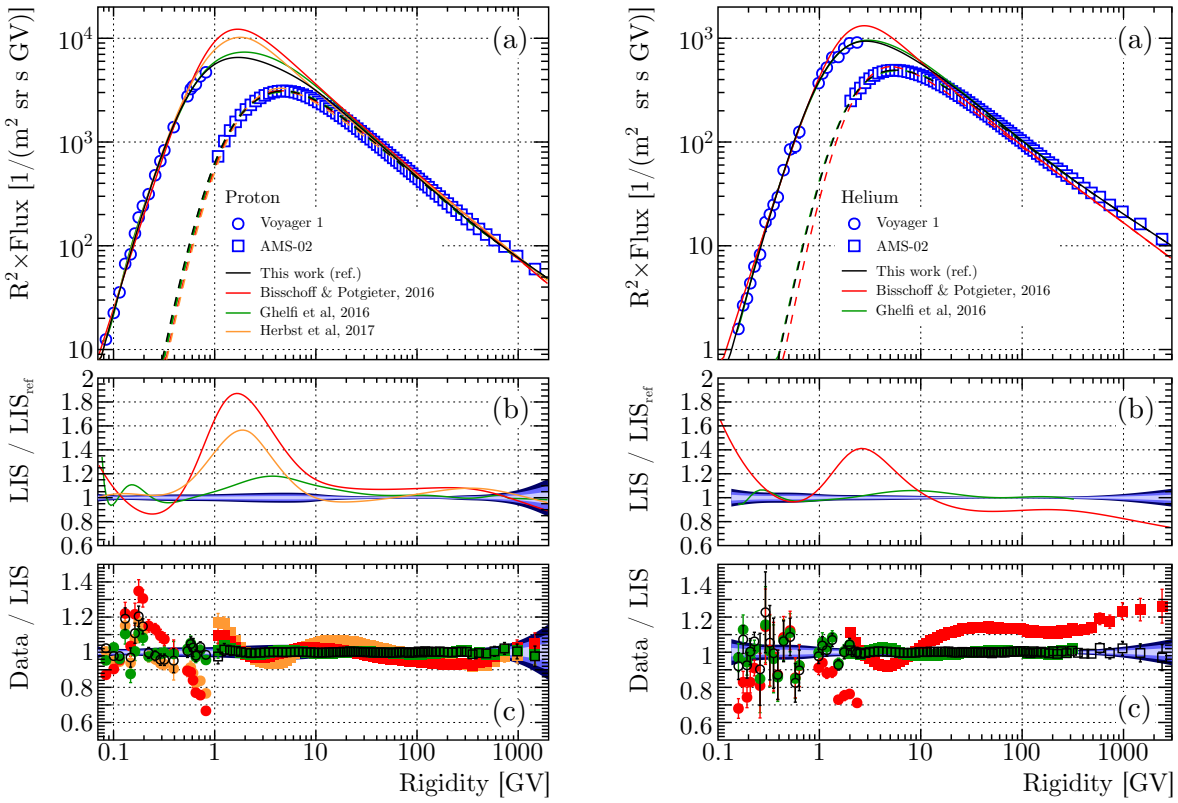

Figure 4.12: Comparison of the LIS derived in this work for protons (**left**) and helium (**right**) with other recent parametrizations. **(a)** Fluxes, rescaled by R^2, measured by *Voyager 1* (circles) and AMS (squares), along with the LIS parametrizations (solid lines). The dashed lines are the modulated fluxes fitted to the AMS data. **(b)** Ratio of the parametrizations to the one from this work, used as reference. The three colored bands are the 1, 2 and 3 σ confidence intervals on the reference LIS. **(c)** Ratio of *Voyager 1* and AMS data to the different LIS parametrizations.

ment with us, while BP16 has a 40 % difference around 3 GV and a systematic 10 % down-shift above 20 GV, due the issue with the reacceleration model described above. G16 is actually the sum of ^{3}He and ^{4}He: treating all He as ^{4}He introduces a bias, especially if the two isotopes do not modulate in the same way, so part of the discrepancy at low rigidity could be due to this approximation. In the bottom panel, the ratio between data and the parametrizations is presented. The ratio from G16 is consistent with our ratio, both for *Voyager 1* and AMS proton and helium data. BP16 and H16 show larger deviations in the *Voyager 1* range, while matching AMS proton data within 10 %. It is worth mentioning that both parametrizations consistently overestimate the proton flux from 80 GV to 800 GV. BP16 does not agree with the AMS helium data above 20 GV, having a discrepancy bigger than 10 % which rises with increasing rigidity: The bias introduced by not considering the ^{3}He component in this comparison should reduce this discrepancy. The good agreement between us and G16 and between these two models and the data, suggest that the LIS is lower than what

predicted from GALPROP between 0.5 GV and 10 GV.

The discrepancies between BP16 and H17 and the AMS data reflect also in the goodness of the fits to the BR fluxes with the modified force-field. BP16 has a normalized chi-squared between 4 and 5 for protons and above 15 for helium, while H17 ranges from 5 to 10. The normalized chi-squared of G16 is instead on the same level of the one shown in Figure 4.10, for both protons and helium. All parametrizations have the same χ^2 structure in time, when fitted with the force-field approximation, *i.e.*, a big increase during the period of the magnetic polarity reversal. This means that the results presented in the last section are not qualitatively dependent on a given LIS parametrization, but are a physical manifestation of the complexity of the solar modulation during the maximum of the solar cycle.

4.6 Comparison with neutron monitors

The effect of the solar modulation on GCRs has been continuously measured on ground since the 1950's with the world network of NMs, which measure the integral of the GCR flux above the rigidity cutoff pertaining to the NM location. In order to extract the solar modulation parameter from NM data, the shape of the LIS and the elemental composition of GCRs must be assumed, usually from measurements made by balloon- and space-borne experiments.

Figure 4.13 left shows the comparison between the low-rigidity solar modulation parameter, ϕ_L, obtained from the fits of Equation 4.4 to the PAMELA proton fluxes, and the parameter derived from NMs, ϕ_{NM} [161, 162], using the BPH00 parametrization as the LIS.

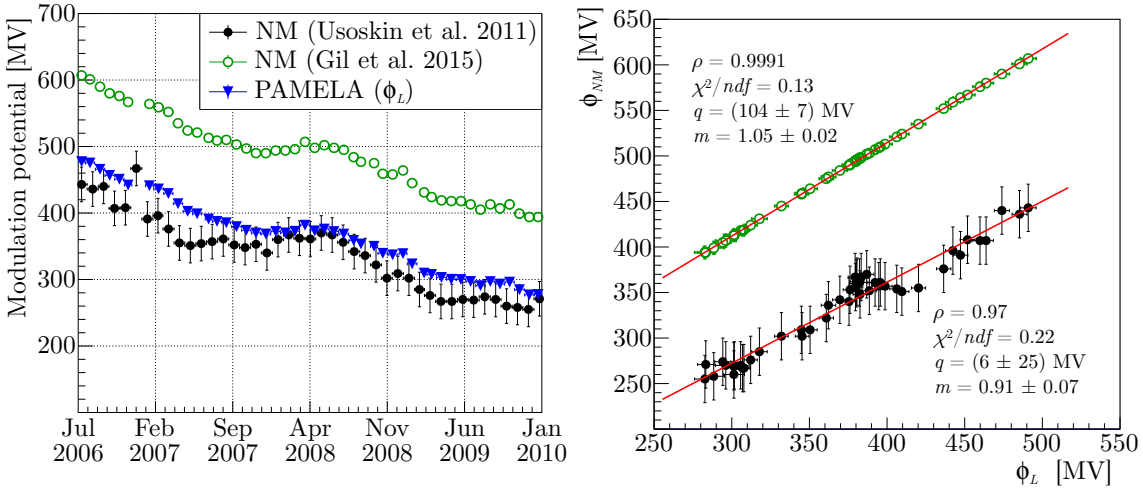

Figure 4.13: **Left**: Low-rigidity solar modulation parameter extracted from the PAMELA monthly proton fluxes (down triangles) compared with the one derived from neutron monitors (filled and hollow dots). **Right**: Correlation between ϕ_L and ϕ_{NM}; the solid lines are linear fits.

With respect to [161], [162] uses a new improved yield function that takes into account the

effect of the finite lateral size of the atmospheric showers induced by GCR [163] and calibrates the normalization of different NM stations with the proton monthly fluxes measured by PAMELA. The very small difference between ϕ_L and ϕ_{NM} from [161] is by accident, since in this case, in addition to the different LIS used to fit the data, the yield function did not include the effect described in [163]. The comparison with ϕ_{NM} from [162] results in a better correlation ($\rho = 0.9991$ versus $\rho = 0.97$) and the shift of ≈ 100 MV is due only to the different LIS adopted in [162] with respect to the one used in this work. Figure 4.13 right shows the correlation between ϕ_L and ϕ_{NM} from the two cited works. Assuming that the linear relation between ϕ_L and ϕ_{NM}, shown in Figure 4.13 right, holds also for different periods of solar modulation, we can use the following expressions to compute the modulation parameter associated with the new parametrization of the proton LIS throughout the whole period of data taking of NMs:

$$\begin{aligned} \phi_L &= (1.10 \pm 0.08)\phi_{NM,Usoskin} - (7 \pm 27) \text{ MV} \\ \phi_L &= (0.95 \pm 0.08)\phi_{NM,Gil} - (99 \pm 7) \text{ MV}. \end{aligned} \tag{4.8}$$

CHAPTER 5
SOLAR MODULATION OF AMS-02 PROTONS WITH A NUMERICAL MODEL

In the previous chapter, the monthly proton fluxes measured by AMS have been described using a modified version of the force-field approximation. Although some insights can be gained by looking at the time dependence of the fitted modulation potentials, the force-field solution is not able to provide a comprehensive picture of why the fluxes are modulated in that way: where is the difference in the time behavior between low and high rigidities coming from? How is the change in polarity related to the observed variation of the fluxes?
In this chapter, a numerical model will be used to solve the Parker equation and to reproduce the monthly proton fluxes measured by AMS.

5.1 Numerical model description

5.1.1 Brief history of numerical models

The first numerical solution of the Parker equation was developed by Fisk in 1971 [164], by using a one-dimensional (radial) steady-state approximation. A second spatial dimension, the polar angle, was added in the following years by Fisk [165, 166], Moraal and Gleeson [167] and Cecchini and Quenby [168]. In 1979, Jokipii and Kopriva [169] and Moraal et al. [170] separately included gradient and curvature drifts with a flat heliospheric current sheet (HCS). The first model which used a wavy HCS was made by Potgieter in 1984 [171] and later improved by Burger [172], Potgieter and Moraal [173], Burger and Potgieter [174], Hattingh [175] and Langner [176]. The first comprehensive 3D steady state model with a wavy HCS was developed by Kóta and Jokipii in 1983 [177] and later by Hattingh [178]. Despite the advent of 3D models, 2D models remained popular because they required less computing resources, while providing similar results, with differences of the order of 20 % or less [178, 179]. However, the new high-precision data by PAMELA and AMS need a full 3D description.

Time-dependent models appeared at later times, the first one being developed by Perko and Fisk in 1983 [180]. Le Roux [181] and Ficthner et al. [182] extended it to 2 and 3 dimensions. The effects of the termination shock, *i.e.* of diffusive shock acceleration (DSA) inside the heliosphere, were extensively studied by many authors [183, 184, 185, 186, 176, 187, 188, 189]. Of particular interest was the modeling of global merging interaction regions (GMIRs) propagating outwards at large radial distances [190, 191].

All these models were based on the finite difference approach, but, more recently, an entire new class of numerical solutions based on stochastic differential equations (SDEs) appeared [192, 193,

194, 195, 196, 197, 198]. The advantage of SDEs over finite differences is that they are always numerically stable (see Section 5.1.6) and allow the direct computation of propagation times and energy losses [199].

The model used in this work is a 3D steady-state finite difference model, initially developed in Fortran by Hattingh in 1998 [178] and then translated in C by Vos in 2011 [200].

5.1.2 Numerical scheme

The Parker equation is solved in a reference frame co-rotating with the Sun, using spherical coordinates. Let's rewrite the Parker equation 1.23 in a more compact way:

$$\begin{aligned} &a(r,\theta,\phi,R)\frac{\partial f}{\partial r} + b(r,\theta,\phi,R)\frac{\partial f}{\partial \theta} + c(r,\theta,\phi,R)\frac{\partial f}{\partial \phi} + d(r,\theta,\phi,R)\frac{\partial^2 f}{\partial r\,\partial \phi} + \\ &+e(r,\theta,\phi,R)\frac{\partial^2 f}{\partial r^2} + l(r,\theta,\phi,R)\frac{\partial^2 f}{\partial \theta^2} + m(r,\theta,\phi,R)\frac{\partial^2 f}{\partial \phi^2} + \\ &+s(r,\theta,\phi)\frac{\partial f}{\partial \ln R} = 0, \end{aligned} \tag{5.1}$$

where

$$\begin{aligned} a(r,\theta,\phi,R) &= \frac{1}{r^2}\frac{\partial}{\partial r}\left(r^2 \mathsf{K}_{rr}\right) + \frac{1}{r\sin\theta}\frac{\partial}{\partial \theta}\left(\mathsf{K}_{\theta r}\sin\theta\right) + \frac{1}{r\sin\theta}\frac{\partial}{\partial \phi}\mathsf{K}_{\phi r} - V_{sw} \\ b(r,\theta,\phi,R) &= \frac{1}{r^2}\frac{\partial}{\partial r}\left(r\mathsf{K}_{r\theta}\right) + \frac{1}{r^2\sin\theta}\frac{\partial}{\partial \theta}\left(\mathsf{K}_{\theta\theta}\sin\theta\right) + \frac{1}{r^2\sin\theta}\frac{\partial}{\partial \phi}\mathsf{K}_{\phi\theta} \\ c(r,\theta,\phi,R) &= \frac{1}{r^2\sin\theta}\frac{\partial}{\partial r}\left(r\mathsf{K}_{r\phi}\right) + \frac{1}{r^2\sin\theta}\frac{\partial}{\partial \theta}\mathsf{K}_{\theta\phi} + \frac{1}{r^2\sin^2\theta}\frac{\partial}{\partial \phi}\mathsf{K}_{\phi\phi} - \Omega \\ d(r,\theta,\phi,R) &= \frac{2\mathsf{K}_{r\phi}}{r\sin\theta} \\ e(r,\theta,\phi,R) &= \mathsf{K}_{rr} \\ l(r,\theta,\phi,R) &= \frac{\mathsf{K}_{\theta\theta}}{r^2} \\ m(r,\theta,\phi,R) &= \frac{\mathsf{K}_{\phi\phi}}{r^2\sin^2\theta} \\ s(r,\theta,\phi) &= \frac{1}{3r^2}\frac{\partial}{\partial r}\left(r^2 V_{sw}\right). \end{aligned}$$

Equation 5.1 is a parabolic differential equation that can be solved with a variation of the Crank-Nicholson [201] finite difference method, called the alternating direction implicit (ADI) method. The ADI method was developed in 1955 by Peaceman and Rachford [202] and Douglas [203] for two spatial coordinates plus time and was extended to three spatial dimensions plus time in 1962 by Douglas [204]. In this case, the time coordinate is replaced by the rigidity.

First, a partial solution is computed at one third of a rigidity step, by solving Equation 5.1 implicitly in the radial direction. This solution is used to solve Equation 5.1 implicitly in the polar direction,

by advancing the rigidity of another third of a step. Finally, at a full step in rigidity, Equation 5.1 is solved implicitly in the azimuthal direction, in terms of the two previous solutions. Repeating this process for all the rigidity steps, we obtain a system of linear equations which can be arranged in a tridiagonal matrix. The Thomas algorithm is then used to solve the system.

The heliosphere is divided in a three-dimensional spherical grid, with uniform steps in the radial, polar and azimuthal directions. Let N_r, N_θ and N_ϕ be the number of steps in the three directions, and let Δr, $\Delta\theta$ and $\Delta\phi$ be the steps. Then, we have $r_i = r_1 + (i-1)\Delta r$, $\theta_j = (j-1)\Delta\theta$ and $\phi_k = (k-1)\Delta\phi$, where i runs from 1 to N_r, j from 1 to N_θ, k from 1 to N_ϕ and $r_1 > r_\odot$ is the inner boundary of the heliosphere, $r_\odot \approx 0.0047\,\mathrm{AU}$ being the radius of the Sun. The outer boundary of the heliosphere is taken to be the heliopause, $r_{N_r} = r_{HP}$, *i.e.* the surface beyond which the flux is not affected anymore by the solar modulation. With these definitions, the steps can be computed as $\Delta r = (r_{HP} - r_1)/(N_r - 1)$, $\Delta\theta = \pi/(N_\theta - 1)$ and $\Delta\phi = 2\pi/(N_\phi - 1)$.
The rigidity range is divided in N_R logarithmically uniform steps, *i.e.* $\ln R_n = \ln R_1 + (n-1)\Delta \ln R$. The rigidity steps are sorted in decreasing order, so that the first step R_1 corresponds to the maximum rigidity R_{max}, assumed to be unaffected by the solar modulation, and the last step is the minimum rigidity R_{min}. The rigidity step is then $\Delta \ln R = \ln(R_{max}/R_{min})/(N_R - 1)$.

Let's define $f_{i,j,k,n} = f(r_i, \theta_j, \phi_k, R_n)$. The derivatives in Equation 5.1 are approximated by central differences:

$$\frac{\partial f}{\partial x} = \frac{f(x+\Delta x) - f(x-\Delta x)}{2\Delta x} = \frac{f_{i+1} - f_{i-1}}{2\Delta x} \tag{5.2}$$

$$\frac{\partial^2 f}{\partial x^2} = \frac{f(x+\Delta x) - 2f(x) + f(x-\Delta x)}{\Delta^2 x} = \frac{f_{i+1} - 2f_i + f_{i-1}}{\Delta^2 x} \tag{5.3}$$

$$\begin{aligned}\frac{\partial^2 f}{\partial x\,\partial y} &= \frac{f(x+\Delta x,\, y+\Delta y) - f(x+\Delta x,\, y-\Delta y)}{4\Delta x\Delta y} + \\ &+ \frac{f(x-\Delta x,\, y-\Delta y) - f(x-\Delta x,\, y+\Delta y)}{4\Delta x\Delta y} = \\ &= \frac{f_{i+1,j+1} - f_{i+1,j-1} - f_{i-1,j+1} + f_{i-1,j-1}}{4\Delta x\Delta y}.\end{aligned} \tag{5.4}$$

It can be shown, using a Taylor expansion of f, that the truncation error due to this approximation is $O(\Delta^2 x)$ for the first and the second derivative and $O(\Delta x \Delta y)$ for the mixed derivative. Let's indicate the partial solutions as:

$$\begin{aligned} f_{i,j,k,n} &\equiv f_{i,j,k} \\ f_{i,j,k,n+\frac{1}{3}} &\equiv f^*_{i,j,k} \\ f_{i,j,k,n+\frac{2}{3}} &\equiv g_{i,j,k} \\ f_{i,j,k,n+1} &\equiv h_{i,j,k}. \end{aligned} \tag{5.5}$$

Equation 5.1 is solved for $f^*_{i,j,k}$ in the radial direction by replacing the first and second derivatives

with respect to r with half of the central differences computed at the current rigidity step and half at the current step plus one third, while the other derivatives are computed with central differences at the current rigidity step:

$$\begin{aligned}
&\frac{a_{i,j,k,n}}{4\Delta r}\left(f^*_{i+1,j,k}-f^*_{i-1,j,k}+f_{i+1,j,k}-f_{i-1,j,k}\right)+\\
&+\frac{b_{i,j,k,n}}{2\Delta\theta}\left(f_{i,j+1,k}-f_{i,j-1,k}\right)+\frac{c_{i,j,k,n}}{2\Delta\phi}\left(f_{i,j,k+1}-f_{i,j,k+1}\right)+\\
&+\frac{d_{i,j,k,n}}{4\Delta r\Delta\phi}\left(f_{i+1,j,k+1}-f_{i+1,j,k-1}-f_{i-1,j,k+1}+f_{i-1,j,k-1}\right)+\\
&+\frac{e_{i,j,k,n}}{2\Delta^2 r}\left(f^*_{i+1,j,k}-2f^*_{i,j,k}+f^*_{i-1,j,k}+f_{i+1,j,k}-2f_{i,j,k}+f_{i-1,j,k}\right)+\\
&+\frac{l_{i,j,k,n}}{\Delta^2\theta}\left(f_{i,j+1,k}-2f_{i,j,k}+f_{i,j-1,k}\right)+\frac{m_{i,j,k,n}}{\Delta^2\phi}\left(f_{i,j,k+1}-2f_{i,j,k}+f_{i,j,k-1}\right)+\\
&+\frac{s_{i,j,k}}{\Delta\ln R}\left(f^*_{i,j,k}-f_{i,j,k}\right)=0.
\end{aligned}\tag{5.6}$$

With $f^*_{i,j,k}$ known, the equation is solved for $g_{i,j,k}$ in the polar direction, replacing the derivatives with the central differences in the same way as done before, but computing the differences in θ at the current rigidity step plus two thirds:

$$\begin{aligned}
&\frac{a_{i,j,k,n}}{4\Delta r}\left(f^*_{i+1,j,k}-f^*_{i-1,j,k}+f_{i+1,j,k}-f_{i-1,j,k}\right)+\\
&+\frac{b_{i,j,k,n}}{4\Delta\theta}\left(g_{i,j+1,k}-g_{i,j-1,k}+f_{i,j+1,k}-f_{i,j-1,k}\right)+\\
&+\frac{c_{i,j,k,n}}{2\Delta\phi}\left(f_{i,j,k+1}-f_{i,j,k+1}\right)+\\
&+\frac{d_{i,j,k,n}}{4\Delta r\Delta\phi}\left(f_{i+1,j,k+1}-f_{i+1,j,k-1}-f_{i-1,j,k+1}+f_{i-1,j,k-1}\right)+\\
&+\frac{e_{i,j,k,n}}{2\Delta^2 r}\left(f^*_{i+1,j,k}-2f^*_{i,j,k}+f^*_{i-1,j,k}+f_{i+1,j,k}-2f_{i,j,k}+f_{i-1,j,k}\right)+\\
&+\frac{l_{i,j,k,n}}{2\Delta^2\theta}\left(g_{i,j+1,k}-2g_{i,j,k}+g_{i,j-1,k}+f_{i,j+1,k}-2f_{i,j,k}+f_{i,j-1,k}\right)+\\
&+\frac{m_{i,j,k,n}}{\Delta^2\phi}\left(f_{i,j,k+1}-2f_{i,j,k}+f_{i,j,k-1}\right)+\\
&+\frac{s_{i,j,k}}{\Delta\ln R}\left(g_{i,j,k}-f_{i,j,k}\right)=0.
\end{aligned}\tag{5.7}$$

The final solution $h_{i,j,k}$ at the next rigidity step, in terms of $f_{i,j,k}$, $f^*_{i,j,k}$ and $g_{i,j,k}$, is obtained by replacing the ϕ derivatives:

$$\begin{aligned}
&\frac{a_{i,j,k,n}}{4\Delta r}\left(f^*_{i+1,j,k}-f^*_{i-1,j,k}+f_{i+1,j,k}-f_{i-1,j,k}\right)+\\
&+\frac{b_{i,j,k,n}}{4\Delta\theta}\left(g_{i,j+1,k}-g_{i,j-1,k}+f_{i,j+1,k}-f_{i,j-1,k}\right)+\\
&+\frac{c_{i,j,k,n}}{4\Delta\phi}\left(h_{i,j,k+1}-h_{i,j,k+1}+f_{i,j,k+1}-f_{i,j,k+1}\right)+
\end{aligned}$$

$$
\begin{aligned}
&+\frac{d_{i,j,k,n}}{4\Delta r\Delta\phi}\left(f_{i+1,j,k+1}-f_{i+1,j,k-1}-f_{i-1,j,k+1}+f_{i-1,j,k-1}\right)+ \\
&+\frac{e_{i,j,k,n}}{2\Delta^2 r}\left(f^*_{i+1,j,k}-2f^*_{i,j,k}+f^*_{i-1,j,k}+f_{i+1,j,k}-2f_{i,j,k}+f_{i-1,j,k}\right)+ \\
&+\frac{l_{i,j,k,n}}{2\Delta^2\theta}\left(g_{i,j+1,k}-2g_{i,j,k}+g_{i,j-1,k}+f_{i,j+1,k}-2f_{i,j,k}+f_{i,j-1,k}\right)+ \\
&+\frac{m_{i,j,k,n}}{2\Delta^2\phi}\left(h_{i,j,k+1}-2h_{i,j,k}+h_{i,j,k-1}+f_{i,j,k+1}-2f_{i,j,k}+f_{i,j,k-1}\right)+ \\
&+\frac{s_{i,j,k}}{\Delta\ln R}\left(h_{i,j,k}-f_{i,j,k}\right)=0.
\end{aligned}
\tag{5.8}
$$

The boundary conditions necessary for solving the Parker equation are:

1. At the outer boundary, the local interstellar spectrum (LIS) f_{LIS} is used as the input spectrum, *i.e.* $f(r_{HP},\,\theta,\,\phi,\,R)=f_{LIS}(R)$.
2. The radial gradient of f at the inner boundary is supposed to be continuous, which can be expressed as $f_{0,j,k}=2f_{1,j,k}-f_{2,j,k}$ for all values of j and k.
3. $\partial f/\partial\theta=0$ for $\theta=0$ and $\theta=\pi$, which means that $f_{i,0,k}=f_{i,2,k}$ and $f_{i,N_\theta+1,k}=f_{i,N_\theta-1,k}$.

5.1.3 Solar wind, HMF and HCS

The solar wind velocity profile is assumed to be separable in a radial and latitudinal component:

$$
\mathbf{V}_{sw}(r,\,\theta)=V_0V_r(r)V_\theta(\theta)\hat{\mathbf{r}},
\tag{5.9}
$$

where V_0 sets the overall velocity scale. The radial component describes the fast rise to supersonic speed within the first 0.3 AU from the Sun (first term) and the transition to subsonic speed at the termination shock (second term):

$$
\begin{aligned}
V_r(r)=1-\exp\left[\frac{40}{3}\left(\frac{r_\odot-r}{r_0}\right)\right]+ \\
+\left[\frac{s+1}{2s}-\frac{s-1}{2s}\tanh\left(\frac{r-r_{TS}}{L}\right)-1\right],
\end{aligned}
\tag{5.10}
$$

where $r_0=1\,\mathrm{AU}$, r_{TS} is the radial position of the termination shock (which, in principle, can vary in time), $L=1.2\,\mathrm{AU}$ is the width of the shock barrier and $s=2.5$ is the shock compression ratio in the downstream region, *i.e.* the ratio of the velocity before and after the shock.

The latitudinal term describes the transition between the slow and fast component of the solar wind:

$$
V_\theta(\theta)=\frac{V_{fast}+V_{slow}}{2V_0}\mp\frac{V_{fast}-V_{slow}}{2V_0}\tanh\left[6.8\left(\theta-\frac{\pi}{2}\pm\xi\right)\right],
\tag{5.11}
$$

where V_{fast} and V_{slow} are, respectively, the polar and equatorial component, while ξ is the polar angle at which the transition between the slow and fast streams begins. The top and bottom signs

correspond, respectively, to the northern ($0 < \theta < \pi/2$) and southern ($\pi/2 < \theta < \pi$) hemisphere. During periods of solar maximum, there is no clear latitudinal dependence of the solar wind speed, so that $V_{fast} = V_{slow}$ and the second term vanishes.
The solar wind velocity transition at the termination shock has not been treated as an actual shock, *i.e.* the divergence of the velocity (the last term of the Parker equation) is computed as if the termination shock was not present, while the drop in velocity is taken into account in the evaluation of the heliospheric magnetic field (HMF) and the diffusion tensor, reproducing the actual diffusion barrier present at the shock. This means that the reacceleration at the termination shock via DSA is not included in the model: anyway, the treatment of the DSA would also require the model to be time-dependent, which is not the case. Furthermore, Langner showed that for protons above 1 GV the effects of the termination shock reacceleration at Earth are negligible [176].

The HMF implemented in this model is the Parker field with the Smith-Bieber modification:

$$\mathbf{B}(r,\,\theta,\,\phi) = B_n \left(\frac{r}{r_0}\right)^2 \left(\hat{\mathbf{r}} - \tan\psi\hat{\boldsymbol{\phi}}\right) \left[1 - 2H(\theta - \theta_{HCS})\right], \tag{5.12}$$

where B_n is a normalization factor dependent on the observed magnitude of the HMF at Earth, B_0; H is the Heaviside step function, which takes care of the opposite polarity above and below the HCS; θ_{HCS} is the polar position of the HCS; ψ is the spiral angle, *i.e.* the angle between the direction of the HMF and the radial direction. ψ is defined as:

$$\tan\psi(r,\,\theta) = \frac{\Omega(r-b)\sin\theta}{V_{sw}(r,\,\theta)} - \frac{r}{b}\frac{V_{sw}(b,\,\theta)}{V_{sw}(r,\,\theta)}\frac{B_T(b)}{B_R(b)}, \tag{5.13}$$

where Ω is the angular rotation frequency of the Sun, $b = 20\ r_\odot$ is the distance from the Sun where the HMF becomes fully radial and $B_T(b)/B_R(b) \approx -0.02$ is the ratio of the azimuthal-to-radial magnetic field components. Imposing $B(r_0,\,\pi/2) = B_0$, we obtain $B_n = B_0/\sqrt{1 + \tan\psi(r_0,\,\pi/2)}$.

The position of the HCS is given by [177]:

$$\theta_{HCS}(r,\,\theta,\,\phi) = \frac{\pi}{2} - \tan^{-1}\left[\tan\alpha\sin\left(\phi + \Omega\frac{r - r_\odot}{V_{sw}(r,\,\theta)}\right)\right], \tag{5.14}$$

where α is the tilt angle, *i.e.* the maximum latitudinal extent of the HCS. To avoid problems created by the discontinuity of the polarity flip when passing from one side of the HCS to the other, the Heaviside function is replaced with a smooth transition function:

$$A\tanh\left(0.549\frac{\theta_{HCS} - \theta}{\Delta\theta_{HCS}}\right), \tag{5.15}$$

where A is the HMF polarity (± 1) and $\Delta\theta_{HCS} = 2r_L/r = 2R/(rBc)$ is the angle spanned by two

gyroradii for a particle with rigidity R: basically, the HCS drift effects are taken into account only if the particle is within 2 gyroradii from the HCS.

5.1.4 Diffusion and drift coefficients

The rigidity dependence of the parallel diffusion coefficient (DC) is approximated with a double power-law with a smooth change of slope, while the radial dependence is assumed to be inversely proportional to the magnitude of the HMF:

$$k_{\parallel} = k_{\parallel}^{0} \beta \frac{B_0}{B} \left(\frac{R}{R_k} \right)^{a} \left[1 + \left(\frac{R}{R_k} \right)^{\frac{b-a}{c}} \right]^{c}, \tag{5.16}$$

where $\beta = v/c$, R_K is the rigidity at which the transition between the two power-laws happens, a and b are, respectively, the slopes of the low- and high-rigidity power-laws and c controls the smoothness of the transition. The perpendicular DCs are assumed to be proportional to the parallel DC:

$$k_{\perp,r} = k_{\perp,r}^{0} k_{\parallel} \qquad k_{\perp,\theta} = u(\theta) k_{\perp,\theta}^{0} k_{\parallel}. \tag{5.17}$$

$u(\theta)$ is a function that enhances the perpendicular diffusion in the polar regions and it's defined as:

$$u(\theta) = \frac{3}{2} + \frac{1}{2} \tanh \left[8 \left(\left| \theta - \frac{\pi}{2} \right| - 35^{\circ} \right) \right], \tag{5.18}$$

where the numerical values are chosen to reproduce the anisotropic perpendicular diffusion observed by the *Ulysses* spacecraft [205, 206, 207]. In this work, the slopes of the perpendicular diffusion are not constrained to be equal to the ones of the parallel DC, therefore we introduce the parameters $a_{\parallel}$, $b_{\parallel}$ (slopes of the parallel DC) and $a_{\perp}$, $b_{\perp}$ (slopes of the perpendicular DC). The transition rigidity R_k and the smoothness factor c are assumed instead to be the same.

The drift coefficient is defined as:

$$k_A = k_A^{0} \frac{\beta R}{3B} \frac{\left(\frac{R}{R_A} \right)^2}{1 + \left(\frac{R}{R_A} \right)^2}, \tag{5.19}$$

where R_A is the rigidity below which the drift is suppressed due to scattering.

5.1.5 Code parallelization

In the last years, the field of computing has been revolutionized by the advent of parallel programming, which allows to spread a calculation on multiple processors, thereby decreasing the running time of computational intensive applications. The idea of parallel programming was born in the

1960s, but it was always difficult to write code that could work on parallel systems. Recently, many progresses, both on the hardware and the software side, simplified the task of writing parallel code to the point that nowadays almost every commercial computer and device (like smartphones and tablets) is able to run multi-threaded programs.

Unfortunately, the computations in the ADI method are not parallelizable, because the solution at a given step depends on the solution at the previous step. However, the variables describing the heliosphere (solar wind, HMF, HCS and the diffusion tensor) must be calculated at each point of the three-dimensional grid, which can easily have from 10^5 to 10^6 or more points. In particular, the diffusion and drift coefficients and the HCS transition function are rigidity-dependent, so they must be evaluated at every rigidity step. Since the values of these quantities at different spatial positions are independent from each other, their computation can be parallelized.

The program has been written with the support for CUDA (Compute Unified Device Architecture), the hardware architecture and the C/C++ bindings that allow to run parallel code on the discrete graphics cards (GPUs) produced by Nvidia [208]. The parallelization of the calculation of the heliospheric variables and their derivatives reduces the running time by a factor 3. With this optimization, each rigidity step is solved in $0.2 \div 0.3$ sec, depending on the GPU type: a model with 100 steps will run in half a minute, which is still too slow if the number of models to be generated is of the order of 10^4 or more. The solution is to dispatch the program on multiple computers, each one with its own GPU, so that many models can be produced at the same time. The drawback of this solution is that GPU clusters are either rare or expensive: in particular, during the course of this study, only one GPU was available for running the model. For this reason, the code has been converted from CUDA to OpenMP (Open Multi-Processing), a framework for shared memory multiprocessing in C/C++ [209, 210]. With respect to the GPU model, the program, running on 6 cores, is 30 % slower, but since it can run on a multi-core CPU, a standard computing cluster can be used and more models can be processed in parallel. The models produced in this work have been run on the CERN Batch Service, a collection of multi-core machines used mainly by the Large Hadron Collider experiments, where the AMS collaboration has a dedicated queue.

5.1.6 Numerical instabilities

Every numerical algorithm is affected by numerical errors, due to the discretization of the equations and to the finite precision used to represent real numbers on a machine. For example, the distribution of the difference of the modulated flux between the same model run on an Intel CPU and on a Nvidia GPU has a mean equal to zero and a RMS of 0.1 % below 40 GV and 1 % above. Comparing the same model run on a CPU with double precision and with quadruple precision, below 40 GV the modulated flux is on average the same, with a RMS of 0.2 %, while above 40 GV the double precision models are on average underestimated by 1 % and the RMS is 2.5 %. Quadruple precision models are more accurate, but on average they are 50 % slower, so it's not feasible to use them for this

study.

Numerical models are also divided in *stable* and *unstable* models: a model is stable if the numerical error made at a given step does not grow while carrying the computation forward. Usually, the stability of a model depends on the detail of the grid used to calculate the solution: a model is said *unconditionally stable* if its stability is independent on the values of the steps. ADI models are unconditionally stable if the number of spatial dimensions is less than 3, thus the solutions obtained with the model used in this work sometimes can be unstable. Figure 5.1 show some examples of numerical instabilities in the modulated flux at Earth. A good model is shown as reference in the top left panel. The instabilities have been divided in three categories: oscillatory behavior (top right panel), where the modulated flux oscillates around a seemingly correct solution with an amplitude of the order of at most few tens of percent; fake reacceleration (bottom left panel), where the modulated flux (red line) becomes higher than the input LIS (black line): since reacceleration processes are not included in the model, this behavior must be considered an instability; very large positive and negative flux (bottom right panel), where the amplitude of the oscillations is at least one order of magnitude larger than the flux itself, sometimes even infinite. The first and the last category are due to different effects: the small amplitude oscillations always happen in the range between 20 to 30 GV, while the large oscillations are limited below 20 GV, and there is no continuous transition between one behavior and the other.

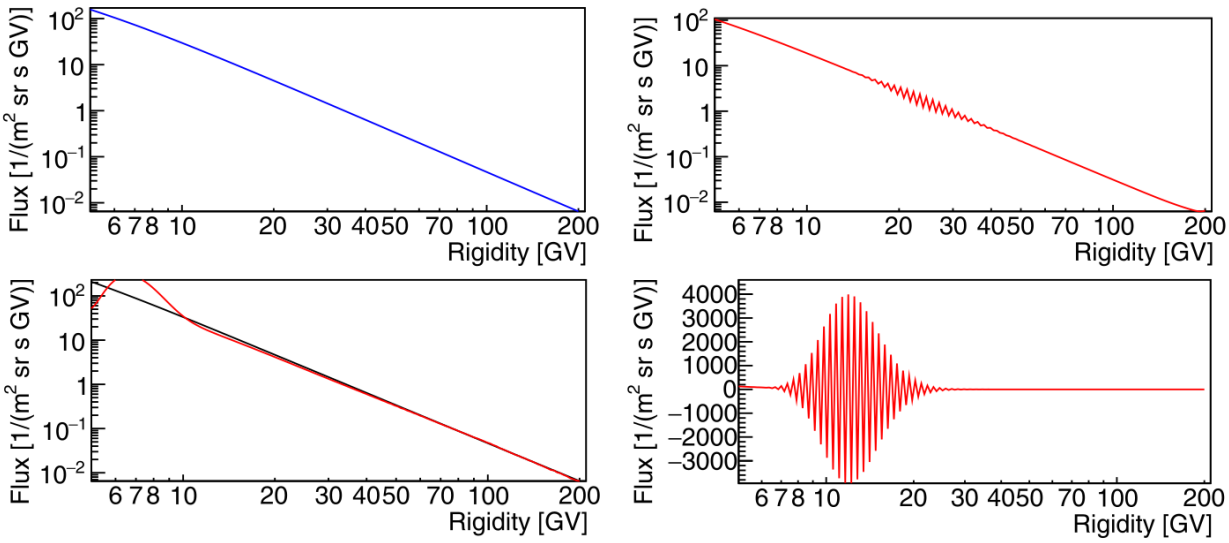

Figure 5.1: Examples of model outputs with numerical instabilities. **Left top**: Good model. **Right top**: Spurious oscillations around 25 GV. **Left bottom**: Fake reacceleration. **Right bottom**: Negative flux.

Clearly, models with such instabilities cannot be used in the analysis, so an automatic algorithm was developed to identify good and bad models:

1. The flux must always be positive and finite, thus avoiding the instabilities of the third category.
2. The flux must be smaller than the LIS below 70 GV, thus discarding the second category. Ideally, one would like to require the modulated flux to stay always below the LIS at all rigidities, but using a higher rigidity threshold would cut too many models which are good at low rigidities.
3. The maximum percent difference between two consecutive rigidity steps must be less than 3 % below 40 GV, thus removing the first category. In this rigidity range, the error on the measured monthly proton fluxes is around 1.5 %, so basically we allow the models to have oscillations within 2 sigmas from the data. The cut at 40 GV is chosen because above it the differences between GPU and CPU models can reach the same level of the error on the data.

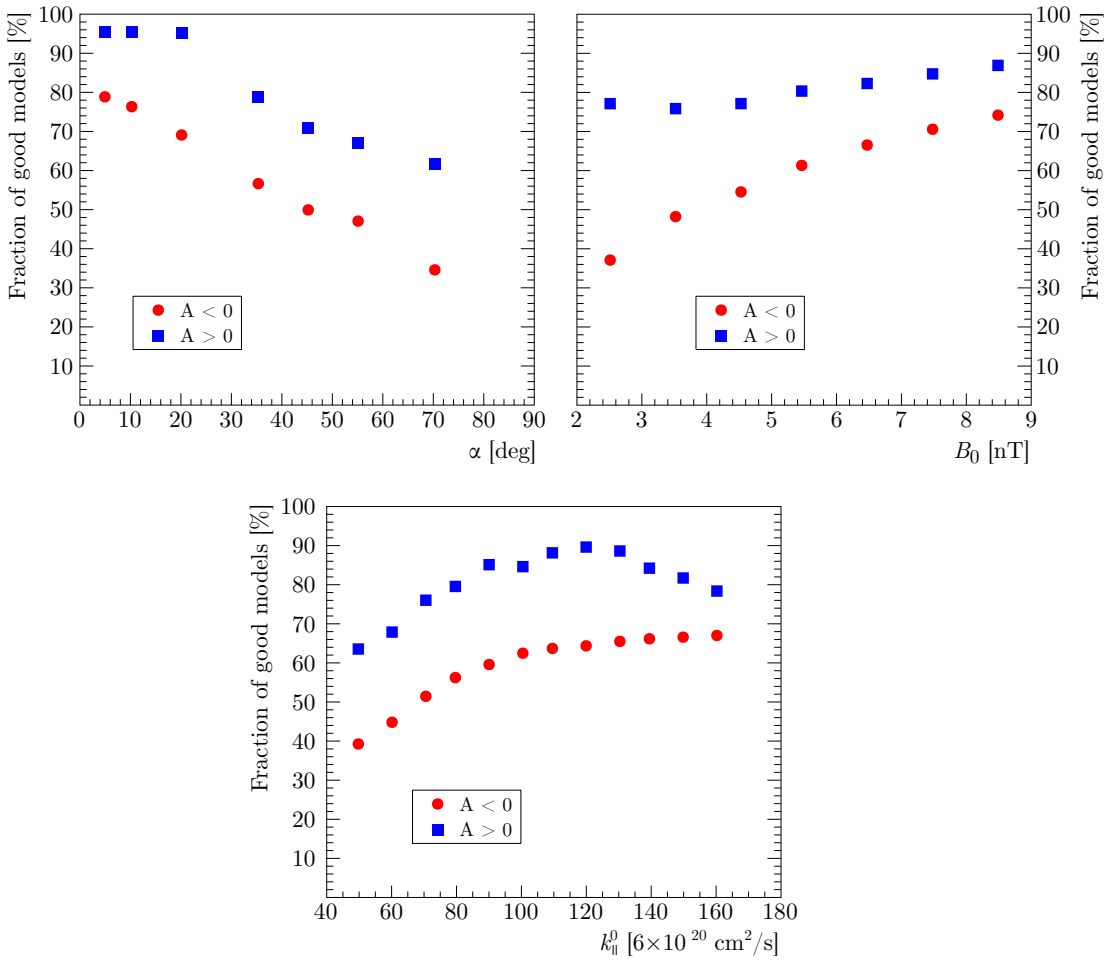

Figure 5.2: Dependence of the fraction of good models on the input parameters, separately for models with negative polarity (red circles) and positive polarity (blue squares).

By running a large number of models on a multi-dimensional grid in various parameters (α, B_0,

$k_{\parallel}^{0}$, $a_{\parallel}$, $b_{\parallel}$, $a_{\perp}$ and $b_{\perp}$), we can define the efficiency of models production as the fraction of good models with respect to the total number of generated models. Figure 5.2 shows the dependence of this efficiency on the parameters used to run the models.

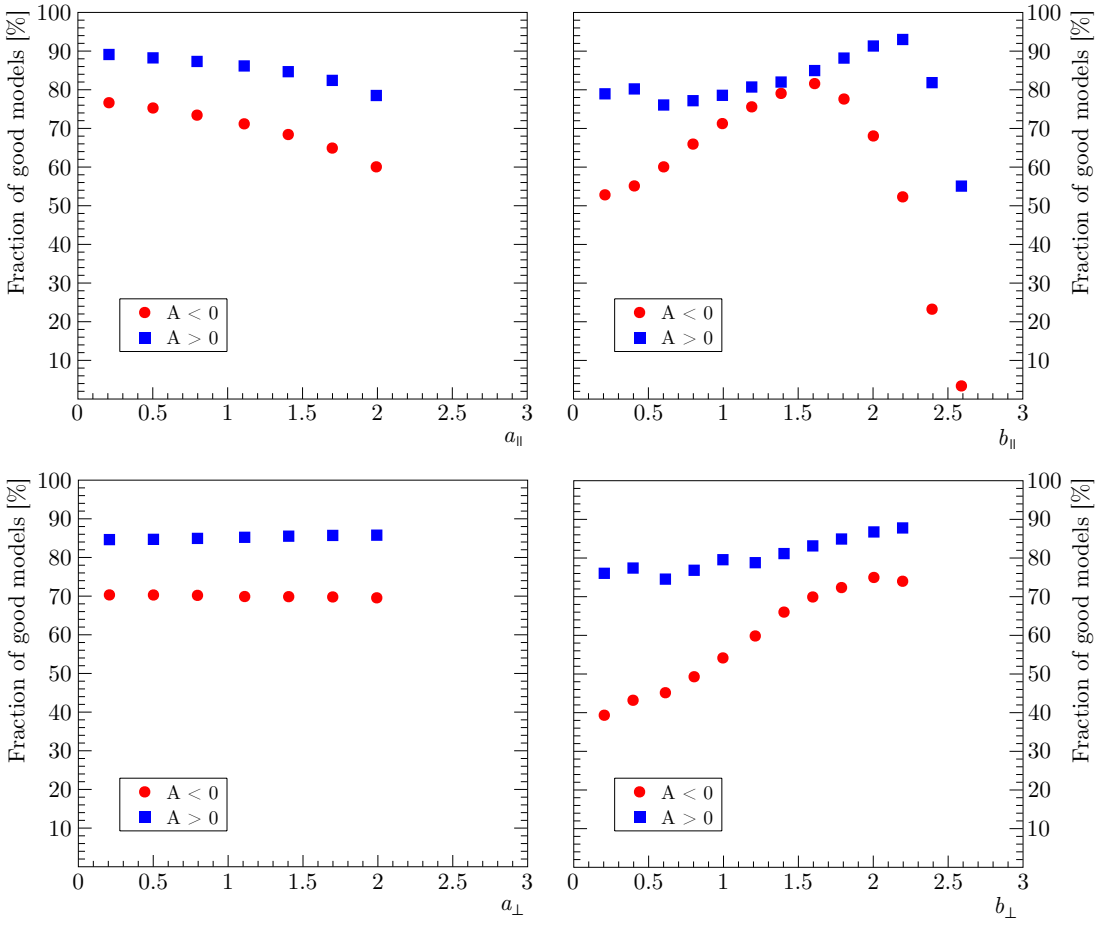

Figure 5.2 (Continued): Dependence of the fraction of good models on the input parameters, separately for models with negative polarity (red circles) and positive polarity (blue squares).

The first thing to note is that models with positive polarity have always a higher fraction of good models: in fact, when $A < 0$, protons arrive at Earth mostly by drifting along the HCS, so they spend more time in the heliosphere and can experience larger gradients, which increase the instability of the solution. For the same reason, a larger tilt angle is associated with a larger fraction of failed models. The relation between the efficiency of models production and the physics underlying a certain parameter is not always obvious. For example, the efficiency rises as expected with larger values of $k_{\parallel}^{0}$ and $b_{\perp}$ and smaller values of $a_{\parallel}$, *i.e.* when the modulation strength decreases because the diffusion mean free path increases. However, a less intense HMF means less modulation, but the efficiency decreases for lower values of B_0, a counter-intuitive behavior. The dependence of the efficiency on $b_{\parallel}$ instead is more complicated: it decreases at lower values of $b_{\parallel}$, as we would

expect due to a smaller mean free path, reaches a maximum and then sharply drops for $b_{\parallel} \gtrsim 2$, when the modulation strength decreases, especially at high rigidities. This might indicate that very large values of $b_{\parallel}$ are unphysical or that the spatial and rigidity grid is not optimized for such a range. Unexpectedly, the efficiency seems to be independent from $a_{\perp}$. The take-away message from this study is that numerical instabilities affect the result of the analysis in two ways. First, even if the models are generated using a flat distribution in all the parameters, the resulting coverage of the parameters phase space will not be flat, introducing a bias in the final result. Second, the number of models available for the analysis, *i.e.* the good models, is reduced by this inefficiency, therefore, to have a good statistics, more models need to be generated, increasing the computing time.

5.2 Fit of the AMS monthly proton fluxes

The standard approach of a least-squares fit with `MINUIT` is not feasible in this case, since a single model runs too slowly to allow the thousands of sequential iterations needed to find a global minimum. Furthermore, the fit should be repeated for each of the 75 Bartels rotations (BRs) observed by AMS, potentially generating a given model multiple times, thus wasting computing time. To solve this issue, a different strategy has been developed.
An ensemble of models is created in parallel, each with a different combination of input parameters. The resulting multi-dimensional grid of models is interpolated to find the set of parameters that minimizes the chi-squared between the models and the data. This way, the models are generated once and for all, and they can be reused in the fitting of every monthly flux, avoiding their duplication.

The parameters and their values defining the multi-dimensional grid are listed in Table 5.1. The normalization of the perpendicular radial and polar DCs has been kept fixed at $k^0_{\perp,r} = 0.02$ and $k^0_{\perp,\theta} = 0.01$, consistent with the values found by Vos [211] and Zhao et al. [212] analyzing data from PAMELA and with the expectation of turbulent theory [213, 214, 52]. The parameters describing the drift processes, R_A and k^0_A, are set to the one used for reproducing PAMELA data, *i.e.* respectively, 0.55 GV and 1. The transition rigidity R_k and the smoothness of the change of slope c are the same for all the three DCs and are equal to, respectively, 4.3 GV and 2.2. The termination shock is fixed at 80 AU and the heliopause at 122 AU, consistent with the *Voyager* observations. The fast and slow solar wind components have been assumed to have the same speed $V_{SW} = 440$ km/s, since we are analyzing the solar maximum. The input LIS is the one defined in Section 4.2 (see Figure 4.5 and Table 4.2).
The spatial grid has 609 steps in the radial direction, from 0.4 AU to 122 AU, 145 steps in the polar direction, from 0 to π, and 33 steps in the longitudinal direction, from 0 to 2π. The rigidity grid has been divided in 245 steps, uniformly distributed in logarithmic space between 1 and 200 GV. To reduce the output file size, the solution has been saved in a reduced spatial grid, with a radial

Table 5.1: Definition of the grid of input parameters used to generate the numerical models.

Parameter	Symbol	Units	# of values	Values
HMF polarity	A	–	2	-1, +1
Tilt angle	α	°	6	20, 25, 30, 35, 40, 65
HMF intensity at Earth	B_0	nT	6	4.5, 5.5, 6.0, 6.5, 7.5, 8.5
Normalization of the parallel DC	$k_{\parallel}^0$	$6\times10^{20}\mathrm{cm}^2/\mathrm{s}$	7	50, 70, 90, 110, 130, 150, 170
Low-rigidity slope of the parallel DC	$a_{\parallel}$	–	7	0.2, 0.5, 0.8, 1.1, 1.4, 1.7, 2.0
High-rigidity slope of the parallel DC	$b_{\parallel}$	–	8	0.2, 0.5, 0.8, 1.1, 1.4, 1.7, 2.0, 2.3
Low-rigidity slope of the perpendicular DC	$a_{\perp}$	–	7	0.2, 0.5, 0.8, 1.1, 1.4, 1.7, 2.0
High-rigidity slope of the perpendicular DC	$b_{\perp}$	–	8	0.2, 0.5, 0.8, 1.1, 1.4, 1.7, 2.0, 2.3

step of 2 AU, a latitudinal step of 5° and at $\phi = 0$. This last choice is justified by the fact that the modulated flux at Earth is not much dependent on the heliographic longitude: indeed, the flux variation around the average value is of the order of 0.3 %.
Almost 1.6 million models have been generated, for a running time of four weeks and a total disk size of 2.5 TB.

5.2.1 Fixing the heliosphere status

A steady-state model assumes that the heliosphere status is frozen throughout the whole time interval during which the particles propagate from the heliopause to Earth. Clearly, this assumption is never valid in a dynamical system like the heliosphere, especially during periods of high solar activity, when the HMF and the tilt angle can have large variations on a monthly basis. Nevertheless, the steady-state approximation is widely used, due to the simplicity of treatment of the numerical solution of the Parker equation.
As a first approximation, a way to take into account the time-varying status of the heliosphere is to use an average value for α and B_0. Given a BR, we take the average of the tilt angle and HMF over a time period preceding the selected BR. This time period has been chosen such that the average values of α and B_0 reflect the average conditions sampled by galactic cosmic rays (GCRs) while propagating from the heliopause to Earth. Since the HMF is frozen in the solar wind, it propagates with the same velocity: if $V_{SW} = 440\,\mathrm{km/s}$, taking into account the drop in velocity at the termination shock, the propagation time is of the order of two years. However, GCRs diffuse inward in a much shorter period of time, between 1 and 4 months [199], and do not spend the same

amount of time at all radial distances: in fact, the more they penetrate the heliosphere, the more energy they lose, so that the residing time increases going toward the Sun. At the same time, most of the modulation happens in the heliosheath, as observed by *Voyager 1*. We decided to consider a period of 1 year, during which the heliosphere conditions affect the GCRs.
Figure 5.3 illustrates the time variation of the tilt angle, measured every Carrington rotation by the Wilcox Solar Observatory (WSO), and of the daily HMF observed at Earth by the Advanced Composition Explorer (ACE) and *Wind* spacecraft [1]. The values used as input for the models are computed with a 1-year backward moving average (BMA) and are shown in circles. As an example, the BR 2426 (May 15 – June 10, 2011) is identified by the two dotted-dashed vertical black lines, and the preceding 1-year period used for the average is highlighted in gray.

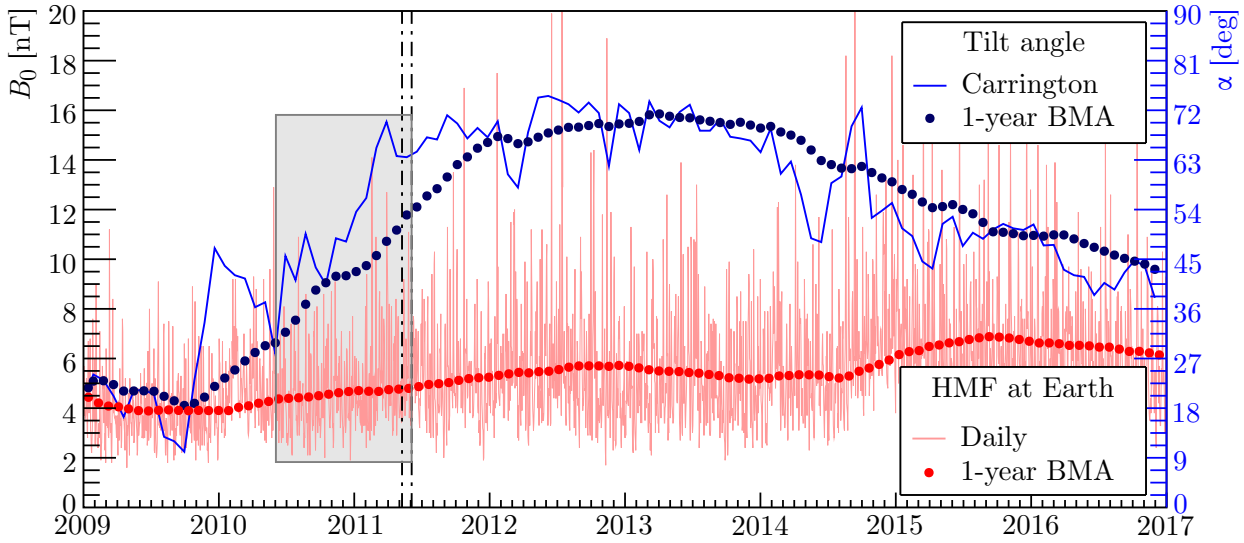

Figure 5.3: Time variation of the line-of-sight tilt angle measured in Carrington rotations by the WSO (blue line) and of the daily HMF obtained by OMNIWeb (pink line). The dark blue and red dots are the 1-year backward moving average of, respectively, the tilt angle and the HMF for every BR. As an example, BR 2426 (May 15 – June 10, 2016) is identified by the two vertical dashed-dotted black lines. The corresponding 1-year period prior to (and including) this BR, used for computing the moving average, is highlighted with a gray rectangle.

For each BR, the tilt angle and the HMF are fixed to the values $\alpha^{(avg)}$ and $B_0^{(avg)}$ obtained by the BMA. Since the grid has only a few discrete values of α and B_0, a two-dimensional linear interpolation is used to obtain the modulated flux $\Phi(\alpha^{(avg)}, B_0^{(avg)})$ corresponding to the averaged heliosphere status. Let's define $\Phi_{i,j} = \Phi(R; \alpha_i, B_{0,j}; \vec{q})$, where $\vec{q}$ is a vector representing one of the possible combinations of the remaining parameters of the grid, while i and j are the points on, respectively, the α axis and the B_0 axis for which $\alpha_i \leqslant \alpha^{(avg)}$ and $B_{0,j} \leqslant B_0^{(avg)}$. Let's also define

[1] The HMF have been downloaded by the NASA/GSFC's OMNI data set through OMNIWeb: `https://omniweb.gsfc.nasa.gov/index.html`

the interpolating factors $s_\alpha = (\alpha^{(avg)} - \alpha_i)/(\alpha_{i+1} - \alpha_i)$ and $s_{B_0} = (B_0^{(avg)} - B_{0,i})/(B_{0,i+1} - B_{0,i})$. If $\alpha^{(avg)}$ or $B_0^{(avg)}$ is outside the range covered by the generated grid, then s_α and s_{B_0} are computed using the two closest points to $\alpha^{(avg)}$ and $B_0^{(avg)}$. A first interpolation is performed on the B_0 axis: $\Phi_i(B_0^{(avg)}) = (1 - s_{B_0})\Phi_{i,j} + s_{B_0}\Phi_{i,j+1}$ and $\Phi_{i+1}(B_0) = (1 - s_{B_0})\Phi_{i+1,j} + s_{B_0}\Phi_{i+1,j+1}$. The final interpolation is carried on on the α axis: $\Phi(\alpha^{(avg)}, B_0^{(avg)}) = (1 - s_\alpha)\Phi_i(B_0^{(avg)}) + s_\alpha\Phi_{i+1}(B_0^{(avg)})$. Figure 5.4 shows an example of the interpolation procedure. On the left, the grid projected on the α and B_0 axes is displayed, with the four points identifying the fluxes $\Phi_{i,j}$. We highlight the fact that each of these four points does not correspond to a single flux, but to the ensemble of fluxes determined by all the generated combinations of $\vec{q}$: the 2D interpolation is computed separately for each $\vec{q}$. On the right, the fluxes $\Phi_{i,j}$ are shown as colored lines, while the interpolated flux is in black.

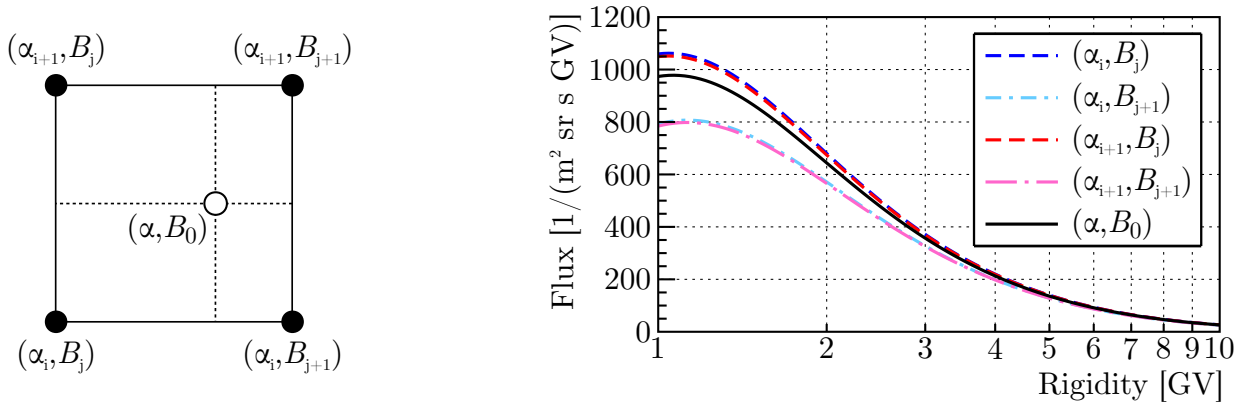

Figure 5.4: Example of 2D flux interpolation in the (α, B_0) grid. **Left**: The grid in tilt angle and HMF is used to find the four points closest to the requested couple ($\alpha^{(avg)}$, $B_0^{(avg)}$). Each dot in the grid represent an ensemble of models with fixed values of α and B_0, while all the other parameters are varied. **Right**: For each combination of all the other parameters, the fluxes at the four closest grid points (colored lines) are interpolated to obtain the flux corresponding to ($\alpha^{(avg)}$, $B_0^{(avg)}$) (black line).

A good fraction of the monthly fluxes have been collected during the period of the magnetic field polarity reversal. Since the model expects a well-defined polarity, it's not possible to correctly describe the heliosphere status in this time interval. For this reason, both models with negative and positive polarity have been used to describe the BRs between October 2013 and February 2015, while before October 2013 the polarity was only negative and after February 2015 only positive. The reversal period ended in February 2104, but we decided to extend it up to 1 year later to take into account the propagation throughout the heliosphere.

For simplicity, the Earth's position has been assumed to be fixed at the average position $r = 1$ AU and $\theta = 90°$. In reality, the variation around this point is ± 0.02 AU and $\pm 7°$. Figure 5.5 top shows the radial and latitudinal dependence of the modulated flux, normalized by the value at Earth,

for both positive and negative polarity. The bottom panel represents a zoomed region around the average position. As can be seen, $r = 1\,\mathrm{AU}$ does not introduce any bias, since the $\pm 0.02\,\mathrm{AU}$ translates into a flux difference of less than permille for both polarities. Regarding the latitudinal dependence, for $A < 0$ the difference is at most 0.5 %, but for $A > 0$ it can be more than 5 %: this is due to the fact that, when the polarity is positive, protons mostly arrive at Earth passing through the polar regions of the heliosphere, thus they are more sensitive to the heliographic latitude of the Earth's orbit.

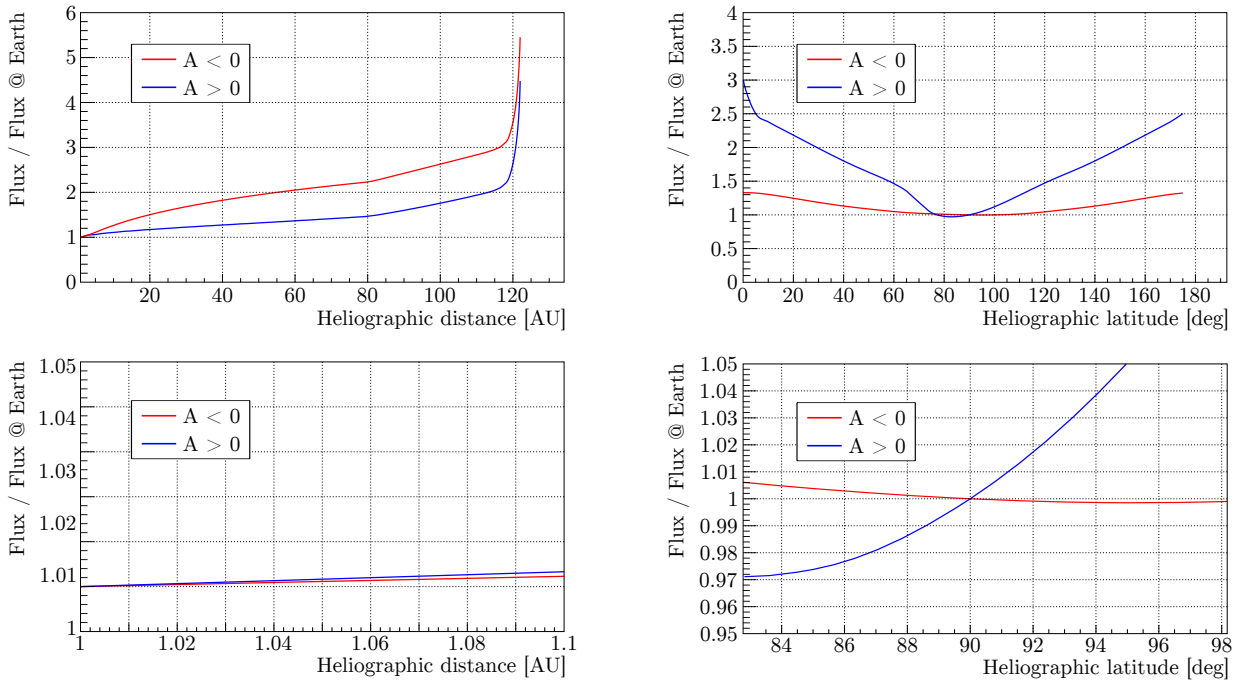

Figure 5.5: Radial (**left**) and latitudinal (**right**) dependence of the modulated flux at $R = 1\,\mathrm{GV}$ throughout the heliosphere, normalized to the value at Earth, for models with negative and positive polarity (respectively, red and blue). **Bottom**: Zoom around Earth's average position.

5.2.2 Best-fit parameters estimation

Once the heliosphere status is fixed, the interpolated fluxes are used to estimate the best-fit parameters $k_{\parallel}^{0}$, $a_{\parallel}$, $b_{\parallel}$, $a_{\perp}$and $b_{\perp}$. For every BR, the chi-squared between each interpolated model and the data is computed. Only models with $a_{\perp} \leqslant a_{\parallel}$ and $b_{\perp} \leqslant b_{\parallel}$, in accordance with the predictions of turbulence theory [64, 214], have been taken into consideration. The estimation of a given parameter X proceeds in the following way: for every value x of the parameter, the minimum chi-squared $\chi^2_{min}(x)$ is found, regardless of the values of all the other parameters, *i.e.* we marginalize over the other parameters. If some of the values x are close to the true value of $\widehat{X}$, the distribution of $\chi^2_{min}(x)$ is approximately locally parabolic. In this case, the point with the minimum chi-squared

$\chi^2_{min} = \min_x \chi^2_{min}(x)$ is found and its left and right neighbors are used to build the unique parabola passing through them. In case the minimum is the first (last) point on the X axis of the grid, the two right (left) neighbors are selected.
Given a set of three points (x_0, x_1, x_2), it's always possible to find a parabola satisfying the system of equations:

$$\begin{cases} y_0 = ax_0^2 + bx_0 + c \\ y_1 = ax_1^2 + bx_1 + c \\ y_2 = ax_2^2 + bx_2 + c \end{cases} \implies \begin{pmatrix} y_0 \\ y_1 \\ y_2 \end{pmatrix} = \begin{pmatrix} x_0^2 & x_0 & 1 \\ x_1^2 & x_1 & 1 \\ x_2^2 & x_2 & 1 \end{pmatrix} \begin{pmatrix} a \\ b \\ c \end{pmatrix} \tag{5.20}$$

which can be solved by inverting the matrix of the xs. Let's define the quantities $\Delta_{ij} = x_i - x_j$, $\sigma_{ij} = x_i + x_j$ and $\pi_{ij} = x_i x_j$; the determinant of the matrix can be written as $\delta = \frac{1}{2}\sum_{i,j,k=0}^{2} \epsilon_{ijk}\pi_{ij}\Delta_{ij} = \pi_{01}\Delta_{01} + \pi_{12}\Delta_{12} + \pi_{20}\Delta_{20}$. Then, the solution is:

$$\begin{cases} a = \dfrac{y_0\Delta_{12} + y_1\Delta_{20} + y_2\Delta_{01}}{\delta} \\ b = \dfrac{y_0\Delta_{12}\sigma_{12} + y_1\Delta_{20}\sigma_{20} + y_2\Delta_{01}\sigma_{01}}{\delta} \\ c = \dfrac{y_0\Delta_{12}\pi_{12} + y_1\Delta_{20}\pi_{20} + y_2\Delta_{01}\pi_{01}}{\delta} \end{cases} \tag{5.21}$$

From this, we can estimate the true global minimum chi-squared $\widehat{\chi}^2_{min} = c - b^2/(4a)$, the best-fit parameter $x_{min} = -b/(2a)$ and the uncertainty on the parameter $\sigma_x = 1/\sqrt{a}$, defined as the difference $\sigma_x = x_{min} - x_l = x_r - x_{min}$, where x_l and x_r are the values of X for which $\chi^2_{min}(x_{l,r}) = \chi^2_{min} + 1$, respectively on the left and on the right of x_{min}.

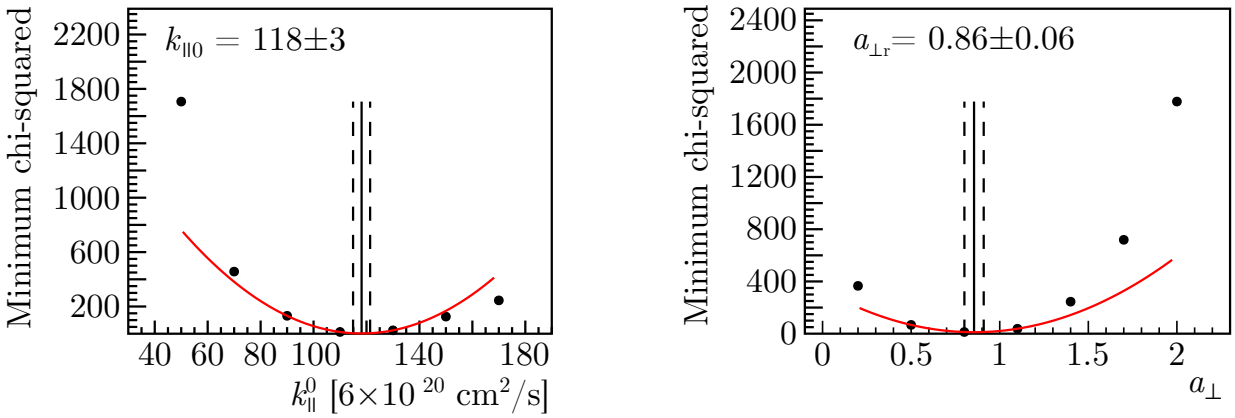

Figure 5.6: Examples of parameter estimation ($k^0_\parallel$ on the **left**, $a_\perp$ on the **right**) using the minimum chi-squared shape (black dots). The red curve is the parabola defined in Equation 5.21 passing through the lowest point. The vertical black solid line represents the position of the minimum of the parabola, while the two dashed lines are positioned at the parameter values such that $\chi^2 = \chi^2_{min} + 1$.

Figure 5.6 shows two examples of best-fit parameter estimation for $k_{\parallel}^{0}$ and $a_{\perp}$: the black dots are the marginalized $\chi^2_{min}(x)$, the red line is the parabola defined in Equation 5.21, while the vertical black lines mark the position of x_{min} (solid line) and the uncertainty σ_x (dashed lines).

With a little abuse of notation, we can define the "likelihood" of a model $\mathscr{L} = e^{-\chi^2/2}$. Technically speaking, since this kind of analysis is frequentist and not Bayesian, this is not a real likelihood, but nevertheless it's a quantity useful to estimate the probability of a given model. Weighting each model by its likelihood, we can obtain the distribution of the modulated fluxes in every rigidity bin: again, if this was a Bayesian analysis, this distribution would represent the actual probability density function of the modulated flux, hence it would be possible to define a credible interval on the theoretical flux. While in this case this interpretation is not possible, we can still use the weighted distribution to estimate the uncertainty on the best-fit model.

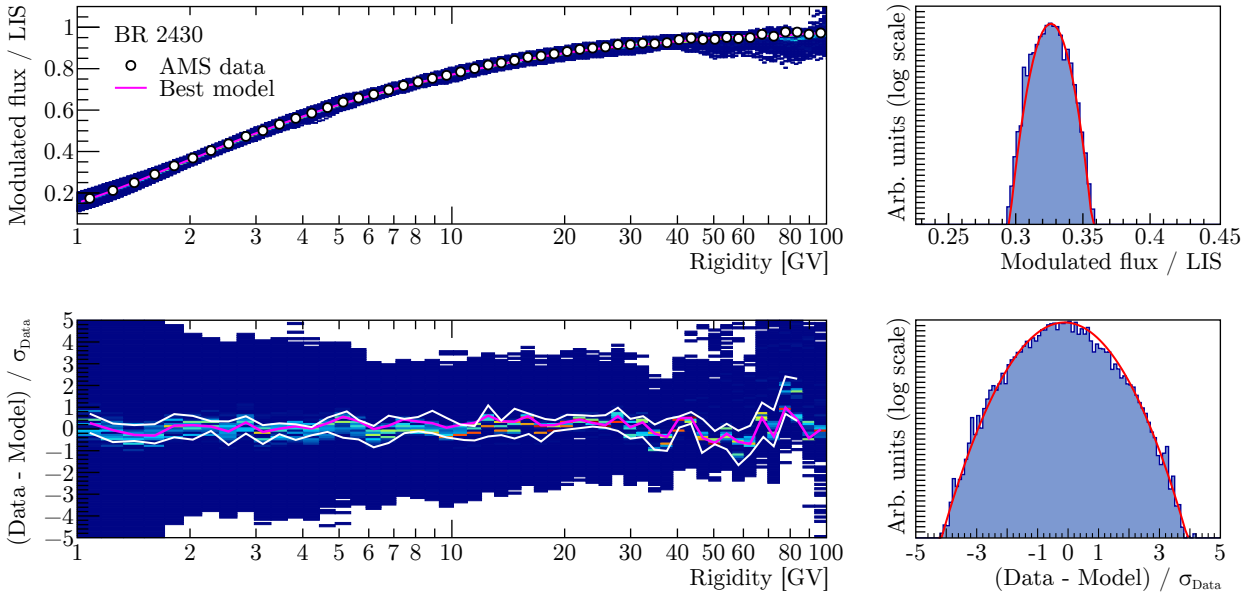

Figure 5.7: **Top left**: Distribution of the modulation fraction (modulated flux to LIS ratio) weighted by each model likelihood. The white circles are the modulation fraction measured by AMS during BR 2430, while the magenta line is the modulation fraction of the model with the minimum chi-squared. **Top right**: Slice of the likelihood-weighted distribution of the modulation fraction around 4 GV (blue histogram), with a gaussian fit (red line). **Bottom left**: Likelihood-weighted distribution of the residuals between data and models. The magenta line is the residual of the model with the minimum chi-squared, while the two white lines indicate the RMS of the residuals distribution. **Bottom right**: Slice of the likelihood-weighted distribution of the residuals around 4 GV (blue histogram), with a gaussian fit (red line).

Figure 5.7 top shows the distribution of the modulated flux divided by the LIS, weighted by the likelihood[2], while the bottom panel shows the distribution of the residuals $(\Phi_{data} - \Phi_{model})/\sigma_{data}$,

[2]Because of numerical instabilities, the unweighted distribution of the modulated flux in a given rigidity bin is

weighted by the likelihood. The small panels on the right display a slice of the distributions around 4 GV in logarithmic scale, together with a gaussian fit (red line).

The distribution is remarkably gaussian, also in the tails, demonstrating that the chi-squared is well behaved and can be approximated as a parabola around the minimum. The white lines in the bottom left panels are positioned at $\mu \pm \sigma$, where μ is the mean of the fitted gaussian and σ its width. The magenta line represents the residual for the model with the minimum chi-squared χ^2_{min} (not to be confused with the estimated true global minimum $\widehat{\chi}^2_{min}$, which is closer to the gaussian mean). This plot shows that the uncertainty on the modulated fluxes is on par with the uncertainty on the data, usually a little bit smaller.

5.3 Results

The values of the best-fit parameters, together with their estimated uncertainty, are listed in Tables B.1 and B.2. The time variation of the best-fit parameters is analyzed in Figure 5.8. In the top panel, the tilt angle and the HMF used as input in every BR are displayed for reference. The vertical magenta lines mark the period of the magnetic polarity reversal.

The second panel shows the normalized minimum chi-squared, both χ^2_{min}/dof (dashed lines) and $\widehat{\chi}^2_{min}$/dof (solid lines), which are anyway very close to each other. Beginning in May 2011, $\widehat{\chi}^2_{min}$/dof is consistently around 0.5: as already discussed in Section 3.10.2, the total error on the AMS monthly proton flux is probably overestimated for time-variation studies, since some of the included systematics are time-independent. The normalized chi-squared increases during the period of the polarity reversal: these BRs have been fitted with models of both polarity, but looking at the chi-squared values there does not seem to be a preferred polarity. From November 2015, χ^2_{min} starts to increase: this effect is not due to a worst description of the physics involved in this months, but it's rather an artificial effect due to the limited range in which $k^0_{\parallel}$ has been varied.

Indeed, panel (c) shows that, from November 2015, the best-fit $k^0_{\parallel}$ is always very close to the upper limit. This is particularly evident by looking at the dashed blue line, which represents the value of $k^0_{\parallel}$ of the models with the minimum chi-squared. During all these months, the curve of $\chi^2_{min}(k^0_{\parallel})$ is truncated on the right, because the true global minimum is outside the grid range, hence the derived parabola does not correctly describe the shape around the minimum. Analyzing the rest of the months, we see that the variations of $k^0_{\parallel}$ follow closely the variation of the observed fluxes, as it was expected, $k^0_{\parallel}$ being the main parameter that controls the level of modulation. For example, we can see the drops in $k^0_{\parallel}$ (*i.e.* short-term increases in the modulation strength) in correspondence of the drops of the proton fluxes, *e.g.* in March 2012 or October 2011. A caveat of this result is that we know these drops are due to coronal mass ejections (CMEs) hitting the Earth, *i.e.* local disturbances, which are not included in the model. Nevertheless, the model is able to reproduce the

not flat in all the parameters, so the likelihood-weighted distribution is normalized to the unweighted distribution, to remove any artificial structures induced by the non-uniform coverage of the parameters phase space.

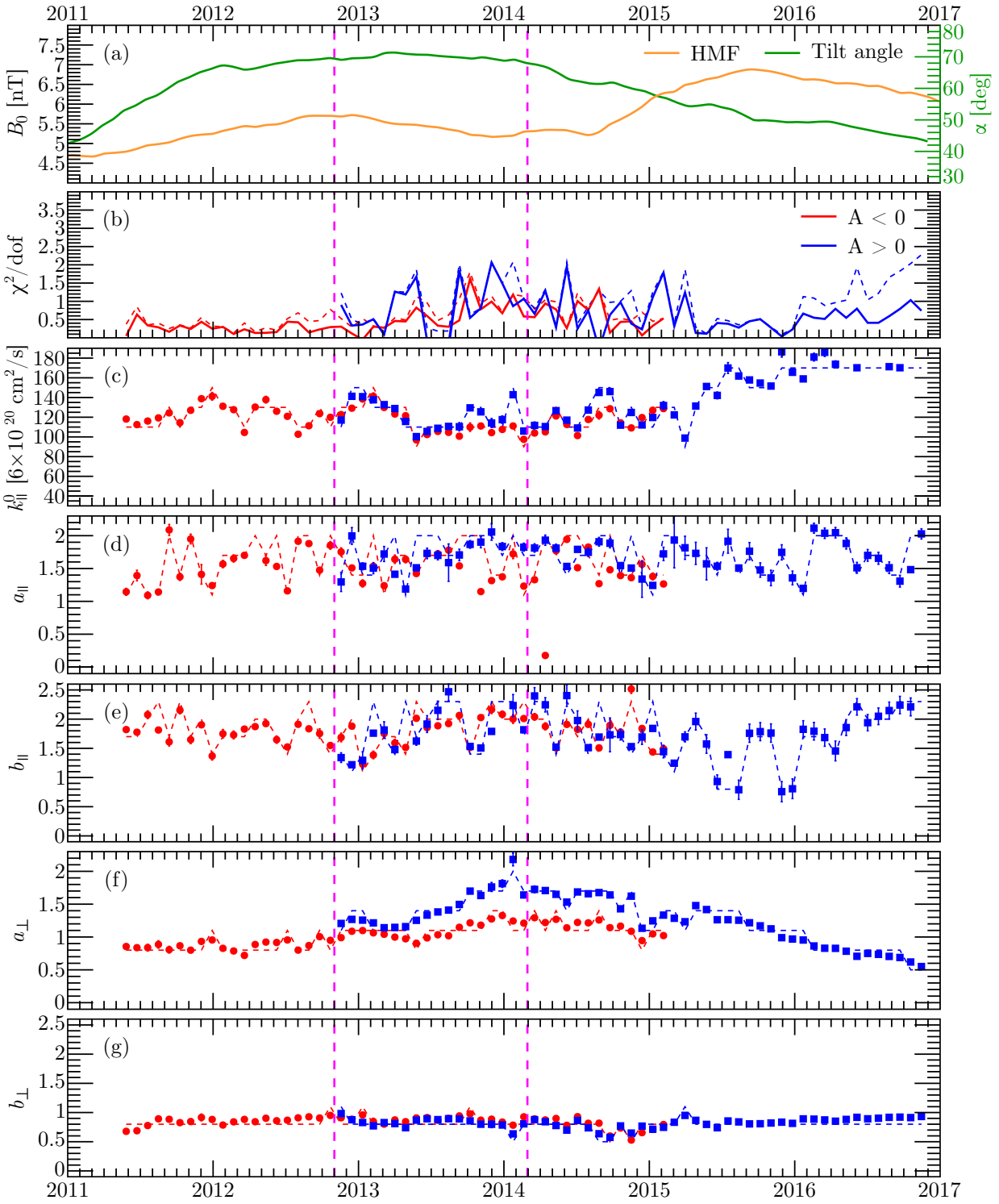

Figure 5.8: **(a)**: HMF and tilt angle used as input parameters in the models. **(b)**: Normalized chi-squared of the best-fit models. Time variation of the best-fit parameters (circles and squares) for models with negative (red) and positive (blue) polarity: $k_{\|}^0$**(c)**, $a_{\|}$**(d)**, $b_{\|}$**(e)**, $a_{\perp}$**(f)**, $b_{\perp}$**(g)**. The dashed lines correspond to the values of the models with the minimum chi-squared. The vertical magnet lines mark the period of the magnetic polarity reversal.

flux, by changing globally the DC in order to match the local conditions: we can expect that, in these cases, the solution at positions far from Earth will not be accurate, since the diffusion in these positions is not affected by the CME. It is worth noting that, in the period of the polarity reversal, the best-fit $k_{\parallel}^{0}$ obtained from models with negative polarity agree with the one from models with positive polarity, *i.e.* the normalization of the parallel DC seems to be mostly insensitive to the sign of the HMF polarity.

Panels (d) and (e) shows the time variation of the low- and high-rigidity slope of the parallel DC, $a_{\parallel}$ and $b_{\parallel}$. The best-fit values seems to vary a lot from month to month, making it difficult to discern any clear time-dependent pattern. The uncertainty on the fitted values is also larger than with respect to the other parameters, meaning that the $\chi^2_{min}(a_{\parallel})$ and $\chi^2_{min}(b_{\parallel})$ distribution are wider around the minimum. Indeed, sometimes the $\chi^2_{min}(x)$ curve has two local minima or it does not have a parabolic behavior. This means that these two parameters are not well constrained, *i.e.* the modulated flux is not so sensitive to the values of $a_{\parallel}$ and $b_{\parallel}$. A possible explanation is that the parallel diffusion dominates very close to the Sun, when most of the modulation has already happened (see Figure 5.5). From Equation 1.22, the DC in the radial direction is $\mathsf{K}_{rr} = k_{\parallel}\cos^2\psi + k_{\perp,r}\sin^2\psi$; imposing equality between the two terms yields $\tan^2\psi \simeq 1/k^{0}_{\perp,r} = 50$, corresponding to a spiral angle $\psi \approx 80°$, which can be found already around 5 AU, a mere 0.01 % of the whole heliosphere volume.

The parameters describing the perpendicular DC are shown in the panels (f) and (g), respectively $a_{\perp}$ and $b_{\perp}$. Remarkably, $b_{\perp}$ is almost constant with time, both for positive and negative polarity, whose best-fit values agree in almost all the overlapping months. $a_{\perp}$ is mostly flat before the maximum of solar activity, when $A < 0$, while during the period of the polarity reversal the best-fit values with opposite polarity are clearly not consistent with each other. In particular, $b_{\perp}$ for models with $A > 0$ displays a large increase, almost doubling its value in correspondence of the peak of the solar activity with respect to the beginning of the polarity reversal. This tells us that, on top of the overall modulation scale driven by $k_{\parallel}^{0}$, low rigidities experience an even smaller mean free path. The fact that the rise for $A < 0$, contrary to the $A > 0$ case, is not so significant means that drift processes play a key role in the transport of protons during this period.
If we recall the discussions of Sections 3.10.1 and 4.4, in this period the low-rigidity flux and the high-rigidity flux have a significant different behavior, both signaled by the absence of correlations between different bins and by the flatness of the high-rigidity modulation potential with respect to the rising of the low-rigidity potential. The numerical model reveals that this behavior is due to the rigidity slope of the perpendicular DC.

5.3.1 Time variation of the proton flux at Mars

Matching a model with the flux observed at Earth, allows to obtain the modulated flux at all positions in the heliosphere for a given time interval. Knowing the modulated flux at Mars is of

particular importance for radiation safety assessment for a human space mission to the red planet. The best-fit models have been computed at the average position of Mars in each BR. Figure 5.9 bottom shows the ratio of the flux at Mars to the flux at Earth, for different polarities, while the top panel shows the orbital position of Mars. The radial gradient in the inner heliosphere is small, and Mars is on average 0.5 AU far from Earth, so we do not expect a big increase in the GCR flux: indeed, for $A < 0$, the Mars-to-Earth flux ratio is around 2 %, consistent with zero within the modulated flux uncertainty. During the period with positive polarity, the ratio can display oscillations correlated with the latitudinal position of Mars: when the orbit is below the Sun equatorial plane, the flux at Mars is 2 % *lower* than at Earth, while, vice versa, it's 2 % higher when the planet orbits above the equatorial plane. This behavior is due to the protons drifting mainly from the poles in $A > 0$ cycles.

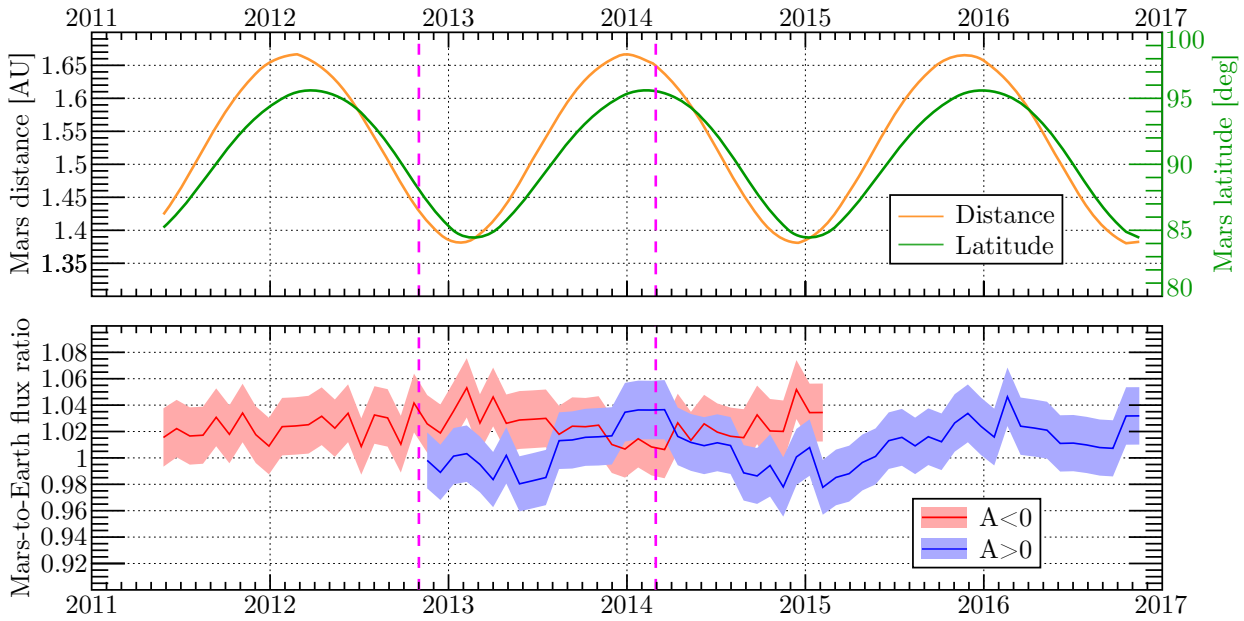

Figure 5.9: **Top**: Heliographic distance (orange) and latitude (green) of Mars. **Bottom**: Time variation of the Mars-to-Earth flux ratio for models with negative polarity (red) and positive (blue).

CHAPTER 6
SUMMARY

The focus of this thesis has been the study of the time variation of the proton and helium fluxes in galactic cosmic rays (GCRs) measured by the Alpha Magnetic Spectrometer (AMS) between May 20, 2011 and November 26, 2016, during the maximum of the solar cycle 24. The work carried on in these years can be divided into two parts: the first one was dedicated to the analysis of the data collected by AMS, contributing to the measurement of the monthly fluxes, while the second one was devoted to the theoretical interpretation of the experimental result.

An overview of the various concepts involved in the physics of cosmic rays in the heliosphere is given in Chapter 1. After a generic introduction to the history and theory of GCR acceleration, the chapter moves to the description of the heliosphere and its components: the solar wind, the heliospheric magnetic field (HMF) and the neutral heliospheric current sheet (HCS). The rest of the chapter focus on the theory of the solar modulation of cosmic rays and its main equation: the Parker transport equation. The physical processes contained in this equation are: convection by the solar wind, diffusion via scattering on the magnetic field irregularities, drifts due to magnetic field gradients and to the HCS and the adiabatic energy losses due to the expansion of the solar wind. The derivation of the diffusion and drift coefficients from turbulence theory is also covered. The final part of the chapter is dedicated to the force-field approximation, a widely used analytical solution of the Parker equation depending on one single parameter (the modulation potential). The validity of this approximation under various conditions is discussed.

Chapter 2 describes the AMS apparatus, with its sub-detectors: a transition radiation detector (TRD), a time of flight (TOF), a silicon tracker immersed in a magnetic field, a ring imaging Cherenkov (RICH) and an electromagnetic calorimeter (ECAL). The first results published by AMS are reported and their significance for the theory of GCRs acceleration and propagation is briefly illustrated.

Chapter 3 revolves around the experimental work of the thesis: it contains the description of the data analysis of the monthly proton and helium fluxes, explaining in details all the needed steps. The main contributions to the measurements of the time variation of the fluxes were:

1. **Study of the digital signal processor (DSP) errors**. The harsh particle radiation environment in which AMS and the International Space Station resides can induce errors in the many electronic components of the detector. The time dependence and distribution among different categories of electronic boards of these errors has been studied, to asses their effect on the exposure time of the experiment. The errors are mostly concentrated in the South Atlantic Anomaly, a region where the Earth magnetic field is lower and where the rate of low-energy particles increases. This region is excluded from the analysis, so the conclusion of this study is that the DSP errors do not affect the measurement.

2. **Study of the energy losses**. Particles with low-rigidity, below 2 GV, lose an important fraction of their energy while traversing the detector, hence biasing the rigidity measurement of the tracker. The details of the energy losses have been studied with a dedicated Monte Carlo simulation and a procedure for their recovery on an event-by-event basis and on average has been developed. The results of this study show that the uncorrected rate at 1 GV is underestimated by 5 %, while at 0.6 GV it is overestimated by more than 20 %.

3. **Rigidity unfolding**. An algorithm for correcting the migration of the events between different bins, due to energy losses, interactions and finite tracker resolution, is presented. The resulting flux obtained with the unfolding procedure described here is consistent with the one published by the AMS collaboration.

4. **Systematic errors due to the rigidity measurement**. The different factors affecting the measurement of the rigidity with the tracker have been analyzed and the systematic errors on the flux due to them has been estimated: the value of the errors is consistent with the official analysis of the AMS experiment.

5. **Study of the modulation effects at different rigidities**. A model-independent analysis based on the correlation between the time variation of the proton fluxes at different rigidities is described. The main result is that, during the period of the maximum solar activity and of the HMF polarity reversal, particles at lower rigidities experience a different modulation than particles at higher rigidities.

The aim of Chapter 4 is to study the solar modulation of protons and helium in the framework of the force-field approximation. First, a new parametrization of the local interstellar spectrum (LIS) has been derived from the latest data of *Voyager 1* and AMS. Then, the monthly proton fluxes measured by PAMELA during the minimum between solar cycles 23 and 24 are reproduced with the LIS modulated according to the force-field approximation. Some discrepancies between the data and the analytical model compel us to develop a modified version of the force-field approximation, in which the modulation is now rigidity-dependent. Using this new analytical model, the charge-dependence of the solar modulation is studied, by analyzing the proton and monthly fluxes measured by BESS: a time dependence of the proton-to-helium modulation potential ratio is observed, possibly correlated with the change in polarity of the HMF. Applying the same model on the monthly proton and helium fluxes measured by AMS confirms the conclusion of the model-independent study conducted in Chapter 3: the flux modulates differently below and above few GV. In particular, above 5 GV the modulation potential displays a flatter behavior in time with respect to the modulation potential around 1 GV.

Finally, in Chapter 5 a numerical model solving the Parker equation in three dimensions is used to reproduce the monthly proton fluxes by AMS. After a brief historical overview of numerical models used in solar modulation studies, the algorithm used for the solution of the Parker equation is

described. Particular care has been put into studying and avoiding the instability of some solutions, due to the complexity of the model. A best-fit parameters estimation procedure has been developed, since the usual approach of a least-squares fit is not feasible because of a limitations in the available computational resources. The model is able to reproduce the different rigidity-dependence of the time variation and the main results is that, in order to reproduce the observed fluxes, the mean free path for diffusion in the direction perpendicular to the HMF must decrease at low rigidities in correspondence of the maximum of the solar activity, while at high rigidity is almost constant in time.

The next step in understanding better the solar modulation during the solar maximum is to study the numerical instabilities, in order to reduce the fraction of failed models, and then to implement a more realistic description of the highly dynamical heliosphere status. A comparison with the fluxes measured by *Voyager 2* in the heliosheath in the same time period of the AMS data taking will provide additional constraints to the model parameters.

APPENDIX A
FITTED SOLAR MODULATION PARAMETERS

Table A.1: Solar modulation parameters in units of MV derived from proton fluxes. The error contributions from the fit of the modulated fluxes (σ_{fit}) and from the uncertainty on the LIS (σ_{LIS}) are reported separately. ϕ is the modulation parameter obtained with the force-field approximation, while ϕ_L and ϕ_H are the modulation parameters obtained with the modified force-field approximation.

Date	Experiment	ϕ	σ_{fit}	σ_{LIS}	ϕ_L	σ_{fit}	σ_{LIS}	ϕ_H	σ_{fit}	σ_{LIS}
1993 Jul 01	BESS93	492.9	6.3	4.0	449.1	6.9	4.2	532	22	17
1997 Jul 27	BESS97	353.5	5.3	3.2	341.3	5.8	3.7	289	21	16
1998 Jul 29	BESS98	449.8	5.9	3.5	439.9	6.7	4.0	354	23	17
1999 Aug 11 – 12	BESS99	526.4	6.3	3.7	506.5	7.1	4.4	475	24	17
2000 Aug 10 – 11	BESS00	1170.6	9.6	5.3	1158.0	12	6.8	989	27	18
2002 Aug 07	BESS-TeV	973.5	5.2	5.0	989.4	7.0	6.2	734	13	17
2004 Dec 13 – 21	BESS-Polar I	647.4	1.9	4.4	635.7	2.4	5.0	524.2	5.8	17
2007 Dec 22 – 2008 Jan 19	BESS-Polar II	397.5	1.7	3.8	369.6	2.0	3.9	377.6	5.9	16
2006 Jul – 2008 Dec	PAMELA	412.1	3.4	4.1	383.0	4.1	4.2	375	11	16
2006 Jul 07 – 2006 Jul 26	PAMELA	490.9	3.8	3.4	475.4	4.1	3.8	431	13	17
2006 Jul 27 – 2006 Aug 22	PAMELA	485.3	3.6	3.3	473.7	3.8	3.8	407	13	17
2006 Aug 24 – 2006 Sep 19	PAMELA	474.0	3.6	3.3	464.3	3.9	3.8	382	13	17
2006 Sep 20 – 2006 Oct 16	PAMELA	463.8	3.5	3.2	455.3	3.8	3.7	368	13	17
2006 Oct 17 – 2006 Nov 12	PAMELA	459.9	3.5	3.2	449.4	3.7	3.7	379	13	17
2006 Nov 13 – 2006 Dec 04	PAMELA	451.8	3.5	3.2	440.6	3.8	3.6	375	13	17
2007 Jan 11 – 2007 Feb 02	PAMELA	447.3	3.6	3.1	439.8	3.9	3.6	347	14	17
2007 Feb 03 – 2007 Mar 02	PAMELA	442.4	3.6	3.1	435.0	3.9	3.6	343	14	17
2007 Mar 03 – 2007 Mar 29	PAMELA	436.5	3.5	3.1	428.1	3.8	3.6	347	14	17
2007 Mar 30 – 2007 Apr 25	PAMELA	420.2	3.5	3.0	412.9	3.7	3.5	326	14	17
2007 Apr 26 – 2007 May 22	PAMELA	409.5	3.5	3.0	401.4	3.7	3.5	324	14	17
2007 May 23 – 2007 Jun 17	PAMELA	406.2	3.4	3.0	397.5	3.7	3.4	326	14	17
2007 Jun 27 – 2007 Jul 16	PAMELA	398.7	3.5	3.0	389.7	3.7	3.4	321	14	17
2007 Jul 17 – 2007 Aug 12	PAMELA	394.7	3.4	2.9	386.3	3.6	3.4	314	14	17
2007 Aug 13 – 2007 Sep 06	PAMELA	395.7	3.5	3.0	383.8	3.7	3.4	339	14	17
2007 Sep 09 – 2007 Oct 06	PAMELA	388.6	3.4	3.0	378.2	3.6	3.4	325	14	17
2007 Oct 07 – 2007 Nov 02	PAMELA	382.6	3.4	2.9	372.7	3.6	3.3	316	14	17
2007 Nov 03 – 2007 Nov 29	PAMELA	376.1	3.3	2.9	368.8	3.6	3.3	291	14	17
2007 Nov 30 – 2007 Dec 27	PAMELA	375.5	3.4	2.9	367.3	3.6	3.3	297	14	17
2007 Dec 28 – 2008 Jan 23	PAMELA	380.2	3.4	2.9	371.0	3.6	3.3	309	14	17
2008 Jan 24 – 2008 Feb 19	PAMELA	379.4	3.4	3.0	368.6	3.6	3.3	320	14	17
2008 Feb 20 – 2008 Mar 17	PAMELA	380.6	3.5	3.0	371.2	3.7	3.4	309	14	17
2008 Mar 19 – 2008 Apr 14	PAMELA	392.3	3.6	3.0	380.0	3.8	3.4	345	15	17
2008 Apr 15 – 2008 May 11	PAMELA	382.2	3.6	2.9	371.6	3.8	3.4	323	15	17
2008 May 12 – 2008 Jun 07	PAMELA	386.9	3.6	3.0	374.1	3.7	3.3	345	15	17

Table A.1 (Continued)

Date	Experiment	ϕ	σ_{fit}	σ_{LIS}	ϕ_L	σ_{fit}	σ_{LIS}	ϕ_H	σ_{fit}	σ_{LIS}
2008 Jun 08 – 2008 Jul 04	PAMELA	383.3	3.7	3.0	370.4	3.8	3.4	341	15	17
2008 Jul 05 – 2008 Aug 01	PAMELA	379.7	3.7	3.0	366.6	3.8	3.3	338	15	17
2008 Aug 02 – 2008 Aug 28	PAMELA	369.6	3.7	2.9	357.2	3.8	3.3	326	15	17
2008 Aug 29 – 2008 Sep 11	PAMELA	362.2	3.7	2.9	352.0	3.9	3.3	302	15	17
2008 Oct 01 – 2008 Oct 21	PAMELA	360.9	3.6	2.9	348.4	3.8	3.3	321	15	17
2008 Oct 22 – 2008 Nov 18	PAMELA	345.3	3.4	2.7	338.4	3.7	3.2	265	15	17
2008 Nov 19 – 2008 Dec 15	PAMELA	344.8	3.4	2.8	335.9	3.6	3.2	283	15	17
2008 Dec 20 – 2009 Jan 11	PAMELA	350.4	3.6	2.9	337.2	3.7	3.2	323	15	17
2009 Jan 12 – 2009 Feb 08	PAMELA	332.0	3.4	2.8	322.3	3.5	3.1	280	15	17
2009 Feb 21 – 2009 Mar 07	PAMELA	317.8	4.2	2.8	308.5	4.4	3.2	258	18	16
2009 Mar 08 – 2009 Apr 03	PAMELA	312.2	3.3	2.6	307.0	3.5	3.0	223	15	16
2009 Apr 04 – 2009 May 01	PAMELA	307.8	3.2	2.6	302.4	3.4	3.0	224	15	16
2009 May 02 – 2009 May 28	PAMELA	306.9	3.3	2.6	299.4	3.4	3.0	243	15	17
2009 May 29 – 2009 Jun 24	PAMELA	305.7	4.9	2.5	299.0	5.1	3.0	248	26	17
2009 Jun 25 – 2009 Jul 21	PAMELA	301.3	4.7	2.4	296.2	4.9	2.9	227	26	17
2009 Jul 22 – 2009 Aug 18	PAMELA	294.2	4.7	2.4	290.0	4.9	2.9	210	26	17
2009 Aug 19 – 2009 Sep 14	PAMELA	301.6	4.8	2.4	295.9	5.0	2.9	234	26	17
2009 Sep 15 – 2009 Oct 11	PAMELA	296.1	6.3	2.4	292.3	6.6	2.9	207	36	17
2009 Oct 12 – 2009 Nov 07	PAMELA	301.4	6.3	2.4	295.0	6.6	2.9	249	37	17
2009 Nov 08 – 2009 Dec 05	PAMELA	288.4	6.4	2.3	283.9	6.8	2.9	210	37	17
2009 Dec 06 – 2010 Jan 01	PAMELA	282.7	6.3	2.4	275.8	6.5	2.9	240	37	17
2010 Jan 02 – 2010 Jan 23	PAMELA	283.3	4.8	2.4	276.4	4.9	2.9	234	26	17
2011 May 19 – 2013 Nov 26	AMS-02	600	8	–	587.4	7.9	–	481	22	–
2011 May 20 – 2011 Jun 10	AMS-02	530.1	3.2	6.0	453.3	5.1	4.4	468.8	5.2	17
2011 Jun 11 – 2011 Jul 07	AMS-02	562.1	3.2	6.1	482.7	5.2	4.6	500.1	5.1	17
2011 Jul 08 – 2011 Aug 03	AMS-02	527.3	3.1	5.9	475.2	5.1	4.5	445.8	5.1	17
2011 Aug 04 – 2011 Aug 30	AMS-02	519.8	3.1	5.8	482.3	5.1	4.5	426.3	5.0	17
2011 Aug 31 – 2011 Sep 26	AMS-02	513.0	3.1	5.8	474.8	5.1	4.5	420.4	5.0	17
2011 Sep 27 – 2011 Oct 23	AMS-02	560.0	3.1	5.9	519.0	5.2	4.7	467.4	5.1	17
2011 Oct 24 – 2011 Nov 19	AMS-02	526.2	3.1	5.8	485.6	5.1	4.5	435.1	5.1	17
2011 Nov 20 – 2011 Dec 16	AMS-02	495.1	3.0	5.7	468.0	5.0	4.5	394.0	5.0	17
2011 Dec 17 – 2012 Jan 12	AMS-02	489.4	3.0	5.7	458.8	5.0	4.4	391.7	5.0	17
2012 Jan 13 – 2012 Feb 08	AMS-02	519.5	3.1	5.8	474.2	5.1	4.5	433.0	5.1	17
2012 Feb 09 – 2012 Mar 06	AMS-02	531.1	3.1	5.9	485.2	5.1	4.5	444.3	5.1	17
2012 Mar 07 – 2012 Apr 02	AMS-02	636.4	3.2	6.1	579.4	5.5	4.9	552.3	5.2	17
2012 Apr 03 – 2012 Apr 29	AMS-02	545.0	3.1	5.8	525.9	5.2	4.7	434.1	5.1	17
2012 Apr 30 – 2012 May 26	AMS-02	527.2	3.1	5.7	506.0	5.2	4.6	418.9	5.1	17
2012 May 27 – 2012 Jun 22	AMS-02	567.6	3.1	5.9	536.7	5.3	4.7	466.0	5.1	17
2012 Jun 23 – 2012 Jul 19	AMS-02	588.0	3.2	5.9	548.8	5.3	4.8	492.6	5.1	17
2012 Jul 20 – 2012 Aug 15	AMS-02	669.8	3.2	6.1	627.4	5.6	5.1	572.6	5.2	17
2012 Aug 16 – 2012 Sep 11	AMS-02	650.9	3.1	5.9	645.7	5.6	5.1	522.8	5.1	17
2012 Sep 12 – 2012 Oct 08	AMS-02	616.0	3.1	5.8	618.0	5.5	5.0	482.4	5.1	17
2012 Oct 09 – 2012 Nov 04	AMS-02	641.1	3.1	5.9	644.9	5.5	5.1	504.9	5.1	17

Table A.1 (Continued)

Date	Experiment	ϕ	σ_{fit}	σ_{LIS}	ϕ_L	σ_{fit}	σ_{LIS}	ϕ_H	σ_{fit}	σ_{LIS}
2012 Nov 05 – 2012 Dec 01	AMS-02	630.9	3.1	5.8	637.0	5.5	5.1	492.8	5.1	17
2012 Dec 02 – 2012 Dec 28	AMS-02	614.0	3.1	5.7	629.1	5.4	5.0	467.3	5.1	17
2012 Dec 29 – 2013 Jan 24	AMS-02	587.2	3.0	5.7	601.6	5.3	4.9	441.9	5.1	17
2013 Jan 25 – 2013 Feb 20	AMS-02	573.9	3.0	5.7	581.9	5.3	4.9	435.4	5.1	17
2013 Feb 21 – 2013 Mar 19	AMS-02	586.5	3.1	5.8	578.4	5.3	4.9	463.4	5.1	17
2013 Mar 20 – 2013 Apr 15	AMS-02	614.7	3.1	5.8	611.2	5.4	5.0	486.1	5.1	17
2013 Apr 16 – 2013 May 12	AMS-02	619.5	3.1	5.9	608.3	5.4	5.0	497.9	5.1	17
2013 May 13 – 2013 Jun 08	AMS-02	721.2	3.2	6.1	698.7	5.8	5.3	605.3	5.2	17
2013 Jun 09 – 2013 Jul 05	AMS-02	708.2	3.2	6.0	720.9	5.7	5.4	561.6	5.2	17
2013 Jul 06 – 2013 Aug 01	AMS-02	699.5	3.1	5.9	719.9	5.7	5.4	545.4	5.2	17
2013 Aug 02 – 2013 Aug 28	AMS-02	693.2	3.1	5.8	724.6	5.7	5.4	528.6	5.1	17
2013 Aug 29 – 2013 Sep 24	AMS-02	711.7	3.1	5.8	762.0	5.8	5.5	527.4	5.1	17
2013 Sep 25 – 2013 Oct 21	AMS-02	685.2	3.0	5.7	752.0	5.8	5.5	482.4	5.1	17
2013 Oct 22 – 2013 Nov 17	AMS-02	690.3	3.0	5.7	748.8	5.7	5.4	495.8	5.1	17
2013 Nov 18 – 2013 Dec 14	AMS-02	704.6	3.1	5.7	763.3	5.7	5.5	509.6	5.1	17
2013 Dec 15 – 2014 Jan 10	AMS-02	712.7	3.1	5.7	773.2	5.7	5.5	515.0	5.1	17
2014 Jan 11 – 2014 Feb 06	AMS-02	707.3	3.1	5.7	762.0	5.7	5.5	515.6	5.1	17
2014 Feb 07 – 2014 Mar 05	AMS-02	759.6	3.2	6.0	790.1	5.9	5.6	594.0	5.2	17
2014 Mar 06 – 2014 Apr 01	AMS-02	732.1	3.1	5.8	788.8	5.8	5.6	539.2	5.1	17
2014 Apr 02 – 2014 Apr 28	AMS-02	725.8	3.1	5.8	771.2	5.8	5.5	544.9	5.2	17
2014 Apr 29 – 2014 May 25	AMS-02	684.8	3.1	5.7	734.6	5.6	5.4	498.9	5.1	17
2014 May 26 – 2014 Jun 21	AMS-02	698.8	3.1	5.8	737.5	5.7	5.4	525.1	5.1	17
2014 Jun 22 – 2014 Jul 18	AMS-02	721.2	3.1	5.9	758.1	5.7	5.5	549.3	5.2	17
2014 Jul 19 – 2014 Aug 14	AMS-02	671.7	3.1	5.7	712.5	5.6	5.3	495.8	5.1	17
2014 Aug 15 – 2014 Sep 10	AMS-02	637.7	3.1	5.8	656.3	5.5	5.1	486.2	5.1	17
2014 Sep 11 – 2014 Oct 08	AMS-02	666.0	3.2	5.9	660.8	5.4	5.1	536.5	5.2	17
2014 Oct 08 – 2014 Nov 03	AMS-02	707.7	3.5	5.8	697.1	6.0	5.4	581.4	5.9	17
2014 Nov 04 – 2014 Nov 30	AMS-02	756.0	3.5	6.2	705.4	5.9	5.4	663.3	5.7	17
2014 Dec 01 – 2014 Dec 27	AMS-02	680.8	3.3	6.2	627.9	5.4	5.0	592.6	5.2	17
2014 Dec 28 – 2015 Jan 23	AMS-02	675.1	3.2	6.1	645.8	5.5	5.1	567.2	5.2	17
2015 Jan 24 – 2015 Feb 19	AMS-02	673.2	3.2	6.1	646.1	5.5	5.1	563.5	5.2	17
2015 Feb 20 – 2015 Mar 18	AMS-02	701.2	3.2	6.1	678.4	5.6	5.2	586.5	5.2	17
2015 Mar 19 – 2015 Apr 14	AMS-02	748.1	3.3	6.2	730.5	5.8	5.4	627.0	5.2	17
2015 Apr 15 – 2015 May 11	AMS-02	720.1	3.2	6.0	729.0	5.7	5.4	576.1	5.2	17
2015 May 12 – 2015 Jun 07	AMS-02	655.5	3.1	5.8	668.1	5.5	5.2	509.4	5.1	17
2015 Jun 08 – 2015 Jul 04	AMS-02	665.8	3.2	6.0	648.5	5.4	5.1	547.9	5.2	17
2015 Jul 05 – 2015 Jul 31	AMS-02	624.6	3.1	5.9	617.5	5.4	5.0	498.8	5.1	17
2015 Aug 01 – 2015 Aug 27	AMS-02	608.4	3.1	5.8	597.8	5.3	4.9	486.7	5.1	17
2015 Aug 28 – 2015 Sep 23	AMS-02	609.9	3.1	5.9	586.2	5.3	4.9	500.2	5.1	17
2015 Sep 24 – 2015 Oct 20	AMS-02	601.7	3.1	5.9	573.2	5.2	4.8	496.8	5.1	17
2015 Oct 21 – 2015 Nov 16	AMS-02	597.3	3.2	5.9	562.2	5.2	4.8	498.5	5.1	17
2015 Nov 17 – 2015 Dec 13	AMS-02	559.6	3.1	5.9	521.0	5.1	4.6	465.8	5.1	17
2015 Dec 14 – 2016 Jan 09	AMS-02	544.0	3.1	5.9	499.7	5.0	4.6	456.2	5.1	17

Table A.1 (Continued)

Date	Experiment	ϕ	σ_{fit}	σ_{LIS}	ϕ_L	σ_{fit}	σ_{LIS}	ϕ_H	σ_{fit}	σ_{LIS}
2016 Jan 10 – 2016 Feb 05	AMS-02	507.5	3.1	5.7	473.7	5.0	4.5	412.2	5.1	17
2016 Feb 06 – 2016 Mar 03	AMS-02	492.4	3.1	5.7	459.5	4.9	4.4	397.1	5.1	17
2016 Mar 04 – 2016 Mar 30	AMS-02	488.7	3.1	5.7	449.5	4.9	4.4	399.5	5.1	17
2016 Mar 31 – 2016 Apr 26	AMS-02	486.8	3.1	5.7	444.8	4.9	4.4	400.4	5.1	17
2016 Apr 27 – 2016 May 23	AMS-02	476.0	3.1	5.7	434.2	4.8	4.3	390.0	5.1	17
2016 May 24 – 2016 Jun 19	AMS-02	455.1	3.0	5.7	415.4	4.8	4.3	368.2	5.0	17
2016 Jun 20 – 2016 Jul 16	AMS-02	463.0	3.1	5.7	418.6	4.8	4.3	379.8	5.0	17
2016 Jul 17 – 2016 Aug 12	AMS-02	460.0	3.0	5.7	416.3	4.8	4.3	376.4	5.0	17
2016 Aug 13 – 2016 Sep 08	AMS-02	446.5	3.0	5.7	403.5	4.8	4.2	363.3	5.0	17
2016 Sep 09 – 2016 Oct 05	AMS-02	433.4	3.0	5.7	387.2	4.7	4.2	353.8	5.0	17
2016 Oct 06 – 2016 Nov 01	AMS-02	416.5	3.0	5.6	366.4	4.7	4.1	341.4	5.0	17
2016 Nov 02 – 2016 Nov 26	AMS-02	397.7	3.0	5.6	347.4	4.6	4.0	324.0	5.0	17

Table A.2: Solar modulation parameters in units of MV derived from helium fluxes. The error contributions from the fit of the modulated fluxes (σ_{fit}) and from the uncertainty on the LIS (σ_{LIS}) are reported separately. ϕ is the modulation parameter obtained with the force-field approximation, while ϕ_L and ϕ_H are the modulation parameters obtained with the modified force-field approximation.

Date	Experiment	ϕ	σ_{fit}	σ_{LIS}	ϕ_L	σ_{fit}	σ_{LIS}	ϕ_H	σ_{fit}	σ_{LIS}
1993 Jul 01	BESS93	552.0	14	3.0	475.0	18	2.0	732.0	37	7.6
1997 Jul 27	BESS97	385.9	8.5	2.5	374.0	13	1.9	421.0	25	6.9
1998 Jul 29	BESS98	475.9	9.2	2.7	455.0	13	1.9	531.0	25	7.5
1999 Aug 11 – 12	BESS99	652.9	9.6	2.8	550.0	14	2.1	597.0	26	7.5
2000 Aug 10 – 11	BESS00	1161.0	14	3.7	1217.0	24	3.1	1084.0	31	8.1
2002 Aug 07	BESS-TeV	944.0	14	3.3	1009.0	24	2.8	834.0	33	7.7
2004 Dec 13 – 21	BESS-Polar I	604.3	2.2	2.7	616.9	3.2	2.2	576.4	6.8	7.4
2007 Dec 22 – 2008 Jan 19	BESS-Polar II	350.2	2.0	2.3	339.5	2.8	1.7	389.4	6.9	7.2
2011 May 19 – 2013 Nov 26	AMS-02	568	8	–	568	10	–	570	15	–
2011 May 20 – 2011 Jun 10	AMS-02	488.3	3.6	3.9	425.0	6.9	1.4	535.5	5.9	8.0
2011 Jun 11 – 2011 Jul 07	AMS-02	537.5	3.5	4.0	462.7	6.7	1.4	591.4	5.7	8.2
2011 Jul 08 – 2011 Aug 03	AMS-02	506.2	3.4	3.9	456.1	6.7	1.4	543.6	5.6	8.1
2011 Aug 04 – 2011 Aug 30	AMS-02	497.3	3.3	3.8	465.2	6.6	1.4	522.4	5.5	8.0
2011 Aug 31 – 2011 Sep 26	AMS-02	496.0	3.3	3.9	456.9	6.5	1.4	526.1	5.5	8.1
2011 Sep 27 – 2011 Oct 23	AMS-02	538.7	3.4	3.9	507.5	6.7	1.5	562.7	5.5	8.1
2011 Oct 24 – 2011 Nov 19	AMS-02	505.9	3.3	3.9	472.2	6.6	1.4	532.2	5.5	8.1
2011 Nov 20 – 2011 Dec 16	AMS-02	475.0	3.3	3.8	440.4	6.5	1.4	502.4	5.5	8.0
2011 Dec 17 – 2012 Jan 12	AMS-02	466.5	3.3	3.8	436.7	6.4	1.4	490.5	5.5	8.0
2012 Jan 13 – 2012 Feb 08	AMS-02	500.1	3.4	3.9	456.3	6.6	1.4	533.6	5.5	8.1
2012 Feb 09 – 2012 Mar 06	AMS-02	512.0	3.4	3.9	474.1	6.6	1.4	541.0	5.5	8.1
2012 Mar 07 – 2012 Apr 02	AMS-02	614.5	3.5	4.1	566.1	7.1	1.6	648.4	5.7	8.2
2012 Apr 03 – 2012 Apr 29	AMS-02	526.0	3.3	3.8	513.1	6.7	1.5	537.2	5.5	8.1

Table A.2 (Continued)

Date	Experiment	ϕ	σ_{fit}	σ_{LIS}	ϕ_L	σ_{fit}	σ_{LIS}	ϕ_H	σ_{fit}	σ_{LIS}
2012 Apr 30 – 2012 May 26	AMS-02	509.2	3.3	3.8	485.3	6.6	1.4	528.6	5.5	8.1
2012 May 27 – 2012 Jun 22	AMS-02	546.7	3.4	3.9	520.3	6.8	1.5	567.4	5.5	8.1
2012 Jun 23 – 2012 Jul 19	AMS-02	567.3	3.4	3.9	537.2	6.9	1.5	590.4	5.6	8.1
2012 Jul 20 – 2012 Aug 15	AMS-02	647.4	3.5	4.0	632.8	7.3	1.7	659.2	5.6	8.2
2012 Aug 16 – 2012 Sep 11	AMS-02	626.7	3.4	3.9	647.7	7.3	1.7	613.5	5.6	8.1
2012 Sep 12 – 2012 Oct 08	AMS-02	589.3	3.4	3.8	609.5	7.1	1.6	576.2	5.6	8.1
2012 Oct 09 – 2012 Nov 04	AMS-02	612.1	3.4	3.9	632.5	7.3	1.7	599.1	5.6	8.1
2012 Nov 05 – 2012 Dec 01	AMS-02	605.5	3.4	3.9	626.0	7.2	1.7	592.2	5.6	8.1
2012 Dec 02 – 2012 Dec 28	AMS-02	586.7	3.4	3.8	610.8	7.1	1.6	570.4	5.6	8.1
2012 Dec 29 – 2013 Jan 24	AMS-02	559.0	3.3	3.8	579.6	7.0	1.6	545.2	5.5	8.1
2013 Jan 25 – 2013 Feb 20	AMS-02	543.1	3.3	3.8	560.5	6.8	1.6	531.7	5.5	8.0
2013 Feb 21 – 2013 Mar 19	AMS-02	558.1	3.4	3.8	557.0	6.9	1.6	560.7	5.5	8.1
2013 Mar 20 – 2013 Apr 15	AMS-02	587.4	3.4	3.9	589.4	7.0	1.6	587.8	5.6	8.1
2013 Apr 16 – 2013 May 12	AMS-02	594.8	3.4	3.9	593.4	7.0	1.6	597.5	5.6	8.2
2013 May 13 – 2013 Jun 08	AMS-02	701.7	3.6	4.1	696.6	7.6	1.8	707.0	5.7	8.3
2013 Jun 09 – 2013 Jul 05	AMS-02	678.7	3.5	3.9	716.5	7.5	1.8	653.8	5.6	8.2
2013 Jul 06 – 2013 Aug 01	AMS-02	670.5	3.4	3.9	710.4	7.5	1.8	643.7	5.6	8.2
2013 Aug 02 – 2013 Aug 28	AMS-02	663.4	3.4	3.9	719.7	7.5	1.8	624.1	5.6	8.1
2013 Aug 29 – 2013 Sep 24	AMS-02	679.0	3.4	3.8	764.6	7.7	1.9	617.8	5.6	8.1
2013 Sep 25 – 2013 Oct 21	AMS-02	652.9	3.4	3.8	738.8	7.5	1.8	589.3	5.6	8.1
2013 Oct 22 – 2013 Nov 17	AMS-02	654.7	3.4	3.8	738.5	7.6	1.8	593.0	5.7	8.1
2013 Nov 18 – 2013 Dec 14	AMS-02	663.6	3.4	3.8	741.6	7.5	1.8	606.4	5.6	8.1
2013 Dec 15 – 2014 Jan 10	AMS-02	672.4	3.4	3.8	744.3	7.5	1.8	620.6	5.6	8.1
2014 Jan 11 – 2014 Feb 06	AMS-02	667.7	3.4	3.8	737.5	7.5	1.8	617.4	5.6	8.1
2014 Feb 07 – 2014 Mar 05	AMS-02	719.7	3.5	3.9	779.6	7.7	1.9	679.1	5.7	8.2
2014 Mar 06 – 2014 Apr 01	AMS-02	696.9	3.4	3.9	773.7	7.7	1.9	642.4	5.6	8.1
2014 Apr 02 – 2014 Apr 28	AMS-02	690.1	3.4	3.9	753.1	7.6	1.8	645.8	5.6	8.2
2014 Apr 29 – 2014 May 25	AMS-02	639.7	3.3	3.7	723.0	7.5	1.8	578.3	5.6	8.0
2014 May 26 – 2014 Jun 21	AMS-02	661.6	3.4	3.8	718.7	7.4	1.8	621.1	5.6	8.1
2014 Jun 22 – 2014 Jul 18	AMS-02	685.9	3.4	3.9	739.8	7.6	1.8	648.9	5.6	8.2
2014 Jul 19 – 2014 Aug 14	AMS-02	630.6	3.4	3.8	684.2	7.3	1.7	592.1	5.6	8.1
2014 Aug 15 – 2014 Sep 10	AMS-02	601.0	3.4	3.8	634.2	7.1	1.7	577.9	5.6	8.1
2014 Dec 01 – 2014 Dec 27	AMS-02	656.4	3.6	4.1	598.3	7.1	1.6	697.1	5.7	8.3
2014 Dec 28 – 2015 Jan 23	AMS-02	646.6	3.5	4.0	623.5	7.2	1.6	664.4	5.7	8.3
2015 Jan 24 – 2015 Feb 19	AMS-02	647.5	3.5	4.0	624.2	7.2	1.6	665.4	5.7	8.3
2015 Feb 20 – 2015 Mar 18	AMS-02	671.5	3.5	4.0	662.6	7.4	1.7	679.3	5.7	8.3
2015 Mar 19 – 2015 Apr 14	AMS-02	715.0	3.6	4.1	722.4	7.6	1.8	711.8	5.7	8.3
2015 Apr 15 – 2015 May 11	AMS-02	687.0	3.5	4.0	716.6	7.6	1.8	668.2	5.7	8.2
2015 May 12 – 2015 Jun 07	AMS-02	619.7	3.4	3.9	643.5	7.2	1.7	603.9	5.6	8.2
2015 Jun 08 – 2015 Jul 04	AMS-02	636.3	3.5	4.0	622.7	7.2	1.6	647.6	5.7	8.2
2015 Jul 05 – 2015 Jul 31	AMS-02	592.2	3.4	3.9	584.4	7.0	1.6	599.5	5.6	8.2
2015 Aug 01 – 2015 Aug 27	AMS-02	572.8	3.4	3.9	571.9	6.9	1.6	575.1	5.6	8.1
2015 Aug 28 – 2015 Sep 23	AMS-02	575.2	3.4	3.9	549.6	6.9	1.5	595.2	5.6	8.2

Table A.2 (Continued)

Date	Experiment	ϕ	σ_{fit}	σ_{LIS}	ϕ_L	σ_{fit}	σ_{LIS}	ϕ_H	σ_{fit}	σ_{LIS}
2015 Sep 24 – 2015 Oct 20	AMS-02	569.5	3.4	3.9	542.6	6.9	1.5	590.4	5.6	8.2
2015 Oct 21 – 2015 Nov 16	AMS-02	563.6	3.4	3.9	533.7	6.8	1.5	586.7	5.6	8.1
2015 Nov 17 – 2015 Dec 13	AMS-02	535.5	3.4	3.9	489.6	6.7	1.5	570.1	5.6	8.1
2015 Dec 14 – 2016 Jan 09	AMS-02	513.6	3.4	3.9	463.6	6.6	1.4	551.5	5.6	8.1
2016 Jan 10 – 2016 Feb 05	AMS-02	481.1	3.3	3.8	438.0	6.4	1.4	514.6	5.5	8.1
2016 Feb 06 – 2016 Mar 03	AMS-02	462.7	3.3	3.8	429.3	6.4	1.4	489.6	5.5	8.0
2016 Mar 04 – 2016 Mar 30	AMS-02	458.9	3.3	3.8	413.9	6.3	1.3	494.5	5.5	8.1
2016 Mar 31 – 2016 Apr 26	AMS-02	459.7	3.3	3.8	414.8	6.3	1.3	495.1	5.5	8.0
2016 Apr 27 – 2016 May 23	AMS-02	450.7	3.3	3.8	400.2	6.3	1.3	489.9	5.5	8.0
2016 May 24 – 2016 Jun 19	AMS-02	431.6	3.3	3.8	377.4	6.2	1.3	474.2	5.5	8.0
2016 Jun 20 – 2016 Jul 16	AMS-02	440.9	3.3	3.8	386.0	6.3	1.3	483.2	5.5	8.0
2016 Jul 17 – 2016 Aug 12	AMS-02	440.0	3.3	3.8	380.7	6.2	1.3	485.8	5.5	8.0
2016 Aug 13 – 2016 Sep 08	AMS-02	423.4	3.3	3.8	367.1	6.2	1.3	467.3	5.4	8.0
2016 Sep 09 – 2016 Oct 05	AMS-02	412.7	3.3	3.8	354.8	6.2	1.2	457.8	5.4	8.0
2016 Oct 06 – 2016 Nov 01	AMS-02	400.5	3.3	3.8	324.2	6.1	1.2	459.1	5.5	8.0
2016 Nov 02 – 2016 Nov 26	AMS-02	381.2	3.3	3.8	308.6	6.0	1.2	438.0	5.5	8.0

APPENDIX B
BEST-FIT PARAMETERS FOR THE NUMERICAL MODEL

Table B.1: Best-fit parameters used as input for numerical models with negative polarity. BR is the Bartels rotation number: Table B.3 contains the start and ending dates for each BR. α is the tilt angle, in degrees; B_0 is the HMF magnitude at Earth, in nT; $k_{\parallel}^0$ is the normalization of the parallel DC, in $6\times10^{20}\mathrm{cm}^2/\mathrm{s}$; $a_{\parallel}$ and $b_{\parallel}$ are, respectively, the low- and high-rigidity slope of the parallel DC; $a_{\perp}$ and $b_{\perp}$ are the corresponding slopes for the perpendicular DC. The uncertainty on $a_{\parallel}$ and $b_{\parallel}$ sometimes is ∞: in these cases, the shape of the chi-squared was not parabolic at the minimum. The parallel mean free path, $\lambda_{\parallel}$, at 1 GV at Earth, in AU, is also reported for reference. Its uncertainty is computed by propagating the uncertainty on $k_{\parallel}^0$, $a_{\parallel}$ and $b_{\parallel}$.

BR	α	B_0	$k_{\parallel}^0$	$\lambda_{\parallel}$	$a_{\parallel}$	$b_{\parallel}$	$a_{\perp}$	$b_{\perp}$
2426	53.02	4.80	118 ± 3	0.090 ± 0.006	1.15 ± 0.05	1.82 ± 0.04	0.86 ± 0.05	0.68 ± 0.04
2427	54.48	4.87	113 ± 2	0.060 ± 0.007	1.39 ± 0.08	1.78 ± 0.03	0.84 ± 0.04	0.69 ± 0.04
2428	56.47	4.95	116 ± 3	0.097 ± 0.006	1.09 ± 0.05	2.08 ± 0.07	0.84 ± 0.05	0.78 ± 0.04
2429	57.78	4.99	119 ± 3	$0.09 \pm \infty$	1.14 ± 0.05	$1.80 \pm \infty$	0.89 ± 0.06	0.89 ± 0.05
2430	59.91	5.03	124 ± 3	0.024 ± 0.004	2.09 ± 0.08	1.61 ± 0.07	0.81 ± 0.05	0.88 ± 0.05
2431	62.15	5.12	114 ± 3	0.063 ± 0.005	1.37 ± 0.06	2.15 ± 0.06	0.87 ± 0.04	0.83 ± 0.04
2432	63.55	5.19	127 ± 3	0.029 ± 0.004	1.95 ± 0.07	1.65 ± 0.07	0.80 ± 0.05	0.85 ± 0.05
2433	65.13	5.23	139 ± 3	0.072 ± 0.015	1.41 ± 0.15	1.90 ± 0.04	0.93 ± 0.05	0.92 ± 0.06
2434	66.17	5.25	141 ± 4	0.093 ± 0.005	1.24 ± 0.04	1.37 ± 0.07	0.96 ± 0.03	0.88 ± 0.05
2435	67.24	5.32	131 ± 3	0.054 ± 0.005	1.57 ± 0.06	1.75 ± 0.07	0.83 ± 0.04	0.79 ± 0.05
2436	66.87	5.38	128 ± 3	0.046 ± 0.004	1.65 ± 0.05	1.73 ± 0.07	0.79 ± 0.04	0.84 ± 0.04
2437	65.95	5.44	105 ± 2	0.035 ± 0.003	1.70 ± 0.05	1.83 ± 0.03	0.72 ± 0.04	0.88 ± 0.03
2438	66.28	5.42	130 ± 3	0.001 ± 0.001	4.51 ± 0.22	1.87 ± 0.04	0.89 ± 0.04	0.84 ± 0.04
2439	67.12	5.47	138 ± 3	0.052 ± 0.006	1.62 ± 0.07	1.92 ± 0.04	0.92 ± 0.05	0.90 ± 0.05
2440	67.89	5.49	126 ± 3	$0.05 \pm \infty$	$1.50 \pm \infty$	1.65 ± 0.06	0.92 ± 0.05	0.86 ± 0.05
2441	68.42	5.55	121 ± 3	0.090 ± 0.005	1.16 ± 0.04	1.52 ± 0.04	0.96 ± 0.03	0.87 ± 0.04
2442	68.91	5.65	103 ± 3	0.025 ± 0.002	1.91 ± 0.05	1.91 ± 0.05	0.80 ± 0.05	0.91 ± 0.04
2443	68.95	5.70	111 ± 3	$0.03 \pm \infty$	1.88 ± 0.04	$1.80 \pm \infty$	0.87 ± 0.04	0.93 ± 0.04
2444	69.24	5.70	124 ± 3	0.058 ± 0.004	1.48 ± 0.05	1.75 ± 0.08	1.00 ± 0.04	0.91 ± 0.04
2445	69.59	5.70	120 ± 3	0.032 ± 0.004	1.85 ± 0.06	1.55 ± 0.04	0.95 ± 0.03	0.95 ± 0.04
2446	69.06	5.69	123 ± 3	0.038 ± 0.004	1.75 ± 0.06	1.69 ± 0.07	0.99 ± 0.04	0.91 ± 0.04
2447	69.52	5.72	129 ± 3	0.058 ± 0.004	1.51 ± 0.04	1.88 ± 0.04	1.09 ± 0.05	0.86 ± 0.04
2448	69.64	5.69	138 ± 3	0.087 ± 0.006	1.27 ± 0.05	1.23 ± 0.05	1.10 ± 0.04	0.96 ± 0.03
2449	69.98	5.62	141 ± 3	$0.06 \pm \infty$	$1.50 \pm \infty$	1.37 ± 0.07	1.06 ± 0.04	0.85 ± 0.06
2450	71.18	5.55	130 ± 3	0.086 ± 0.004	1.24 ± 0.03	1.76 ± 0.07	1.04 ± 0.03	0.80 ± 0.04
2451	71.34	5.50	123 ± 3	0.045 ± 0.005	1.64 ± 0.06	1.59 ± 0.06	1.00 ± 0.05	0.87 ± 0.04
2452	70.92	5.49	122 ± 3	0.045 ± 0.004	1.64 ± 0.05	1.52 ± 0.03	0.97 ± 0.05	0.84 ± 0.04
2453	70.70	5.47	97 ± 2	0.049 ± 0.003	1.42 ± 0.04	2.01 ± 0.03	0.91 ± 0.03	0.91 ± 0.03
2454	70.63	5.44	102 ± 2	0.033 ± 0.004	1.73 ± 0.05	1.86 ± 0.04	0.99 ± 0.03	0.91 ± 0.03
2455	70.26	5.41	106 ± 2	0.034 ± 0.003	1.73 ± 0.04	1.89 ± 0.03	1.03 ± 0.03	0.89 ± 0.03
2456	70.01	5.36	105 ± 2	0.031 ± 0.003	1.78 ± 0.04	1.92 ± 0.03	1.02 ± 0.04	0.90 ± 0.03

Table B.1 (Continued)

BR	α	B_0	$k_\parallel^0$	$\lambda_\parallel$	$a_\parallel$	$b_\parallel$	$a_\perp$	$b_\perp$
2457	69.78	5.31	101 ± 3	$0.04 \pm \infty$	$1.50 \pm \infty$	2.06 ± 0.05	1.15 ± 0.04	0.94 ± 0.03
2458	69.45	5.22	110 ± 4	$20 \pm \infty$	$-2.7 \pm \infty$	1.52 ± 0.03	1.22 ± 0.04	0.98 ± 0.05
2459	69.83	5.21	111 ± 3	$0.09 \pm \infty$	$1.10 \pm \infty$	2.03 ± 0.04	1.18 ± 0.03	0.87 ± 0.03
2460	69.32	5.17	104 ± 3	0.062 ± 0.004	1.32 ± 0.04	2.16 ± 0.07	1.28 ± 0.03	0.89 ± 0.04
2461	68.78	5.18	108 ± 2	0.059 ± 0.003	1.37 ± 0.04	2.08 ± 0.06	1.33 ± 0.03	0.84 ± 0.03
2462	69.08	5.20	111 ± 3	0.036 ± 0.005	1.72 ± 0.07	2.00 ± 0.08	1.24 ± 0.03	0.78 ± 0.04
2463	68.07	5.30	98 ± 2	0.066 ± 0.002	1.23 ± 0.03	2.01 ± 0.03	1.21 ± 0.03	0.93 ± 0.03
2464	67.50	5.32	104 ± 2	0.061 ± 0.003	1.33 ± 0.04	2.04 ± 0.06	1.29 ± 0.03	0.89 ± 0.03
2465	66.56	5.35	105 ± 3	$0.3 \pm \infty$	$0.18 \pm \infty$	1.88 ± 0.06	1.22 ± 0.03	0.87 ± 0.04
2466	64.80	5.34	121 ± 3	0.037 ± 0.003	1.77 ± 0.05	1.51 ± 0.03	1.27 ± 0.04	0.90 ± 0.04
2467	62.88	5.33	113 ± 2	0.027 ± 0.002	1.94 ± 0.05	1.91 ± 0.03	1.14 ± 0.03	0.78 ± 0.03
2468	62.15	5.27	101 ± 3	$0.05 \pm \infty$	$1.50 \pm \infty$	1.82 ± 0.03	1.22 ± 0.03	0.93 ± 0.05
2469	61.52	5.21	118 ± 2	0.033 ± 0.003	1.83 ± 0.04	1.91 ± 0.03	1.22 ± 0.04	0.82 ± 0.04
2470	61.42	5.29	122 ± 4	0.077 ± 0.005	1.27 ± 0.05	1.51 ± 0.03	1.26 ± 0.03	0.82 ± 0.05
2471	61.82	5.49	129 ± 3	$0.06 \pm \infty$	$1.50 \pm \infty$	1.89 ± 0.03	1.14 ± 0.04	0.60 ± 0.03
2472	60.72	5.62	114 ± 2	0.061 ± 0.004	1.39 ± 0.05	1.78 ± 0.04	1.16 ± 0.04	0.74 ± 0.04
2473	59.74	5.76	109 ± 2	0.062 ± 0.004	1.36 ± 0.04	2.52 ± 0.08	1.09 ± 0.03	0.53 ± 0.03
2474	59.03	5.94	120 ± 2	0.049 ± 0.004	1.56 ± 0.05	1.84 ± 0.04	0.95 ± 0.03	0.66 ± 0.03
2475	57.64	6.16	127 ± 2	0.068 ± 0.005	1.38 ± 0.05	1.44 ± 0.04	1.05 ± 0.04	0.71 ± 0.04
2476	56.77	6.28	129 ± 3	0.082 ± 0.005	1.27 ± 0.05	1.49 ± 0.06	1.02 ± 0.03	0.80 ± 0.05

Table B.2: Best-fit parameters used as input for numerical models with positive polarity. See Table B.1 for the description of the columns.

BR	α	B_0	$k_\parallel^0$	$\lambda_\parallel$	$a_\parallel$	$b_\parallel$	$a_\perp$	$b_\perp$
2446	69.06	5.69	117 ± 3	0.038 ± 0.004	1.30 ± 0.10	1.34 ± 0.08	1.21 ± 0.04	0.98 ± 0.04
2447	69.52	5.72	141 ± 3	0.058 ± 0.004	2.00 ± 0.10	1.22 ± 0.04	1.27 ± 0.04	0.88 ± 0.03
2448	69.64	5.69	141 ± 3	0.087 ± 0.006	1.53 ± 0.05	1.30 ± 0.10	1.26 ± 0.03	0.83 ± 0.04
2449	69.98	5.62	138 ± 3	$0.06 \pm \infty$	1.51 ± 0.08	$2 \pm \infty$	1.21 ± 0.05	0.77 ± 0.04
2450	71.18	5.55	133 ± 3	0.086 ± 0.003	1.70 ± 0.10	1.80 ± 0.10	1.14 ± 0.04	0.83 ± 0.03
2451	71.34	5.50	129 ± 3	0.045 ± 0.005	$1 \pm \infty$	1.48 ± 0.06	1.15 ± 0.04	0.81 ± 0.05
2452	70.92	5.49	116 ± 3	0.044 ± 0.004	1.19 ± 0.04	4.80 ± 0.30	1.16 ± 0.04	0.74 ± 0.04
2453	70.70	5.47	100 ± 2	0.049 ± 0.003	$2 \pm \infty$	1.62 ± 0.07	1.25 ± 0.03	0.87 ± 0.03
2454	70.63	5.44	106 ± 2	0.033 ± 0.003	1.73 ± 0.08	1.90 ± 0.10	1.33 ± 0.03	0.89 ± 0.03
2455	70.26	5.41	109 ± 2	0.034 ± 0.003	1.70 ± 0.07	2.20 ± 0.20	1.38 ± 0.04	0.88 ± 0.03
2456	70.01	5.36	111 ± 3	0.031 ± 0.002	1.60 ± 0.30	2.50 ± 0.20	1.41 ± 0.04	0.89 ± 0.03
2457	69.78	5.31	110 ± 4	$0.04 \pm \infty$	1.71 ± 0.09	2.70 ± 0.20	1.50 ± 0.04	0.89 ± 0.04
2458	69.45	5.22	130 ± 3	$20 \pm \infty$	1.87 ± 0.06	1.53 ± 0.05	1.70 ± 0.04	0.86 ± 0.03
2459	69.83	5.21	125 ± 3	$0.08 \pm \infty$	1.90 ± 0.09	1.51 ± 0.04	1.63 ± 0.04	0.80 ± 0.03
2460	69.32	5.17	114 ± 5	0.062 ± 0.003	2.10 ± 0.10	$2 \pm \infty$	1.76 ± 0.07	0.80 ± 0.06
2461	68.78	5.18	118 ± 4	0.059 ± 0.003	1.83 ± 0.06	2.60 ± 0.20	1.81 ± 0.06	0.79 ± 0.05
2462	69.08	5.20	143 ± 2	0.036 ± 0.005	2.50 ± 0.10	2.20 ± 0.20	2.18 ± 0.10	0.63 ± 0.02

Table B.2 (Continued)

BR	α	B_0	$k_{\parallel}^0$	$\lambda_{\parallel}$	$a_{\parallel}$	$b_{\parallel}$	$a_{\perp}$	$b_{\perp}$
2463	68.07	5.30	106 ± 2	0.066 ± 0.002	1.82 ± 0.06	1.82 ± 0.03	1.64 ± 0.03	0.81 ± 0.03
2464	67.50	5.32	112 ± 3	0.061 ± 0.003	1.81 ± 0.06	2.40 ± 0.10	1.73 ± 0.05	0.88 ± 0.03
2465	66.56	5.35	110 ± 3	$0.3 \pm \infty$	1.93 ± 0.08	2.20 ± 0.10	1.71 ± 0.05	0.84 ± 0.04
2466	64.80	5.34	127 ± 2	0.037 ± 0.003	1.81 ± 0.06	1.52 ± 0.04	1.65 ± 0.04	0.78 ± 0.03
2467	62.88	5.33	117 ± 3	0.027 ± 0.002	1.53 ± 0.03	2.40 ± 0.20	1.53 ± 0.03	0.70 ± 0.05
2468	62.15	5.27	109 ± 2	$0.05 \pm \infty$	1.79 ± 0.05	2.00 ± 0.20	1.69 ± 0.04	0.86 ± 0.03
2469	61.52	5.21	127 ± 3	0.033 ± 0.003	1.75 ± 0.07	1.51 ± 0.04	1.66 ± 0.05	0.74 ± 0.03
2470	61.42	5.29	145 ± 3	0.077 ± 0.005	1.91 ± 0.07	$2 \pm \infty$	1.68 ± 0.04	0.64 ± 0.02
2471	61.82	5.49	146 ± 2	$0.06 \pm \infty$	1.89 ± 0.07	1.70 ± 0.30	1.64 ± 0.04	0.57 ± 0.02
2472	60.72	5.62	112 ± 2	0.061 ± 0.004	1.54 ± 0.04	1.74 ± 0.09	1.43 ± 0.03	0.77 ± 0.03
2473	59.74	5.76	125 ± 2	0.062 ± 0.004	$2 \pm \infty$	1.53 ± 0.03	1.62 ± 0.03	0.65 ± 0.03
2474	59.03	5.94	112 ± 2	0.049 ± 0.004	1.30 ± 0.30	1.70 ± 0.10	1.13 ± 0.03	0.77 ± 0.03
2475	57.64	6.16	120 ± 3	0.068 ± 0.005	1.24 ± 0.04	$2 \pm \infty$	1.25 ± 0.04	0.71 ± 0.04
2476	56.77	6.28	132 ± 4	0.082 ± 0.005	1.70 ± 0.10	1.40 ± 0.10	1.33 ± 0.04	0.75 ± 0.05
2477	55.38	6.32	122 ± 2	$0.05 \pm \infty$	1.90 ± 0.40	1.25 ± 0.03	1.29 ± 0.03	0.83 ± 0.03
2478	54.35	6.49	99 ± 2	0.024 ± 0.003	1.80 ± 0.20	1.70 ± 0.09	1.23 ± 0.03	0.95 ± 0.03
2479	54.55	6.54	131 ± 3	0.040 ± 0.003	1.70 ± 0.20	2.00 ± 0.10	1.48 ± 0.03	0.87 ± 0.03
2480	54.90	6.63	151 ± 2	0.034 ± 0.007	1.60 ± 0.20	1.60 ± 0.20	1.42 ± 0.04	0.80 ± 0.03
2481	54.02	6.68	142 ± 3	$0.05 \pm \infty$	1.53 ± 0.06	0.90 ± 0.10	1.26 ± 0.03	0.74 ± 0.03
2482	53.24	6.77	170 ± 6	0.086 ± 0.006	1.90 ± 0.20	$1 \pm \infty$	1.26 ± 0.02	0.86 ± 0.03
2483	51.67	6.83	162 ± 3	0.046 ± 0.004	1.51 ± 0.05	0.80 ± 0.20	1.26 ± 0.02	0.84 ± 0.02
2484	49.97	6.88	158 ± 2	0.053 ± 0.006	1.80 ± 0.10	1.80 ± 0.20	1.22 ± 0.04	0.81 ± 0.03
2485	49.88	6.86	155 ± 2	0.060 ± 0.020	1.50 ± 0.10	1.80 ± 0.20	1.17 ± 0.04	0.81 ± 0.03
2486	49.64	6.83	152 ± 2	0.052 ± 0.008	1.40 ± 0.10	1.80 ± 0.20	1.12 ± 0.03	0.82 ± 0.03
2487	49.26	6.77	186 ± 5	0.122 ± 0.005	1.70 ± 0.10	0.80 ± 0.20	0.99 ± 0.03	0.83 ± 0.03
2488	49.32	6.70	166 ± 3	$0.07 \pm \infty$	1.40 ± 0.10	0.80 ± 0.20	0.97 ± 0.02	0.81 ± 0.03
2489	49.18	6.63	159 ± 3	0.058 ± 0.006	1.20 ± 0.03	1.80 ± 0.10	0.95 ± 0.02	0.89 ± 0.02
2490	49.42	6.63	181 ± 4	0.074 ± 0.007	2.11 ± 0.08	1.80 ± 0.20	0.86 ± 0.03	0.89 ± 0.02
2491	49.40	6.60	186 ± 4	0.086 ± 0.007	2.04 ± 0.08	1.70 ± 0.10	0.83 ± 0.03	0.87 ± 0.02
2492	48.68	6.53	174 ± 3	0.087 ± 0.007	2.05 ± 0.08	1.50 ± 0.20	0.83 ± 0.03	0.85 ± 0.02
2493	47.85	6.53	211 ± 5	0.104 ± 0.008	1.88 ± 0.08	1.90 ± 0.10	0.78 ± 0.03	0.88 ± 0.02
2494	47.85	6.51	170 ± 3	0.154 ± 0.009	1.51 ± 0.08	2.20 ± 0.10	0.71 ± 0.03	0.92 ± 0.02
2495	47.16	6.46	314 ± 9	0.122 ± 0.008	1.70 ± 0.09	1.90 ± 0.10	0.75 ± 0.03	0.89 ± 0.02
2496	46.46	6.46	209 ± 5	0.128 ± 0.008	1.66 ± 0.09	2.00 ± 0.10	0.74 ± 0.03	0.90 ± 0.02
2497	45.75	6.38	171 ± 3	0.160 ± 0.010	1.51 ± 0.09	2.10 ± 0.10	0.70 ± 0.03	0.92 ± 0.02
2498	45.15	6.29	170 ± 3	0.184 ± 0.006	1.31 ± 0.09	2.20 ± 0.10	0.69 ± 0.02	0.92 ± 0.02
2499	44.65	6.29	192 ± 5	0.201 ± 0.006	$1 \pm \infty$	2.20 ± 0.20	0.62 ± 0.03	0.91 ± 0.02
2500	44.12	6.23	263 ± 7	0.073 ± 0.008	2.03 ± 0.08	2.70 ± 0.20	0.55 ± 0.03	0.93 ± 0.02

Table B.3: Start and ending dates of Bartels rotations.

BR	Date	BR	Date	BR	Date
2426	2011/05/20 – 2011/06/10	2451	2013/03/20 – 2013/04/15	2476	2015/01/24 – 2015/02/19
2427	2011/06/11 – 2011/07/07	2452	2013/04/16 – 2013/05/12	2477	2015/02/20 – 2015/03/18
2428	2011/07/08 – 2011/08/03	2453	2013/05/13 – 2013/06/08	2478	2015/03/19 – 2015/04/14
2429	2011/08/04 – 2011/08/30	2454	2013/06/09 – 2013/07/05	2479	2015/04/15 – 2015/05/11
2430	2011/08/31 – 2011/09/26	2455	2013/07/06 – 2013/08/01	2480	2015/05/12 – 2015/06/07
2431	2011/09/27 – 2011/10/23	2456	2013/08/02 – 2013/08/28	2481	2015/06/08 – 2015/07/04
2432	2011/10/24 – 2011/11/19	2457	2013/08/29 – 2013/09/24	2482	2015/07/05 – 2015/07/31
2433	2011/11/20 – 2011/12/16	2458	2013/09/25 – 2013/10/21	2483	2015/08/01 – 2015/08/27
2434	2011/12/17 – 2012/01/12	2459	2013/10/22 – 2013/11/17	2484	2015/08/28 – 2015/09/23
2435	2012/01/13 – 2012/02/08	2460	2013/11/18 – 2013/12/14	2485	2015/09/24 – 2015/10/20
2436	2012/02/09 – 2012/03/06	2461	2013/12/15 – 2014/01/10	2486	2015/10/21 – 2015/11/16
2437	2012/03/07 – 2012/04/02	2462	2014/01/11 – 2014/02/06	2487	2015/11/17 – 2015/12/13
2438	2012/04/03 – 2012/04/29	2463	2014/02/07 – 2014/03/05	2488	2015/12/14 – 2016/01/09
2439	2012/04/30 – 2012/05/26	2464	2014/03/06 – 2014/04/01	2489	2016/01/10 – 2016/02/05
2440	2012/05/27 – 2012/06/22	2465	2014/04/02 – 2014/04/28	2490	2016/02/06 – 2016/03/03
2441	2012/06/23 – 2012/07/19	2466	2014/04/29 – 2014/05/25	2491	2016/03/04 – 2016/03/30
2442	2012/07/20 – 2012/08/15	2467	2014/05/26 – 2014/06/21	2492	2016/03/31 – 2016/04/26
2443	2012/08/16 – 2012/09/11	2468	2014/06/22 – 2014/07/18	2493	2016/04/27 – 2016/05/23
2444	2012/09/12 – 2012/10/08	2469	2014/07/19 – 2014/08/14	2494	2016/05/24 – 2016/06/19
2445	2012/10/09 – 2012/11/04	2470	2014/08/15 – 2014/09/10	2495	2016/06/20 – 2016/07/16
2446	2012/11/05 – 2012/12/01	2471	2014/09/11 – 2014/10/08	2496	2016/07/17 – 2016/08/12
2447	2012/12/02 – 2012/12/28	2472	2014/10/08 – 2014/11/03	2497	2016/08/13 – 2016/09/08
2448	2012/12/29 – 2013/01/24	2473	2014/11/04 – 2014/11/30	2498	2016/09/09 – 2016/10/05
2449	2013/01/25 – 2013/02/20	2474	2014/12/01 – 2014/12/27	2499	2016/10/06 – 2016/11/01
2450	2013/02/21 – 2013/03/19	2475	2014/12/28 – 2015/01/23	2500	2016/11/02 – 2016/11/26

BIBLIOGRAPHY

[1] N. Meyer-Vernet. *Basics of the solar wind*. Cambridge University Press, 2007.

[2] D.H. Hathaway. "The solar cycle". *Living Reviews in Solar Physics*, 12(1):4, 2015. doi:10.1007/lrsp-2015-4.

[3] D.J. McComas, F. Allegrini, P. Bochsler, et al. "Global observations of the interstellar interaction from the Interstellar Boundary Explorer (IBEX)". *Science*, 326(5955):959–962, 2009. doi:10.1126/science.1180906.

[4] D.J. McComas, D. Alexashov, M. Bzowski, et al. "The heliosphere's interstellar interaction: no bow shock". *Science*, 336(6086):1291–1293, 2012. doi:10.1126/science.1221054.

[5] E.C. Stone, A.C. Cummings, F.B. McDonald, et al. "Voyager 1 observes low-energy galactic cosmic rays in a region depleted of heliospheric ions". *Science*, 341(6142):150–153, 2013. doi:10.1126/science.1236408.

[6] D.A. Gurnett, W.S. Kurth, L.F. Burlaga, and N.F. Ness. "In situ observations of interstellar plasma with Voyager 1". *Science*, 341(6153):1489–1492, 2013. doi:10.1126/science.1241681.

[7] L.A. Fisk and G. Gloeckler. "On whether or not Voyager 1 has crossed the heliopause". *The Astrophysical Journal*, 789(1):41, 2014. doi:10.1088/0004-637X/789/1/41.

[8] X. Guo and V. Florinski. "Galactic cosmic-ray modulation near the heliopause". *The Astrophysical Journal*, 793(1):18, 2014. doi:10.1088/0004-637X/793/1/18.

[9] L. Biermann. "Kometenschweife und solare Korpuskularstrahlung". *Zeitschrift für Astrophysik*, 29:274–286, 1951. ADS:1951ZA.....29..274B.

[10] L. Biermann. "Physical processes in comet tails and their relation to solar activity". In *Proceedings of the 4th Colloque International d'Astrophysique (Liège)*, pages 251–262, 1952. ADS:1952LIACo...4..251B.

[11] E.N. Parker. "Dynamics of the interplanetary gas and magnetic fields". *The Astrophysical Journal*, 128:664–676, 1958. doi:10.1086/146579.

[12] E.N. Parker. "Dynamical theory of the solar wind". *Space Science Reviews*, 4(5-6):666–708, 1965. doi:10.1007/BF00216273.

[13] S. Chapman. "The viscosity and thermal conductivity of a completely ionized gas". *The Astrophysical Journal*, 120:151–155, 1954. doi:10.1086/145890.

[14] M. Druckmüller, S.R. Habbal, and H. Morgan. "Discovery of a new class of coronal structures in white light eclipse images". *The Astrophysical Journal*, 785(1):14, 2014. doi:10.1088/0004-637X/785/1/14.

[15] J.A. Simpson, J.D. Anglin, A. Balogh, et al. "The Ulysses cosmic ray and solar particle investigation". *Astronomy & Astrophysics Supplement Series*, 92(2):365–399, 1992. ADS:1992A\&AS...92..365S.

[16] E.J. Smith, R.G. Marsden, A. Balogh, et al. "The Sun and heliosphere at solar maximum". *Science*, 302(5648):1165–1169, 2003. doi:10.1126/science.1086295.

[17] D.J. McComas, H.A. Elliot, N.A. Schwadron, et al. "The three-dimensional solar wind around solar maximum". *Geophysical Research Letters*, 30(10):1517, 2003. doi:10.1029/2003GL017136.

[18] E.C. Stone, A.C. Cummings, F.B. McDonald, et al. "Voyager 1 explores the termination shock region and the heliosheath beyond". *Science*, 309(5743):2017–2020, 2005. doi:10.1126/science.1117684.

[19] R.B. Decker, S.M. Krimigis, E.C. Roelof, et al. "Voyager 1 in the foreshock, termination shock, and heliosheath". *Science*, 309(5743):2020–2024, 2005. doi:10.1126/science.1117569.

[20] E.C. Stone, A.C. Cummings, F.B. McDonald, et al. "An asymmetric solar wind termination shock". *Nature*, 454(7200):71–74, 2008. doi:10.1038/nature07022.

[21] L.F. Burlaga, N.F. Ness, M.H. Acuña, et al. "Magnetic fields at the solar wind termination shock". *Nature*, 454 (7200):75–77, 2008. doi:10.1038/nature07029.

[22] H. Alfvén. "Existence of electromagnetic-hydrodynamic waves". *Nature*, 150(3805):405–406, 1942. ADS:10. 1038/150405d0.

[23] M.J. Owens and R.J. Forsyth. "The heliospheric magnetic field". *Living Reviews in Solar Physics*, 10(1):5, 2013. doi:10.12942/lrsp-2013-5.

[24] E.J. Smith and A. Balogh. "Ulysses observations of the radial magnetic field". *Geophysical Research Letters*, 22(23):3317–3320, 1995. doi:10.1029/95GL02826.

[25] E.J. Smith. "The global heliospheric magnetic field", In *The heliosphere through the solar activity cycle*, pages 79–150. Springer, 2008. doi:10.1007/978-3-540-74302-6_4.

[26] C.W. Smith and J.W. Bieber. "Solar cycle variation of the interplanetary magnetic field spiral". *The Astrophysical Journal*, 370:435–441, 1991. doi:10.1086/169830.

[27] J. Kóta and J.R. Jokipii. "Corotating variations of cosmic rays near the south heliospheric pole". *Science*, 268 (5213):1024–1025, 1995. doi:10.1126/science.268.5213.1024.

[28] L.A. Fisk. "Motion of the footpoints of heliospheric magnetic field lines at the Sun: implications for recurrent energetic particle events at high heliographic latitudes". *Journal of Geophysical Research (Space Physics)*, 101 (7):15547–15553, 1996. doi:10.1029/96JA01005.

[29] K.H. Schatten, J.M. Wilcox, and N.F.Ness. "A model of interplanetary and coronal magnetic fields". *Solar Physics*, 6(3):442–455, 1969. doi:10.1007/BF00146478.

[30] M.D. Altschuler and G. Newkirk. "Magnetic fields and the structure of the solar corona. I: methods of calculating coronal fields". *Solar Physics*, 9(1):131–149, 1969. doi:10.1007/BF00145734.

[31] J.T. Hoeksema, J.M. Wilcox, and P.H. Scherrer. "The structure of the heliospheric current sheet – 1978-1982". *Journal of Geophysical Research (Space Physics)*, 88(11):9910–9918, 1983. doi:10.1029/JA088iA12p09910.

[32] K. Whitman. *The influence of short-term solar activity on the proton flux measured by AMS during solar cycle 24*. PhD thesis, University of Hawaii at Manoa, 2017.

[33] J. Giacalone, J.F. Drake, and J.R. Jokipii. "The acceleration mechanism of anomalous cosmic rays". *Space Science Reviews*, 173(1):283–307, 2012. doi:10.1007/s11214-012-9915-z.

[34] J. Giacalone. "Energetic particle transport", In *Heliophysics – Space storms and radiation: causes and effects*, pages 233–262. Cambridge University Press, 2010.

[35] A. De Angelis. "Domenico Pacini, uncredited pioneer of the discovery of cosmic rays". *Rivista del Nuovo Cimento*, 33(12):713–756, 2010. doi:10.1393/ncr/i2011-10060-9.

[36] C. Patrignani et al. "Review of particle physics". *Chinese Physics C*, 40(10), 2016. doi:10.1088/1674-1137/40/10/100001.

[37] P. Blasi. "The origin of galactic cosmic rays". *Astronomy & Astrophysics Review*, 21(1):70, 2013. doi:10.1007/s00159-013-0070-7.

[38] M. Ackermann et al. (Fermi LAT Collaboration). "Detection of the characteristic pion-decay signature in supernova remnants". *Science*, 339(6121):807–811, 2013. doi:10.1126/science.1231160.

[39] D. Breitschwerdt and T. Schmutzler. "The dynamical signature of the ISM in soft X-rays. I. Diffuse soft X-rays from galaxies". *Astronomy & Astrophysics*, 347:650–668, 1999. ADS:1999A\&A...347..650B.

[40] A.W. Strong and I.V. Moskalenko. "Propagation of cosmic-ray nucleons in the galaxy". *The Astrophysical Journal*, 509(1):212–228, 1998. doi:10.1086/306470.

[41] R. Beck. "Galactic and extragalactic magnetic fields – a concise review". *Astrophysics and Space Sciences Transactions*, 5(1):43–47, 2009. doi:10.5194/astra-5-43-2009.

[42] G. Brunetti, P. Blasi, R. Cassano, and S. Gabici. "Alfvénic reacceleration of relativistic particles in galaxy clusters: MHD waves, leptons and hadrons". *Monthly Notices of the Royal Astronomical Society*, 350(4):1174–1194, 2004. doi:10.1111/j.1365-2966.2004.07727.x.

[43] A.W. Strong, I.V. Moskalenko, and V.S. Ptuskin. "Cosmic-ray propagation and interactions in the galaxy". *Annual Review of Nuclear and Particle Science*, 57:285–327, 2007. doi:10.1146/annurev.nucl.57.090506.123011.

[44] V. Bindi, C. Corti, C. Consolandi, J. Hoffman, and K. Whitman. "Overview of galactic cosmic ray solar modulation in the AMS-02 era". *Advances in Space Research*, In press, 2017. doi:10.1016/j.asr.2017.05.025.

[45] P. Carlson. "Discovery of cosmic rays". In *Proceedings of the Centenary Symposium 2012: Discovery of Cosmic Rays*, *AIP Conference Proceedings*, 1516(1):9–16, 2013. doi:10.1063/1.4792532.

[46] L.W. Jones. "High energy physics in cosmic rays". In *Proceedings of the Centenary Symposium 2012: Discovery of Cosmic Rays*, *AIP Conference Proceedings*, 1516(1):17–22, 2013. doi:10.1063/1.4792533.

[47] J.W. Bieber. "Neutron monitoring: past, present, future". In *Proceedings of the Centenary Symposium 2012: Discovery of Cosmic Rays*, *AIP Conference Proceedings*, 1516(1):234–238, 2013. doi:10.1063/1.4792575.

[48] J. Mitchell et al. (BESS Collaboration). "The BESS program". *Nuclear Physics B - Proceedings Supplements*, 134:31–38, 2004. doi:10.1016/j.nuclphysbps.2004.08.003.

[49] C.F. Hall. "Pioneer 10". *Science*, 183(4122):301–302, 1974. doi:10.1126/science.183.4122.301.

[50] C.E. Kohlhase and P.A. Penzo. "Voyager mission description". *Space Science Reviews*, 21(2):77–101, 1977. doi:10.1007/BF00200846.

[51] J. Kóta and J.R. Jokipii. "Are cosmic rays modulated beyond the heliopause?". *The Astrophysical Journal*, 782 (1):24, 2014. doi:10.1088/0004-637X/782/1/24.

[52] R.D. Strauss, M.S. Potgieter, S.E.S. Ferreira, H. Fichtner, and K. Scherer. "Cosmic ray modulation beyond the heliopause: a hybrid modeling approach". *The Astrophysical Journal Letters*, 765(1):L18, 2013. doi: 10.1088/2041-8205/765/1/L18.

[53] X. Luo, M. Zhang, M.S. Potgieter, X. Feng, and N.V. Pogorelov. "A numerical simulation of cosmic-ray modulation near the heliopause". *The Astrophysical Journal*, 808(1):82, 2015. doi:10.1088/0004-637X/808/1/82.

[54] E.C. Stone, C.M.S. Cohen, W.R. Cook, et al. "The Cosmic-Ray Isotope Spectrometer for the Advanced Composition Explorer". *Space Science Reviews*, 86(1):285–356, 1998. doi:10.1023/A:1005075813033.

[55] V. Bonvicini et al. (PAMELA Collaboration). "The PAMELA experiment in space". *Nuclear Instruments and Methods in Physics Research A*, 461(1-3):262–268, 2001. doi:10.1016/S0168-9002(00)01221-3.

[56] D. Maurin, F. Melot, and R. Taillet. "A database of charged cosmic rays". *Astronomy & Astrophysics*, 569: A13, 2014. doi:10.1051/0004-6361/201321344.

[57] E.N. Parker. "The passage of energetic charged particles through interplanetary space". *Planetary and Space Science*, 13(1):9–49, 1965. doi:10.1016/0032-0633(65)90131-5.

[58] H. Moraal. "Cosmic-ray modulation equations". *Space Science Reviews*, 176(1):299–319, 2013. doi:10.1007/s11214-011-9819-3.

[59] L.M.M.L. Batalha. *Solar modulation effects on cosmic rays – Modelization with force field approximation, 1D and 2D numerical approaches and characterization with AMS-02 proton fluxes.* Master's thesis, Universidade Técnica de Lisboa, 2012.

[60] L.J. Gleeson and W.I. Axford. "Cosmic rays in the interplanetary medium". *The Astrophysical Journal*, 149: L115–L118, 1967. doi:10.1086/180070.

[61] A.H. Compton and I.A. Getting. "An apparent effect of galactic rotation on the intensity of cosmic rays". *Physical Review*, 47(1):817–821, 1935. ADS:10.1103/PhysRev.47.817.

[62] L.J. Gleeson and W.I. Axford. "The Compton-Getting effect". *Astrophysics and Space Science*, 2(4):431–437, 1968. doi:10.1007/BF02175919.

[63] J.R. Jokipii. "Cosmic-ray propagation. I. Charged particles in a random magnetic field". *The Astrophysical Journal*, 146:480–487, 1966. doi:10.1086/148912.

[64] W.H. Matthaeus, G.Qin, J.W. Bieber, and G.P. Zank. "Nonlinear collisionless perpendicular diffusion of charged particles". *The Astrophysical Journal*, 590(1):L53–L56, 2003. doi:10.1086/376613.

[65] J.A. Earl. "The diffusive idealization of charged-particle transport in random magnetic fields". *The Astrophysical Journal*, 193:231–242, 1974. doi:10.1086/153152.

[66] R. Schlickeiser. *Cosmic ray astrophysics.* Springer, 2002. ADS:2002cra..book.....S.

[67] A. Shalchi and R. Schlickeiser. "The parallel mean free path of heliospheric cosmic rays in composite slab/two-dimensional geometry. I. The damping model of dynamical turbulence". *The Astrophysical Journal*, 604(2): 861–873, 2004. doi:10.1086/382065.

[68] A. Teufel and R. Schlickeiser. "Analytic calculation of the parallel mean free path of heliospheric cosmic rays. I. Dynamical magnetic slab turbulence and random sweeping slab turbulence". *Astronomy & Astrophysics*, 393 (2):703–715, 2002. doi:10.1051/0004-6361:20021046.

[69] A. Teufel and R. Schlickeiser. "Analytic calculation of the parallel mean free path of heliospheric cosmic rays. II. Dynamical magnetic slab turbulence and random sweeping slab turbulence with finite wave power at small wavenumbers". *Astronomy & Astrophysics*, 397(1):15–25, 2003. doi:10.1051/0004-6361:20021471.

[70] J.R. Jokipii, E.H. Levy, and W.B. Hubbard. "Effects of particle drift on cosmic-ray transport. I – General properties, application to solar modulation". *The Astrophysical Journal*, 213:861–868, 1977. doi:10.1086/155218.

[71] B. Heber and M.S. Potgieter. "Cosmic rays at high heliolatitudes". *Space Science Reviews*, 127(1):117–194, 2006. doi:10.1007/s11214-006-9085-y.

[72] J. Giacalone. "Particle transport and acceleration at corotating interaction regions". *Advances in Space Research*, 23(3):581–590, 1999. doi:10.1016/S0273-1177(99)80014-3.

[73] J. Minnie, J.W. Bieber, W.H. Matthaeus, and R.A. Burger. "Suppression of particle drifts by urbulence". *The Astrophysical Journal*, 670(2):1149–1158, 2006. doi:10.1086/522026.

[74] R.C. Tautz and A. Shalchi. "Drift coefficients of charged particles in turbulent magnetic fields". *The Astrophysical Journal*, 744(2):125, 2012. doi:10.1088/0004-637X/744/2/125.

[75] M.D. Ngobeni and M.S. Potgieter. "Modelling the effects of scattering parameters on particle-drift in the solar modulation of galactic cosmic rays". *Advances in Space Research*, 56(7):1525–1537, 2015. doi:10.1016/j.asr.2015.06.034.

[76] L.J. Gleeson and W.I. Axford. "Solar modulation of galactic cosmic rays". *The Astrophysical Journal*, 154: 1011–1026, 1968. doi:10.1086/149822.

[77] R.A. Caballero-Lopez and H. Moraal. "Limitations of the force field equation to describe cosmic ray modulation". *Journal of Geophysical Research (Space Physics)*, 109(1):101, 2004. doi:10.1029/2003JA010098.

[78] M.Y. Khlopov, S.G. Rubin, and A.S. Sakharov. "Possible origin of antimatter regions in the baryon dominated universe". *Physical Review D*, 62(8):083505, 2000. doi:10.1103/PhysRevD.62.083505.

[79] A. Kounine. "The Alpha Magnetic Spectrometer on the International Space Station". *International Journal of Modern Physics E*, 21(08):1230005, 2012. doi:10.1142/S0218301312300056.

[80] F. Zwicky. "Die Rotverschiebung von extragalaktischen Nebeln". *Helvetica Physica Acta*, 6:1101–127, 1933. ADS:1933AcHPh...6..110Z.

[81] V.C. Rubin and W.K. Jr. Ford. "Rotation of the Andromeda nebula from a spectroscopic survey of emission regions". *The Astrophysical Journal*, 159:379–404, 1970. doi:10.1086/150317.

[82] L. Bergström. "Dark matter candidates". *New Journal of Physics*, 11(10):105006, 2009. doi:10.1088/1367-2630/11/10/105006.

[83] M.S. Turner and F. Wilczek. "Positron line radiation as a signature of particle dark matter in the halo". *Physical Review D*, 42(4):1001–1007, 1990. doi:10.1103/PhysRevD.42.1001.

[84] F. Donato, N. Fornengo, and P. Salati. "Antideuterons as a signature of supersymmetric dark matter". *Physical Review D*, 62(4):043003, 2000. doi:10.1103/PhysRevD.62.043003.

[85] M. Cirelli, G. Corcella, A. Hektor, et al. "PPPC 4 DM ID: a poor particle physicist cookbook for dark matter indirect detection". *Journal of Cosmology and Astro-Particle Physics*, 2011(03):051, 2011. doi:10.1088/1475-7516/2011/03/051.

[86] D. Hooper, P. Blasi, and P.D. Serpico. "Pulsars as the sources of high energy cosmic ray positrons". *Journal of Cosmology and Astro-Particle Physics*, 2009(1):025, 2009. doi:10.1088/1475-7516/2009/01/025.

[87] M. Aguilar et al. (AMS-02 Collaboration). "First result from the Alpha Magnetic Spectrometer on the International Space Station: precision measurement of the positron fraction in primary cosmic rays of 0.5–350 GeV". *Physical Review Letters*, 110(14):141102, 2013. doi:10.1103/PhysRevLett.110.141102.

[88] M. Aguilar et al. (AMS-02 Collaboration). "Antiproton flux, antiproton-to-proton flux ratio, and properties of elementary particle fluxes in primary cosmic rays measured with the Alpha Magnetic Spectrometer on the International Space Station". *Physical Review Letters*, 117(9):091103, 2016. doi:10.1103/PhysRevLett.117.091103.

[89] M. Aguilar et al. (AMS-02 Collaboration). "Precision measurement of the proton flux in primary cosmic rays from rigidity 1 GV to 1.8 TV with the Alpha Magnetic Spectrometer on the International Space Station". *Physical Review Letters*, 114(17):171103, 2015. doi:10.1103/PhysRevLett.114.171103.

[90] M. Aguilar et al. (AMS-02 Collaboration). "Precision measurement of the helium flux in primary cosmic rays of rigidities 1.9 GV to 3 TV with the Alpha Magnetic Spectrometer on the International Space Station". *Physical Review Letters*, 115(21):211101, 2015. doi:10.1103/PhysRevLett.115.211101.

[91] M. Aguilar et al. (AMS-02 Collaboration). "Precision measurement of the boron to carbon flux ratio in cosmic rays from 1.9 GV to 2.6 TV with the Alpha Magnetic Spectrometer on the International Space Station". *Physical Review Letters*, 117(23):231102, 2016. doi:10.1103/PhysRevLett.117.231102.

[92] K. Whitman, V. Bindi, C. Consolandi, C. Corti, and B. Yamashiro. "Implications of improved measurements of the highest energy SEPs by AMS and PAMELA". *Advances in Space Research*, In press, 2017. doi:10.1016/j.asr.2017.02.042.

[93] V.L. Ginzburg. "Transition radiation and transition scattering". *Physica Scripta*, T2A:182–191, 1982. doi:10.1088/0031-8949/1982/T2A/024.

[94] P. von Doetinchem, S. Fopp, W. Karpinski, et al. "Performance of the AMS-02 transition radiation detector". *Nuclear Instruments and Methods in Physics Research A*, 558(2):526–535, 2006. doi:10.1016/j.nima.2005.12.187.

[95] V. Bindi, D. Casadei, G. Castellini, et al. "The scintillator detector for the fast trigger and time-of-flight (TOF) measurement of the space experiment AMS-02". *Nuclear Instruments and Methods in Physics Research A*, 623 (3):968–981, 2010. doi:10.1016/j.nima.2010.08.019.

[96] V. Bindi, A. Basili, D. Casadei, et al. "The TOF-ACC flight electronics for the fast trigger and time of flight of the AMS-02 cosmic ray spectrometer". *Nuclear Instruments and Methods in Physics Research A*, 707:99–113, 2013. doi:10.1016/j.nima.2012.12.089.

[97] L. Quadrani, V. Bindi, E. Choumilov, et al. "The AMS-02 time of flight (TOF) system: construction and overall performances in space". In *Proceedings of the 33rd International Cosmic Ray Conference (Rio de Janeiro)*, 2013. `http://www.cbpf.br/~icrc2013/papers/icrc2013-1046.pdf`.

[98] T. Bruch and W. Wallraff. "The Anti-Coincidence Counter shield of the AMS tracker". *Nuclear Instruments and Methods in Physics Research A*, 572(1):505–507, 2007. doi:10.1016/j.nima.2006.10.376.

[99] P. von Doetinchem, W. Karpinski, T. Kirn, et al. "The AMS-02 anticoincidence counter". *Nuclear Physics B - Proceedings Supplements*, 197(1):15–18, 2009. doi:10.1016/j.nuclphysbps.2009.10.025.

[100] K. Lübelsmeyer, A. Schultz von Dratzig, M. Wlochal, et al. "Upgrade of the Alpha Magnetic Spectrometer (AMS-02) for long term operation on the International Space Station (ISS)". *Nuclear Instruments and Methods in Physics Research A*, 654(1):639–648, 2011. doi:10.1016/j.nima.2011.06.051.

[101] M. Duranti. *Measurement of the atmospheric muon flux on ground with the AMS-02 detector*. PhD thesis, Università degli Studi di Perugia, 2011.

[102] P. Zuccon. "The AMS silicon tracker: construction and performance". *Nuclear Instruments and Methods in Physics Research A*, 596(1):74–78, 2008. doi:10.1016/j.nima.2008.07.116.

[103] P. Zuccon, G. Ambrosi, P. Azzarello, et al. "AMS-02 track reconstruction and rigidity measurement". In *Proceedings of the 33rd International Cosmic Ray Conference (Rio de Janeiro)*, 2013. `http://www.cbpf.br/~icrc2013/papers/icrc2013-1064.pdf`.

[104] S. Natale and S. Schael. "The AMS-2 Tracker Alignment System: design and performance". In *Proceedings of the 31st International Cosmic Ray Conference (Łódź)*, 2009. `http://icrc2009.uni.lodz.pl/proc/pdf/icrc0245.pdf`.

[105] P. Saouter, G. Ambrosi, P. Azzarello, et al. "Nuclear charge measurement with the AMS-02 silicon tracker". In *Proceedings of the 33rd International Cosmic Ray Conference (Rio de Janeiro)*, 2013. `http://www.cbpf.br/~icrc2013/papers/icrc2013-0789.pdf`.

[106] Z. Zhang, X.-H. Sun, G.-N. Tong, et al. "Stable and self-adaptive performance of mechanically pumped CO_2 two-phase loops for AMS-02 tracker thermal control in vacuum". *Applied Thermal Engineering*, 31(17):3783–3791, 2011. doi:10.1016/j.applthermaleng.2011.07.015.

[107] M. Aguilar-Benitez, L. Arruda, F. Barao, et al. "In-beam aerogel light yield characterization for the AMS RICH detector". *Nuclear Instruments and Methods in Physics Research A*, 614(2):237–249, 2010. doi:10.1016/j.nima.2009.12.027.

[108] H. Liu, J. Casaus, F. Giovacchini, A. Oliva, and X. Xia. "The RICH detector of AMS-02: 5 years of operation in space". *Nuclear Instruments and Methods in Physics Research A*, In press, 2016. doi:10.1016/j.nima.2016.12.011.

[109] F. Cervelli, G. Chen, G. Coignet, et al. "A reduced scale e.m. calorimeter prototype for the AMS-02 experiment". *Nuclear Instruments and Methods in Physics Research A*, 490(1):132–139, 2002. doi:10.1016/S0168-9002(02)00915-4.

[110] F. Cadoux, F. Cervelli, V. Chambert-Hermel, et al. "The AMS-02 electromagnetic calorimeter". *Nuclear Physics B - Proceedings Supplements*, 113(1):156–165, 2002. doi:10.1016/S0920-5632(02)01836-4.

[111] C. Adloff, L. Basara, G. Bigongiari, et al. "The AMS-02 lead-scintillating fibres Electromagnetic Calorimeter". *Nuclear Instruments and Methods in Physics Research A*, 714:147–154, 2002. doi:10.1016/j.nima.2013.02.020.

[112] S. Di Falco et al. (AMS-02/ECAL Collaboration). "Performance of the AMS-02 electromagnetic calorimeter in space". In *Proceedings of the 33rd International Cosmic Ray Conference (Rio de Janeiro)*, 2013. `http://www.cbpf.br/~icrc2013/papers/icrc2013-0855.pdf`.

[113] V. Vagelli. *Identification of positrons and electrons in the cosmic radiation with the electromagnetic calorimeter ECAL for the AMS-02 experiment*. Master's thesis, Università degli Studi di Pisa, 2011.

[114] C. Corti. *Measurement of the positrons fraction in cosmic rays with AMS-02*. Master's thesis, Università degli Studi di Pisa, 2012.

[115] C.H. Chung et al. (AMS-02 Collaboration). "AMS on ISS – Construction of a particle physics detector on the International Space Station". 2004. http://www-ekp.physik.uni-karlsruhe.de/~deboer/html/Forschung/AMS.pdf.

[116] S. Agostinelli et al. (Geant4 Collaboration). "Geant4 – A simulation toolkit". *Nuclear Instruments and Methods in Physics Research A*, 506(3):250–303, 2003. doi:10.1016/S0168-9002(03)01368-8. http://geant4.cern.ch/.

[117] J. Allison et al. (Geant4 Collaboration). "Geant4 developments and applications". *IEEE Transactions on Nuclear Science*, 53(2):270–278, 2006. doi:10.1109/TNS.2006.869826.

[118] J. Allison et al. (Geant4 Collaboration). "Recent developments in Geant4". *Nuclear Instruments and Methods in Physics Research A*, 835:186–225, 2016. doi:10.1016/j.nima.2016.06.125.

[119] N. Tomassetti and A. Oliva. "Identification of light cosmic-ray nuclei with AMS-02". In *Proceedings of the 33rd International Cosmic Ray Conference (Rio de Janeiro)*, 2013. http://www.cbpf.br/~icrc2013/papers/icrc2013-0896.pdf.

[120] M. Pohl. "AMS tracking in-orbit performance". In *Proceedings of the 24th International Workshop on Vertex Detectors (Santa Fe)*, *Proceedings of Science*, 2015. arXiv:1508.07759.

[121] D.K. Singh, R.P. Singh, and A.K. Kamra. "The electrical environment of the Earth's atmosphere: a review". *Space Science Reviews*, 113(3):375–408, 2004. doi:10.1023/B:SPAC.0000046747.32359.d8.

[122] M. Ackermann et al. (Fermi LAT Collaboration). "In-flight measurement of the absolute energy scale of the Fermi Large Area Telescope". *Astroparticle Physics*, 35(6):346–353, 2012. doi:10.1016/j.astropartphys.2011.10.007.

[123] NASA Jet Propulsion Laboratory. "Space radiation effects on microelectronics". http://parts.jpl.nasa.gov/docs/Radcrs_Final.pdf.

[124] V. Karimäki. "Explicit covariance matrix for particle measurement precision". *Nuclear Instruments and Methods in Physics Research A*, 410(2):284–292, 1998. doi:10.1016/S0168-9002(98)00279-4.

[125] T. Bowen, M. Di Corato, W.H. Moore, and G. Tagliaferri. "Absorption cross sections of carbon, iron and lead for 1.5 GeV negative pions and 2.8 GeV protons". *Il Nuovo Cimento*, 9(5):908–919, 1958. doi:10.1007/BF02903132.

[126] G. Bellettini, G. Cocconi, A.N. Diddens, et al. "Proton-nuclei cross sections at 20 GeV". *Nuclear Physics*, 79 (3):609–624, 1966. doi:10.1016/0029-5582(66)90267-7.

[127] S.P. Denisov, S.V. Donskov, Yu.P. Gorin, et al. "Absorption cross sections for pions, kaons, protons and antiprotons on complex nuclei in the 6 to 60 GeV/c momentum range". *Nuclear Physics B*, 61:62–76, 1973. doi:10.1016/0550-3213(73)90351-9.

[128] A.S. Carroll, I-H. Chiang, T.F. Kycia, et al. "Absorption cross section of $\pi^{\pm}$, $K^{\pm}$, p and p on nuclei between 60 and 280 GeV/c". *Physics Letters B*, 80(3):319–322, 1979. doi:10.1016/0370-2693(79)90226-0.

[129] J.R. Letaw, R. Silberberg, and C.H. Tsao. "Proton-nucleus total inelastic cross sections – an empirical formula for E greater than 10 MeV". *The Astrophysical Journal Supplement Series*, 51:271–275, 1983. doi:10.1086/190849.

[130] N. Abgrall et al. (NA61/SHINE Collaboration). "Measurements of cross sections and charged pion spectra in proton-carbon interactions at 31 GeV/c". *Physical Review C*, 84(3):034604, 2011. doi:10.1103/PhysRevC.84.034604.

[131] M.J. Oreglia. *A study of the reactions $\psi' \to \gamma\gamma\psi$*. PhD thesis, SLAC, 1980.

[132] J. Bartles. "Twenty-seven day recurrences in terrestrial-magnetic and solar activity, 1923–1933". *Terrestrial Magnetism and Atmospheric Electricity*, 39(3):201–202, 1934. doi:10.1029/TE039i003p00201.

[133] SILSO World Data Center, Royal Observatory of Belgium. "The international sunspot number". *International Sunspot Number Monthly Bulletin and online catalogue*. `http://www.sidc.be/silso`.

[134] J.T. Hoeksema. "The large-scale structure of the heliospheric current sheet during the Ulysses epoch". *Space Science Reviews*, 72(1):137–148, 1995. doi:10.1007/BF00768770.

[135] X. Sun, J.T. Hoeksema, Y. Liu, and J. Zhao. "On polar magnetic field reversal and surface flux transport during solar cycle 24". *The Astrophysical Journal*, 798(2):114, 2015. doi:10.1088/0004-637X/798/2/114.

[136] O. Tange. "GNU parallel – The command-line power tool". *;login: The USENIX Magazine*, 36(1):42–47, 2011. `http://www.gnu.org/s/parallel`.

[137] O. Adriani et al. (PAMELA Collaboration). "PAMELA measurements of cosmic-ray proton and helium spectra". *Science*, 332(6025):69–72, 2011. doi:10.1126/science.1199172.

[138] I.G. Usoskin, K. Alanko-Huotari, G.A. Kovaltsov, and K. Mursula. "Heliospheric modulation of cosmic rays: monthly reconstruction for 1951–2004". *Journal of Geophysical Research (Space Physics)*, 110(12):12108, 2005. doi:10.1029/2005JA011250.

[139] Y. Shikaze et al. (BESS Collaboration). "Measurements of 0.2–20 GeV/n cosmic-ray proton and helium spectra from 1997 through 2002 with the BESS spectrometer". *Astroparticle Physics*, 28(1):154–167, 2007. doi:10.1016/j.astropartphys.2007.05.001.

[140] M. Garcia-Munoz, G.M. Mason, and J.A. Simpson. "The anomalous He-4 component in the cosmic-ray spectrum at below approximately 50 MeV per nucleon during 1972-1974". *The Astrophysical Journal*, 202(1):265–275, 1975. doi:10.1086/153973.

[141] U.W. Langner and M.S. Potgieter. "Solar wind termination shock and heliosheath effects on the modulation of protons and antiprotons". *Journal of Geophysical Research (Space Physics)*, 109(1):01103, 2004. doi:10.1029/2003JA010158.

[142] W.R. Webber and P.R. Higbie. "Production of cosmogenic Be nuclei in the Earth's atmosphere by cosmic rays: its dependence on solar modulation and the interstellar cosmic ray spectrum". *Journal of Geophysical Research (Space Physics)*, 108(9):1355, 2003. doi:10.1029/2003JA009863.

[143] A. Neronov, D.V. Semikoz, and A.M. Taylor. "Low-energy break in the spectrum of galactic cosmic rays". *Physical Review Letters*, 108(5):051105, 2012. doi:10.1103/PhysRevLett.108.051105.

[144] F. James and M. Roos. "Minuit – a system for function minimization and analysis of the parameter errors and correlations". *Computer Physics Communication*, 10(6):343–367, 1975. doi:10.1016/0010-4655(75)90039-9.

[145] G.D. Lafferty and T.R. Wyatt. "Where to stick your data points: the treatment of measurements within wide bins". *Nuclear Instruments and Methods in Physics Research A*, 355(2):541–547, 1994. doi:10.1016/0168-9002(94)01112-5.

[146] O. Adriani et al. (PAMELA Collaboration). "Time dependence of the proton flux measured by PAMELA during the 2006 July–2009 December solar minimum". *The Astrophysical Journal*, 765(2):91, 2013. doi:10.1088/0004-637X/765/2/91.

[147] M.S. Potgieter, E.E. Vos, M. Boezio, et al. "Modulation of galactic protons in the heliosphere during the unusual solar minimum of 2006 to 2009". *Solar Physics*, 289(1):391–406, 2014. doi:10.1007/s11207-013-0324-6.

[148] E.E. Vos and M.S. Potgieter. "New modeling of galactic proton modulation during the minimum of solar cycle 23/24". *The Astrophysical Journal*, 815(2):119, 2015. doi:10.1088/0004-637X/815/2/119.

[149] J. Gieseler, B. Heber, and K. Herbst. "The solar modulation potential derived by spacecraft measurements modified to describe GCRs at energies below neutron monitors and above". In *Proceedings of the 34th International Cosmic Ray Conference (The Hague)*, *Proceedings of Science*, 2015. `https://indico.cern.ch/event/344485/contributions/1744430`.

[150] T. Sanuki et al. (BESS Collaboration). "Precise measurement of cosmic-ray proton and helium spectra with the BESS spectrometer". *The Astrophysical Journal*, 545(2):1135–1142, 2000. doi:10.1086/317873.

[151] J. Wang et al. (BESS Collaboration). "Measurement of cosmic-ray hydrogen and helium and their isotopic composition with the BESS experiment". *The Astrophysical Journal*, 564(1):244–259, 2002. doi:10.1086/324140.

[152] S. Haino et al. (BESS Collaboration). "Measurements of primary and atmospheric cosmic-ray spectra with the BESS-TeV spectrometer". *Physics Letters B*, 594(1-2):35–46, 2004. doi:10.1016/j.physletb.2004.05.019.

[153] K. Abe et al. (BESS Collaboration). "Measurements of cosmic-ray proton and helium spectra from the BESS-Polar long-duration balloon flights over Antarctica". *The Astrophysical Journal*, 822(2):65, 2016. doi:10.3847/0004-637X/822/2/65.

[154] K. Herbst, A. Kopp, B. Heber, et al. "On the importance of the local interstellar spectrum for the solar modulation parameter". *Journal of Geophysical Research (Atmospheres)*, 115(D1):00I20, 2010. doi:10.1029/2009JD012557.

[155] Y.-M. Wang, N.R. Sheeley Jr., and M.D. Andrews. "Polarity reversal of the solar magnetic field during cycle 23". *Journal of Geophysical Research (Space Physics)*, 107(12):1465, 2002. doi:10.1029/2002JA009463.

[156] D. Bisschoff and M.S. Potgieter. "New local interstellar spectra for protons, helium and carbon derived from PAMELA and Voyager 1 observations". *Astrophysics and Space Science*, 361(2):48, 2016. doi:10.1007/s10509-015-2633-8.

[157] A. Ghelfi, F. Barao, L. Derome, and D. Maurin. "Non-parametric determination of H and He interstellar fluxes from cosmic-ray data". *Astronomy & Astrophysics*, 591:A94, 2016. doi:10.1051/0004-6361/201527852.

[158] K. Herbst, R. Muscheler, and B. Heber. "The new local interstellar spectra and their influence on the production rates of the cosmogenic radionuclides ^{10}Be and ^{14}C". *Journal of Geophysical Research (Space Physics)*, 122(1):23–34, 2017. doi:10.1002/2016JA023207.

[159] U.W. Langner, M.S. Potgieter, and W.R. Webber. "Modulation of cosmic ray protons in the heliosheath". *Journal of Geophysical Research (Space Physics)*, 108(10):8039, 2003. doi:10.1029/2003JA009934.

[160] I.V. Moskalenko, A.W. Strong, F.J. Ormes, M.S. Potgieter, and U.W. Langner. "Secondary antiprotons in cosmic rays". In *Proceedings of the 27th International Cosmic Ray Conference (Hamburg)*, 2001. arXiv:astro-ph/0106503.

[161] I.G. Usoskin, G.A. Bazilevskaya, and G.A. Kovaltsov. "Solar modulation parameter for cosmic rays since 1936 reconstructed from ground-based neutron monitors and ionization chambers". *Journal of Geophysical Research (Space Physics)*, 116(2):02104, 2011. doi:10.1029/2010JA016105.

[162] A. Gil, I.G. Usoskin, G.A. Kovaltsov, et al. "Can we properly model the neutron monitor count rate?". *Journal of Geophysical Research (Space Physics)*, 120(9):7172–7178, 2015. doi:10.1002/2015JA021654.

[163] A.L. Mishev, I.G. Usoskin, and G.A. Kovaltsov. "Neutron monitor yield function: new improved computations". *Journal of Geophysical Research (Space Physics)*, 118(6):2783–2788, 2013. doi:10.1002/jgra.50325.

[164] L.A. Fisk. "Solar modulation of galactic cosmic rays, 2". *Journal of Geophysical Research*, 76(1):221–226, 1971. doi:10.1029/JA076i001p00221.

[165] L.A. Fisk. "Possible evidence for latitude-dependent cosmic-ray modulation". In *Proceedings of the 14th International Cosmic Ray Conference (Munich)*, 1975. ADS:1975ICRC....3..905F.

[166] L.A. Fisk. "Solar modulation of galactic cosmic rays. IV – Latitude-dependent modulation". *Journal of Geophysical Research*, 81(25):4646–4650, 1976. doi:10.1029/JA081i025p04646.

[167] H. Moraal and J. Gleeson. "Three-dimensional models of the galactic cosmic-ray modulation". In *Proceedings of the 14th International Cosmic Ray Conference (Munich)*, 1975. ADS:1975ICRC...12.4189M.

[168] S. Cecchini and J.J. Quenby. "Three-dimensional models of galactic cosmic ray modulation". In *Proceedings of the 14th International Cosmic Ray Conference (Munich)*, 1975. ADS:1975ICRC....3..911C.

[169] J.R. Jokipii and D.A. Kopriva. "Effects of particle drift on the transport of cosmic rays. III – Numerical models of galactic cosmic-ray modulation". *The Astrophysical Journal*, 234:384–392, 1979. doi:10.1086/157506.

[170] H. Moraal, L.J. Gleeson, and G.M. Webb. "Effects of charged particle drifts on the modulation of the intensity of galactic cosmic rays". In *Proceedings of the 16th International Cosmic Ray Conference (Tokyo)*, 1979. ADS:1979ICRC....3....1G.

[171] M.S. Potgieter. *The modulation of galactic cosmic rays as described by a three-dimensional drift model.* PhD thesis, Potchefstroom University for CHE, 1984.

[172] R.A. Burger. *On the theory and application of drift motion of charged particles in inhomogeneous magnetic fields.* PhD thesis, Potchefstroom University for CHE, 1987.

[173] M.S. Potgieter and H. Moraal. "A drift model for the modulation of galactic cosmic rays". *The Astrophysical Journal*, 294:425–440, 1985. doi:10.1086/163309.

[174] R.A. Burger and M.S. Potgieter. "The calculation of neutral sheet drift in two-dimensional cosmic-ray modulation models". *The Astrophysical Journal*, 339:501–511, 1989. doi:10.1086/167313.

[175] M. Hattingh. *Drift of cosmic rays at a wavy neutral sheet in the heliosphere (in Afrikaans).* Master's thesis, Potchefstroom University for CHE, 1993.

[176] U.W. Langner. *Effects of termination shock acceleration on cosmic rays in the heliosphere*. PhD thesis, Potchefstroom University for CHE, 2004.

[177] J. Kóta and J.R. Jokipii. "Effects of drift on the transport of cosmic rays. VI – A three-dimensional model including diffusion". *The Astrophysical Journal*, 265:573–581, 1983. doi:10.1086/160701.

[178] M. Hattingh. *The modulation of galactic cosmic rays in a three-dimensional heliosphere*. PhD thesis, Potchefstroom University for CHE, 1998.

[179] S.E.S Ferreira. *A study of the modulation of cosmic ray electrons in the heliosphere*. Master's thesis, Potchefstroom University for CHE, 1998.

[180] J.S. Perko and L.A. Fisk. "Solar modulation of galactic cosmic rays. V – Time-dependent modulation". *Journal of Geophysical Research (Space Physics)*, 88(11):9033–9036, 1983. doi:10.1029/JA088iA11p09033.

[181] J.A. le Roux. *The solar modulation of galactic cosmic rays as described by a time-dependent drift model*. PhD thesis, Potchefstroom University for CHE, 1990.

[182] H. Fichtner, M.S. Potgieter, S.E.S. Ferreira, B. Heber, and R.A. Burger. "Time-dependent 3-D modelling of the heliospheric propagation of few-MeV electrons". In *Proceedings of the 27th International Cosmic Ray Conference (Hamburg)*, 2001. ADS:2001ICRC....9.3666F.

[183] J.R. Jokipii. "Particle acceleration at a termination shock 1. Application to the solar wind and the anomalous component". *Journal of Geophysical Research (Space Physics)*, 91(3):2929–2932, 1986. doi:10.1029/JA091iA03p02929.

[184] M.S. Potgieter. "Heliospheric terminal shock acceleration and modulation of the anomalous cosmic-ray component". *Advances in Space Research*, 9(12):21–24, 1989. doi:10.1016/0273-1177(89)90304-9.

[185] R. Steenkamp. *Shock acceleration as source of the anomalous component of cosmic rays in the heliosphere*. PhD thesis, Potchefstroom University for CHE, 1995.

[186] J.A. le Roux, M.S. Potgieter, and V.S. Ptuskin. "A transport model for the diffusive shock acceleration and modulation of anomalous cosmic rays in the heliosphere". *Journal of Geophysical Research (Space Physics)*, 101(3):4791–4803, 1996. doi:10.1029/95JA03472.

[187] R.D. Strauss. *Modelling of anomalous cosmic rays*. Master's thesis, North-West University, 2010.

[188] R.D. Ngobeni. *Modeling of galactic cosmic rays in the heliosphere*. PhD thesis, North-West University, 2015.

[189] P.L. Prinsloo. *Acceleration of cosmic rays in the outer heliosphere*. Master's thesis, North-West University, 2016.

[190] M.S. Potgieter and J.A. le Roux. "The long-term heliospheric modulation of galactic cosmic rays according to a time-dependent drift model with merged interaction regions". *The Astrophysical Journal*, 423:817–827, 1994. doi:10.1086/173860.

[191] J.A. le Roux and M.S. Potgieter. "The simulation of complete 11 and 22 year modulation cycles for cosmic rays in the heliosphere using a drift model with global merged interaction regions". *The Astrophysical Journal*, 442:847–851, 1995. doi:10.1086/175487.

[192] M. Zhang. "A Markov stochastic process theory of cosmic-ray modulation". *The Astrophysical Journal*, 513(1): 409–420, 1999. doi:10.1086/306857.

[193] V. Florinski and N.V. Pogorelov. "Four-dimensional transport of galactic cosmic rays in the outer heliosphere and heliosheath". *The Astrophysical Journal*, 701(1):642–651, 2009. doi:10.1088/0004-637X/701/1/642.

[194] C. Pei, J.W. Bieber, R.A. Burger, and J. Clem. "A general time-dependent stochastic method for solving Parker's transport equation in spherical coordinates". *Journal of Geophysical Research (Space Physics)*, 115 (12):12107, 2010. doi:10.1029/2010JA015721.

[195] R.D. Strauss, M.S. Potgieter, I. Büsching, and A. Kopp. "Modeling the modulation of galactic and Jovian electrons by stochastic processes". *The Astrophysical Journal*, 735(2):83, 2011. doi:10.1088/0004-637X/735/2/83.

[196] S. Della Torre. *A Monte Carlo approach for the solar modulation.* PhD thesis, Università degli studi dell'Insubria, 2012.

[197] R.D. Strauss. *Modelling of cosmic rays in the heliosphere by stochastic processes.* PhD thesis, North-West University, 2013.

[198] X. Luo, M. Zhang, H.K. Rassoul, N.V. Pogorelov, and J. Heerikhuisen. "Galactic cosmic-ray modulation in a realistic global magnetohydrodynamic heliosphere". *The Astrophysical Journal*, 764(1):85, 2013. doi:10.1088/0004-637X/764/1/85.

[199] R.D. Strauss, M.S. Potgieter, A. Kopp, and I. Büsching. "On the propagation times and energy losses of cosmic rays in the heliosphere". *Journal of Geophysical Research (Space Physics)*, 116(12):12105, 2011. doi:10.1029/2011JA016831.

[200] E. Vos. *Cosmic ray modulation processes in the heliosphere.* Master's thesis, North-West University, 2011.

[201] J. Crank and P. Nicholson. "A practical method for numerical evaluation of solutions of partial differential equations of the heat-conduction type". *Mathematical Proceedings of the Cambridge Philosophical Society*, 43 (1):50–67, 1947. doi:10.1017/S0305004100023197.

[202] D.W. Peaceman and H.H. Rachford Jr. "The numerical solution of parabolic and elliptic differential equations". *Journal of the Society for Industrial and Applied Mathematics*, 3(1):28–41, 1955. doi:10.1137/0103003.

[203] J. Douglas Jr. "On the numerical integration of $\partial^2 u/\partial x^2 + \partial^2 u/\partial y^2 = \partial u/\partial t$ by implicit methods". *Journal of the Society for Industrial and Applied Mathematics*, 3(1):42–65, 1955. doi:10.1137/0103004.

[204] J. Douglas Jr. "Alternating direction methods for three space variables". *Numerische Mathematik*, 4(1):41–63, 1962. doi:10.1007/BF01386295.

[205] M.S. Potgieter and L.J. Haasbroek. "The simulation of base-line cosmic-ray modulation for the Ulysses trajectory". In *Proceedings of the 23rd International Cosmic Ray Conference (Calgary)*, 1993. ADS:1993ICRC....3..457P.

[206] J. Kóta and J.R. Kokipii. "3-D distribution of cosmic rays in the outer heliosphere". In *Proceedings of the 24th International Cosmic Ray Conference (Rome)*, 1995. ADS:1995ICRC....4..680K.

[207] U.W. Langner. *Effects of different local interstellar spectra on the heliospheric modulation of cosmic rays.* Master's thesis, Potchefstroom University for CHE, 2000.

[208] J. Nickolls, I. Buck, M. Garland, and K. Skadron. "Scalable Parallel Programming with CUDA". *ACM Queue – GPU Computing*, 6(2):40–53, 2008. doi:10.1145/1365490.1365500.

[209] L. Dagum and R. Menon. "OpenMP: an industry standard API for shared-memory programming". *IEEE Computational Science and Engineering*, 5(1):46–55, 1998. doi:10.1109/99.660313.

[210] OpenMP Architecture Review Board. "OpenMP Application Program Interface, version 3.0", 2008. `http://www.openmp.org/mp-documents/spec30.pdf`.

[211] E. Vos. *Modelling charge-sign dependent modulation of cosmic rays in the heliosphere*. PhD thesis, North-West University, 2016.

[212] L.-L. Zhao, G. Qin, M. Zhang, and B. Heber. "Modulation of galactic cosmic rays during the unusual solar minimum between cycles 23 and 24". *Journal of Geophysical Research (Space Physics)*, 119(3):1493, 2014. doi:10.1002/2013JA019550.

[213] R.A. Burger, M.S. Potgieter, and B. Heber. "Rigidity dependence of cosmic ray proton latitudinal gradients measured by the Ulysses spacecraft: implications for the diffusion tensor". *Journal of Geophysical Research (Space Physics)*, 105(12):27447–27455, 2000. doi:10.1029/2000JA000153.

[214] J.W. Bieber, W.H. Matthaeus, A. Shalchi, and G. Qin. "Nonlinear guiding center theory of perpendicular diffusion: general properties and comparison with observation". *Geophysical Research Letters*, 31(10):L10805, 2004. doi:10.1029/2004GL020007.

[215] R. Brun and F. Rademakers. "ROOT – An object oriented data analysis framework". In *Proceedings of the 5th International Workshop on software Engineering and Artificial Intelligence for high energy and nuclear physics (Lausanne)*, *Nuclear Instruments and Methods in Physics Research A*, 389(1-2):81–86, 1997. doi:10.1016/S0168-9002(97)00048-X. `http://root.cern.ch`.